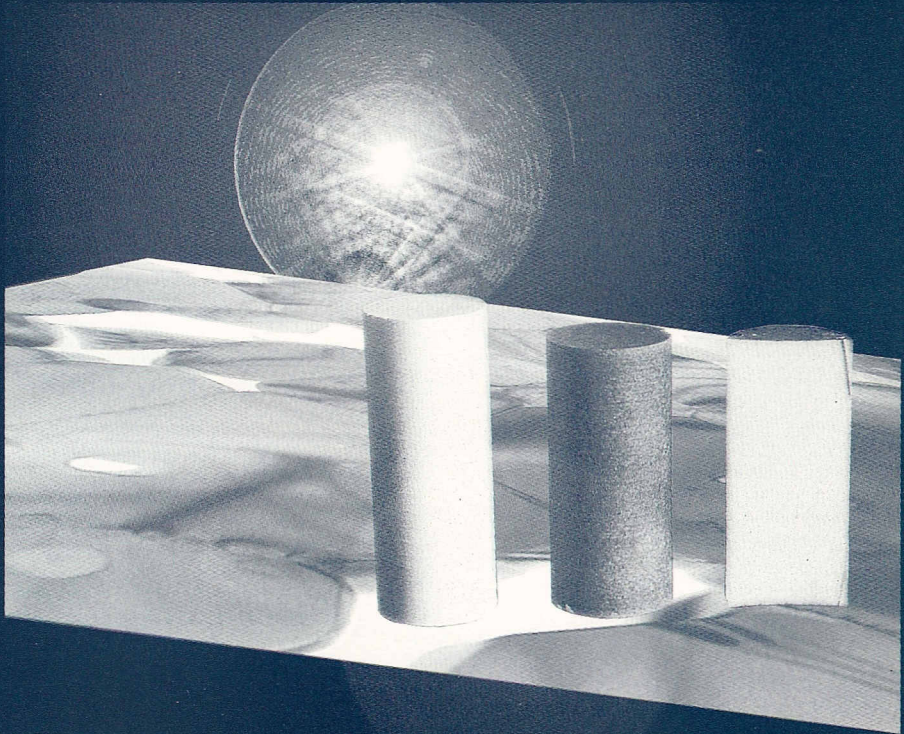


GEOLOGICA ULTRAIECTINA

Mededelingen van de
Faculteit Aardwetenschappen
Universiteit Utrecht

No. 152

Deformation of fine-grained synthetic peridotite under wet conditions



Robert D. McDonnell

GEOLOGICA ULTRAIECTINA

Mededelingen van de
Faculteit Aardwetenschappen
Universiteit Utrecht

No. 152

Deformation of fine-grained synthetic peridotite under wet conditions

Robert D. McDonnell

Artwork cover: **AudioVisuele Dienst**, Aardwetenschappen • Universiteit Utrecht

ISBN : 90-5744-010-5

Deformation of fine-grained synthetic peridotite under wet conditions

Deformatie van fijnkorrelige synthetische peridotiet
in aanwezigheid van water

(met een samenvatting in het Nederlands)

PROEFSCHRIFT

TER VERKRIJGING VAN DE GRAAD VAN DOCTOR AAN DE UNIVERSITEIT
UTRECHT, OP GEZAG VAN DE RECTOR MAGNIFICUS, PROF. DR. H.O. VOORMA,
INGEVOLGE HET BESLUIT VAN HET COLLEGE VAN DEKANEN IN HET OPENBAAR
TE VERDEDIGEN OP DONDERDAG 11 SEPTEMBER 1997 DES NAMIDDAGS TE 12.45
UUR

DOOR

ROBERT DENIS McDONNELL

GEBOREN OP 30 OKTOBER 1963 TE WINDLESHAM, ENGELAND.

PROMOTOR:

PROF. DR. C.J. SPIERS

CO-PROMOTOR:

DR. C.J. PEACH

EXAMINING COMMITTEE:

PROF. DR. B.H.W.S. DE JONG
Utrecht University, the Netherlands.

PROF. DR. S-I. KARATO
University of Minnesota, USA.

PROF. DR. S. MACKWELL
Universitaet Bayreuth, Germany.

PROF. DR. S.H. WHITE
Utrecht University, the Netherlands.

“Making mayonnaise for the first time can be a daunting experience,
but only if the process is not explained properly”

Delia Smith

*for Sue
and in
memory of
my parents*

Contents

| | | |
|------------------|------------------------------------------------------------------------------------------------------------------------------------------|-----------|
| | Summary | II |
| Chapter 1 | Introduction: Problem definition and aims | 15 |
| 1.1. | Scope and motivation | 15 |
| 1.2. | Background | 15 |
| 1.2.1. | Previous work on the rheology of olivine | 15 |
| 1.2.2. | Olivine rheology and the strength of the lithosphere in extension | 17 |
| 1.3. | Problem definition | 18 |
| 1.4. | Present aims | 20 |
| 1.5. | Structure of the thesis | 20 |
| Chapter 2 | Fabrication and characterization of dense fine-grained forsterite and forsterite-enstatite ceramics for deformation studies | 21 |
| 2.1. | Introduction | 21 |
| 2.2. | Background | 23 |
| 2.2.1. | Sol-gel processing - an introduction | 23 |
| 2.2.2. | Previous work on sol-gel synthesis of forsterite and enstatite powders and ceramics | 27 |
| 2.3. | Pilot trials of diphasic sol-gel routes and lessons learned | 30 |
| 2.4. | Final methodology | 32 |
| 2.4.1. | Reagents and reagent proportions | 35 |
| 2.4.2. | Sol-gel stage | 37 |
| 2.4.3. | Reaction sintering | 37 |
| 2.4.4. | Powder processing | 38 |
| 2.4.5. | Ceramic forming | 38 |
| 2.4.6. | Firing | 38 |
| 2.4.7. | Machining | 39 |
| 2.5. | Process progress and material characterization | 39 |
| 2.5.1. | General results | 40 |
| 2.5.2. | Chemical characterization of the final ceramic | 44 |
| 2.5.3. | Density and microstructure of the final ceramic | 47 |
| 2.6. | Discussion | 49 |
| 2.7. | Conclusions | 50 |
| Chapter 3 | Experimental apparatus | 51 |
| 3.1. | Introduction | 51 |
| 3.2. | General configuration | 51 |
| 3.3. | Sample assembly | 58 |
| 3.3.1. | Sample encapsulation | 58 |

| | | |
|--------|-----------------------------------------------------------|----|
| 3.3.2. | Sample holder | 60 |
| 3.4. | Calibration | 60 |
| 3.4.1. | Load cell calibration | 60 |
| 3.4.2. | Load cell pressure correction calibration | 61 |
| 3.4.3. | Compliance calibration | 61 |
| 3.4.4. | Temperature measurement and thermal gradient minimization | 61 |
| 3.5. | Data acquisition and processing | 62 |

| | | |
|------------------|--------------------------------------------------------------------------------------------------|-----------|
| Chapter 4 | Flow behaviour of fine-grained synthetic dunite in the presence of 0.5 wt% H₂O | 63 |
| 4.1. | Introduction | 63 |
| 4.2. | Experimental method | 69 |
| 4.2.1. | Sample preparation | 69 |
| 4.2.2. | Deformation apparatus | 70 |
| 4.2.3. | Hot isostatic pressing (HIPing) stage | 71 |
| 4.2.4. | Deformation testing and termination procedure | 71 |
| 4.2.5. | Data acquisition and processing | 72 |
| 4.3. | HIPing results and mechanical data | 73 |
| 4.4. | Microstructural analysis | 83 |
| 4.4.1. | Techniques | 83 |
| 4.4.2. | General microstructural description | 84 |
| 4.4.3. | Quantitative microstructural data | 92 |
| 4.4.4. | Electron backscatter diffraction | 95 |
| 4.5. | Discussion | 95 |
| 4.5.1. | Interpretation of mechanical data | 95 |
| 4.5.2. | Interpretation of microstructural observations | 99 |
| 4.5.3. | Comparison with previous experiments | 100 |
| 4.5.4. | The role of water | 101 |
| 4.5.5. | Empirical flow relation and its implications | 101 |
| 4.6. | Conclusions | 105 |

| | | |
|------------------|-------------------------------------------------------------------------------------------------------------------|------------|
| Chapter 5 | The effect of varying enstatite content on the deformation behaviour of fine-grained synthetic peridotite. | 107 |
| 5.1. | Introduction | 107 |
| 5.2. | Experiments | 109 |
| 5.2.1. | Sample preparation | 109 |
| 5.2.2. | Deformation apparatus | 111 |
| 5.2.3. | Hot isostatic pressing stage | 111 |
| 5.2.4. | Deformation testing procedure | 112 |
| 5.2.5. | Data acquisition and processing | 112 |
| 5.3. | Results | 113 |
| 5.3.1. | Mechanical results | 113 |
| 5.3.2. | SEM observations | 122 |

| | | |
|-----------|-----------------------------------------------------------------------------------------------------------|-----|
| 5.3.3. | TEM observations | 126 |
| 5.3.4. | Crystallographic orientation data | 131 |
| 5.4. | Discussion | 132 |
| 5.4.1. | HIPing behaviour | 133 |
| 5.4.2. | Flow behaviour and likely mechanisms | 133 |
| 5.4.3. | The relative roles of enstatite content and grain size | 134 |
| 5.4.4. | Implications | 138 |
| 5.5. | Conclusions | 139 |
| | Appendix | 140 |
| | | |
| Chapter 6 | The effect of varying water content on the deformation behaviour of fine-grained synthetic dunite. | 143 |
| 6.1. | Introduction | 143 |
| 6.2. | Experiments | 144 |
| 6.2.1. | Sample preparation | 144 |
| 6.2.2. | Deformation apparatus and testing procedure | 146 |
| 6.2.3. | Data acquisition and processing | 147 |
| 6.3. | Results | 148 |
| 6.3.1. | Hot isostatic pressing results and mechanical data | 148 |
| 6.3.2. | Grain size analysis and microstructural observations | 152 |
| 6.4. | Discussion | 161 |
| 6.4.1. | Partitioning of water and estimation of fluid pressures and water fugacities | 162 |
| 6.4.2. | Observed deformation behaviour and the role of water in the experiments | 165 |
| 6.4.3. | Some comparisons with previous work | 168 |
| 6.4.4. | Extrapolation and implications | 168 |
| 6.5. | Conclusions | 171 |
| | | |
| Chapter 7 | General conclusions and suggestions for further work | 173 |
| 7.1 | Sol-gel synthesis of fine-grained forsterite-enstatite materials | 173 |
| 7.2 | Deformation behaviour of wet, fine-grained forsterite-enstatite materials | 174 |
| 7.2.1 | Water weakening and flow behaviour | 174 |
| 7.2.2 | Effect of enstatite and water content | 174 |
| 7.2.3 | Final flow equation including the effect of grain size and water content | 175 |
| 7.2.4 | Implications for grain size sensitive flow of wet peridotites in the upper mantle. | 177 |
| 7.3 | Suggestions for further work | 178 |
| | | |
| | References | 181 |
| | | |
| | Dutch summary (Nederlandse samenvatting) | 189 |
| | | |
| | Acknowledgements | 193 |
| | | |
| | Curriculum Vitae | 195 |

Summary

Fine-grained hydrated peridotite mylonites have been proposed to play an important role in controlling the strength of the continental lithosphere during rifting. For this reason, the deformation behaviour of wet fine-grained forsterite and forsterite-enstatite materials and the underlying deformation mechanisms, form a subject of considerable interest in structural geology and tectonophysics. In addition, the deformation of polycrystalline forsterite-rich material is of fundamental interest for understanding the behaviour of upper-mantle materials in general. This thesis reports an experimental, materials science oriented investigation aimed at providing a better understanding of the deformation behaviour of wet fine-grained olivine and olivine-enstatite material, under conditions favouring grain size sensitive deformation processes.

In Chapter 1, the problems addressed in this thesis are introduced, and the aims of the present study are identified.

In Chapter 2, a practical and reliable sol-gel based method for the manufacture of forsterite and two-phase forsterite-enstatite ceramics, in the system MgO-SiO_2 , is described. These materials have foam textures and are homogeneously fine-grained ($1-2 \mu\text{m}$). The enstatite contents can be carefully controlled and densities up to 98 % theoretical density can be achieved. The method developed has been used to produce cylindrical samples 25 mm in length and 10 mm in diameter suitable for wet deformation experiments.

In Chapter 3, the gas medium deformation apparatus used in the current investigation is described. This apparatus is currently configured to measure differential stress, axial strain and strain rate, at confining pressures up to 700 MPa and sample temperatures up to $\sim 1100 \text{ }^\circ\text{C}$, in constant displacement rate tests.

In Chapter 4, the deformation behaviour of synthetic dunite (forsterite plus 2.5 vol% enstatite reference material) with a grain size of $1.2 \mu\text{m}$ has been investigated with and without added water ($\sim 0.5 \text{ wt}\%$) in combined displacement rate and temperature stepping/cycling tests performed at a confining pressure of $\sim 600 \text{ MPa}$. The results demonstrate that, whereas dry material behaves purely elastically at $950 \text{ }^\circ\text{C}$ and strain rates of 1×10^{-6} and $1 \times 10^{-7} \text{ s}^{-1}$, wet samples deform mostly by (near) steady state flow at temperatures between 850 and $1000 \text{ }^\circ\text{C}$ (1123 to 1273 K) and strain rates between 5×10^{-5} and $2 \times 10^{-7} \text{ s}^{-1}$. The wet samples flowed at differential stresses mainly between 5 and 60 MPa, and strains up to 12% have been achieved. The stress and temperature dependence of flow rate observed in the wet samples has been fitted to a Dorn type power law resulting in stress exponents (n) ranging from 1.3 to 2.2, for individual isotherm fits. Full non-linear regression analysis to the complete set of near steady state data yielded $n = 2.14 \pm 0.18$. The value of apparent activation energy (Q_c) for creep has been determined as ~ 285 and $320 \pm 40 \text{ kJ mol}^{-1}$ from the isothermal and full regression fits respectively. The wet deformed samples show polygonal grains, no crystallographic preferred orientation, little or no grain growth or recrystallization, no subgrains, low dislocation densities, and evidence for grain boundary cavitation. Comparison of the mechanical data and microstructural observations with both microphysical models for creep and previous work on fine-grained olivine leads to the conclusion that the wet samples probably deformed by a grain size sen-

sitive (GSS) grain boundary sliding (GBS) dominated mechanism, though the nature of the mechanism accommodating GBS remains unclear, and the possibility of transitional behaviour between dislocation creep and diffusion creep cannot be eliminated. Extrapolation of the flow equation determined for the wet material, to natural strain rates expected in hydrated, peridotite mylonites confirm the prediction of Vissers et al. (1995) that localized deformation in upper mantle mylonite zones, under conditions corresponding to lithospheric extension/rifting, will lead to a highly significant weakening of the upper 10 to 20 km of the lithospheric upper mantle.

In Chapter 5, the effect of varying enstatite content in the range 0 to 20 % on deformation behaviour of the forsterite–enstatite reference material with ~ 0.5 wt% added water was investigated at temperatures of 850 to 1006 °C (1123 to 1279 K), strain rates of between 2×10^{-7} and $5 \times 10^{-5} \text{ s}^{-1}$ and at a confining pressure of ≤ 600 MPa. The samples exhibited near steady state flow at stresses ≤ 60 MPa with a few runs showing work hardening at high stresses. The near steady state results show that, at constant strain rate, increasing enstatite content is associated with sharp decrease (factor 3 to 10) in flow strength in the range 0 to 2.5 % enstatite, with little further change at higher enstatite contents. Otherwise, the observed flow behaviour (average $n \approx 1.7$, $Q_c = 305 \pm 142 \text{ kJ mol}^{-1}$) and microstructures were similar to those reported in Chapter 4 for material with 2.5 wt% enstatite, indicating generation of the same deformation mechanism. Significantly, grain size analysis showed a negative correlation between grain size (range only 1 to 2 μm) and enstatite content (0 to 20 vol%), indicating that enstatite content played a role in controlling the grain size of the starting materials. On further investigation, a high correlation between measured flow strength and grain size was found, consistent with a grain size exponent of -3 in a conventional GSS flow equation. A water enhanced deformation mechanism involving GBS accommodated probably by grain boundary diffusion and/or dislocation activity was inferred, with the effect of enstatite content on flow strength being an indirect physical effect caused by grain size control. Other effects of second phase content, such as weakening caused by interphase boundary diffusion/migration processes (Wheeler, 1992) were accordingly inferred to be unimportant under the conditions investigated.

In Chapter 6 an attempt to systematically investigate the effect of bulk water content on the flow behaviour of fine-grained forsterite plus enstatite materials, under the same conditions as addressed in Chapters 4 and 5, is described. The experiments were thus carried out on forsterite–enstatite reference material containing 2.5 vol% enstatite with a grain size of 1 to 2 μm at a temperature of 950 °C (1223 K) and at 600 MPa confining pressure. Water contents of 0.48, 0.28, 0.11, 0.05, 0.02 (wt%) and nominally dry were investigated. In accordance with the previous results, the dry sample behaved elastically, whereas samples with water contents > 0.1 wt % showed near steady state, low stress flow with stress exponents (n) of around 1.6 and microstructures consistent with the previous inferred GBS dominated mechanism. However, a change in water content from 0.48 to 0.11 wt% led to an increase in flow stress at constant strain rate by a factor 2 to 3. At water contents < 0.1 wt% only very minor weakening was observed. This implies extreme sensitivity to water content in the range of 0.02 to 0.11 wt%. On the basis of tentative activation energy, water fugacity and microstructural arguments, the water weakening observed in samples with > 0.1 wt%, relative to dry material, is believed to result from enhanced grain boundary diffusivity related to the formation of water related grain boundary defects and/or associated grain boundary structural changes. In view of the

observed extreme sensitivity to water contents in the range 0.02 to 0.11 wt %, caution is advised when applying wet diffusion creep data, obtained at water contents > 0.1 wt %, to lower water contents such as generally expected for the upper mantle (~ 0.1 wt% - Ringwood, 1975).

In Chapter 7, the results are drawn together, general conclusions are presented, and suggestions made for further work.

Introduction:

Problem definition and aims

1.1. Scope and motivation

The research reported in this thesis is concerned with gaining a fundamental understanding of the deformation behaviour of wet, fine-grained peridotitic materials under conditions where grain size sensitive flow mechanisms are expected to dominate. The approach adopted has involved the development of a production method for very fine-grained synthetic forsterite-enstatite materials in the system (MgO-SiO₂), and the deformation of these reference materials using a gas medium deformation apparatus at temperature in the range 850 to 1000 °C and at a confining pressure of 600 MPa. The study was principally motivated by recent structural geological findings suggesting that fluid enhanced grain size sensitive (GSS) mechanisms, operating in mylonite zones in the top 10 to 20 km of the lithospheric upper mantle, may be important in controlling the strength of the lithosphere during rifting. More general motivations include a need to answer questions raised in the literature regarding the possible effects of second phase content on flow behaviour, and the need for information on the dependence of flow behaviour on water content for purposes of extrapolation to nature.

1.2. Background

1.2.1. Previous work on the rheology of olivine

Understanding upper mantle rheology is of key importance to modelling numerous geodynamic processes. The major mineral constituents of the upper mantle are olivine (\sim Fo₉₀), orthopyroxene and clinopyroxene with an additional aluminous phase (plagioclase, spinel or garnet; Ringwood, 1975), and the dynamics of the Earth's lithospheric and asthenospheric mantle are widely believed to be controlled by the rheological properties of the most abundant and probably weakest mineral constituent, olivine (\approx 50 vol. %). As a result, a vast number of experimental investigations have been performed, since the late 1960s, on the creep behaviour of natural and synthetic olivine and olivine-rich rocks at high temperatures and pressures. This work has addressed the deformation behaviour of single crystals and of polycrystalline aggregates, of natural and near natural compositions, at temperatures in the range 600 to 1600 °C, strain rates in the range 10⁻⁴ to 10⁻⁷ s⁻¹, and pressures from 1 atmosphere to 3 GPa. In broad terms, two main types of behaviour have been reported, namely grain size *insensitive* (GSI) dislocation creep (e.g. Chopra and Paterson, 1981, 1984; Karato et al., 1986)

and grain size *sensitive* (GSS) diffusion creep (e.g. Karato et al., 1986; Wolfenstine and Kohlstedt, 1994), with water having significant weakening effects in both cases (e.g. Karato et al., 1986). As well as solid state diffusion creep, diffusion creep involving an intergranular melt phase may also occur, if melt is present (e.g. Cooper and Kohlstedt, 1986).

Deformation studies on olivine single crystals have allowed detailed investigation of crystal plasticity and the influence of chemical environment (oxygen fugacity - fO_2 , oxide activity and H_2O content) on dislocation creep mechanisms (Raleigh, 1968; Young, 1969; Phakey et al., 1972; Kohlstedt and Goetze, 1974; Durham and Goetze, 1977 a,b; Durham et al., 1977, 1979; Jaoul et al., 1980; Darot and Gueguen, 1981; Kohlstedt and Hornack, 1981; Kohlstedt and Ricoult, 1984; Poumellec and Jaoul, 1984; Ricoult and Kohlstedt, 1985; Mackwell et al., 1985; Bai et al., 1991; Bai and Kohlstedt, 1992 a,b). The dislocation creep behaviour of polycrystalline olivine has also been investigated in detail (e.g. Carter and Ave'Lallemant, 1970; Post, 1977; Chopra and Paterson, 1981, 1984; Karato, Paterson and FitzGerald, 1986; Borch and Green, 1989; Hirth and Kohlstedt, 1995a). This is generally represented using a conventional Dorn-type power law relation written $\dot{\epsilon} = A \cdot \exp(-Q_d / RT) \cdot \sigma^n$, where $\dot{\epsilon}$ is the strain rate (s^{-1}), σ is the differential stress (MPa), Q_d is the apparent activation energy for creep, R is the gas constant ($J \text{ mol}^{-1} \text{ K}^{-1}$), T is the absolute temperature (K), n is the stress exponent or stress sensitivity and A is the pre-exponential constant ($\text{MPa}^{-n} \text{ s}^{-1}$). Generally speaking, dislocation creep of dry and wet olivine polycrystals is characterized by stress exponents (n) in the range 3 to 5 and average apparent activation energies of ~ 536 and ~ 462 kJ mol^{-1} for dry and wet creep respectively (Carter and Ave'Lallemant, 1970; Post, 1977; Chopra and Paterson, 1981, 1984; Karato, Paterson and FitzGerald, 1986; Borch and Green, 1989). In addition, a marked water weakening in the dislocation creep regime has been observed by several workers (Chopra and Paterson, 1981, 1984; Karato et al., 1986) with the dry samples being stronger by a factor ranging between ~ 2.5 (Karato et al, 1986) to ~ 6.5 times (Hirth and Kohlstedt, 1996) at constant strain rate.

Grain-size-sensitive (GSS) diffusion creep behaviour has been identified in a number of experimental investigations of creep in fine-grained (0.1 to 30 μm) polycrystalline olivine aggregates conducted at temperatures between 300 and 1600 $^{\circ}\text{C}$ (Schwenn and Goetze, 1978; Relandeau, 1981; Chopra, 1986; Karato, 1986; Rutter and Brodie, 1988; Wolfenstine and Kohlstedt, 1994; Hirth and Kohlstedt 1995a). In accordance with theoretical models for GSS creep, the grain size dependence is represented by introducing a factor d^{-p} into the right hand side of the Dorn equation, where d is grain size and p is the grain size exponent or sensitivity. For dry systems deforming by GSS creep, stress exponents (n) fall close to 1, grain size exponents in the range 2 to 3, and apparent activation energies are in the range 300 to 400 kJ mol^{-1} (Relandeau, 1981; Cooper and Kohlstedt, 1984a; Karato et al., 1986; Wolfenstine and Kohlstedt, 1994; Hirth and Kohlstedt, 1995a). For wet systems, assumed to be largely melt-free, the stress exponent (n) falls between 1 and 2 (Chopra 1986; Karato et al. 1986; Rutter and Brodie 1988). Experimentally determined values of the apparent activation energy for wet diffusion creep are poorly constrained with values of 190 and 240 kJ mol^{-1} having been determined by Chopra (1986), and a value of 240 ± 40 kJ mol^{-1} by Rutter and Brodie (1988). Karato et al. (1986) found a sensitivity of $p = -2$ to -3 and estimated the activation energy for wet diffusion creep to be 250 kJ mol^{-1} , taking a value $2/3$ of the activation energy for volume diffusion of O and Si in olivine

(Jaoul et al., 1980, 1981; Karato and Ogawa, 1982) assuming grain boundary diffusion control. Karato et al (1986) showed that in the finer grained materials deforming in the GSS regime, the wet samples are 10 to 20 times weaker than the dry samples at constant strain rate. At present, the most widely accepted descriptions of the high temperature flow behaviour of polycrystalline olivine are those afforded by the data of Chopra and Paterson (1981, 1984) and Karato et al. (1986).

1.2.2. Olivine rheology and the strength of the lithosphere in extension

The above creep data have been widely used in recent years to model flow in the lithospheric and asthenospheric upper mantle during extension (e.g. Bassi and Bonnin, 1988; Braun and Beaumont, 1989; Cloetingh et al., 1995), assuming this to be a relatively homogeneous, distributed phenomenon (McKenzie, 1978). Most modelling work follows Brace & Kohlstedt (1980) and Sawyer (1985) in assuming that the rheology of the upper mantle is controlled by a frictional sliding law in the brittle/frictional region and by either a wet or dry dislocation creep law for olivine in the ductile region (e.g. Lynch & Morgan, 1987; Bassi & Bonnin, 1988; Braun & Beaumont, 1989; Dunbar & Sawyer, 1989; Govers and Wortel, 1993; Bassi, 1995; Cloetingh et al., 1995). These rheologies predict a strength profile with a maximum in the upper 10 to 20 km of the continental lithospheric mantle, and this thin, mechanically strong layer plays a major role in controlling the modelled dynamics.

In contrast to the assumptions of the above-mentioned modelling studies, however, there is growing seismic evidence to suggest that, in regions of continental extension and/or rifting, flow in the lithospheric upper mantle may be localized into asymmetric shear zones in line with the extension model proposed by Wernicke (1985); see Goleby et al. (1988), Flack et al. (1990), Reston (1990), Meier and Eisbacher (1991), Keen et al. (1991), and Reston (1993). Moreover, structural geological studies of shear zones found within mantle peridotites occurring in the Voltri Massif (N.W. Italy; Drury et al., 1990; Drury et al., 1991; Hoogerduijn-Strating, 1991) provide evidence that extensional deformation of the lithosphere, during Jurassic rifting to form the Piemonte-Ligurian ocean, was accommodated by localization of deformation into hydrated mylonitic shear zones. It follows, therefore, that the deformation behaviour of fine-grained peridotite mylonite under hydrous conditions may have important consequences for the strength and dynamics of continental lithosphere undergoing extension/rifting (Vissers et al., 1995). Notably, the microstructure of mylonites from the Voltri (Erro-Tobio) peridotites show many of the characteristics of GSS flow (i.e. diffusional or superplastic mechanisms rather than dislocation creep) including fine-grain size (1 to 10 μm), equiaxed grain shape and low dislocation densities (Vissers et al., 1995; cf. Boullier and Gueguen, 1975). Accordingly, Vissers et al. (1995) have proposed that shear localization during extension/rifting of the lithospheric upper mantle may lead to extreme weakness of the lithosphere, since GSS flow in wet, fine grained olivine comparable to Voltri mylonitic material is expected to proceed at very low stresses. To underpin this argument, Vissers et al. (1995) applied the wet, diffusion creep equation of Karato et al. (1986) to calculate flow stresses within mylonitic shear zones in the top 10 to 20 km of the upper mantle under hydrated conditions corresponding to lithospheric extension. The results obtained by Vissers et al. (1995) indeed showed dramatic weakening of the lithospheric upper mantle through the action of the shear zones.

1.3. Problem definition

Despite the large amount of work carried out on the rheology of olivine rich rocks and aggregates, a number of general problems remain as well as specific problems relating to the GSS processes relevant to the localization of deformation in mylonite zones discussed above. This thesis focuses on the following problems remaining in the area of GSS creep under wet conditions.

1) Problems with partial melting, compositional control and microstructure of the experimental starting material.

Previous experimental work relevant to GSS creep under wet conditions has been carried out on either synthetic aggregates prepared by hot pressing naturally derived fine-grained olivine (Chopra, 1986; Karato et al., 1986), or on natural materials (Rutter and Brodie, 1986). In the high temperature experiments (1300 °C) of Karato et al. (1986), some evidence was found for minor partial melting. The presence of intergranular melts and the operation of melt-assisted diffusion creep mechanisms cannot therefore be excluded in high temperature experiments on wet olivine materials/rocks in general. Such subsolidus melting phenomena are likely to be caused by the combined effects of impurities and added water, and may have important effects on flow behaviour not relevant to the behaviour of natural material at lower temperatures. Aside from impurity controlled partial melting, the use of natural experimental materials also entails problems such as those associated with the presence of additional phases (e.g. spinel, serpentine) and with poorly controlled water content. Moreover, experiments employing natural olivine compositions ($\sim\text{Fo}_{90}$) require effective buffering of oxygen fugacity ($f\text{O}_2$) to remain in the olivine stability field. In addition, the synthetic olivine aggregates produced to date, and natural olivine rocks, are generally relatively coarse-grained ($\geq 10 \mu\text{m}$), which means that GSS behaviour can only be accessed at high temperatures and low strain rates. This is compounded further by the finding of Karato et al. (1986) that grain growth can occur when working at high temperatures. Taken together, these points serve to illustrate a need for experiments on high purity, very fine-grained olivine or olivine-plus-orthopyroxene reference material with well-controlled and stable microstructure.

2) Problems with extrapolation of existing data

The findings of Vissers et al. (1995), regarding the role of wet mylonitic shear zones in the upper 10 to 20 km of the lithospheric upper mantle in controlling the strength of the lithosphere, are strongly dependent upon the accuracy and validity of extrapolation of the flow law of Karato et al. (1986) from the experimental conditions ($T = 1300 \text{ }^\circ\text{C}$, strain rates in the range 10^{-4} to 10^{-6} s^{-1}) to those of the upper mantle in an extensional setting ($T = 800$ to $950 \text{ }^\circ\text{C}$, strain rates in the range 10^{-13} to 10^{-14}). As already mentioned, Karato et al. (1986) did not experimentally determine the apparent activation energy for creep (Q_c), drawing the validity of 'long-range' extrapolation into question. On the other hand, use of the wet diffusion creep law of Karato et al. (1986), with the assumed $Q_c = 250 \text{ kJ mol}^{-1}$ appropriate for grain boundary diffusion control, is supported by the studies of Chopra (1986) and Rutter and Brodie (1988), who report similar values for Q_c . Although several additional studies have investigated the flow behaviour of fine-grained olivine polycrystals under dry conditions (Beeman and Kohlstedt, 1993; Hirth and Kohlstedt, 1995a), available data appropriate for extrapola-

tion to wet mylonitic shear zones in the upper mantle remain limited. Unfortunately, the range of conditions and grain sizes explored in most wet experiments has been too narrow for accurate determination of flow parameters. All this argues for the need for additional experiments on olivine rich materials extending existing data on wet GSS creep to lower temperatures and finer grain sizes.

3) The role of second-phase content

Previous investigations of GSS flow have generally concentrated on near single phase olivine systems. However, experimental evidence exists for effects of second-phase content on flow behaviour in a range of materials, and theoretical models have been developed which predict such effects. For example, it is well known that the presence of a second phase can promote superplasticity by inhibiting grain growth (Chen, 1982). Important chemical interaction effects associated with the addition of a second phase and potentially affecting GSS flow include a) changes in point defect chemistry which may influence diffusion rates in both phases, b) interphase boundary diffusion (Martin and Perrailon, 1979), and c) coupled effects related to the presence of interphase boundaries, involving stress induced interface reactions, interphase boundary migration and interphase boundary diffusion (Chen, 1982, 1985; Wheeler, 1992). The latter lead to rate control by the fastest rather than the slowest diffusing species and can therefore produce weakening relative to regular grain boundary diffusion creep in the pure phases. This type of weakening mechanism has attracted considerable attention recently, since it implies that data on GSS flow in single-phase materials may not be appropriate for extrapolation to natural polyphase systems (Fliervoet, 1995).

Despite the above-mentioned possible effects of second phase content, only very few studies, using synthetic aggregates, have specifically attempted to systematically study the role of second phase content on olivine rheology (Hitchings et al., 1989; Gleason et al., 1994; Daines and Kohlstedt, 1996). On the basis of the existing data, it appears that the addition of enstatite to forsterite produces a weakening effect in the dislocation creep field (Hitchings et al., 1989; Daines and Kohlstedt, 1996) with little effect in the diffusion creep (low n) field (Daines and Kohlstedt, 1996). However, the available data are extremely limited and the observed behaviour is poorly understood. In the interests of applying laboratory data to the upper mantle, the question of the effect of enstatite content on the flow behaviour of olivine needs further investigation. An issue of particular interest at present is the effect of enstatite content on the GSS flow of fine-grained olivine-enstatite aggregates under wet conditions. In the context of this thesis, enstatite will be treated simply as a second phase with the composition $MgSiO_3$ and details of its polymorphic phase relations will not be considered. The reader should however note that although the materials were initially synthesised within the protoenstatite stability field, the deformation experiments were carried out in the stability field of orthoenstatite. The author is currently collaborating with other workers to study the details of the polymorphic phase transitions involved. However, this work falls outside the scope of this thesis.

4) The role of water

Previous experiments on the influence of water on dislocation and diffusion creep in olivine have been carried out with water contents generally in the range 0.1 to 0.5 wt %. The role of water in weakening polycrystalline olivine can be highly complex because: a) water may be active within the grains, producing changes in point defect chemistry and leading to enhanced self-diffusion and/or increased dislocation glide or climb mobility (Hobbs, 1984; Poumellec and Jaoul, 1984; Mackwell et

al. 1985; Bai and Kohlstedt, 1992, 1993; Hirth and Kohlstedt, 1996); b) water may be chemically active along grain boundaries and within pores, leading to enhanced grain boundary self-diffusivity, facilitating solution-precipitation mechanisms, causing melting and/or enhancing grain boundary sliding (Chopra and Paterson, 1981, 1984; Karato et al., 1986); and c) water may have direct physical effects such as reducing the effective stress and mechanically decoupling grain boundaries, thus also facilitating grain boundary sliding (Chopra and Paterson, 1981). These possible roles of water may work in parallel to produce the weakening observed. However, little is known about their relative importance or about the effects of and sensitivity to varying water content. This poses considerable problems for extrapolation of laboratory flow equations for wet rocks to natural conditions.

1.4. Present aims

In view of the problems identified above, the aims of this thesis can be specified as follows:

- 1) To develop a method for producing very fine-grained forsterite-enstatite reference materials of sufficient purity to remove the problem of impurity related melting, and with well-controlled, stable microstructure. The present approach involves the production of dense, very fine-grained olivine-bearing (forsterite) materials in the MgO - SiO₂ system. Although departing from natural olivine-enstatite compositions (Fe-bearing), this system was chosen because of its high purity, its high wet solidus temperature (Kushiro and Yoder, 1969) and its insensitivity to oxygen fugacity, which facilitate synthesis and experimentation.
- 2) To determine the flow behaviour and deformation mechanisms operative in the above reference material under wet conditions expected to favour GSS flow at temperatures of 800 to 1000 °C, i.e. at temperatures closer to those relevant for the top of the upper mantle and well below the solidus.
- 3) To determine the role of varying enstatite content on the flow behaviour of forsterite-enstatite reference materials in the wet GSS field, by systematically varying the enstatite content in the range 1 to 20 vol%.
- 4) To determine the role of bulk water content on the flow behaviour of fine-grained forsterite-enstatite materials in the GSS field by systematically varying the water content between 0 and 0.5 wt %.

1.5. Structure of the thesis

This thesis has been structured in such a way that the chapters addressing the above aims and containing the main results (2,4,5 and 6) can be submitted in future as papers. This format inevitably leads to a degree of repetition, particularly when describing experimental methods.

Fabrication and characterization of dense fine-grained forsterite and forsterite-enstatite ceramics for deformation studies

2.1. Introduction

The physical and chemical properties of forsterite (fo - magnesium orthosilicate, Mg_2SiO_4) and enstatite (en - magnesium metasilicate, MgSiO_3), the magnesium end-members of the olivine and pyroxene mineral groups, and their Fe-bearing solid-solutions, are of major scientific and technological interest. For example, the condensation and reaction of these refractory phases in primordial solar nebulae are believed to play an important role in the fractionation of elements prior to planet formation (Grossman, 1972; Anders and Ebihara, 1982; Ringwood, 1989). In addition, both forsterite and enstatite are major components of the Earth's upper mantle and thus of considerable importance in the Earth sciences, notably with regard to the seismic properties, rheological behaviour, and thermal structure of the upper mantle (Ringwood, 1969). Furthermore, there has recently been renewed interest in technological applications of forsterite with the discovery of the near-infrared lasing properties of chromium-doped single crystals (Petricevic et al., 1988; Garrett et al., 1991).

Common to experimental studies in all of the above fields is the need for well characterized starting materials with careful control of both chemistry and microstructure. This Chapter describes in detail the fabrication of dense, fine-grained, pure forsterite and two-phase, forsterite plus enstatite ceramics, using a state-of-the-art materials science approach involving sol-gel synthesis, powder processing and sintering. The method described allows the production of fine-grained (1 to 2 μm), high purity forsterite and forsterite-enstatite ceramics with controlled phase content and porosities down to a limit of $\sim 2\%$, i.e. $\sim 98\%$ of theoretical density (TD). To date ceramics with enstatite contents ranging between 0 to 50 volume percent have been successfully fabricated and gels up to 100 percent enstatite composition have been successfully synthesized. Therefore it is likely that the method can be applied to produce two phase materials across the whole range of forsterite-enstatite contents. Completely independent control of grain size, enstatite content and porosity is not currently possible due to the fact that densification is achieved by sintering, in which the reduction of porosity is coupled to grain coarsening which is itself influenced by second phase content. Cylindrical samples 25 mm in length and 10 mm in diameter have been produced, although other shapes and sizes could

easily be obtained by varying the forming and machining steps.

The synthesis method described here was developed specifically to produce starting materials for experiments designed to gain insight into the deformation mechanisms operative in wet peridotitic material, in particular fine-grained, hydrous peridotite mylonites. Such mylonites have recently been proposed as playing a major role in controlling the strength of the continental lithosphere during extension/rifting (Drury et al., 1990; Hoogerduijn Strating et al., 1993; Vissers et al., 1995). A chemically simple, iron-free system was chosen in order to reduce the overall complexity and to allow careful investigation of the effects of strain rate, temperature (Chapter 4), second-phase content (Chapter 5) and water content (Chapter 6) on deformation behaviour without the need to control oxygen fugacity.

Previous deformation studies on olivine polycrystals at high pressures and temperatures have employed a variety of starting materials including a) natural rocks, e.g. the Aheim and Anita bay dunites used by Chopra and Paterson (1981, 1984); b) synthetic polycrystals produced from natural olivine by grinding, sieving and Stokes settling, e.g. San Carlos olivine used by Schwenn and Goetze (1978) and Karato et al. (1986); and c) truly synthetic materials produced either by grinding synthetic crystals (e.g. pure forsterite used by Relandeau, 1981) or by sol-gel processing (e.g. iron-bearing olivine produced by Beeman and Kohlstedt, 1993; see also Burlitch et al., 1991).

Natural rocks have the drawback that they are chemically complex, may contain additional phases (e.g. spinel, serpentine) and have a water content which cannot easily be controlled. Furthermore, they are in general relatively coarse grained and may have coexisting phases with compositions which are not at equilibrium when brought to the pressure and temperature conditions required for experimentation.

Synthetic polycrystalline aggregates produced from natural mineral powders allow investigations to be extended to finer grain sizes. However, such methods also have disadvantages. Firstly, high densities can only be achieved from such powders by hot isostatically pressing (HIPing) low density compacts prior to the deformation experiments, which greatly complicates and prolongs the experimental procedures (e.g. Karato et al., 1986; Hitchings et al., 1989). Secondly, as the natural compositions used are iron-bearing, control of oxygen fugacity is essential to ensure that the olivine remains within its stability field during both HIPing and experimental deformation. Thirdly, the grinding necessary in powder preparation can lead to both chemical contamination and can introduce mechanical damage into the grains. Moreover, individual grains produced by grinding are often angular and have a relatively wide grain size distribution. These features can lead to exaggerated grain growth during HIPing which limits the minimum achievable grain size.

In contrast, sol-gel methods have been used successfully to produce fine-grained Fe-bearing olivine powders with narrow grain size distributions which were subsequently HIPed to produce dense, polycrystalline aggregates without significant grain growth (Beeman and Kohlstedt, 1993). The present approach involves the production of dense fine-grained olivine-bearing (forsterite) materials in the MgO - SiO₂ system *without* the need to perform the time-consuming and technically difficult operation of HIPing low density powders, and without the need to control oxygen fugacity at any stage. A disadvantage is that natural Fe compositions are not achieved, but modification to the method will allow this in future.

2.2. Background

2.2.1. Sol-gel processing - an introduction

An introduction to sol-gel processing is included here to allow the non-specialist to appreciate how the synthesis method described in this Chapter fits into the field of sol-gel processing as a whole, and to introduce essential terminology and methodology. For a more detailed discussion of sol-gel techniques, the reader is referred to the reviews by Johnson (1985), Ramsay (1988), Segal (1989) and Hench and West (1990).

Experimental petrologists have for many years synthesized starting materials for their experiments via gel routes following the methods first developed and described by Roy (Roy and Roy, 1954; Roy, 1956; Luth and Ingamells, 1965; Hamilton and Henderson, 1968). Importantly, sol-gel processing has attracted great interest since the mid-1970s within the materials science community, and the technique is used today for a variety of applications including nuclear fuel preparation (Fletcher and Hardy, 1968; Brambilla et al., 1970; Marples et al., 1981), preparation of ceramic powders (Mazdiyasi, 1982), and the preparation of thin films (Nelson et al., 1981; Dislich and Hinz, 1982; Scot and Woodhead, 1982; Puyane and Gonzalez-Oliver, 1983), bulk glasses (Johnson et al., 1983; Wood et al., 1983; Rabinovich et al., 1983, 1984;), optical fibers (Puyane et al., 1982; Sudo et al., 1983) and glass-ceramics (e.g. MacKenzie, 1982; Nogami and Moriya, 1982).

Terminology and key aspects

The term *sol-gel*, as used within the ceramics community, can best be considered as an abbreviation for “*solution gelation*” (Johnson, 1985). The *solution* in this case is either

- a true sol, i.e. a stable suspension of solid colloidal particles in a liquid, or

- a true solution (liquid phase), e.g. of organometallics such as metal (M) alkoxides ($M(OR)_z$ where R represents, for example, the methyl or ethyl functional groups), formates ($M(CHOO)_z$) and acetates ($M(CH_3COO)_z$) which can react to form solid colloidal particles.

Gelation refers to the process of condensation and consolidation of sol particles and/or the reaction of solutions to form condensed solid colloidal particles. Gelation is usually induced by deliberately modifying the solution chemistry, and by definition a sol or solution becomes a gel when the solid colloidal particles become sufficiently consolidated to support stress elastically. At this stage the gel is still *wet*, consisting of condensed solid colloidal particles forming a percolating network permeated by a liquid phase remaining from the initial suspension or resulting from the gelation reactions. Such residual liquid phases are commonly water- or alcohol-based and give rise to the terms *hydrogel* (or *aquagel*) and *alcogel* respectively. The nature of the residual fluid phase has important implications for subsequent drying of the wet gels. On drying, the gels generally undergo dramatic shrinkage and cracking resulting in a so-called *xerogel*. Shrinkage can be substantially reduced by supercritical drying of wet gel with the retention of the highly porous gel network structure, leading to the formation of *aerogels* with very high specific surface area. These have found important applications in industry, e.g. as catalyst supports.

The key point of the sol-gel process, with regard to the production of a uniformly fine-grained (monodispers) product, is the thorough mixing of several components in the highly fluid solution phase, followed by gelation and drying so as to preserve the intimate mixing of components. By starting with well-mixed solutions amorphous, chemically homogeneous, multicomponent oxide xerogels can be obtained with mixing of components on the molecular scale. Alternatively, by using multiphase sols or sols mixed with solutions, chemically and structurally polyphasic xerogels can be obtained. These have been referred to as *maximally heterogeneous nanocomposites* by Roy et al. (1986). The structurally polyphasic (crystalline + amorphous) nature of these nanocomposites, coupled with their chemical heterogeneity on the colloidal scale, has important consequences for nucleation, growth (epitaxy) and hence grain size distribution of the crystalline phases produced from these gels (Komarneni et al., 1987; Roy et al., 1986; Suwa et al., 1986a,b).

Advantages of sol-gel processing

Sol-gel processing has several inherent advantages when compared with more conventional ceramic/mineral synthesis routes such as the use of oxide powders. Firstly, the high surface area and intimate mixing of the colloidal particles results in very high reactivity which allows low temperature synthesis and the formation of non-equilibrium phases (Edgar, 1973). Secondly, the nanometer grain size powders produced by sol-gel processing have enhanced sinterability compared to coarser grained powders produced by the reaction of oxides. Thirdly, chemical contamination can be kept to a minimum as little or no comminution is necessary during processing. Lastly, the sol-gel process can provide a means of conveniently shaping products using low temperature casting methods (e.g. Omatete et al., 1991). The formation of non-equilibrium phases from highly reactive xerogels is not always advantageous, and can be overcome by either seeding homogeneous amorphous monophasic gels with crystalline phases (e.g. Komarneni et al., 1987; Liu et al., 1995) or by using the structurally polyphasic heterogeneous gels as a means of reducing the barrier to nucleation.

Classification of sol-gel methods

Sol-gel processing encompasses a diverse set of methods for different materials and applications. Johnson (1985) broadly divides these into two categories, namely those using sols of dispersed colloidal particles, and those using alkoxide solutions which hydrolyze and polymerize into gels (Figure. 2.1).

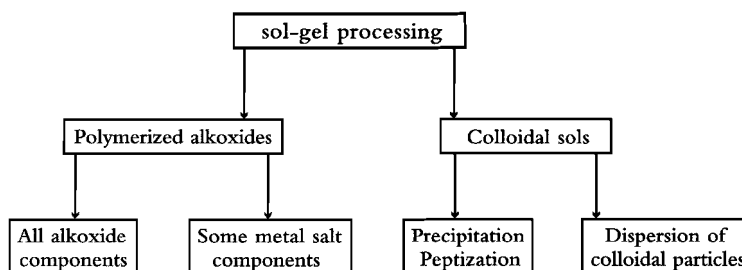


Figure 2.1. Classification of sol-gel routes from Johnson (1985).

This classification is useful as it allows subdivision of the major processes involved in sol-gel processing. However, in practice many workers have developed hybrid methods using both colloidal sols and alkoxides and so, in a sense, any such subdivisions are false.

Sol-gel processing involving colloidal sols (right hand branch, Figure 2.1) can follow a number of routes (see Figure 2.2). In the dispersed colloidal sol-gel method (Figure 2.2 route 'A'), a stable sol is produced by dispersing colloidal particles, with or without the aid of peptization (the process of stabilization of a colloidal suspension by adsorption of electrolytes). In multicomponent systems, the components are mixed as sols (or added to the main sol in solution or as oxides) before gelation. Gelation commonly involves the modification of surface charge to reduce repulsive electrostatic forces between the particles and to allow them to coalesce and gel into a continuous network. Thus, gelation in such colloidal systems can be seen as the opposite process to peptization and in fact the sol-gel transitions in such systems are often reversible. The use of colloidal boehmite [AlO (OH)] in sols as a source of alumina is a good example of the dispersed colloidal sol approach. The second major colloidal route, precipitation-peptization, involves the precipitation of colloidal particles from a solution which may directly, or after peptization, form a stable sol (Figure 2.2 route 'B'). Yet another alternative combines precipitation and gelation in one step (Figure 2.2 route 'C'). An example of this is given by Marples et al. (1981) as a route to producing $\text{UO}_2 - \text{PuO}_2$ spheres for nuclear fuel. The sol stage is bypassed in this process, which can better be regarded as gel-processing.

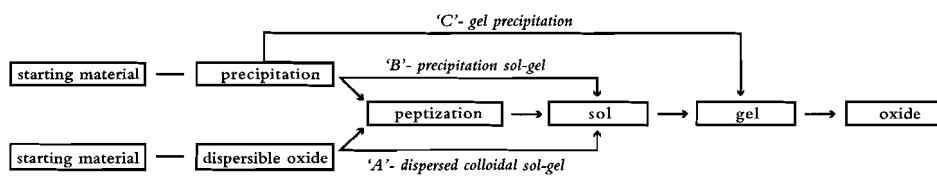


Figure 2.2. Colloidal sol-gel routes after Woodhead and Segal (1984) and Segal (1989).

The remaining major class of sol-gel techniques includes routes which also lack a stable sol stage and are truly irreversible in nature. These are the alkoxide routes (left hand branch of Figure 2.1) in which metal (or semi metal) alkoxides ($\text{M}(\text{OR})_z$) are hydrolyzed to form gels directly. This is illustrated in Figure 2.3 for the commonly used silicon alkoxide, tetraethyl orthosilicate (TEOS - $\text{Si}(\text{OC}_2\text{H}_5)_4$). Whilst colloidal methods allow mixing at the colloidal level (10^3 to 10^9 molecules), alkoxide routes, with cross-condensation of several metal alkoxides, can achieve mixing at the molecular level. Alkoxide routes fall into two main categories, namely all-alkoxide routes and routes where additional components are added as soluble salts. In multicomponent all-alkoxide routes, hydrolysis is often carefully controlled to counteract the differing hydrolysis rates of the alkoxides involved, thus avoiding chemical inhomogeneity caused by the formation of polymerized clusters of one component (Yoldas, 1988).

Sol-gel processing of silicates

In the sol-gel processing of silicates alkoxide routes employing TEOS are the most commonly used. When alcohol is used as a mutual solvent, TEOS becomes miscible with water and many aqueous

salt solutions (Hamilton and Henderson, 1968). These solutions are slow to hydrolyze and it is therefore common practice to use acid or base catalysts to speed hydrolysis and gelation. In general, base-catalyzed TEOS-derived gels are opaque and are believed to contain linked SiO_2 clusters, whereas acid-catalyzed gels are transparent and contain more linear polymer chains (Keefer, 1984).

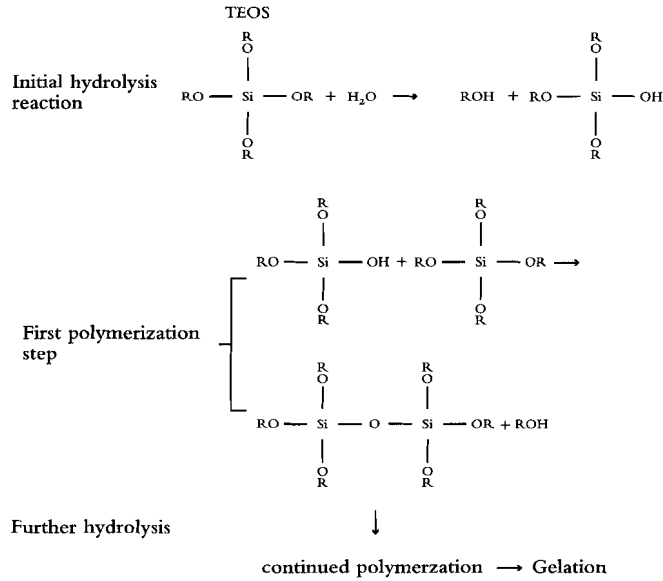


Figure 2.3 Schematic representation of the hydrolysis and self-condensation of TEOS.

Future perspectives

It should be clear from this introduction that sol-gel processing is an extremely diverse field of material synthesis. There are an almost infinite number of possible routes to a given product. Moreover, sol-gel science is currently undergoing rapid development, with many groups actively researching the detailed physical and chemical mechanisms involved, while experimental workers in the field are constantly finding useful synthesis routes for the production of new materials which were previously unobtainable by more traditional approaches. The recent developments in this area of materials science have opened up many new possibilities for both mineral physicists and experimental Earth scientists alike, and will continue to do so.

2.2.2. Previous work on sol-gel synthesis of forsterite and enstatite powders and ceramics

There have been a number of previous studies into the synthesis of forsterite and enstatite powders and high density forsterite ceramics by a variety of methods, including conventional oxide reactant and sol-gel routes (Table 2.1). The main sol-gel based routes proposed for the production of forsterite/olivine ceramics (Kazakos et al., 1990; Burlitch et al., 1991; Shiono et al., 1991; Shiono and Okamoto pers. comm., 1994) are illustrated in Figure 2.4 and outlined below.

Kazakos et al. (1990) described a method for the preparation of forsterite ceramics by nanocomposite (structurally diphasic) sol-gel processing. In this method, magnesia (MgO) powder with a grain size of 10 nm (UBE Industries Ltd, Japan) was added to water, peptized with acid, and stirred to resemble an opalescent colloidal suspension (sol). A stoichiometric proportion of Ludox™ (silica sol ; Du Pont AS40) was then added while stirring continuously. This mixture was then dried at 100 °C and the resulting powder then calcined at 400 °C for several hours. Calcination is a high temperature reaction whereby one solid material dissociates to form a gas and a new solid. The powder was pellet pressed and fired at temperatures between 1100 and 1500 °C to form forsterite ceramic. This method has been extensively tested during the current study.

Burlitch and coworkers (Burlitch et al., 1991; Yeager and Burlitch, 1991; Yeager et al., 1993; Park et al., 1993, 1994 a,b) have presented a H₂O₂-assisted alkoxide route for the production of forsterite, iron-bearing olivine (Fo₉₀) and chromium-doped forsterite powders. Powders produced by this method have been HIPed (1250 °C, 300 MPa, 3 hrs) by previous workers to produce high density olivine ceramics for deformation studies (Beeman and Kohlstedt, 1993). The method has not been attempted by the author as it is highly complicated and time-consuming.

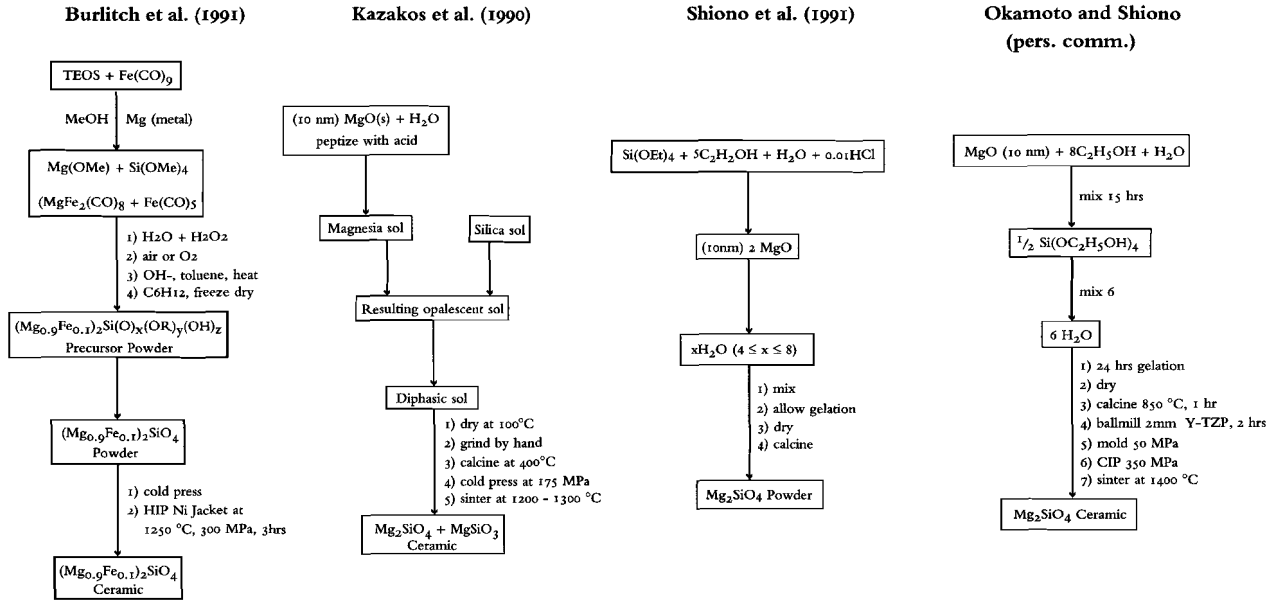
Shiono et al. (1991) described a method for the preparation of forsterite powder derived from TEOS and MgO powder, using ethanol as the solvent. In this procedure, TEOS was first partially hydrolyzed, in the presence of a HCl catalyst. MgO powder of 10 nm grain size was then added to the partially hydrolyzed TEOS. The solution was subsequently gelled by the addition of distilled water. This method has been tested during the current investigations.

A further method was personally communicated to the author by Dr Shiono and Dr Okamoto of the Department of Chemistry and Materials Technology, Kyoto Institute of Technology, Japan; see Figure 2.4. This method involves the suspension of 10 nm MgO powder in ethanol with a small amount of water. TEOS was added to the mixture and allowed to prehydrolyze before gelation was achieved by the further addition of distilled water, *without* the use of a catalyst. After trials and several modifications, this method provided the foundation of the current approach.

| Authors | Technique | Main reagents | Phases | Comments |
|-----------------------------|----------------------------------|-------------------------------------------------------------------------------------------------------------------------------|------------------------------------------------------|-----------------------------------------------------------------------------------------------|
| Finnerty et al. (1978) | freeze drying | Ludox (silica), magnesium citrate | forsterite | hydrothermal crystallization at 900 °C and 250 bars. 1 - 5 µm |
| Gonczy et al. (1986) | sol-gel | alkoxide routes | forsterite + enstatite | general patent covering numerous alkoxide routes |
| De Mott (1987) | sol-gel | ? | fayalite | |
| Beeman, M. (1989) | sol-gel | Nyacol (silica), magnesium nitrate, iron sulphate | olivine | |
| Kazakos et al. (1990) | diphasic sol-gel | Ludox, 10 nm MgO | forsterite + enstatite | |
| | sol-gel | TEOS, magnesium nitrate, EtOH | forsterite (+ ?) | |
| Shiono et al. (1991) | diphasic sol-gel | TEOS, EtOH, HCl _(aq) , MgO, H ₂ O | forsterite (only) | |
| Yeager and Burlitch (1991) | sol-gel | tetramethyl orthosilicate (TMOS), magnesium methoxide (Mg(OMe) ₂), methanol (MeOH), H ₂ O ₂ | forsterite & enstatite | H ₂ O ₂ assisted hydrolysis |
| Burlitch et al. (1991) | sol-gel, freeze drying | TEOS, MeOH, Mg _(s) , Fe ₂ (CO ₃), H ₂ O | olivine- fo ₉₀ | in situ synthesis of Mg(OMe) ₂ , H ₂ O ₂ assisted hydrolysis |
| | sol-gel, freeze drying | TEOS, Mg _(s) , MeOH, H ₂ O ₂ , Bu ₄ NOH, Toluene | forsterite | as above |
| | sol-gel, freeze drying | TEOS, MeOH, Mg _(s) , H ₂ O, CH ₃ COOH | forsterite | coprecipitation without H ₂ O ₂ |
| Echeverria (1992) | sol-gel flame-aerosol | TEOS, Mg(OEt) ₂ , ethylene glycol monomethyl ether | amorphous (siliceous) phase + forsterite + periclase | |
| Hogan et al. (1992) | copolymerization (organic route) | poly(methacrylate) precursors | forsterite, forsterite + periclase | |
| Yeager et al. (1993) | sol-gel | TMOS, Mg(OMe) ₂ , H ₂ O ₂ , H ₂ O | forsterite | detailed study of intermediates |
| Young et al. (1993) | oxides | MgO, SiO ₂ | forsterite | study into properties of tape-casting slurries |
| Park et al. (1993) | sol-gel | TEOS, chromium acetate or chromium trioxide, MeOH, Me(OH) ₂ , H ₂ O ₂ , H ₂ O | chromium-doped forsterite | study of crystallization of precursors |
| Huang et al., (1994) | Pechini process | Ludox AS ₄₀ , magnesium nitrate hexahydrate, citric monohydrate, ethylene glycol, dopants | enstatite | Na ⁺ and Mn ²⁺ doped powders |
| Park, Martin et al. (1994) | organic route | poly(methacrylate) precursors | chromium-doped forsterite | study of crystallization of precursors |
| Park, Duchamp et al. (1994) | sol-gel | H ₂ O ₂ assisted method of Burlitch et al. (1991) | forsterite | study of structural evolution of forsterite during pyrolysis of a xerogel |
| McDonnell (this study) | diphasic sol-gel | TEOS, 50 nm MgO, EtOH, H ₂ O, NH ₃ OH | forsterite, forsterite + enstatite | |

Table 2.1. Summary of previous synthesis methods for fine-grained forsterite, Fe-olivine and enstatite powders and ceramics.

Figure 2.4. Flow diagrams illustrating several previous sol-based routes to olivine ceramics.



2.3. Pilot trials of diphasic sol-gel routes and lessons learned

The development of the sol-gel based synthesis process for the fabrication of starting materials for the present deformation studies was constrained by the need to produce relatively large quantities of materials (~ 6 g per sample) combined with a desire to keep the practical procedures as simple and quick as possible. These considerations led to the decision to concentrate on diphasic routes, using the chemically simple MgO - SiO₂ system, since these are much easier to carry out than the various organometallic routes - including all-alkoxide ones - such as that proposed by Burlitch et al. (1991) and are believed to give good microstructural control (Suwa et al., 1986 a,b). Several attempts were made by the author to reproduce the results described by Kazakos et al. (1990), Shiono et al. (1991) and Shiono and Okamoto (pers. comms., 1994), as detailed below.

Trials using the diphasic method described by Kazakos et al. (1990)

Using the method described by Kazakos et al. (1990), dense forsterite ceramics were successfully produced with grain sizes around 10 μm. However, high densities could only be achieved at high temperatures (~ 1400 °C), contrary to the claims of the original authors (1100 to 1300 °C). Furthermore, some inhomogeneity was observed within the final ceramics with porous, finer grained regions being distributed throughout the dense matrix. This inhomogeneity may have resulted from inhomogeneity in the gel itself or from problems in formation of a suitable greenbody (a ceramic piece formed as a particulate aggregate, that has been dried but not fired), but rendered the material produced inadequate for use in deformation or other experiments. In expounding their methodology, Kazakos et al. (1990) describe their starting suspension, produced by the addition of 10 nm MgO to water, as a *magnesia* sol (Figure 2.4). This is somewhat misleading as in the pilot experiments, colloidal MgO reacted rapidly with water to produce a strongly alkaline magnesium hydroxide (brucite - Mg(OH)₂) suspension. Peptization of this suspension was found to be very difficult. Personal communication with Kazakos led to the use of 1 gram MgO to 50 ml water to 5 ml 1 N HNO₃ (~ 1.7 wt% MgO). However, suspensions treated in this way were found to be unstable, sedimenting in several hours. Furthermore, the addition of Ludox™ AS40 to the suspension results in almost immediate gelation. This makes thorough mixing difficult and may cause the inhomogeneity seen. A weight loss of ~ 20 %, at ~ 360 °C was observed on calcining the various gels, indicating that all the MgO had become hydrated to form brucite; TGA results demonstrating this are presented in Figure 2.5. This dehydration reaction on calcination must have important effects on the microstructure of the resulting precursor. Kazakos et al. (1990) present densification curves which show that the densities of the final ceramic, sintered for 1 hour, formed from both monophasic (91% TD) and diphasic (97.5 % TD) gels are almost independent of the sintering temperature between 1200 and 1500 °C. These results could not be reproduced by following the described procedure, and high densities could only be achieved at high temperatures ~ 1400 °C.

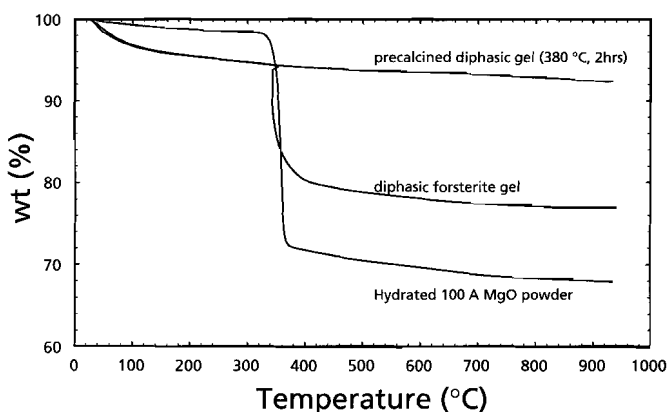


Figure 2.5. Thermogravimetric analysis of dried gel and precalcined gels produced in pilot trials of the method described by Kazakos et al. (1990). 10 nm MgO powder hydrated by suspension in distilled water for 24 hours at room temperature is shown for comparison. Obtained using a TA Instruments TGA 2950 analyzer with heating at 50 °C min⁻¹ RES 5.

Trials using the diphasic methods described by Shiono and Okamoto

As already mentioned, Shiono et al. (1991) described a method for the synthesis of forsterite powders in which TEOS was partially hydrolyzed in ethanol plus water, in the presence of an HCl catalyst, followed by the addition of 10 nm MgO powder (UBE Industries Ltd.) and subsequent gelation by the introduction of distilled water. This method was attempted in a limited series of test runs but the ceramics made from powders produced by this method were found to have high porosities (30 %) after sintering at ~ 1300 °C for several hours. However, communication with Shiono and Okamoto (pers. comm. 1994) suggested an alternative, catalyst free approach in which the MgO powder was first suspended in ethanol plus water (MgO : H₂O = 1 : 1 mole), followed by the addition of TEOS and finally gelation initiated by the addition of water. The method was successful in the production of dense fine-grained forsterite ceramics. However, these were found by the author always to contain MgO, even when aiming for enstatite-bearing silica rich compositions, indicating the incomplete hydrolysis of TEOS during gelation and its loss on subsequent drying. This was confirmed using gas chromatography of distillates produced from gels after 24 hours' gelation.

Lessons learned

Several important lessons have been learned during the trials of the previously described diphasic sol-gel routes. These have played an important role in the development of a successful diphasic approach to the preparation of forsterite-enstatite ceramic materials and are summarized below.

- 1) The use of 50 nm MgO powder instead of 10 nm powder (as used by Kazakos et al., 1990 and Shiono et al., 1991) has little or no effect on the grain size achieved in the final ceramics.
- 2) Atmospheric water adsorbed by the colloidal MgO powder leads to mass changes in the reagent which must be accurately corrected for to obtain the desired reactant and product proportions.
- 3) Colloidal suspensions of MgO in water become rapidly hydrated to form Mg(OH)₂ and cannot be easily stabilized (cf. Kazakos et al., 1990). This hydration (and subsequent dehydration) and poor

stability lead to poor microstructural homogeneity in the final product.

- 4) The suspension of 50 nm MgO in ethanol following Shiono et al. (1991) removes the problem of hydration. The suspensions remain unstable, however, and probably to some extent aggregated, showing signs of sedimentation within ~ 24 hours. Nonetheless, this is sufficiently slow not to lead to problems during synthesis.
- 5) The importance of the prehydrolysis step is not understood and may in fact be redundant (cf. Shiono et al., 1991)
- 6) A catalyst such as HN_3OH is essential to ensure complete hydrolysis of the TEOS and thus a predictable final composition. Its use does not detrimentally affect the remainder of the process.
- 7) Care must be taken to avoid TEOS evaporation during the process which is therefore carried out in a closed container. Loss of TEOS will obviously lead to change to the product phase proportions.
- 8) The heat released from the exothermic forsterite forming reaction during reaction sintering does not lead to excessive sintering and aggregation of the precursor (cf. Shiono et al., 1991).
- 9) The use of an organic binder such as ethylene glycol during greenbody formation is essential to the formation of a homogeneous product.
- 10) Claims (cf. Kazakos et al., 1990; Hogan et al., 1992; Park et al., 1994b) that enstatite always forms as a by-product during attempts to make pure forsterite by diphasic sol-gel routes (due to the slow kinetics of solid state diffusion as seen in oxides by Brindley and Hayami, 1965) are incorrect. They stem from problems in controlling the bulk chemistry caused by the failure to allow for the water content of the MgO reagent (see point 2), and from distribution of reactants in the gels.

2.4. Final methodology

In developing a final methodology, the above mentioned lessons were implemented to make a number of modifications to the method communicated by Shiono and Okamoto. The modifications include the use of the alkaline ($\text{NH}_3\text{OH}_{(\text{aq})}$) catalyst, the use of 50 nm MgO powder, a reduction in the amount of ethanol used to suspend the MgO powder, and the use of the polyethylene glycol binder during cold isostatic pressing (CIPing). Fifty nanometer MgO powder was used in place of the 10 nm powder because it has a much higher density and is therefore significantly easier and safer to handle. The 10 nm powder has an aerated bulk density of $0.05 - 0.06 \text{ g cm}^{-3}$ and a packed bulk density of $0.06 - 0.07 \text{ g cm}^{-3}$, whereas the 50 nm powder has an aerated bulk density of $0.10 - 0.12 \text{ g cm}^{-3}$ and a packed bulk density of $0.14 - 0.17 \text{ g cm}^{-3}$ (data from UBE Industries). The higher density allows processing of larger mass batches and increases the density of the gel. The reduction incurred in BET specific surface area, from 100 to $170 \text{ m}^2 \text{ g}^{-1}$ for the 10 nm powder to 27 to $38 \text{ m}^2 \text{ g}^{-1}$ for the 50 nm powder, does not seem to seriously affect the reactivity of the resulting xerogel. The quantity of ethanol used for suspension of the MgO powder was reduced so that a stiff alcogel can be produced using the 50 nm powder.

The fabrication process finally developed is founded on a hybrid sol/alkoxide sol-gel step which produces a maximally heterogeneous (chemically and structurally) diphasic gel. It can be sub-divided into several stages, namely the sol-gel stage, reaction sintering, powder processing, ceramic form-

ing, firing and machining (see Figures 2.6 and 2.7). These stages will now be described in detail along with the reagents used and the quantities required.

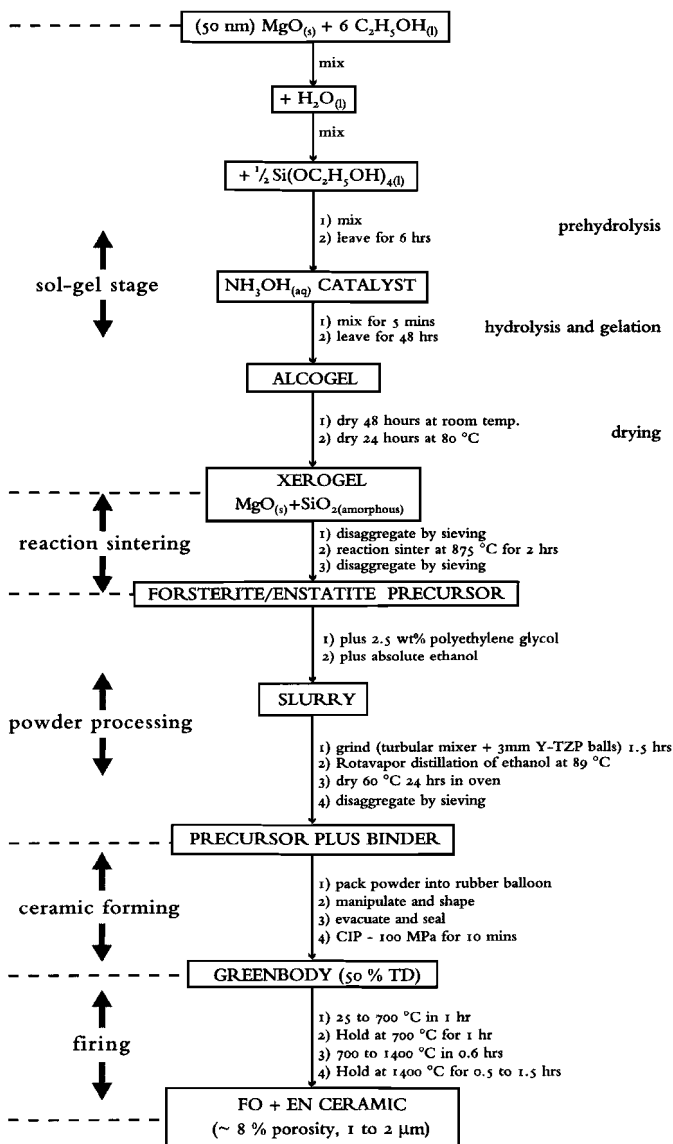


Figure 2.6. Flow diagram of the current sol-gel based fabrication method.

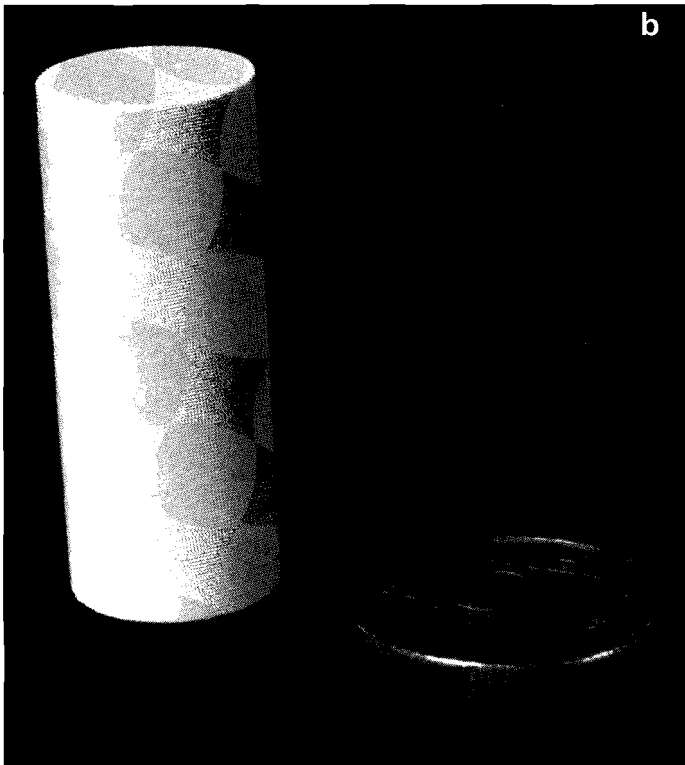
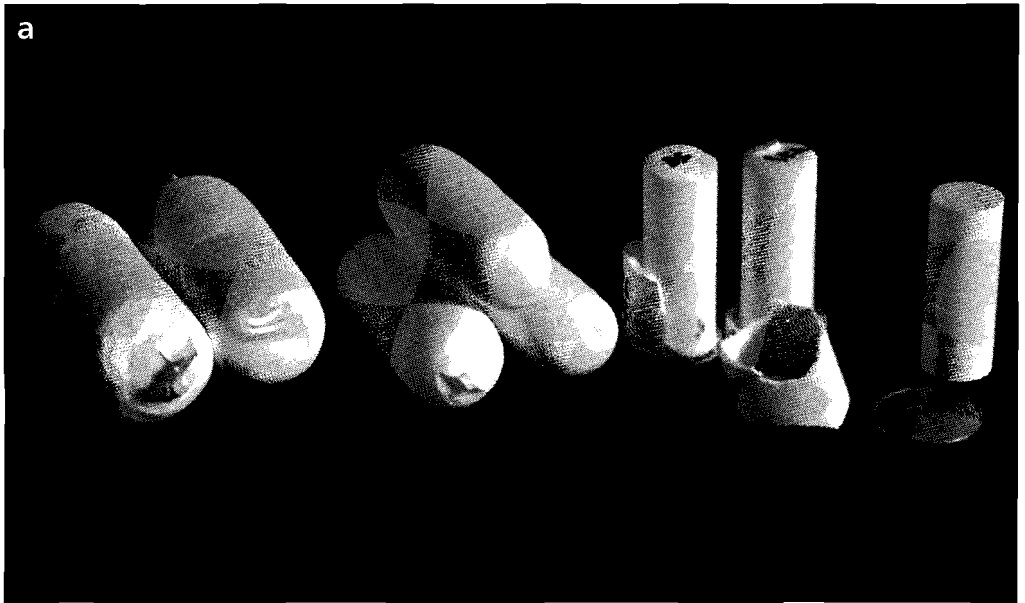


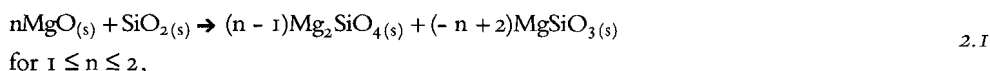
Figure 2.7a,b. Photographs of the products obtained at various stages during fabrication following the present method. From left to right: CIPed greenbody, fired ceramic and machined samples (10 mm diameter x 25 mm long).

2.4.1. Reagents and reagent proportions

The following reagents are required:

1. High purity, ultra-fine (type 500A) 50 nm MgO powder - UBE Industries Japan.
2. Tetraethyl orthosilicate (TEOS > 98 %) - E. Merck, Nederland BV.
3. Absolute ethanol - E. Merck, Nederland BV.
4. Concentrated NH₃OH (68 wt%) - Aldrich BV.
5. Polyethylene glycol (MW 8000) - Aldrich BV.

Note that care should be taken to avoid skin contact and inhalation of the reagents. The reagent proportions needed to obtain specific final ceramic compositions follow from the relevant synthesis reaction. This is given



where n is the molar ratio of MgO to amorphous SiO₂ defined by the choice of reagent proportions. To obtain forsterite plus enstatite ceramics, n must be > 1 and < 2 . If $n > 2$ the stable assemblage is periclase (MgO) plus forsterite and if $n < 1$ the stable assemblage is enstatite plus SiO₂. The volume percentage enstatite obtained when $1 \leq n \leq 2$ can be calculated as follows:

$$\text{vol\% en} = \frac{(-n+2) \cdot \bar{V}_{\text{MgSiO}_3}}{(-n+2) \cdot \bar{V}_{\text{MgSiO}_3} + (n-1) \cdot \bar{V}_{\text{Mg}_2\text{SiO}_4}} \cdot 100 \quad 2.2$$

where n is the molar ratio of MgO:SiO₂ ($1 \leq n \leq 2$), \bar{V}_{MgSiO_3} is the molar volume of enstatite (31.31 cm³ mol⁻¹) and $\bar{V}_{\text{Mg}_2\text{SiO}_4}$ is the molar volume of forsterite (43.79 cm³ mol⁻¹). Another useful equation for calculating the volume percent of enstatite present in a forsterite-enstatite material ($1 \leq n \leq 2$) can be derived by neglecting the small density difference between the two phases ($\rho_{\text{fo}} \sim 3.21$ and $\rho_{\text{en}} \sim 3.20$ g cm⁻³). This is given by

$$\text{vol\% en} = 100 - \left\{ \frac{\text{wt\% MgO} - 40.148}{17.145} \cdot 100 \right\} \quad 2.3$$

and is valid for the range $40.148 \leq \text{wt\% MgO} \leq 57.293$. It implies that every ~ 0.171 wt% less MgO present in the mixture produces ~ 1 vol. % enstatite for compositions in the range given.

As already indicated under 'lessons learned' (Section 2.3), when aiming to produce a specific final forsterite/enstatite volume ratio, it is not simply a matter of adding the MgO and TEOS by weight, as this results in a gel which is *off composition*. In the present procedure, in which the TEOS is completely hydrolyzed by the use of the NH₃OH_(aq) catalyst, this shift in composition can have two main causes. The first is due to the presence of adsorbed water or partial hydration products in the MgO(s) powder - TGA analysis of the 50 nm MgO starting powder used here showed that it contains approximately 2 to 3 wt % H₂O (see Figure. 2.8). The second cause of compositional shift is the evaporation of TEOS during the synthesis procedures. In general a shortfall in MgO will push the bulk composition towards enstatite. In contrast, any shortfall in SiO₂ (due to TEOS evaporation) pushes the composition towards forsterite which, when a pure forsterite composition is required, can lead to an excess of MgO. In order to correct for these small shifts in composition, the reagents and the proce-

dures used were tested for their true yields in terms of the MgO and SiO₂ components required (see Holloway and Wood, 1988 - page 178). Typically a yield of 97.5 wt% for the MgO and 98.0 wt% for TEOS are used to correct for the above effects and an example calculation is shown in Table 2.2. The quantities of distilled H₂O and absolute ethanol required during the sol-gel stage were calculated using the molar ratios with respect to true MgO yield as indicated in Table 2.2. The volume of NH₃OH(aq) (50 ml 68 wt% made up to 500 ml in total - pH ~ 12.32) catalyst required was scaled with respect to the other reagents using a factor ~ 54 x moles MgO as trials indicated that this was sufficient to initiate rapid gelling.

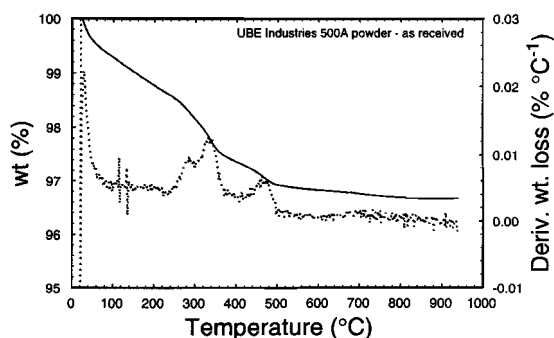


Figure 2.8. Thermogravimetric analysis (TGA) of 50 nm MgO powder as delivered. Data indicate the presence of ~3 wt% water in the powder. Solid line percentage weight loss, dotted line derivative of weight loss. Obtained using a TA Instruments TGA 2950 analyzer with heating at 50 °C min⁻¹ RES 5.

| wt% MgO required | | 56.435wt% | vol % en = | 5.00 |
|---------------------------------------------------|---------------------------------------------------|------------------------|------------|------|
| SiO ₂ required = 43.565wt% | | | | |
| MgO yield | 97.50% (allows for water content of powder) | | | |
| TEOS yield | 98.00% (allows for the shortfall in the TEOS) | | | |
| wt MgO | 50.000g | | | |
| wt MgO | 48.750g (adjusted for yield) | | | |
| wt SiO ₂ | 37.633g (required) | | | |
| wt TEOS | 133.146g (required taking into account the yield) | | | |
| moles MgO | 1.2095 | | | |
| Components in mix : molar ratio for 1 mole of MgO | | | | |
| components | mol ratio | Amount required | | |
| water | 1 | 21.790g | 21.79ml | |
| ethanol | 6 | 334.189g | 424.47ml | |
| TEOS | ***** | 133.146g | 142.31ml | |
| NH ₃ OH (aq) | 54.048 x moles MgO | | 65.37ml | |
| | | Total vol. | 828.4ml | |
| | | Total mass (dried gel) | 86.38g | |

Table 2.2. Example calculation of reagents required to produce a 5 vol.% enstatite ceramic taking into account the reagent yields.

2.4.2. Sol-gel stage

The entire sol-gel process was carried out within a single polypropylene bottle. This approach simplifies the handling of reagents and reduces the chance of contamination and loss of material. Thus, in preparing an individual gel batch, a clean, dry, one-litre polypropylene bottle containing a PTFE coated magnetic stirrer was weighed along with its lid. Approximately 50 g of MgO powder was then transferred to the bottle directly from the manufacturer's bag via an inserted tube. The transferred powder was then *weighed* along with the bottle, lid and magnetic stirrer. The quantities of the other reagents necessary for the synthesis were calculated accordingly and the *volumes* of absolute ethanol and doubly distilled water required were carefully measured out into respective measuring cylinders. The ethanol was then decanted gently into the bottle containing the MgO powder, so as not to displace powder from the bottle. The bottle was then capped and the mixture stirred for ~ 5 minutes using the magnetic stirrer until the powder became homogeneously dispersed in the ethanol. The distilled water was then added to the bottle from the measuring cylinder while the suspension was stirred continuously. The bottle was subsequently closed and the suspension stirred. After approximately half an hour, the appropriate amount of TEOS was carefully *weighed* into a measuring cylinder and added to the MgO suspension while stirring continuously; the measuring cylinder was carefully rinsed several times with ethanol to wash out all the TEOS. The mixture was then left for 6 hours with occasional stirring. Thereafter, the dilute $\text{NH}_3\text{OH}_{(\text{aq})}$ solution, prepared by making 50 ml of concentrated NH_3OH (68 wt%) up to 500 ml (pH = 12.32) in a volumetric flask, was added to initiate gelation. The bottle was closed and stirred for approximately 5 minutes. The mixture - smelling strongly of ammonia - was then left undisturbed to allow gelation to take place.

Within approximately one hour a rigid homogeneous alcogel had formed. However, the gel was left undisturbed for ~ 48 hours to ensure that hydrolysis of the TEOS was complete. The gel was subsequently removed from the bottle into a clean, glazed, flat ceramic bowl and spread evenly to increase its exposed surface area. The bowl plus gel was then placed in a fume cupboard to dry at room temperature for 48 hours. The resulting xerogel was then gently ground in the bowl and left for several hours in the fume cupboard before being dried at 80 °C for 24 hours. Note that care was taken that the gel was fully dry as any residual ethanol can lead to combustion of the gel during reaction sintering. The dried xerogel was then disaggregated by forcing it through a nylon sieve (0.5 x 0.5 mm mesh size) with the aid of a plastic spatula. Please note that, in some instances, xerogels with identical compositions were mixed at this point to produce larger batches for further processing. This fact is reflected in the gel batch numbers used to refer to the materials in subsequent Chapters of the thesis; e.g. material **stm 30.31.32** was produced from combining the 3 sol-gel batches 30, 31 and 32, which had identical compositions, before moving on to the reaction sintering stage.

2.4.3. Reaction sintering

Following synthesis, the dried and disaggregated xerogel was placed in high density, 100% alumina crucibles and reaction sintered at 875 °C for 2 hours. A heating rate of approximately 14 °C min⁻¹ was used to reach this reaction sintering temperature. The resulting forsterite enstatite precursor was allowed to cool to room temperature in the furnace over several hours before being disaggregated by

forcing it twice through the nylon sieve. The term precursor has been used as the material is not fully reacted to forsterite (at a rough estimate being made up of ~ 70% forsterite).

2.4.4. Powder processing

The disaggregated precursor was next placed in a one-litre polypropylene bottle along with 2.5 wt% polyethylene glycol binder (crystalline solid) and sufficient absolute ethanol (~ 500 ml) to produce a liquid slurry. The bottle was filled ~3/4 full with ~3 kg of 3 mm diameter Y-TZP grinding balls (Ytria stabilized zirconia - Cerasec Technical Ceramics BV) and securely capped before being placed in a turbular mixer for 1.5 hours. After grinding the slurry was decanted into a rotavapor™ dryer flask using a ceramic filter funnel to capture the grinding balls (no filter paper required). Slurry remaining on the grinding balls was then rinsed into the flask using absolute ethanol from a wash bottle. The ethanol was then distilled off using a rotavapor™ dryer at ~ 89 °C and the resulting soft cake of forsterite/enstatite precursor plus ethylene glycol binder was removed from the rotavapor and placed in an oven at 60 °C for ~ 24 hours. After drying the cake was gently broken up in a glazed ceramic mortar and pestle and returned to the drying oven at 60 °C. Once fully dry, the powder was disaggregated once again by forcing it through the nylon sieve.

2.4.5. Ceramic forming

To form the appropriately sized individual greenbodies, fifteen gram batches of the ethylene glycol-bonded forsterite/enstatite precursor were weighed out and transferred to small latex balloons (10 x 1.5 cm - uninflated dimensions). The open end of each balloon was next stoppered by the insertion of a 15 cm long steel evacuation tube (6.3 mm OD, 1 mm ID), tipped with a cotton fabric filter, held in place by PVC tape against which the balloon neck formed a tight, powder-free seal.

After insertion of the evacuation pipe, the powder was manually manipulated for several minutes in order to further disaggregate the powder until it had a smooth, well-lubricated, free-flowing, aggregate-free feel. The powder was then shaped into a crude cylinder, ~ 4.5 cm long and ~ 2.0 cm in diameter, and a vacuum (~ 1 Torr) applied using a standard lab vacuum pump. The powder-filled balloon was again manipulated and rolled at this stage to help the air escape and to facilitate closer packing of the grains. As the air was removed the powder became stiff and further shaping was difficult. The balloon was then evacuated for a further 5 minutes before carefully removing the evacuation tube without allowing air back into the balloon. The balloon was tied and placed in a condom which was subsequently evacuated and tied. When several balloons had been filled and evacuated, they were transferred to a pressure vessel for so-called *wet bag* cold isostatic pressing (CIP) conducted using a silicone oil pressure medium at 100 MPa for 10 minutes at room temperature. The samples - now referred to as greenbodies - were retrieved and the rubber jackets removed (Figure 2.7a).

2.4.6. Firing

Firing was carried out in a programmable laboratory furnace with molybdenum disilicide elements (Naber LHT16/R). The CIPed greenbodies were wrapped together in platinum foil, to shield them from direct radiation and contamination from the heating elements, and placed on the floor of the

furnace. The temperature immediately adjacent to the samples was monitored continuously using an S-type thermocouple and logged by computer. The exact sintering temperature and duration required were predetermined from a series of batch-specific test runs. This procedure was found necessary in order to allow for the differences in greenbody structure and composition between sample batches. Following this approach, the desired final porosity of 8.0 ± 0.5 % required for further experimentation was achieved. The furnace heating cycle was controlled using the built-in programmable PID controller and consisted of five steps:

- 1) Heating from room temperature to 700 °C in 1 hour (~ 11.25 °C min⁻¹). This gentle heating of the sample allowed loss of volatiles and binder (polyethylene glycol) burnout.
- 2) Temperature held at 700 °C for 1 hour. This period allowed binder burnout to go to completion.
- 3) Rapid heating from 700 °C to sintering temperature, e.g. 1400 °C, in 36 minutes (19.44 °C min⁻¹). This rapid heating allowed the greenbody to reach the sintering temperature whilst undergoing the minimum of microstructural evolution.
- 4) Temperature held at the firing temperature (typically 1400 to 1450 °C) for 15 - 120 minutes.
- 5) Uncontrolled cooling to room temperature, achieved simply by switching off the furnace. N.B. the furnace buffered the temperature sufficiently to prevent damage by thermal shock (initial cooling rate ~ 7 °C min⁻¹, slowing to ~ 4 °C at ~ 1000 °C).

2.4.7. Machining

After firing, the hard, white forsterite plus enstatite ceramic billets produced were machined to form cylindrical samples using water-cooled diamond tools (Figure 2.7a). First one end of each billet was ground flat, so that it could be fixed upright to a metal block using high strength two-component adhesive. Several samples were mounted on each block and cored to a sample diameter of 10 mm. After removing the samples from the block they were carefully ground to length using a diamond lap with a fixed sample holder, to produce right cylinders 25 mm in length (Figures 2.7 a,b). Finally, the sample ends were carefully polished using fine polishing paper on a lap.

2.5. Process progress and material characterization

In the following, thermal analysis results and other data will be presented on aspects of the fabrication process, on the properties and structure of the material at various intermediate stages, and on the compositional and microstructural characteristics of the final ceramic product. Note that during the present study compositions ranging from forsterite plus 0 to 50 % enstatite and forsterite plus 0 to 10 % MgO and densities up to 98 % TD have been prepared. It has not been possible to fully investigate all aspects of this multistage process.

2.5.1. General results

Xerogel and the reaction sintered precursor

Powder X-ray diffraction (XRD) of the xerogel before reaction sintering showed it to be structurally diphasic, being made up of crystalline MgO and amorphous silica (Figure 2.9 and 2.10a). Differential thermal analysis (DTA) of the xerogel illustrated in Figure 2.11 showed a sharp exothermic peak at 880 °C, corresponding to the forsterite-forming reaction. XRD of the reaction sintered precursor (2 hrs at 875 °C) showed that much of the gel has reacted to forsterite at this stage (Figure 2.9). However, MgO reflections were still present and indicate that the reaction has not gone to completion. High-resolution scanning electron microscopy (HR-SEM) of the reaction sintered precursor showed that the average grain size is ~ 50 to 100 nm (Figure 2.10b).

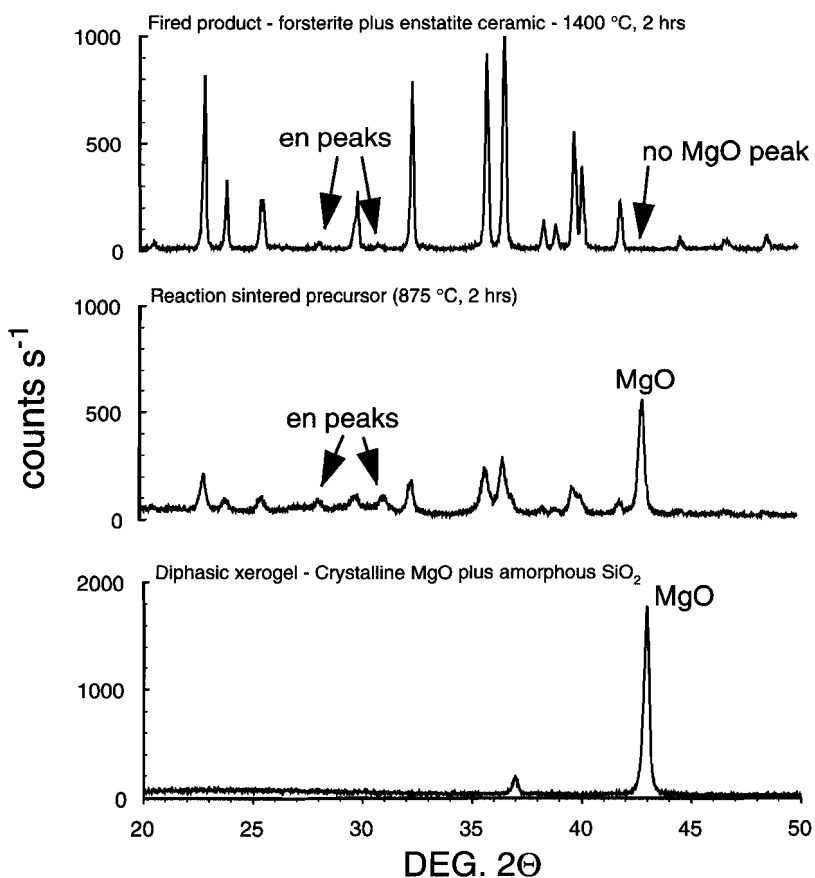


Figure 2.9. Powder X-ray diffractograms of the dried xerogel, the reaction sintered precursor and the final ceramic. The small peak in the xerogel diffractogram is the MgO {111} reflection.

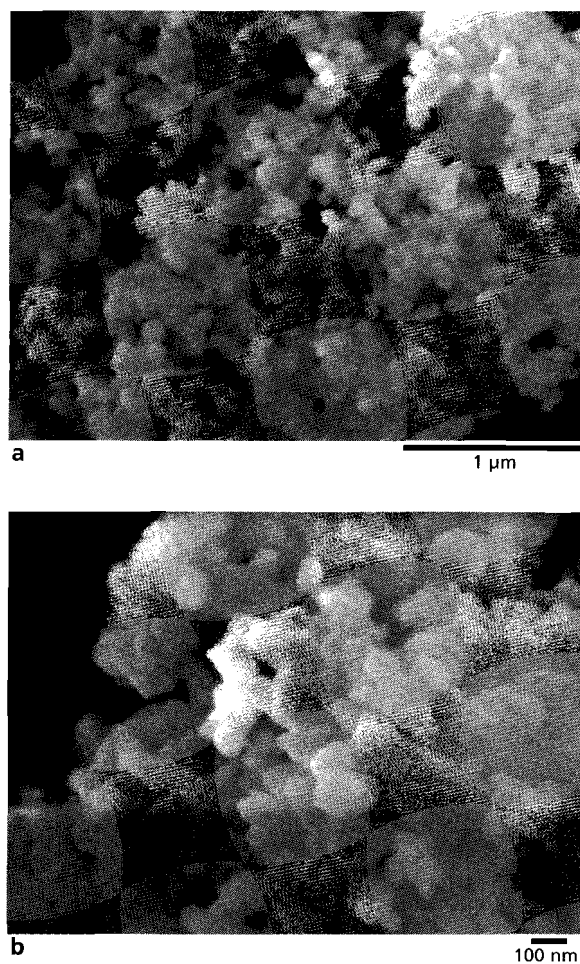


Figure 2.10.

a) High resolution scanning electron microscopy (HR-SEM) micrograph of the xerogel.

b)HR-SEM micrograph of the reaction sintered forsterite-enstatite precursor.

Binder burnout from the greenbody

TGA analysis of the greenbody containing polyethylene glycol binder has shown that binder burnout starts at ~ 250 °C and that weight loss continues up to 550 °C (Figure 2.12). Comparison made between ceramics produced with and without the binder have clearly shown that it plays an important role in the production of a homogeneous greenbody. Ceramics produced without binder were found to have higher porosities and contained occasional large, high coordination pores which presumably resulted from uneven packing of the precursor. No residue from the binder was observed either macroscopically or when examined using SEM and TEM techniques. Ceramics produced

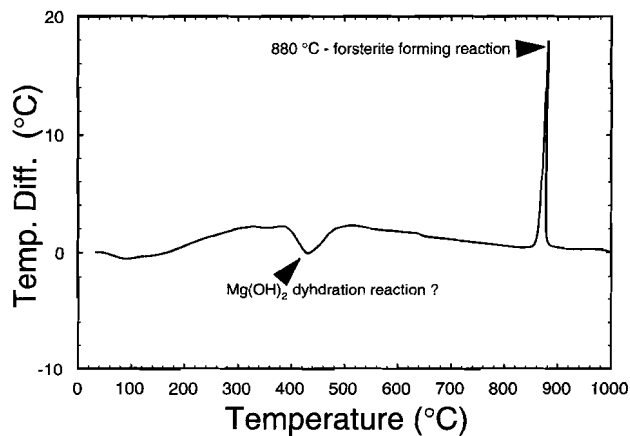


Figure 2.11. Differential thermal analysis of xerogel produced by the current method. Note the exothermic reaction peak at ~ 880 °C corresponding to the formation of forsterite (cf. Shiono et al., 1991). Obtained using a heating rate of 10 °C min^{-1} .

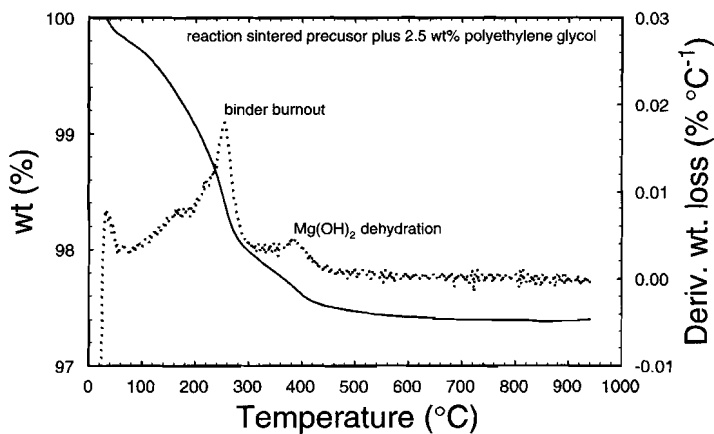


Figure 2.12. Thermogravimetric analysis of reaction sintered precursor with ~ 2.5 wt% polyethylene glycol binder added. Note binder burnout peak at ~ 260 °C. The solid line is the percentage weight loss with temperature. The dotted line is the derivative of weight loss. Obtained using a TA Instruments TGA 2950 analyzer with heating at 50 °C min^{-1} RES 5.

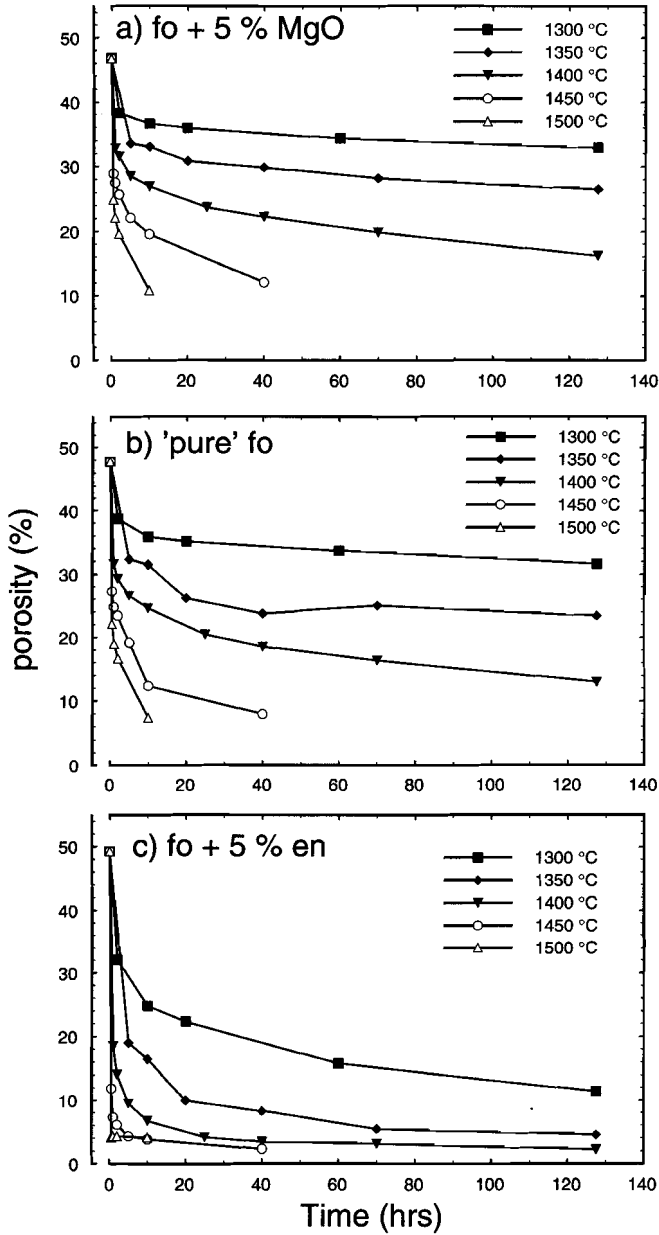


Figure 2.13. Densification curves for forsterite plus 5 vol. % MgO, 'pure' forsterite and forsterite plus 5 vol. % enstatite prepared using the present method. Note the enhanced densification observed in enstatite-bearing materials. Porosities determined using the Archimedes method applied to individual samples treated for different times.

without sufficient disaggregation by sieving were found to have a 'measles' texture (Burke, 1996), resulting from uneven densification of the powder due to the presence of discrete denser aggregated particles.

Firing stage (sintering) behaviour

A detailed study of densification and grain growth during the firing (sintering) stage (steps 3 and 4 of the firing stage in Figure 2.6) has been carried out in collaboration with D. Ellerbroek, the detailed results of which will be presented elsewhere. During this study, the densification behaviour of 5 vol% MgO plus forsterite, nominally pure forsterite and 5 vol% enstatite plus forsterite ceramics has been systematically investigated by means of batch heat treatment experiments conducted at temperatures in the range 1300–1500 °C. The several CIPed rods of the three materials were prepared following the method describe up to stage 3 of the firing stage. After binder burnout they were removed and each was split into small ~ 2 g samples to provide starting material for the densification tests, in which the samples were fired at temperatures between 1300 and 1500 °C for up to 120 hours. The density and grain size of the materials was measured as a function of time by extracting samples at appropriate intervals. Densities were measured using the Archimedes method (Morrel, 1985). The densification results (Figure 2.13) have shown that the presence of enstatite produced an enhanced densification rate at all temperatures compared with 'pure' forsterite and MgO bearing materials. All the materials exhibited increased rates of densification with increasing temperature, with the majority of densification occurring in the first 1 to 5 hours. Enstatite-bearing samples fired at temperatures > 1475 °C showed extremely rapid densification (Figure 2.13 c) which was followed by *abnormal* (discontinuous) grain growth with evidence of melt films.

Returning to the reference material prepared for subsequent deformation experiments, the optimum densification/grain growth behaviour for enstatite bearing compositions in the range (0 - 20 %) was obtained at temperatures between 1400 and 1450 °C for 60 to 120 minutes, which produced samples with porosities of ~ 8 % suitable for controlled water addition. High density forsterite-enstatite (2.5 to 10 % enstatite) samples (porosity ~ 2 %, grain size ~ 2 µm) were optimally produced at between 1400 and 1450 °C using firing times of 3 to 5 hours.

2.5.2. Chemical characterization of the final ceramic

Phase content

Qualitative and semi-quantitative phase analysis of the final ceramics was carried out using a Philips PW-1700 X-ray powder diffraction (XRD) apparatus. The sensitivity of the technique to the presence of MgO and enstatite phases was determined by using mechanical mixtures of MgO plus forsterite and enstatite plus forsterite produced from pure MgO powder (UBE Industries Ltd), commercially available forsterite powder (Cerac BV) and hydrothermally synthesized enstatite (800 MPa and 1000 °C). These standards were prepared by making mixtures containing 0.5, 1.0, 5.0 and 10.0 vol % of either MgO or enstatite which were then ground together under acetone. The results obtained using these mixtures indicated that the standard powder X-ray diffraction procedure used

could detect enstatite contents ≥ 1 vol % and MgO contents ≥ 0.5 vol % (see the appendix of Chapter 5). Only forsterite and enstatite peaks could be identified in the final fired ceramics, indicating that reaction 2.1 (Section 2.4.2) had gone to completion (Figure 2.14). Furthermore, the XRD data indicate enstatite contents closely in line with the starting gel compositions, thus demonstrating that the reagent proportions used give good control of enstatite content to $\sim \pm 1$ %. Dense materials (~ 8 to 2 % porosity) with compositions in the range 0 to 50 % enstatite have been successfully prepared by adjusting the reagent proportions. In addition to the identification of crystalline phase using XRD,

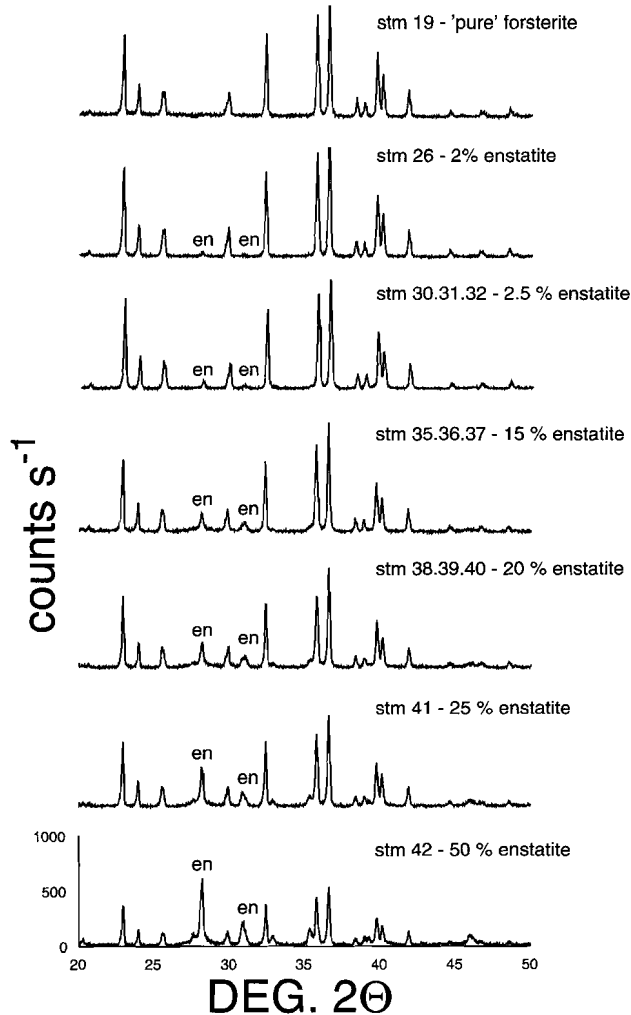


Figure 2.14. Powder X-ray diffractograms (XRD) for final ceramics with enstatite contents up to $\sim 50\%$. N.B. the absence of MgO in all these samples indicates complete reaction of the reagents.

TEM observations indicate that the ceramics produced at temperatures up to 1450 °C are free from bulk melts, although high-resolution TEM has not been attempted and therefore the presence of melt films or blebs at the corresponding scale (≤ 2 nm) cannot be discounted.

Bulk chemistry

The chemistry of the final ceramics is dependent on the purity of the reagents used and the level of contamination during processing. Chemical analysis of the high purity MgO powder used (UBE Industries Ltd.) is shown in Table 2.3. The TEOS is > 98% pure. A preliminary investigation of the bulk chemistry of the final ceramics has been carried out using both electron probe microanalysis (EPMA) and inductively coupled plasma atomic emission spectroscopy (ICP - AES) to determine the level of contamination during processing. EPMA was carried out using a JOEL superprobe using 4 wavelength-dispersive spectrometers (WDS) set up for the elements Al, Ca, Na, K, Fe, Co, Ni, Mo, Y, Zr as these are among the most likely contaminants from grinding media, crucibles, furnace heating elements etc. The beam was defocused giving a width of ~ 10 mm and the analyses obtained were therefore bulk analyses, including several grains and grain boundaries. The only one of the above elements found in measurable concentrations (> 0.02 wt%) was aluminium. Unfortunately, however, the results for aluminium, which were found to be very variable, ranging up to ~ 0.35 wt % Al_2O_3 , cannot be trusted since the probe samples were prepared by polishing with ultra-fine alumina, which may have become lodged in the porous samples. Contamination with Zirconium from the grinding balls appears to be minor.

ICP-AES results indicated that all the expected contaminants including aluminium were below the detection limits of ~ 10 ppm for the technique used. Further chemical analyses are required to accurately determine the trace element chemistry of these ceramics. This is particularly important as small amounts of dopants can have important effects on the point defect chemistry, and therefore the physical and chemical properties of forsterite (Hobbs, 1983).

| wt % oxide | 50 nm MgO |
|-------------------------|------------|
| MgO | > 99.98 |
| Al_2O_3 | < 0.001 |
| SiO_2 | < 0.002 |
| CaO | < 0.002 |
| Fe_2O_3 | < 0.001 |
| ZnO | < 0.007 |
| Na_2O | < 0.001 |
| MnO | < 0.001 |
| NiO | < 0.0001 |
| Cr_2O_3 | < 0.0001 |
| B_2O_3 | undetected |
| U, Th total | 1 ppb |

Table 2.3. Chemical analyses of 50 nm MgO powder (data from UBE Industries Ltd).

2.5.3. Density and microstructure of the final ceramic

Density

The final porosity of the ceramics was determined by three more or less independent approaches: the Archimedes method (see Morrell, 1985), comparison of specific masses with theoretical densities, and image-analysis of SEM micrographs. These methods were crucial to material characterization and therefore to the evaluation of synthesis procedures. Care was taken using the Archimedes method to calculate both the open and closed porosities. Conventional error analysis indicates that the Archimedes method used is accurate to $\pm 0.6\%$ porosity. Estimates based on image analysis of SEM images can be useful but tend to overestimate porosity by up to 3 to 4%. For enstatite-bearing samples, densities as high as $\sim 98\%$ TD have been achieved (Figure 2.15 c,d). Microstructural observations indicate that in high density samples, the last 2% porosity found at intragranular pores and at triple junctions is stable even in long duration sintering experiments, and that these pores effectively pin grain boundaries.

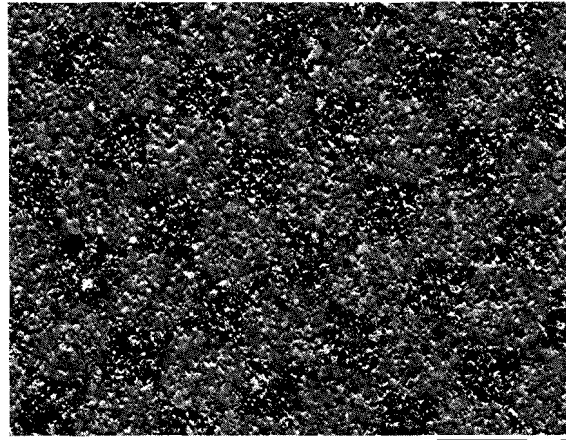
Microstructure

Microstructural observations of the final ceramics were made using scanning electron microscopy (SEM). Later observations were made using a Philips XL30 FEG (field emission gun) SEM operating at 20 kV, and 70° tilt, with dynamic focus and automatic tilt correction, in orientation contrast mode (see Section 4.4.1). Using this technique, unetched, uncoated Syton™ (colloidal silica) polished samples could be observed, the contrast between the grains resulting from their crystallographic orientation. This method was found superior to etching, as detailed microstructural features related to the porosity remained relatively intact compared to etched samples.

The final ceramics (0 to 20% enstatite, $\sim 8\%$ porosity) produced for the deformation studies were found to be microstructurally homogeneous. The microstructure is illustrated in Figure 2.15 a,b. The grains show a foam texture and have a narrow grain size distribution with grain sizes between 1 and 2 μm at final porosities of $\sim 8\%$ after firing at 1400 to 1450 $^\circ\text{C}$ for up to 2 hours. Grain boundaries are straight or gently curved and equilibrium triple junctions of 120° are common. Both intragranular and intergranular pores are present. The bulk of the total porosity is made up of intergranular pores located between 2 to 6 grain neighbours and ranging between one half to one tenth of the average grain diameter in size. Where intergranular pores intersect grain boundaries they are characterized by apparent dihedral angles $> 60^\circ$, and appear rounded and disconnected in two dimensional cross section. No melts or other grain boundary phases have been observed at the scale of observation employed. Quantitative grain size analysis was carried out on a number of samples using computer based image analysis (for technique see Section 4.4.1). Grain size analysis results show that the materials have a very narrow grain size distribution (Figure 2.16), with the equivalent circular diameters (ECDs) of $\sim 60\%$ of the grains falling in a 1 μm interval around a mean value of $\sim 1.3 \mu\text{m}$. The measured grain size distributions are approximately log-normal, a result which is consistent with previous studies of grain size distributions resulting from *normal* grain growth (Hillert, 1965; Mendelson, 1969).

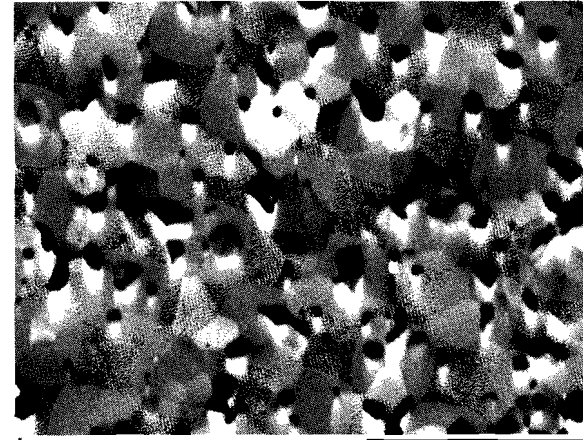
Figure 2.15 a-d.
Philips XL30 FEG
SEM micrographs in
orientation contrast
mode of final
ceramics.

a,b) Material stm
30.31.32 ~ 2.5 vol %
enstatite fired at
1400°C for 60 min-
utes ~ 8% porous.
Similar to the mate-
rials used in the
deformation experi-
ments.



a

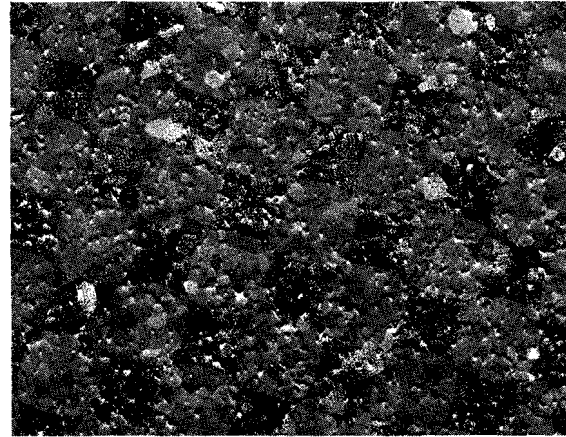
25 μm



b

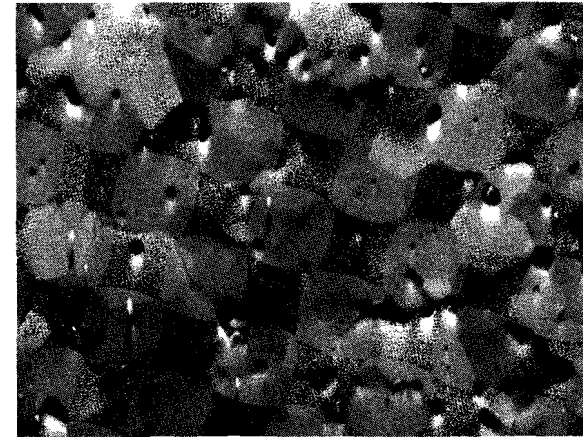
5 μm

c,d) Material stm
30.31.32 ~ 2.5 vol %
enstatite fired at
1400°C for 3 hours
~ 3% porous.



c

25 μm



d

5 μm

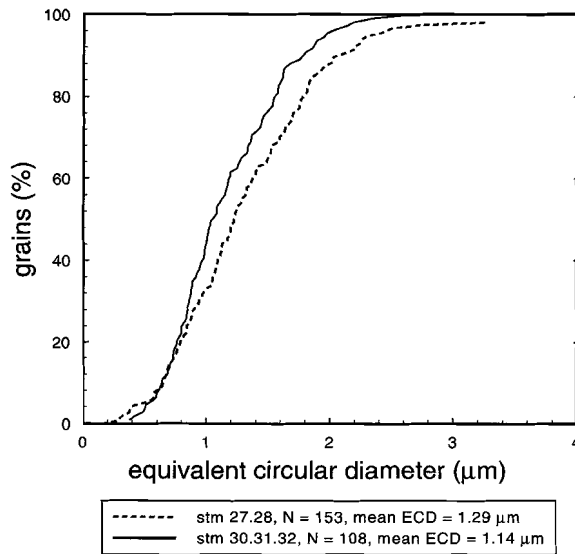


Figure 2.16. Grain size distributions for typical ceramics. Batch stm 27.28 fired at 1400 °C for 60 minutes with a porosity of ~ 8.5 % and batch stm 30.31.32 fired at 1450 °C for 60 minutes with a porosity of ~ 8.8 %. Equivalent circular diameter (ECD) is the diameter of a circle equal in area to the measured grain area

2.6. Discussion

The hybrid sol-gel (sol/alkoxide) based fabrication method developed has been used to successfully produce forsterite, forsterite-enstatite and forsterite-MgO ceramics. However, details of the nano and atomic scale process involved remain poorly understood. The microstructural homogeneity achieved both in the precursors and the final ceramics is believed to be related to the structural and chemical diphasic nature of the xerogel. No attempt has been made during the current study to understand the mechanism. However, Roy and coworkers have proposed that epitaxy may have significant effects in structurally polyphasic gels, leading to the uniform grain growth and enhancing sinterability (Roy et al., 1986; Suwa et al., 1986 a, b; Komarneni et al., 1987). The diphasic gels produced are composed of highly uniform crystalline MgO grains (50 nm) coated with amorphous silica. This spatial, chemical and structural make-up results in highly localized reaction of MgO and SiO₂, probably involving the epitaxial growth of forsterite and enstatite on MgO, leading to an extremely uniform (monodispers) forsterite-enstatite precursor. In short then, the uniform microstructure of the resulting ceramics is inherited from the gel structure.

During the final firing stage, the materials sinter to high density by a diffusion process, during which normal grain growth is accompanied by porosity reduction. The rate of the process is presumably controlled by the porosity and the second phase composition, content and distribution. Enstatite-bearing ceramics have been found to have enhanced sinterability compared with forsterite and forsterite plus MgO materials. This may be related to buffering of the point defect population (see Smyth and Stocker, 1975) which then plays a chemical role in controlling diffusion rates, although this remains speculation.

2.7. Conclusions

Structurally diphasic sol-gel routes to fine-grained forsterite powders developed by previous workers have been tested and a practical, reliable sol/alkoxide method for the manufacture of fine-grained (1-2 μm), foam texture, forsterite and two-phase forsterite-enstatite ceramics, with controlled enstatite content and densities up to 98 % theoretical density (TD) has been developed. Cylindrical samples 25 mm in length and 10 mm in diameter, suitable for deformation studies have been produced, although other shapes and sizes could easily be obtained by varying the forming and machining steps. Independent control of grain size and porosity is not possible due to the fact that densification is achieved by sintering, in which the reduction of porosity is coupled to grain coarsening. However, final porosity obtained can be controlled by careful control of sintering temperature and duration. The grain size of the forsterite powder produced during reaction sintering is inferred to be a function of the distribution and structure of the phases in the original gel. The role of solid state epitaxy in the formation of forsterite has not been investigated in these diphasic gels. However, the work of R. Roy and co-workers (Komarneni et al., 1987; Roy et al., 1986; Suwa et al., 1986 a,b) suggests that epitaxial growth of forsterite on the MgO may have a important effect leading to uniform grain growth and therefore have a marked influence on the densification and sintering behaviour. The production and persistence of enstatite reported by other workers who have attempted to produce pure forsterite via diphasic sol-gel routes is believed to arise from difficulties in controlling the bulk composition of the gel, rather than the slow kinetics of solid-state diffusion-controlled reactions. Enstatite rich compositions show much enhanced densification compared to 'pure' forsterite and MgO bearing compositions. The mechanism of densification has not been investigated but is likely to be a diffusional process involving normal grain growth controlled by the presence of pores and second phase content. The marked effect of a second phase (MgO or enstatite) on the densification kinetics observed may reflect the role of the second phase in controlling point defect chemistry.

Experimental apparatus

3.1. Introduction

The experimental work described in this thesis has been carried out using an internally heated, argon gas medium, constant volume deformation apparatus developed at the HPT laboratory, Utrecht University, by a team including Prof. Chris Spiers, Dr. Colin Peach, Gert Kastelein and Eimert de Graaff. The author's role, as the first user, was principally in testing and calibration and in the development of the temperature measurement software. A description of the apparatus has been included in this thesis as it has not been previously described elsewhere. The apparatus is currently configured to measure conventional rheological parameters (axial stress, strain and strain rate), at confining pressures up to 700 MPa and sample temperatures up to ~ 1100 °C, in constant displacement rate tests. The pressure vessel around which the apparatus is constructed has been designed for routine use at pressures up to 1 GPa and the machine is therefore referred to as the "10 kbar apparatus".

3.2. General configuration

The 10 kbar apparatus is housed within a high pressure testing bunker, with the electronic and pressure control systems situated outside, in the main laboratory. The main component of the apparatus is the horizontally mounted, internally heated, 1 GPa, water cooled, compound pressure vessel (Figures 3.1, 3.2 and 3.3). The vessel comprises an inner steel liner with an 50.4 mm bore and an outer diameter (OD) of 119 mm (modified DIN/Werkstoff Nr. 1.6357); and a water cooled outer steel mantle (OD of 324 mm; modified DIN 1.2312) built by Nova® Swiss (Nova - Werke AG). Force is applied to the sample using an Instron 1362 servo-mechanical testing machine to load a dynamically sealed deformation piston which enters the vessel through one of the end sealing heads (Figure 3.4). Constant volume of the pressure vessel is achieved by a compensation-piston which passes through the opposite sealing head and is coupled to the deformation-piston via a conventional external yoke (Figures 3.1, 3.2 and 3.3). Thus, displacement of the deformation piston does no work against the gas pressure and the confining pressure remains constant during deformation.

The compensation-piston and the sealing section of the deformation-piston are made from tool steel (DIN 1.2379). Dynamic sealing of the pistons within the heads is achieved using Paterson-type floating ring based seals (Paterson, 1962; Tullis and Tullis, 1986; Figure 3.3) employing Arlon (PEEK; poly ether ketone) delta rings which form a seal between the polished bore of the sealing heads (static part) and the (18 mm diameter) polished sections of the pistons (dynamic part). These seals were routinely used for multiple runs. External seals (static) between the sealing heads and the polished (60 mm diameter) seal sections of the pressure vessel, are based on a single metal (Al 0.4 Pb

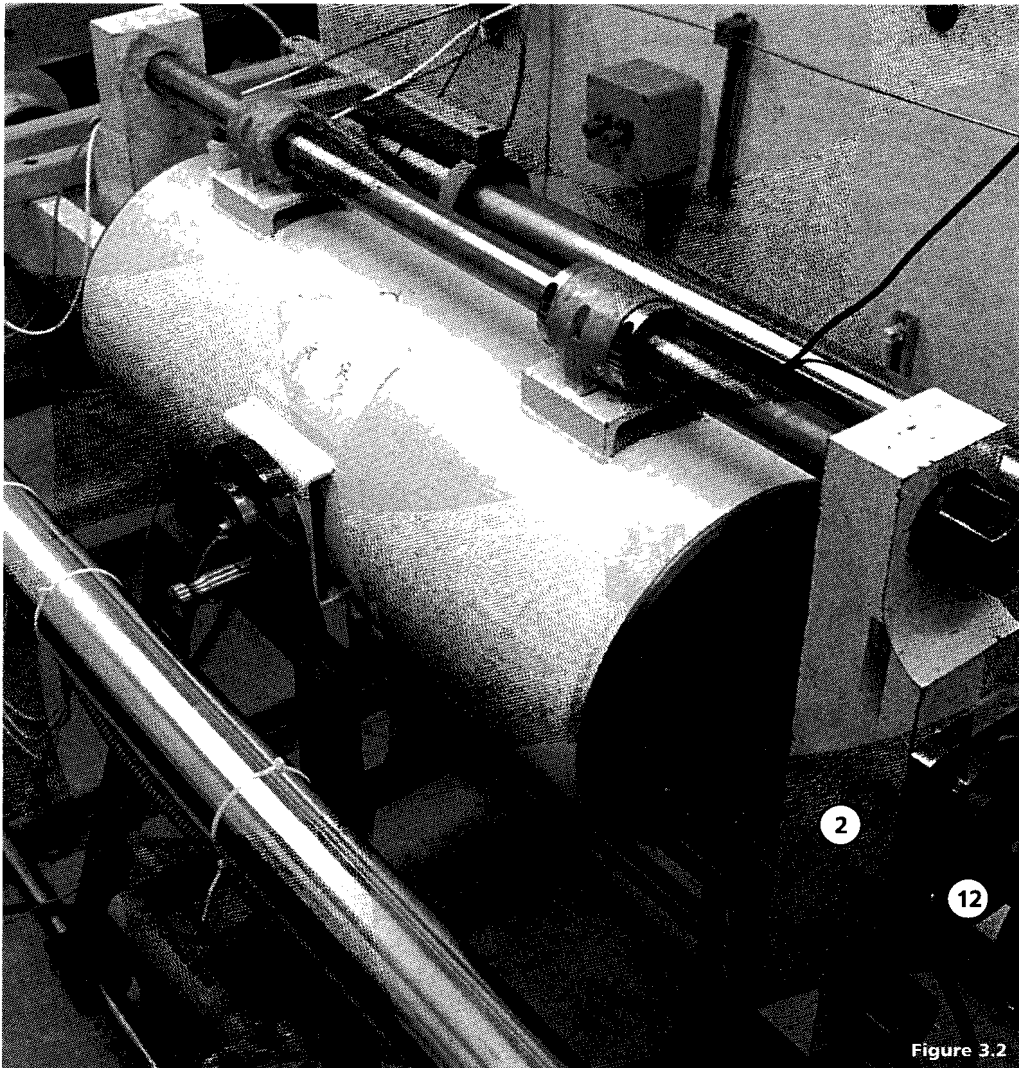


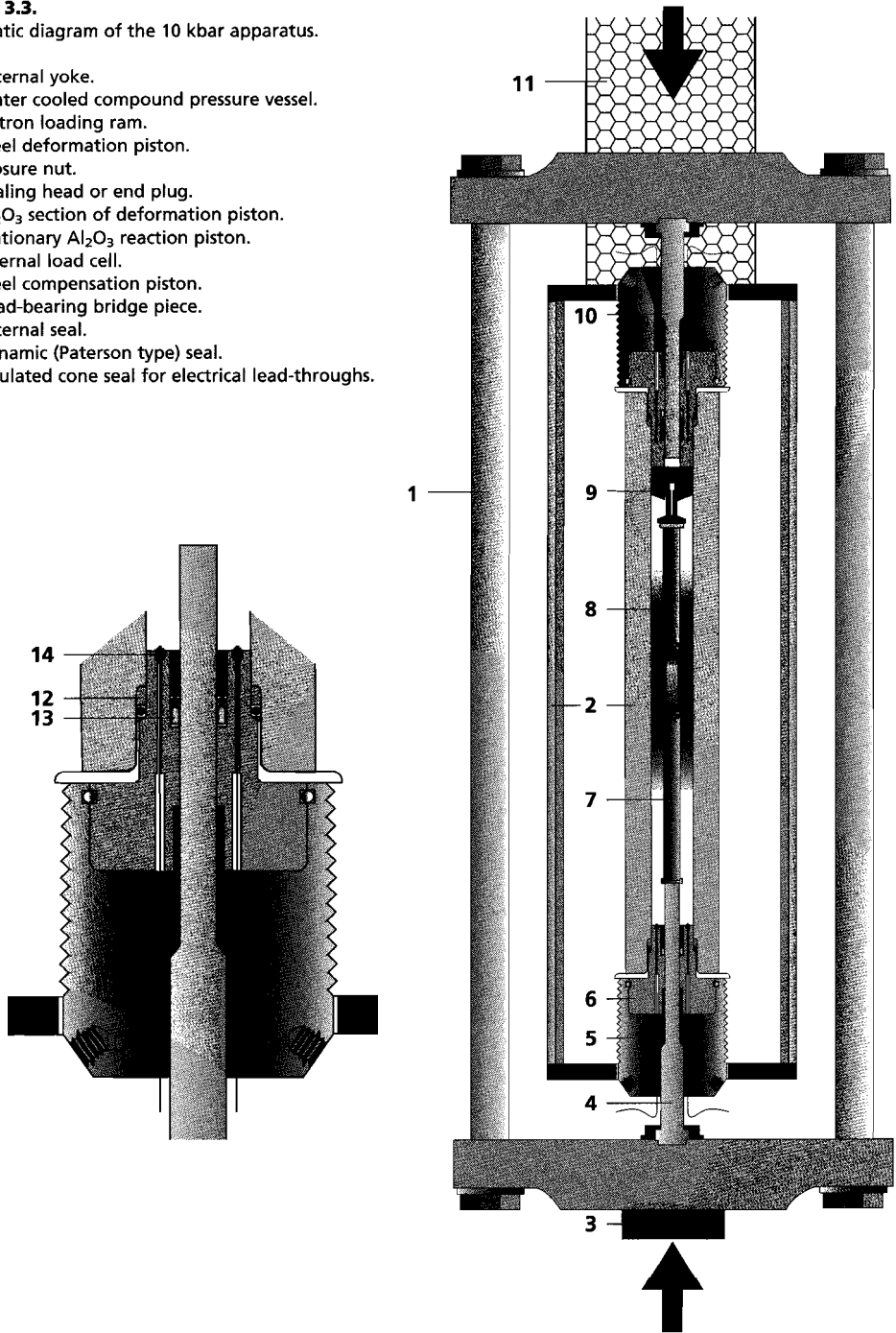
Figure 3.2

Figure 3.1. and 3.2. 10 kbar apparatus.

1. Water cooled compound pressure vessel.
2. External yoke.
3. Instron tie-bar.
4. Instron actuator unit - driving the loading ram and housing the ram displacement transducer (LVDT).
5. Instron 100 kN load cell.
6. Load bearing bridge piece - transmits the force to the external force gauge.
7. High pressure gas line.
8. Pressure transducer.
9. Instron cross-head (fixed).
10. Sample thermocouple compensation cables.
11. Internal load cell connection.
12. Instron ram - transmits force to the external yoke/deformation piston (Figure 3.2).

Figure 3.3.
Schematic diagram of the 10 kbar apparatus.

1. External yoke.
2. Water cooled compound pressure vessel.
3. Instron loading ram.
4. Steel deformation piston.
5. Closure nut.
6. Sealing head or end plug.
7. Al_2O_3 section of deformation piston.
8. Stationary Al_2O_3 reaction piston.
9. Internal load cell.
10. Steel compensation piston.
11. Load-bearing bridge piece.
12. External seal.
13. Dynamic (Paterson type) seal.
14. Insulated cone seal for electrical lead-throughs.



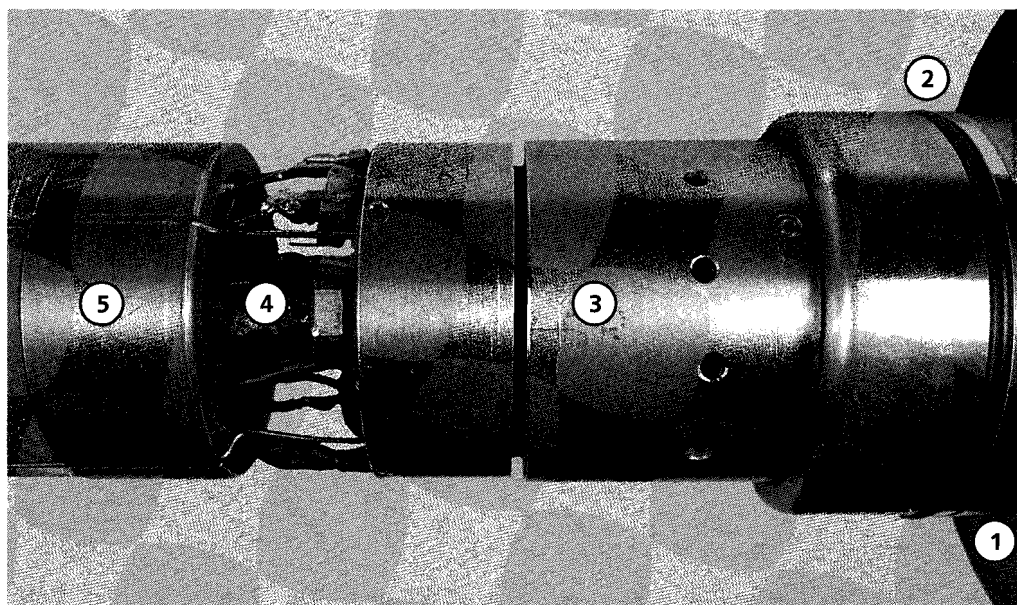


Figure 3.5. Load cell.

- 1. Sealing head.
- 2. External seal - metal delta ring plus O-ring configuration.
- 3. Internal load cell body.
- 4. Load cell stem.
- 5. Furnace module.

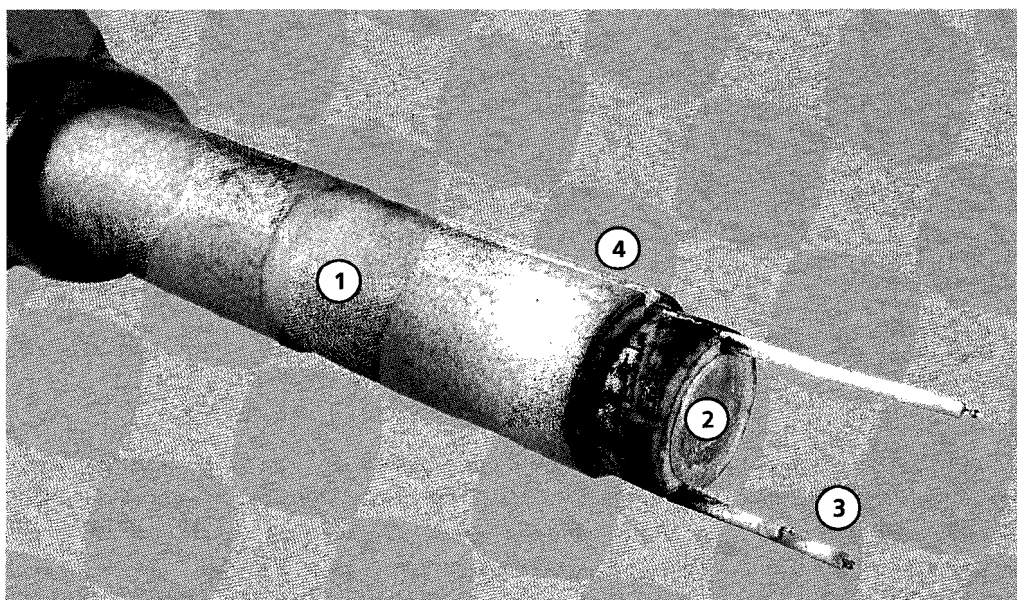


Figure 3.6. Sample thermocouple configuration.

- 1. Al₂O₃ section of deformation piston.
- 2. Gold decoupling foil.
- 3. Sample thermocouples (S-type).
- 4. Thermocouple slots.

the fixed Instron cross-head (Figure 3.1). Confining pressure is measured using a strain gauge type pressure transducer (EBM 6045, Ericha Brosa Messgerate GmbH) attached to the high pressure gas input line immediately outside the vessel (Figure 3.1). The argon gas is brought to a pressure of 600 MPa using a Nova Swiss pressure intensifier system based around a diaphragm compressor (100 MPa output pressure) and an oil driven pressure intensifier constructed for use up to 1 GPa.

High temperatures are achieved using a three-zone Kanthal-AF (0.3 mm diameter) resistance wire heating element, wound on an alumina former. This heating element is supported by fired pyrophyllite components and insulated with Triton Kaowool ceramic fibre, all contained within a stainless steel support tube (OD = 50 mm) to form a robust furnace module (Figure 3.5). Each zone of the heating element is independently powered and power limited. These power modules are controlled collectively by a CAL 9900 proportional- integral-differential (PID) controller. The temperature control signal is provided by a Pt/10% Rh (S-type) thermocouple built into the outer zone on the load cell side of the furnace. The sample temperature is monitored using three S-type sample thermocouples located next to the capsule wall within the temperature homogenizing sample holder (Figure 3.6).

The apparatus is presently configured for axially symmetric compression testing of cylindrical samples (10 mm diameter by 25 mm length), at confining pressures up to 700 MPa and sample temperatures up to ~ 1100 °C, at displacement rates equivalent to sample strain rates as low as $3 \times 10^{-8} \text{ s}^{-1}$. The main specifications of the apparatus are summarized in Table 3.1. During experiments it is possible to measure axial load (stress), displacement (strain) and hence displacement rate (strain rate), external load, sample temperature and confining pressure. The output signals, with the exception of temperature, are recorded using a multi-channel chart recorder linked to a digital data logging system.

| | Operational range of machine | Measurement resolution |
|----------------------------|-------------------------------------|-----------------------------------------------|
| Internal force | up to 70 kN | 20 N (or 254 kPa for a 10 mm diameter sample) |
| External force | up to 100 kN | |
| Displacement | up to 5 mm (~ 20 % strain) | 2 μm |
| Sample temperature | up to ~ 1100 °C | 1°C |
| Confining pressure | up to 700 MPa | 1×10^5 Pa |
| Minimum strain rate | $3 \times 10^{-8} \text{ s}^{-1}$ | |

Table 3.1. Summary of the main specifications of the 10 kbar apparatus

3.3. Sample assembly

3.3.1. Sample encapsulation

After preparation the 10 mm diameter by 25 mm length samples are welded into gold jacketing tube (10 mm ID by 32 mm length, 0.2 mm wall thickness) using preformed end-caps produced from 0.25 mm gold foil (Figure 3.7). When working with water impregnated samples (e.g. Chapter 4), welding must be carried out in such a way as to ensure that no water is lost from the sample. A semi-automated approach is adopted to ensure that the sample remains cool. The capsules are placed in an ice cooled holder ($-10\text{ }^{\circ}\text{C}$) which is mounted on a rotating manipulator. They are then welded using a Tran 200 TIG welder using a 1 mm diameter, 2% Th-tungsten electrode, with a tip ground at an angle of 60° , in a stream of argon gas ($\sim 8\text{ litres min}^{-1}$). The distance between the electrode and the capsule is preset to 0.7 mm and the sample rotated by an electrically driven manipulator. The power is then applied to the electrode manually, using a foot pedal, while carefully watching the progress of the weld. Using this approach, capsules can be welded in one rotation (~ 20 seconds) and remain cool ($< 50\text{ }^{\circ}\text{C}$) throughout. The capsules plus samples are carefully weighed before and after welding to confirm that no water is lost. The integrity of the welds is tested by placing the encapsulated samples in an oil bath at $\sim 120\text{ }^{\circ}\text{C}$ and subsequently in a cold-seal (Tuttle) bomb and pressurizing to 50 MPa with argon gas for 10 minutes. The Tuttle bomb is then rapidly depressurized, after which the capsules are removed and inspected for evidence of leakage. Using this approach only one deformation experiment out of 35 failed due to capsule failure.



Figure 3.7. Sample and capsule.

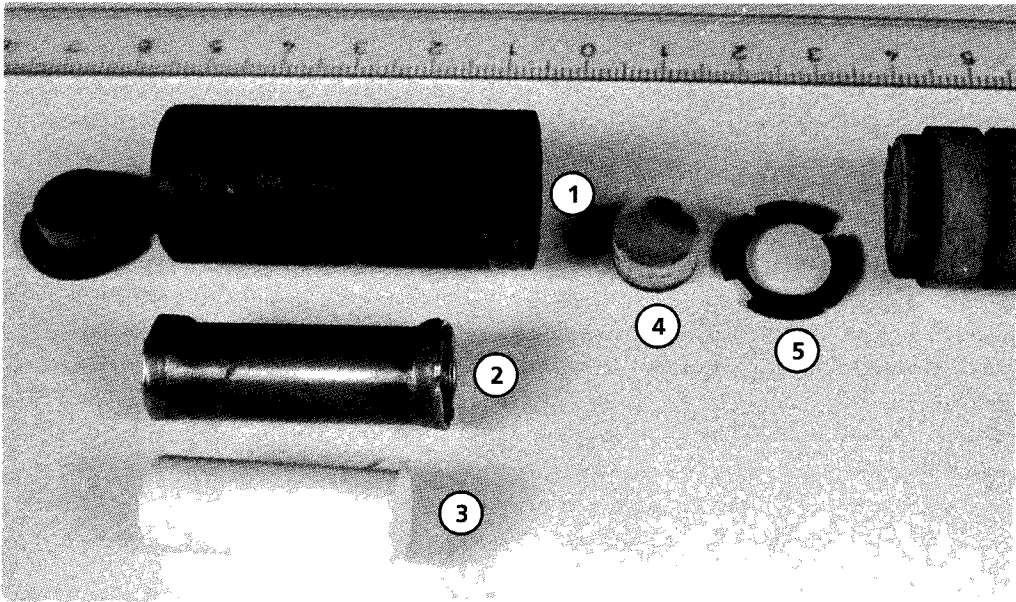


Figure 3.8a. Sample Holder.
 1. Stainless steel sample housing.
 2. Encapsulated sample.
 3. Sample.

4. Al₂O₃ anvil.
 5. stainless steel centering ring.

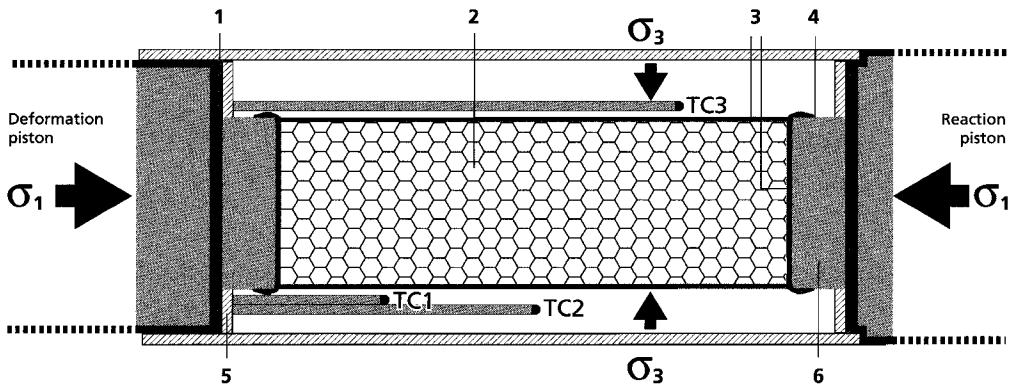


Figure 3.8b. Schematic diagram of Sample Holder.
 1. Gold decoupling foil.
 2. Sample.
 3. Gold capsule.
 4. Weld.
 5. stainless steel centering ring.

6. Al₂O₃ anvil.
 TC1, 2 and 3. Sample thermocouples.

3.3.2. Sample holder

The sample holder, which comprises a 1 mm thick stainless steel housing (18 mm OD by 41 mm length) plus stainless steel centering rings, allows the sample to be aligned and positioned centrally between the alumina sections of the deformation piston and the alumina reaction piston (Figure 3.8 a,b). Stress is transmitted from these pistons to the encapsulated sample via two Al_2O_3 anvils, 10 mm in diameter and 6 mm in length. These are centered using two stainless steel rings. A thin foil of gold (0.05 mm) is located between the anvils and the ceramic pistons and this ensures that any cracks that may be initiated in the anvils cannot propagate into the main ceramic pistons. The stainless steel sample tube acts not only to align the sample and ceramic pistons, but also to evenly distribute the heat and to cut down the effect of argon convection on the sample and on the sample thermocouples. The three sample thermocouples pass into the sample holder via slots in the alumina section of the deformation piston. These are located at $\sim 1/3$ intervals along the sample and lie in the horizontal plane during deformation. During testing, the alumina deformation piston moves into the sample holder and the thermocouples are displaced along with it (up to 2.5 mm for 10% strain). The position of the sample holder remains fixed with respect to the reaction piston during testing. When the apparatus is fully assembled, the sample holder is situated within the central zone of the furnace module.

3.4. Calibration

The following characteristics of the 10 kbar apparatus were calibrated before the experiments were carried out:

- a) the force versus output (mV) characteristics of the internal load cell;
- b) the effect of confining pressure on the internal load cell output (mV);
- c) the compliance characteristics of the loading frame and piston stack.

In addition, temperature gradients were measured using both the standard sample thermocouple arrangements and a dummy sample with embedded sample thermocouples.

3.4.1. Load cell calibration

Two approaches were taken to calibrate the internal load cell. These involved the deformation of brass test pieces with known yield points, and comparison of the output signals from the internal load cell with the external Instron 100 kN load cell. These calibrations were done at room temperature at both atmospheric pressure and a confining pressure of 600 MPa. These two independent approaches were employed because of uncertainties with regard to the effect of pressure on the yield point of brass, and regarding the assumption of constant seal friction during calibration (i.e. constant friction in a *specific* test at a constant displacement rate). The brass test pieces were tested independently in a second Instron 1362 materials testing machine both before and after the calibration tests, in order to accurately bracket the yield points used for the calibration. In comparing the output signals of the internal load cell and the Instron 100 kN load cell for calibrations at 600 MPa, the output signals (mV) were plotted against each other and the plot was found to be very closely linear, indicating that the

dynamic seal friction remained more or less constant throughout individual calibration runs. Both calibration approaches were in good agreement and gave a value of 10.26 mV kN^{-1} at the 600 MPa confining pressure used in all deformation experiments. The effect of confining pressure on the calibration value was of the order of a few % in the range 0 to 600 MPa. Trial deformation experiments performed on Carrara marble at temperatures between 800 and 1000 °C produced steady state flow stresses which agree closely with previous data (Schmid et al., 1980), confirming the reliability of force measurement.

3.4.2. Load cell pressure correction calibration

The internal load cell has a significant sensitivity to the confining pressure in the vessel, in effect working as a pressure transducer. This effect needs to be corrected for, as the confining pressure does not, in general, remain constant throughout long tests (~ 24 hours). This results from minor leaks which can typically lead to a ~ 20 MPa drop in pressure during the test. This effect has been accurately corrected for using the known pressure response of the internal load cell based on calibrations at zero axial load. These were carried out by pressurizing the vessel (to ~ 620 MPa) at room temperature, and allowing gas to escape slowly from the apparatus (to ~ 580 MPa over 12 to 24 hrs), while logging the pressure transducer and internal load cell outputs. The results from such tests show that the behaviour of the load cell output with respect to confining pressure is highly linear and reproducible (also over much larger pressure intervals). The correction factor for the pressure effect in the range 620 to 580 MPa was found to be $0.1489 \text{ kN MPa}^{-1}$.

3.4.3. Compliance calibration

The compliance calibration needed to correct the external displacement measurements for apparatus distortion was carried out using a tool steel dummy sample of known elastic modulus, and was done at 600 MPa pressure and room temperature. At low loads ($< 3.2 \text{ kN}$), the curve was somewhat non-linear, probably due to minor misalignment of the various elements of the loading stack. However, at higher loads the behaviour was found to be closely linear. Therefore, the following 2-stage correction has been applied to the measured displacements:

$$\text{at loads } < 3.22 \text{ kN} \quad D = D_m - 0.0423 \times L$$

$$\text{at loads } \geq 3.22 \text{ kN} \quad D = D_m - ((0.01875 \times L) + 0.07592)$$

where D_m is the measured displacement (mm), L is the axial load (kN) and D is the corrected displacement (mm). No attempt was made to incorporate temperature effects into the compliance corrections since the hot length of the alumina pistons is too short ($\sim 8 \text{ cm}$) to exert a significant influence.

3.4.4. Temperature measurement and thermal gradient minimization

Sample temperature gradients produced by gas convection have been reduced by a) ensuring that the volume and connectivity of gas in the hot zones is reduced using a compartmentalized construction, consisting of furnace support tube, furnace winding tube, steel sample holder, close fitting ceramic pistons and a pyrophyllite furnace-closure, and b) limiting the power supplied to each of the three furnace zones. An exhaustive series of tests, including the use of dummy ceramic samples in which

sample thermocouples were embedded, has shown that temperature gradients in the gas contained within the sample holder are $< 15^{\circ}\text{C}$ in the temperature range 800 to 1000 $^{\circ}\text{C}$. Moreover, the real sample temperature gradients were found to be $< 2^{\circ}\text{C}$ at these temperatures. The tests have also shown that the centre sample thermocouple, which lies close to the capsule wall, provides a measurement of the sample temperature to within $\pm 3^{\circ}\text{C}$. For this reason, and in the interest of consistency, the temperatures quoted for the experiments described in this thesis are based on the centre thermocouple temperature. During experimental runs, the two additional thermocouples provide a check that temperature gradients within the gas adjacent to the sample lie within the bounds described.

3.5. Data acquisition and processing

The 10 kbar apparatus produces DC output signals from the internal load cell, external load cell, Instron displacement transducer (LVDT), confining pressure transducer, 3 sample thermocouple outputs and 1 primary control furnace thermocouple output. The conditioned raw signals, with the exception of the temperature signals, are recorded as a function of time using a chart recorder, the pen positions of which are logged (typically every 60 s) by an IBMTM personal computer via a 16 bit A/D converter. The logging is managed using the program DASHPT (written in Microsoft BASIC by Colin Peach, Bas den Brok and Rolf Brzesowsky). The thermocouple signals are handled separately. After cold junction compensation and amplification these are digitized using a multiplexed 16 bit A/D converter based data acquisition module. The A/D converter is interrogated by a temperature logging and display program (TD.exe written by the author in Borland Pascal V5). This program reads each temperature signal in turn and converts the output signals to temperatures ($^{\circ}\text{C}$) before logging and real time display. Temperature conversion is carried out using one of five polynomial fits to the standard S-type thermocouple output tables (BS 4937; IPTS 1968). These fits, for specific temperature intervals, reproduce the thermocouple output table exactly for all temperatures. Furthermore, the program has the facility to mark the data files, allowing synchronization with the mechanical data logging program.

The mechanical data are processed using a data processing program (DP.exe written by the author in Borland Turbo C++ V3.0) running under Microsoft MS-DOSTM. This program carries out the compliance and load cell pressure corrections for all data and the calculation of stress/strain/strain rate data based on the assumption of constant volume. In order to carry out the load cell pressure correction, the program requires the unloaded load cell output immediately before deformation, i.e. at the experimental pressure and temperature conditions.

Flow behaviour of fine-grained synthetic dunite in the presence of 0.5 wt% H₂O

4.1. Introduction

Understanding upper mantle rheology is of key importance to modelling numerous geodynamic processes. The major mineral constituents of the upper mantle are olivine, orthopyroxene and clinopyroxene with an additional aluminous phase (plagioclase, spinel or garnet; Ringwood, 1975), and the dynamics of the Earth's lithospheric and asthenospheric mantle are widely believed to be controlled by the rheological properties of the most abundant and probably weakest mineral constituent - olivine (≈ 50 vol. %). As a result, many experimental investigations have been performed, since the late 1960s, on high-temperature creep behaviour of olivine and olivine-rich rocks. Deformation mechanisms thus believed to operate under mantle conditions, and their bearing on the rheological behaviour of mantle materials, are discussed in the papers by Gordon (1965), Stocker and Ashby (1973), Raleigh and Kirby (1970), Kirby and Raleigh (1973), Twiss (1976), Ashby and Verrall (1977), Karato (1989a), and Karato and Wu (1993).

Experimental work aimed at establishing the rheological properties of olivine has followed two directions: the deformation of single crystals and of polycrystalline aggregates. In broad terms, two main types of behaviour have been reported, namely grain size *insensitive* (GSI) dislocation creep (e.g. Chopra and Paterson, 1981, 1984; Karato et al., 1986) and grain size *sensitive* (GSS) diffusion creep (e.g. Karato et al., 1986; Wolfenstine and Kohlstedt, 1994), with water having significant weakening effects in both cases (e.g. Karato et al., 1986). Diffusion creep involving an intergranular melt phase may also occur (e.g. Cooper and Kohlstedt, 1986). Data obtained from the principal studies are summarized in Tables 4.1 and 4.2. In all cases, the mechanical data obtained have been fitted to a Dorn type power law steady state creep equation of the form:

$$\dot{\epsilon} = A \cdot \exp(-Q_c / RT) \cdot \sigma^n / d^p \quad 4.1$$

where: $\dot{\epsilon}$ represents the strain rate (s^{-1}), σ is the differential stress ($\sigma_1 - \sigma_3$; MPa), A is a pre-exponential constant ($MPa^{-n} s^{-1} \mu m^p$), Q_c is an apparent activation energy ($J mol^{-1}$), R is the gas constant ($J mol^{-1} K^{-1}$), T is the absolute temperature (K), n is the stress exponent or stress sensitivity, d is grain size (μm), p is the grain size exponent with $p = 0$ for GSI mechanisms. Deformation studies on sin-

gle crystals have allowed detailed investigation of crystal plasticity and the influence of chemical environment (oxygen fugacity - fO_2 , oxide activity and H_2O content) on dislocation creep mechanisms (Raleigh, 1968; Young, 1969; Phakey et al., 1972; Kohlstedt and Goetze, 1974; Durham and Goetze, 1977 a,b; Durham et al., 1977, 1979; Jaoul et al., 1980; Darot and Gueguen, 1981; Kohlstedt and Hornack, 1981; Kohlstedt and Ricoult, 1984; Poumellec and Jaoul, 1984; Ricoult and Kohlstedt, 1985; Mackwell et al., 1985; Bai et al., 1991; Bai and Kohlstedt, 1992 a,b).

| Author | System | Wet/ Dry | T range / Confining P_c | $\log_{10}A$ | n | Q (kJ mol ⁻¹) | Comments |
|----------------------------------------------------|--------------------------------------------------------------------------|-------------|---------------------------------|--------------|-----|------------------------------|------------------------------------------------|
| Carter and Ave'Lallemant 1970, revised Carter 1975 | Mt Burnett Dunite. | Dry | 300 - 1450 °C 500 - 3000 MPa | 3.1 | 3.3 | 465 | Solid media apparatus. |
| Post 1977 | Mt Burnett Dunite. | Wet | 700 - 1300 °C 500 - 1500 MPa | -2.5 | 5.1 | 392 | Solid media apparatus. |
| Chopra and Paterson 1981 | Anita bay. | Wet | 1000 - 1300 °C | 4.0 | 3.4 | 444 | Gas apparatus. |
| | Aheim. | Wet | 300 MPa | 2.6 | 4.5 | 498 | |
| Chopra and Paterson 1984 | Anita bay and Aheim Dunites. | Dry | 1200 - 1400 °C 300 MPa | 4.5 | 3.6 | 535 | Gas apparatus. |
| Karato, Paterson and FitzGerald 1986 | Synthetic aggregates - San Carlos Olivine. | Dry | 1300 °C 300 MPa | 5.4 | 3.5 | (540) | Gas apparatus. Activation energies estimated. |
| | | Wet | | 3.3 | 3.0 | (420) | |
| Borch and Green 1989 | Balsam Gap Dunite + 3% orthopyroxene. | Dry | 977 - 1427 °C 700 - 2200 MPa | 3.5 | 3.3 | 500 | Griggs rig - molten salt cell. |
| Chopra 1986 | San Carlos. | Wet | 1100 °C 300 MPa | 3.3 | | | Gas apparatus. |
| Beeman and Kohlstedt (1993) | San Carlos olivine plus melt. Fe-bearing olivine from sol-gel synthesis. | Dry | 1100 & 1200 °C 300 MPa | 4 | | | Gas apparatus. |
| | | Dry | | 4 | | | |
| Hirth and Kohlstedt (1995 a,b) | San Carlos or Balsam Gap Dunite + Bamle enstatite ± melt. | Dry | 1200 - 1300 °C 300 MPa | ~3.1 | | 575 | Gas apparatus. |
| Hirth and Kohlstedt (1996) | Anita Bay and Aheim Dunites. | Wet | | 6.69 | 3.5 | 515 | Reanalysis of Chopra and Paterson (1981,1984). |
| | | Dry | | 4.69 | 3.5 | 535 | |

Table 4.1. Typical data for GSI dislocation creep in polycrystalline olivine from both natural rocks and synthetic aggregates. Note that the stress exponents (n) fall in the range ~ 3 to 5 and the experimentally determined values for activation energy for wet dislocation creep fall within the range 453 ± 61 kJ mol⁻¹ with a mean of 462 kJ mol⁻¹.

Many workers have also observed GSI dislocation creep behaviour and associated water weakening effects in deformation experiments carried out on olivine-rich polycrystalline aggregates. In the earlier studies, natural rocks, mainly dunites, were used (Carter and Avé Lallemant, 1970; Raleigh and Kirby, 1970; Blacic, 1972; Kirby and Raleigh, 1973; Post, 1977; Goetze, 1978; Goetze and Evans, 1979; Evans and Goetze, 1979; Ross et al., 1979; Chopra and Paterson, 1981, 1984). However, more recently, studies have been carried out on aggregates made from either natural mineral separates (e.g. Zeuch and Green, 1979, 1984a,b; Chopra, 1986; Karato et al., 1986; Hitchings et al., 1989; Borch and Green, 1989; Hirth and Kohlstedt 1995a,b) or synthetic minerals (e.g. Relandeau, 1981; Beeman and Kohlstedt, 1993), allowing greater control of bulk chemistry, grain size, second phase and melt content. Reliable data on the rheology of olivine polycrystals deforming by dislocation creep are relatively scarce due to a variety of experimental difficulties, including problems with the resolution of stress measurement from experiments carried out in solid medium apparatus (see Borch and Green, 1989), problems controlling water content, uncertainties regarding the presence and influence of grain boundary melt films and poor control of oxygen fugacity. Typical, well constrained data for dislocation creep of polycrystals are shown in Table 4.1. The data chosen generally come from more recent studies which have been carried out using gas or molten salt confining media. Dislocation creep of dry and wet olivine polycrystals is characterized by stress exponents (n) in the range 3 to 5 and activation energies of ~ 536 and ~ 462 kJ mol⁻¹, respectively (mean values from the data shown in Table 4.1). A marked water weakening in the dislocation creep regime has been observed by several workers (Chopra and Paterson, 1981, 1984; Karato et al., 1986) with the dry samples being stronger by a factor ranging between ~ 2.5 (Karato et al, 1986) to ~ 6.5 times (Hirth and Kohlstedt, 1996) at constant strain rate.

Grain size sensitive (GSS) diffusion creep behaviour has been identified in a number of experimental investigations of creep in fine-grained polycrystalline olivine aggregates (Schwenn and Goetze, 1978; Relandeau, 1981; Karato et al., 1986; Chopra, 1986, Wolfenstine and Kohlstedt, 1994; Hirth and Kohlstedt 1995a), and typical data are shown in Table 4.2. However, the data are limited in terms of the range of variables investigated. This fact becomes very clear when one compares the detailed conditions of each study, i.e. whether the experiments were wet or dry, with or without melt, specifics of bulk chemistry and second phase content. For wet systems which are assumed to be largely melt free (Chopra 1986; Karato et al. 1986; Rutter and Brodie 1988), the stress exponent (n) falls between 1 and 2. Experimentally determined values of the apparent activation energy for wet, melt-free diffusion creep are poorly constrained with the two values of 190 and 240 kJ mol⁻¹ having been determined by Chopra (1986) and 240 ± 40 kJ mol⁻¹ by Rutter and Brodie (1988). Karato et al. (1986) estimate the activation energy for wet diffusion creep to be 250 kJ mol⁻¹ arbitrarily taking a value 2/3 of the activation energy for volume diffusion of O and Si in olivine (Jaoul et al., 1980, 1981; Karato and Ogawa, 1982) assuming grain boundary diffusion control. Karato et al. (1986) state that in the finer grained materials deforming in the GSS regime the wet samples are 10 to 20 times weaker than the dry samples at constant strain rate.

| Author | System | Wet/ Dry | Grain Size (μm) | T range / Confining P_c | A | n | p | Q (kJ mol ⁻¹) | Comments |
|---------------------------------------------------|-----------------------------------------------------------------------------------------|----------------|------------------------------------|-----------------------------------------|----------------------------------------------------------------------------------------------------------------------------------------------------------------------------|------------------|-------------|------------------------------|------------------------------------------------------------------------------------------------------------------------------------------------------------------------------------------------|
| Schwenn and Goetze (1978) | San Carlos olivine (Fo92) powders. | Wet? | 5 - 2000 | 1000 - 1600 °C 0.1 MPa | | 3.4 1.5 | | 355 ± 127 | Hot pressing densifi- cation experiments. Two fields of beha- viour: GSI and GSS. |
| Relandeau (1981) | Synthetic forsterite aggregates. | Dry | 60, 98 & 132 | 1450 - 1500 °C 0.1 MPa 1600 °C | | 2.5 ~1.0 | 1.5± 0.5 | 418 ---- | Transition to diffusion creep at 1600 °C |
| Cooper and Kohlstedt (1984a) | Balsam Gap Dunite - Fo _{92.4} olivine aggregates. | Dry | 3 to 13 | 1300 - 1400 °C | | 1.1 ± 0.3 | 3 | 380 ± 105 | Densification of fine grained (3-13 μm) powders |
| Chopra (1986) | San Carlos olivine aggregates. | Wet | ~10 | 1200 & 1300 °C 300 MPa | | 1.5 | | 190 & 240 | |
| Karato Paterson and FitzGerald (1986) | San Carlos olivine aggregates. | Dry Wet | 7 to 30 | 1300 °C 300 MPa | 7.7 x 10 ⁻² (MPa ⁻ⁿ s ⁻¹ mm ^p) 1.5 x 10 ⁻³ (MPa ⁻ⁿ s ⁻¹ mm ^p) | 1.4 ± 0.3 | 2 to 3 | (290) (250) | Pre-exponential coef- ficients determined assuming n=1 and p=2 for dry behaviour and p=3 for wet behaviour. Activation energies based on estimates. |
| Rutter and Brodie (1988) | Serpentine. | Wet | 0.1 | 300 - 600 °C 300 MPa | 10 ^{5.62} (MPa ⁻ⁿ s ⁻¹ μm^p) | 1.0 | | 240 ± 40 | Fined grained formed by dehydration controls deformation |
| Wolfenstine and Kohlstedt (1994) | Ni ₂ SiO ₄ + 3 vol% amorphous SiO ₂ . | Dry | 9 to 30 | 1300 - 1540 °C | 4.0 x 10 ⁸ (MPa ⁻ⁿ s ⁻¹ μm^p) | 1.1 | 2.7 | 410 | Coble creep. |
| Hirth and Kohlstedt (1995b) | San Carlos oli- vine + 3-5 wt% Bamle enstatite (~En ₉₀) melt free. | Dry | ~10 | 1200 - 1300 °C | | 1.0 ± 0.1 | 3 | 315 ± 35 | Activation energy determined constraining n=1 and p=3 |
| Daines and Kohlstedt (1996) | San Carlos oli- vine plus Bamble enstatite. mixtures with 5, 50 and 95 wt%. | Dry | <15 | 1150 - 1255 °C 300 MPa | | ~1.2 ~2.5 | | | Two regimes identified at lower stresses < 100 MPa n ~ 1.2 while at higher stresses n ~ 2.5. No significant change in strength with opx content in the low stress regime. |

Table 4.2. Typical data for fine-grained polycrystalline olivine powders and aggregates where diffusion creep has been inferred. Note that several studies report a transition in behaviour from dislocation creep to diffusion creep, diffusion creep being dominant at lower stresses for a given temperature. Stress exponents (n) fall in the range ~ 1 to 2 and activation energies are in general lower than for dislocation creep.

The above creep data have been widely used in recent years to model flow in the lithospheric and asthenospheric upper mantle, focusing on extension (Bassi and Bonnin, 1988; Braun and Beaumont, 1989; Govers and Wortel, 1993; Cloetingh et al., 1995), assuming this to be a relatively homogeneous, distributed phenomenon (McKenzie, 1978). Most modelling work follows Brace & Kohlstedt (1980) and Sawyer (1985) in assuming that the rheology of the upper mantle is controlled by a frictional sliding law in the brittle/frictional region and by either a wet or dry dislocation creep law for olivine in the ductile region (e.g. Lynch & Morgan, 1987; Bassi & Bonnin, 1988; Braun & Beaumont, 1989; Dunbar & Sawyer, 1989; Bassi, 1995; Cloetingh et al., 1995). These rheologies predict a strength profile with a maximum in the upper 10 to 20 km of the continental lithospheric mantle, and this thin, mechanically strong layer plays a major role in controlling the modelled dynamics.

In contrast to the assumptions of the above-mentioned modelling studies, however, there is growing evidence to suggest that flow in the lithospheric upper mantle may be localized into shear zones, notably in regions of continental extension and/or rifting. For example, seismic evidence (Goleby et al., 1988; Flack et al., 1990; Reston, 1990, 1993; Meier and Eisbacher, 1991; Keen et al., 1991) has shown that major crustal shear zones developed in extensional settings may in some cases extend well into or through the lithospheric upper mantle in the form of asymmetric detachment zones (Wernicke, 1985; Lister et al., 1986, 1991). Moreover, structural geological studies of shear zones found within mantle peridotites occurring in the Voltri Massif (N.W. Italy; Drury et al., 1990, 1991; Hoogerduijn-Strating, 1991), and believed to be associated with Jurassic rifting to form the Piemonte-Ligurian ocean, show that the shear zones are dominated by fine-grained hydrated peridotite (olivine/amphibole/pyroxene) mylonite zones (≤ 200 m wide). The associated mineral assemblages and thermobarometry suggest formation in the top 10 to 20 km of the lithospheric upper mantle, during the rifting phase. These shear zones thus provide evidence that extensional deformation of the lithosphere was - and may more generally be - accommodated by localization of deformation into hydrated mylonitic shear zones. It follows, therefore, that the deformation behaviour of fine-grained peridotite mylonite under hydrous conditions may have important consequences for the strength and dynamics of continental lithosphere undergoing extension/rifting (Vissers et al., 1995). Notably, the microstructure of mylonites from the Voltri (Erro-Tobio) peridotites show many of the characteristics of GSS flow (i.e. diffusional or superplastic mechanisms rather than dislocation creep) including fine grain size (1 to 10 μm), equiaxed grain shape and low dislocation densities (Visser et al., 1995; cf. Boullier and Gueguen, 1975).

Focusing on this last point, Vissers et al. (1995) have conjectured that shear localization during extension/rifting of the lithospheric upper mantle may lead to extreme weakness of the lithosphere, since GSS flow in wet, fine grained olivine comparable to Voltri mylonitic material is expected to proceed at very low stresses. To underpin this argument, Vissers et al. (1995) applied the wet, diffusion creep equation of Karato et al. (1986) to calculate flow stresses within mylonitic shear zones in the top 10 to 20 km of the upper mantle under hydrated conditions corresponding to lithospheric extension. The results obtained by Vissers et al. (1995) indeed showed dramatic weakening of the lithospheric upper mantle through the action of the shear zones. However, their findings are strongly dependent upon the accuracy and validity of extrapolation of the flow law of Karato et al. (1986) from the experimental conditions ($T = 1300$ °C, strain rates in the range 10^{-4} to 10^{-6} s⁻¹) to those of

the upper mantle in an extensional setting ($T = 800$ to 950 °C, strain rates in the range 10^{-13} to 10^{-14}). Notably, as already mentioned, Karato et al. (1986) did not experimentally determine the apparent activation energy for creep (Q_c), drawing the validity of the extrapolation into question. However, use of the wet diffusion creep law of Karato et al. (1986), with an assumed $Q_c = 250$ kJ mol⁻¹ appropriate for grain boundary diffusion control, is supported by the studies of Chopra (1986) and Rutter and Brodie (1988) who report similar values for Q_c .

In spite of the fact that several additional studies have investigated the flow behaviour of fine-grained olivine polycrystals (Beeman and Kohlstedt, 1993; Hirth and Kohlstedt, 1995a), available data appropriate for extrapolation to mylonitic shear zones in the upper mantle are still rather limited. Even the most recent experiments have been carried out at high temperatures (1100 – 1300 °C) and generally the temperature range explored is too narrow for accurate determination of activation energy and reliable extrapolation to shear zone temperatures of 800 – 950 °C. Moreover, at the high temperatures used in such experiments, the presence of melt films and the operation of associated diffusion creep mechanisms cannot be excluded, particularly in wet samples, and may have important effects on flow behaviour. Furthermore, Karato et al. (1986) showed that grain growth can be a serious problem when working at high temperatures with fine-grained materials, though they took this carefully into account by using a grain growth law to interpolate between the initial and final grain sizes (see Karato, 1989b). Further problems with previous wet experiments include the control of the water content and initial porosity in tests carried out using wet hot isostatically pressed (HIPed) powders, from which water is expelled during densification (Karato et al., 1986).

In view of the shortcomings in available data indicated above, and particularly focusing on the question of the peridotite mylonite zones raised by Vissers et al. (1995), there is a clear need to determine the deformation behaviour of fine-grained peridotite at low temperatures (800 to 950 °C) with controlled water content and microstructure, in the absence of melt. The present Chapter aims to help provide the data needed. It consists of a systematic study of the temperature and stress dependence of creep in fine-grained synthetic peridotite. A set of combined strain rate and temperature stepping/cycling tests have been carried out on well-characterized, pre-HIPed starting materials with fixed known water content and stable microstructure. The tests were carried out at strain rates in the range 2×10^{-7} to 5×10^{-5} s⁻¹, temperatures between 1123 and 1275 K (850 to 1002 °C), and using gas confining pressures between 585 and 624 MPa. The starting materials are forsterite (Mg₂SiO₄) – enstatite (2.5 vol%, MgSiO₃) ceramics with a controlled water content (0.47 ± 0.02 wt%) and grain size of 1.2 μm. The choice of this high purity, Fe-free refractory system as an analogue for mantle material significantly reduces the complications of oxygen fugacity control in iron-bearing systems, simplifying both material synthesis and experimental procedures, and reducing the likelihood of partial melting. A single dry control experiment is included to illustrate the extent of water-weakening in the material studied.

4.2. Experimental method

4.2.1. Sample preparation

All samples used in the six experiments described here (5 wet and 1 dry) were subjected to a stage of hot isostatic pressing (HIPing) before deformation testing. The starting samples consisted of right cylinders (10 mm diameter by 25 mm in length) cored from sintered billets of forsterite + 2.5 vol.% enstatite ceramic, synthesized using the sol-gel processing based fabrication method described in Chapter 2. This involved the synthesis of a diphasic gel using high purity 50 nm MgO powder and tetraethyl orthosilicate. This was subsequently dried, reaction sintered (875 °C for 2 hrs), cold isostatically pressed (100 MPa) with 2.5 wt% organic binder, sintered (at ~ 1400 °C) and machined to the final dimensions to produce the samples for deformation. The starting ceramic samples had a mean grain size of $1.2 \pm 0.07 \mu\text{m}$ and a porosity of $8.6 \pm 0.4 \%$ (see Table 4.3). Porosities were determined by the Archimedes method (see Chapter 2) and by comparison of the theoretical density with the densities calculated from the sample dimensions and the dry weight (values in brackets in Table 4.3). Note that porosities determined from the sample dimensions were systematically ~ 0.3 % higher than those obtained by the Archimedes method. This probably resulted from the consistent over-estimation of sample volume based on calliper measurements as the cylinders are slightly ridged from coring.

| Experiment/ sample | Gel Batch | vol% enstatite | Sintering temperature (K) and duration (mins) | initial porosity (%) | wt H ₂ O (g) | wt% H ₂ O | mean ECD (μm) |
|-----------------------|--------------|-------------------|--------------------------------------------------------|----------------------------|-------------------------------|-------------------------|----------------------------------|
| Fo17 | stm 26 | 2.0 | 1723 : 120 | 6.8 (7.2) | DRY | ---- | 1.50 |
| Fo21 | stm 30.31.32 | 2.5 | 1673 : 60 | 8.4 (8.6) | 0.0262 | 0.46 | 1.32 |
| Fo22 | stm 30.31.32 | 2.5 | 1673 : 60 | 9.1 (9.4) | 0.0278 | 0.49 | 1.22 |
| Fo23 | stm 30.31.32 | 2.5 | 1673 : 60 | 8.6 (8.9) | 0.0256 | 0.45 | 1.17 |
| Fo24 | stm 30.31.32 | 2.5 | 1673 : 60 | 8.2 (8.7) | 0.0271 | 0.47 | 1.17 |
| Fo25 | stm 30.31.32 | 2.5 | 1673 : 60 | 9.1 (9.4) | 0.0254 | 0.45 | 1.24 |

Table 4.3. Starting sample characteristics including sintering conditions, initial porosities, enstatite content, wt% water added and the mean equivalent circular diameter (ECD) grain size. Two porosities are indicated for each sample. The first value has been determined by the Archimedes method (error $\pm 0.6 \%$ porosity), the second value has been determined by comparison of the sample bulk density with its theoretical density (3.21 g cm^{-3}). All the samples, with the exception of the dry run fo17, have been batch processed throughout and are, therefore, identical as far as possible. The volume percentage enstatite for the two batches has been estimated from the gel starting compositions and checked using X-ray microanalysis of ~ 200 grains using the CM200 TEM.

In preparation for experimentation, the machined ceramic cylinders were cleaned thoroughly using distilled water and placed in an oven at 200 °C for 24 hours to ensure that they were dry. Drying for longer than 24 hours was found to produce no further weight loss and it was therefore assumed (given the low drying temperature) that this treatment was sufficient to dry the samples to water contents below the resolution of the balance used (~ 0.002 wt%). Subsequently, water was introduced into each of the five wet-tested samples by submerging it in a beaker of distilled water under vacuum for ~ 10 minutes. The vacuum was then vented to air and the sample left in the water for up to one hour to allow the water to penetrate into the pores. It was then carefully dried at ~ 95 °C

until the desired final weight, corresponding nominally to ~ 0.5 wt% water content, was achieved (see Table 4.3).

The samples were subsequently carefully welded into gold capsules pre-sealed at one end. Loss of water from the wet samples was avoided during welding of the open end by placing the sample in an ice-cooled block and welding the capsules rapidly (see Chapter 3 for details). The final capsule configuration is shown in Figure 4.1. The integrity of the welds was tested as follows. First, the capsules were placed in a silicone oil bath at 120 °C to check for escaping vapour. They were then placed in a cold-seal pressure vessel, and subjected to 50 MPa argon gas pressure at room temperature for ten minutes and subsequently rapidly depressurized. If the capsule has a leak it will inflate due to trapped argon.

4.2.2. Deformation apparatus

The samples were first HIPed and then deformed, in axially symmetric compression mode at controlled imposed displacement rates, using the gas-medium, constant volume deformation apparatus described in detail in Chapter 3. The central element of this apparatus is a horizontally mounted, internally heated, 1 GPa pressure vessel. Force is applied to the sample using an Instron 1362 Testing Machine to load a dynamically sealed *deformation piston* assembly which enters the vessel through one of the end sealing heads. Constant volume of the pressure vessel is achieved by a compensation piston which is coupled to the deformation piston via a conventional external yoke. Piston/yoke displacement is measured externally using the instron ram linear variable differential transformer (LVDT) displacement transducer. The force on the sample is measured using an internal force gauge (100 kN full scale with a ~ 20 N resolution; see Chapter 3).

External force is measured using an Instron 100 kN load cell (accurate to 0.1% of the cell-rated output or 0.5% of the indicated load, whichever is the greater). Pressure was measured using a strain

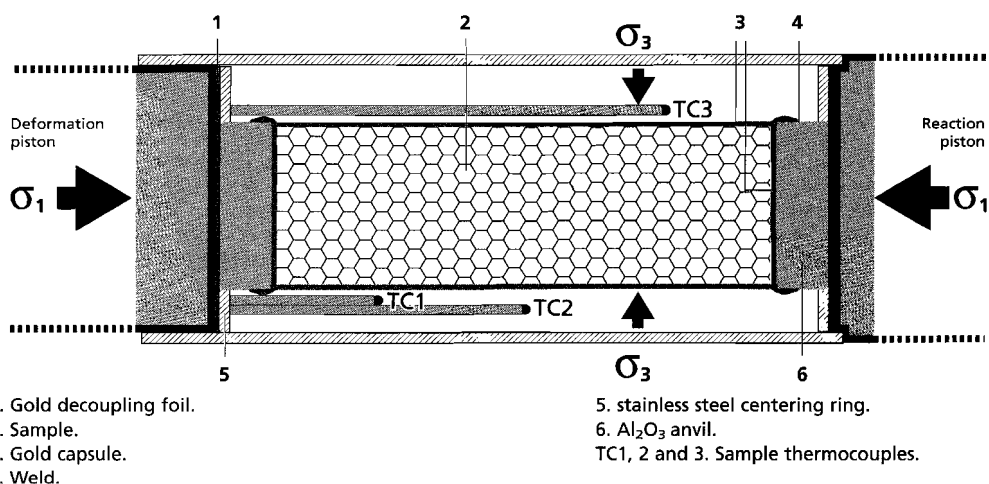


Figure 4.1. Schematic diagram of the sample configuration. Note the positions of the three sample thermocouples (TC) and the fact that the gold capsule ends pass between the piston anvils and the sample.

gauge type pressure transducer (with a 10⁵ Pa resolution). High temperatures are achieved using a three-zone Kanthal-AF wire furnace. This is controlled by a proportional-integral-differential (PID) controller using an S-type (Pt/10% Rh) primary control thermocouple adjacent to the furnace windings in the near-load cell zone. The sample temperature is monitored by 3 S-type sample thermocouples located next to the capsule wall. The maximum temperature gradient measured in the gas adjacent to the sample is ~15 °C and remains almost constant throughout the test. However, calibration runs have shown that the gradients within the sample are much less, being in the order of 1 to 2 °C, and that the sample temperature can be assumed to equal that given by the centre thermocouple.

4.2.3. Hot isostatic pressing (HIPing) stage

In the present experiments, once the sample had been loaded into the apparatus the vessel was flushed with argon and then pressurized at room temperature to ~ 600 MPa with argon gas. The vessel was then left for several hours to check for leakage and the (external) water cooling system was turned on to ensure that the pressure vessel remained cool during subsequent heating. The samples were then brought to a temperature of 1223 K by applying power to the furnace. During heating, gas was bled from the vessel to ensure that the pressure remained at ~ 600 MPa. The entire heating step took approximately 15 minutes before stable conditions were achieved.

As soon as both pressure and temperature were found to be stable, the deformation piston was carefully moved in until a touch was indicated from the internal force gauge, corresponding to the application of a small force (~ 200 N) to the sample. This initial touch position was carefully noted and the sample was then left to hot-isostatically press (HIP) for typically 24 hours. After HIPing, a new touch point was found and the measured displacement used to estimate the amount of compaction undergone by the sample as well as its new porosity. These were calculated from the length change measured during HIPing assuming isotropic strain. Axial load was then removed from the sample by withdrawing the Instron loading ram and jacking the yoke such that the deformation piston was pulled back through the dynamic seal friction so that the sample was fully unloaded. The base load cell output signal, corresponding to zero load at a known confining pressure close to 600 MPa, was then determined.

4.2.4. Deformation testing and termination procedure

In order to deform each sample, the Instron testing machine was used in position-control to run the deformation piston into the sample at a constant displacement rate. Experiments were performed using both displacement rate and temperature stepping methods at strain rates between 2×10^{-7} and $5 \times 10^{-5} \text{ s}^{-1}$, and temperatures between 1123 and 1273 K. Displacement rate (and hence strain rate) stepping was achieved simply by programming a new rate into the Instron ramp function generator (which provides the control signal for the Instron position servocontrol system) in a stepwise manner, allowing typically 1–2 % strain per step. Temperature stepping was achieved by halting deformation and completely unloading the sample prior to changing the temperature. When the new temperature was found to be stable and the pressure had been readjusted to ~ 600 MPa, the test was resumed with a new touch point and new base load cell output. This unloading on temperature step-

ping was necessary to avoid loading/unloading effects due to thermal expansion and contraction, and to remove transient effects of pressure and temperature fluctuations on the load cell output.

After the desired amount of strain was achieved ($\sim 10\%$ for the wet samples), the test was stopped as follows. The deformation piston was halted and the Instron ram slowly returned to its initial position. This unloads the sample until the piston is held by the seal friction. The deformation piston was then jacked back to unload the sample completely, and the final (unloaded) load cell output signal was checked while still at pressure and temperature. The furnace was then switched off, which results in rapid cooling of the sample and a simultaneous pressure drop. The sample reaches room temperature within ~ 10 minutes with a confining pressure of ~ 400 MPa remaining at this temperature. The gas was then released slowly from the vessel, reaching room pressure within ~ 30 minutes. The seals were subsequently allowed to relax for ~ 12 hours before the vessel was opened and the deformed sample removed. The encapsulated samples were reweighed before opening to check that no water was lost. Lastly, the capsules were opened and the final dimensions of the samples measured and their porosities determined using the Archimedes method.

4.2.5. Data acquisition and processing

Output signals from the internal force gauge, gas pressure transducer, Instron ram position/displacement transducer, external Instron force gauge and the three sample and one primary control thermocouples (S-type) undergo conditioning and amplification (see Chapter 3) before analogue to digital conversion and display/logging using two IBMTM-compatible personal computers (one handling temperature signals and one for all other channels). In calculating the differential stress applied to the sample, the internal force gauge readings were corrected for calibrated pressure effects on the load cell output. No correction was made for jacket strength, but data for gold show that this is negligible. The measured displacement data were accurately corrected for apparatus stiffness in order to calculate the sample strain (see Chapter 3 for details). Sample temperatures within a given HIPing, strain rate or temperature step were calculated as the average (settled) value for the step as measured by the central thermocouple (TC2 in Figure 4.1). From the estimated post-HIPing porosities and the measured final (post-deformation) porosities (Table 4.4) it is clear that a post-HIPing densification of ~ 1 vol% takes place during deformation. This compaction has been neglected when calculating the stress on the sample, i.e. constant volume was assumed.

Consider now the contribution to measured strain of the thin gold sheets (capsule end-walls) separating the sample from the piston anvils. Taken together, the gold capsule end-walls have an initial thickness of 2×0.25 mm (see Figure 4.1). During the test these become deformed. However, flow of the gold is strongly restricted by the piston anvils. Trial experiments, performed using rigid ceramic test pieces, have shown that significant deformation of the gold typically requires axial stresses in excess of 50 to 60 MPa under the conditions of the experiments reported here. Moreover, measurement of the final gold thickness after individual tests reaching stresses up to 100 MPa has shown that gold deformation then contributes a maximum of 0.1 mm to the measured displacement, which is equivalent to 0.4% strain. Since the stresses achieved in the wet tests reported here mostly fall below 50 to 60 MPa, no attempt has been made to correct for this gold deformation in calculating the stress strain curves for wet samples. Strain rate or temperature steps reaching higher stresses may be affect-

ed, thus showing strains up to 0.4% greater than actually achieved in the sample. On the other hand, in cases where steady state flow is approached, gold deformation of this order will not significantly affect interpretation of the data in terms of steady state flow and corresponding strain rate. In the case of experiments or stepping increments in which stresses greater than 50 to 60 MPa are achieved, and in which steady state flow is not approached in the sample, errors in the stress strain curve due to gold deformation will be important and, in principle, need to be corrected for. However, the gold deformation behaviour has been found to be insufficiently reproducible at high stresses (>50 MPa) to allow usefully accurate correction. For this reason, the few higher stress curves presented here have also not been corrected for gold deformation and are interpreted accordingly. In conclusion, taking into account all errors, the internal force measurements are accurate to ~ 1% of the measured value and displacements to within ~ 2 μm .

4.3. HIPing results and mechanical data

The results of the HIPing stage of the six experiments are given in Table 4.4, which lists the HIPing duration and the estimated post-HIPing porosities obtained. These data show that the wet samples (fo21 - fo25) all densified during the HIPing stage from an initial porosity of 8 to 9 % (Table 4.3) to a value of 2 to 4 %. In contrast, the single dry control sample (fo17) showed no densification during HIPing (compare Tables 4.3 and 4.4).

| Experiment / Sample No. | HIPing duration (600 MPa and 1223 K) (hrs:mins) | Est. post-HIPing porosity (%) | Final porosity (%) |
|-------------------------|-------------------------------------------------|-------------------------------|--------------------|
| Fo17 | 23:00 | 6.8 | 6.8 |
| Fo21 | 24:50 | 2.6 | 1.91 (2.29) |
| Fo22 | 17:00 | 3.9 | 1.99 (3.45) |
| Fo23 | 24:12 | 3.2 | 1.87 (3.13) |
| Fo24 | 24:55 | 3.5 | 2.21 (2.49) |
| Fo25 | 23:30 | 2.0 | 1.68 (2.74) |

Table 4.4. HIPing conditions, duration, estimated post-HIPing porosities and measured final porosities obtained for all samples tested. Post-HIPing porosities have been calculated from the initial porosities and the axial shortening measured during HIPing assuming isostatic strain. The final porosities in brackets have been estimated from image analysis.

Turning now to the data obtained from the deformation stage of the experiments, Figure 4.2 shows the stress versus strain curve obtained for the single dry sample (fo17) and one wet sample (fo21) tested at the same temperature (1223 K). Recalling that the stress strain curves are uncorrected for gold end-wall deformation of the capsule (which generally becomes significant at differential stresses > 50 to 60 MPa), it is noteworthy that measurement of the dry sample after deformation showed no permanent strain whatsoever, despite the total treatment of 24-hour HIPing at 600 MPa

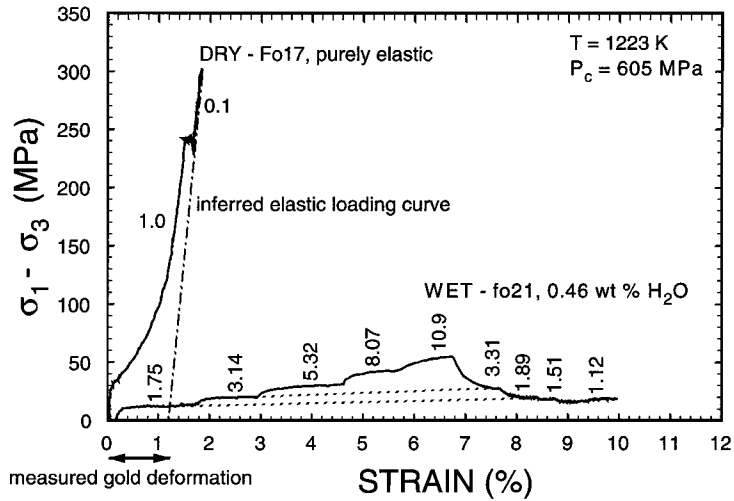


Figure 4.2. Differential stress versus strain curves for dry (fo17) and wet (fo21) samples at a temperature of 1223 K and a confining pressure of ~605 MPa, the strain rate steps were as indicated ($\times 10^{-6} \text{ s}^{-1}$). The measured final dimensions of the dry sample indicated that it behaved purely elastically. The inferred elastic loading curve for this dry sample deformed by near steady state flow to ~ 10% strain and the dotted lines indicate steps at constant displacement rate.

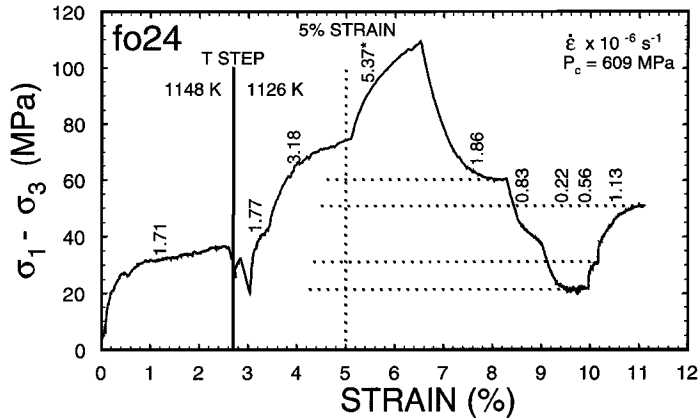


Figure 4.3. Differential stress versus strain curve for run fo24 at a confining pressure 609 MPa and temperatures of 1148 and 1126 K. The position of the temperature step is indicated by the solid vertical line. The strain rate steps are as indicated. The $5.37 \times 10^{-6} \text{ s}^{-1}$ step marked with the asterisk (*) has not been included in the subsequent analysis of stress versus strain rate behaviour as this step is clearly not approaching steady state. The horizontal dotted lines indicate the steps taken to be near steady state.

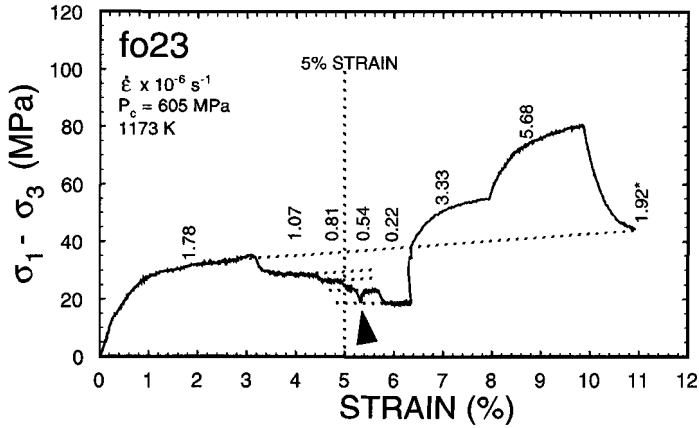


Figure 4.4. Differential stress versus strain curve for run fo23, at a confining pressure of 605 MPa and 1173 K. The strain rate steps are as indicated. The final strain rate step of $1.92 \times 10^{-6} \text{ s}^{-1}$ marked with the asterisk (*) has not been included in subsequent analysis of stress versus strain behaviour as insufficient strain was accumulated. The sub-horizontal dotted lines represent extrapolation from steps assumed to be near to steady state, or interpolation between steps at constant displacement rate, to 5% strain as indicated by the vertical dotted line. A fluctuation in flow stress, caused by unstable sample temperatures, which were in turn due to a temporary water cooling problem, is indicated by the arrow head.

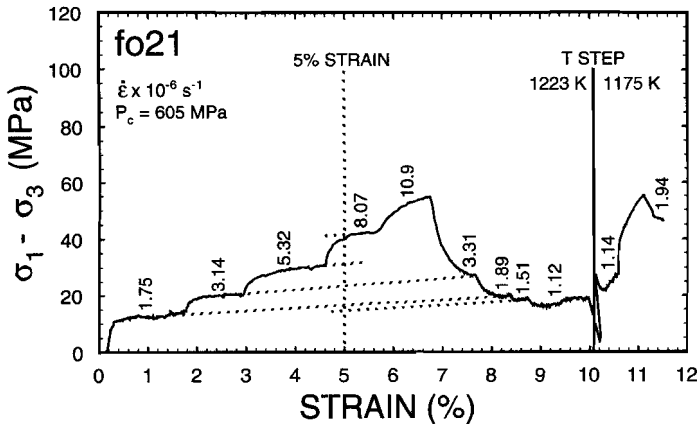


Figure 4.5. Differential stress versus strain curve for run fo21, at a confining pressure of 605 MPa and temperatures of 1223 and 1175 K. The position of the temperature step is indicated by the solid vertical line. The strain rate steps are as indicated. The sub-horizontal dotted lines indicate extrapolation from steps taken to be near steady state or interpolation between steps at constant displacement rate to 5% strain. Note minor hardening even at low flow stress.

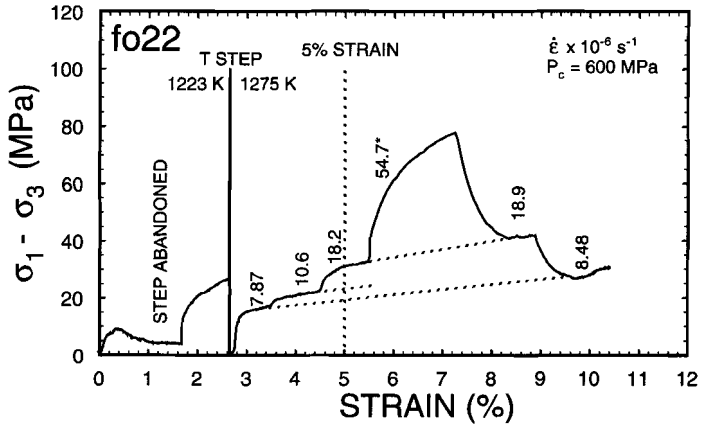


Figure 4.6. Differential stress versus strain curve for run fo22, at a confining pressure of 600 MPa and temperatures of 1223 and 1275 K. The position of the temperature step is indicated by the solid vertical line. The 1223 K step had to be abandoned due to a gas leak. After a good seal was achieved the test was resumed at 1275 K. The strain rate steps are as indicated. The sub-horizontal dotted lines indicate extrapolation from steps taken to be near steady state or interpolation between steps at constant displacement rate to 5% strain. Note the strain hardening in the latter cases.

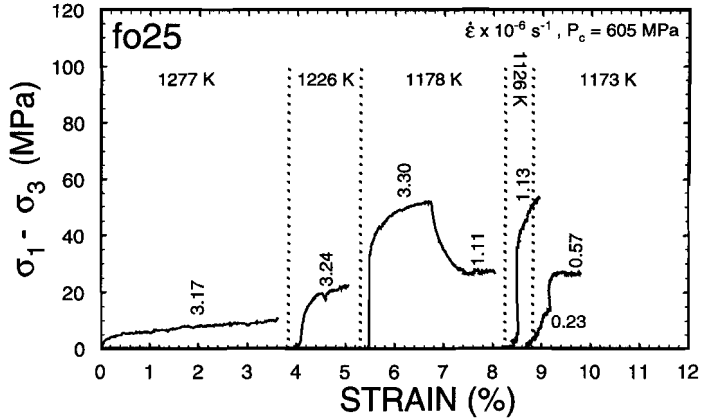


Figure 4.7. Differential stress versus strain curves from temperature stepping test fo25 at a confining pressure of 605 MPa. Temperature and strain rates as indicated. The position of temperature steps is indicated by the vertical dotted lines.

| Expt. | T (K) | Disp. Rate (mm s ⁻¹) | $\sigma_1 - \sigma_3$ (MPa) | Strain rate (s ⁻¹) | P _c (MPa) |
|-------|-------|----------------------------------|-----------------------------|--------------------------------|-------------------------|
| fo17 | 1223 | 2.500 x 10 ⁻⁵ | purely elastic | 1.00 x 10 ⁻⁶ | 608 |
| | 1223 | 2.500 x 10 ⁻⁶ | purely elastic | 1.00 x 10 ⁻⁷ | 598 |
| fo21 | 1223 | 4.237 x 10 ⁻⁵ | 13 | 1.75 x 10 ⁻⁶ | 608 |
| | 1221 | 7.496 x 10 ⁻⁵ | 20 | 3.14 x 10 ⁻⁶ | 607 |
| | 1222 | 1.250 x 10 ⁻⁴ | 30 | 5.32 x 10 ⁻⁶ | 606 |
| | 1221 | 1.872 x 10 ⁻⁴ | 42 | 8.07 x 10 ⁻⁶ | 605 |
| | 1221 | 2.500 x 10 ⁻⁴ | 55 | 1.09 x 10 ⁻⁵ | 605 |
| | 1221 | 7.496 x 10 ⁻⁵ | 27 | 3.31 x 10 ⁻⁶ | 605 |
| | 1222 | 4.237 x 10 ⁻⁵ | 19 | 1.89 x 10 ⁻⁶ | 604 |
| | 1221 | 3.375 x 10 ⁻⁵ | 17 | 1.51 x 10 ⁻⁶ | 603 |
| | 1223 | 2.500 x 10 ⁻⁵ | 15 | 1.12 x 10 ⁻⁶ | 603 |
| | 1176 | 2.500 x 10 ⁻⁵ | 27 | 1.14 x 10 ⁻⁶ | 602 |
| | 1175 | 4.237 x 10 ⁻⁵ | 46 | 1.94 x 10 ⁻⁶ | 602 |
| fo22 | 1274 | 1.873 x 10 ⁻⁴ | 16 | 7.87 x 10 ⁻⁶ | 608 |
| | 1274 | 2.500 x 10 ⁻⁴ | 20 | 1.06 x 10 ⁻⁵ | 608 |
| | 1275 | 4.250 x 10 ⁻⁴ | 32 | 1.82 x 10 ⁻⁵ | 606 |
| | 1276 | 1.250 x 10 ⁻³ | no steady state | 5.47 x 10 ⁻⁵ * | 604 |
| | 1276 | 4.250 x 10 ⁻⁴ | 42 | 1.89 x 10 ⁻⁵ | 602 |
| | 1273 | 1.873 x 10 ⁻⁴ | 31 | 8.48 x 10 ⁻⁶ | 600 |
| fo23 | 1171 | 4.237 x 10 ⁻⁵ | 34 | 1.78 x 10 ⁻⁶ | 605 |
| | 1173 | 2.500 x 10 ⁻⁵ | 28 | 1.07 x 10 ⁻⁶ | 606 |
| | 1173 | 1.873 x 10 ⁻⁵ | 26 | 8.07 x 10 ⁻⁷ | 605 |
| | 1173 | 1.250 x 10 ⁻⁵ | 24 | 5.42 x 10 ⁻⁷ | 605 |
| | 1173 | 5.005 x 10 ⁻⁶ | 18 | 2.18 x 10 ⁻⁷ | 605 |
| | 1173 | 7.496 x 10 ⁻⁵ | 54 | 3.33 x 10 ⁻⁶ | 604 |
| | 1173 | 1.250 x 10 ⁻⁴ | 81 | 5.68 x 10 ⁻⁶ | 604 |
| | 1171 | 4.237 x 10 ⁻⁵ | step too short | 1.92 x 10 ⁻⁶ * | 604 |
| fo24 | 1148 | 4.237 x 10 ⁻⁵ | 35 | 1.75 x 10 ⁻⁶ | 613 |
| | 1126 | 4.237 x 10 ⁻⁵ | 42 | 1.77 x 10 ⁻⁶ | 620 |
| | 1125 | 7.496 x 10 ⁻⁵ | 72 | 3.18 x 10 ⁻⁶ | 618 |
| | 1126 | 1.250 x 10 ⁻⁴ | no steady state | 5.37 x 10 ⁻⁶ * | 616 |
| | 1126 | 4.237 x 10 ⁻⁵ | 60 | 1.86 x 10 ⁻⁶ | 614 |
| | 1126 | 1.873 x 10 ⁻⁵ | 38 | 8.32 x 10 ⁻⁷ | 612 |
| | 1126 | 5.005 x 10 ⁻⁵ | 21 | 2.24 x 10 ⁻⁷ | 605 |
| | 1125 | 1.250 x 10 ⁻⁵ | 31 | 5.62 x 10 ⁻⁷ | 600 |
| | 1126 | 2.500 x 10 ⁻⁵ | 50 | 1.13 x 10 ⁻⁶ | 597 |
| | fo25 | 1277 | 7.496 x 10 ⁻⁵ | 9 | 3.17 x 10 ⁻⁶ |
| 1226 | | 7.496 x 10 ⁻⁵ | 21 | 3.24 x 10 ⁻⁶ | 616 to 610 |
| 1176 | | 7.496 x 10 ⁻⁵ | 52 | 3.30 x 10 ⁻⁶ | 616 to 609 |
| 1179 | | 2.500 x 10 ⁻⁵ | 28 | 1.11 x 10 ⁻⁶ | 609 to 597 |
| 1126 | | 2.500 x 10 ⁻⁵ | 54 | 1.13 x 10 ⁻⁶ | 619 to 607 |
| 1173 | | 5.005 x 10 ⁻⁶ | 13 | 2.26 x 10 ⁻⁷ | 613 to 595 |
| 1173 | | 1.250 x 10 ⁻⁵ | 26 | 5.68 x 10 ⁻⁷ | 595 to 585 |

Table 4.5. The experimental conditions and measured flow stresses for all strain rate and temperature steps performed in the present experiments. Data marked with an asterisk in the strain rate column generally correspond to steps showing strong work hardening and have not been included in non-linear regression analysis of steady state behaviour.

| Expt. No. | T (K) | Disp. Rate (mm s ⁻¹) | $\sigma_1 - \sigma_3$ (MPa) | Strain rate (s ⁻¹) |
|-----------|-------|-------------------------------------|--------------------------------|--------------------------------|
| fo21 | 1221 | 1.873×10^{-4} | 42 | 8.05×10^{-6} |
| | 1222 | 1.250×10^{-4} | 32 | 5.37×10^{-6} |
| | 1221 | 7.496×10^{-5} | 24 | 3.22×10^{-6} |
| | 1222 | 4.237×10^{-5} | 16 | 1.82×10^{-6} |
| | 1221 | 3.375×10^{-5} | 14 | 1.45×10^{-6} |
| fo22 | 1275 | 4.250×10^{-4} | 31 | 1.82×10^{-5} |
| | 1274 | 2.500×10^{-5} | 23 | 1.07×10^{-5} |
| | 1274 | 1.873×10^{-4} | 20 | 8.02×10^{-6} |
| fo23 | 1171 | 4.237×10^{-5} | 38 | 1.83×10^{-6} |
| | 1173 | 2.500×10^{-5} | 28 | 1.08×10^{-6} |
| | 1173 | 1.873×10^{-5} | 26 | 8.08×10^{-7} |
| | 1173 | 1.250×10^{-5} | 24 | 5.39×10^{-7} |
| | 1173 | 5.005×10^{-6} | 18 | 2.16×10^{-7} |
| fo24 | 1126 | 4.237×10^{-5} | 60 | 1.80×10^{-6} |
| | 1126 | 2.500×10^{-5} | 50 | 1.06×10^{-6} |
| | 1125 | 1.250×10^{-5} | 31 | 5.32×10^{-7} |
| | 1126 | 5.005×10^{-6} | 21 | 2.13×10^{-7} |
| fo25 | 1277 | 7.496×10^{-5} | 9 | 3.17×10^{-6} |
| | 1226 | 7.496×10^{-5} | 21 | 3.24×10^{-6} |
| | 1176 | 7.496×10^{-5} | 52 | 3.30×10^{-6} |
| | 1179 | 2.500×10^{-5} | 28 | 1.11×10^{-6} |
| | 1173 | 5.005×10^{-6} | 13 | 2.26×10^{-7} |
| | 1173 | 1.250×10^{-5} | 26 | 5.68×10^{-7} |

Table 4.6. The 'selected data' set extrapolated or interpolated to 5% strain.

and 1223 K followed by axial loading to a differential stress of 300 MPa at rates down to $1 \times 10^{-7} \text{ s}^{-1}$. The dry sample must therefore have behaved elastically in rough accordance with the inferred elastic loading curve inserted into Figure 4.2. In sharp contrast, the wet samples, as exemplified by fo21 (see Figure 4.2), showed ductile flow reaching near steady state mostly at stresses below 50 MPa at strain rates in the range 2×10^{-7} to $5 \times 10^{-5} \text{ s}^{-1}$. Although the present dry control sample comes from a different batch of starting material than the wet samples (see Table 4.3), further tests have shown that the water weakening effect described here is also observed in this material (see Chapter 5 – tests fo18, fo19 and fo20). Final porosity (i.e. post-deformation) data for wet and dry samples are given in Table 4.4.

The complete set of stress versus strain curves obtained for the five wet experiments are shown in Figures 4.3 to 4.7. The temperatures and strain rates were as indicated. Note that all curves show ductile flow with near steady state being achieved in many – but certainly not all – of the strain rate and temperature steps performed. Notably, most of the steps achieving stresses < 50 MPa approach steady state, though some hardening was observed, as illustrated by the dotted tie-lines joining steps performed at the same displacement rate. Steps reaching stresses > 50 MPa often show quite marked work hardening (see fo22 and fo23 in Figures 4.4 and 4.6).

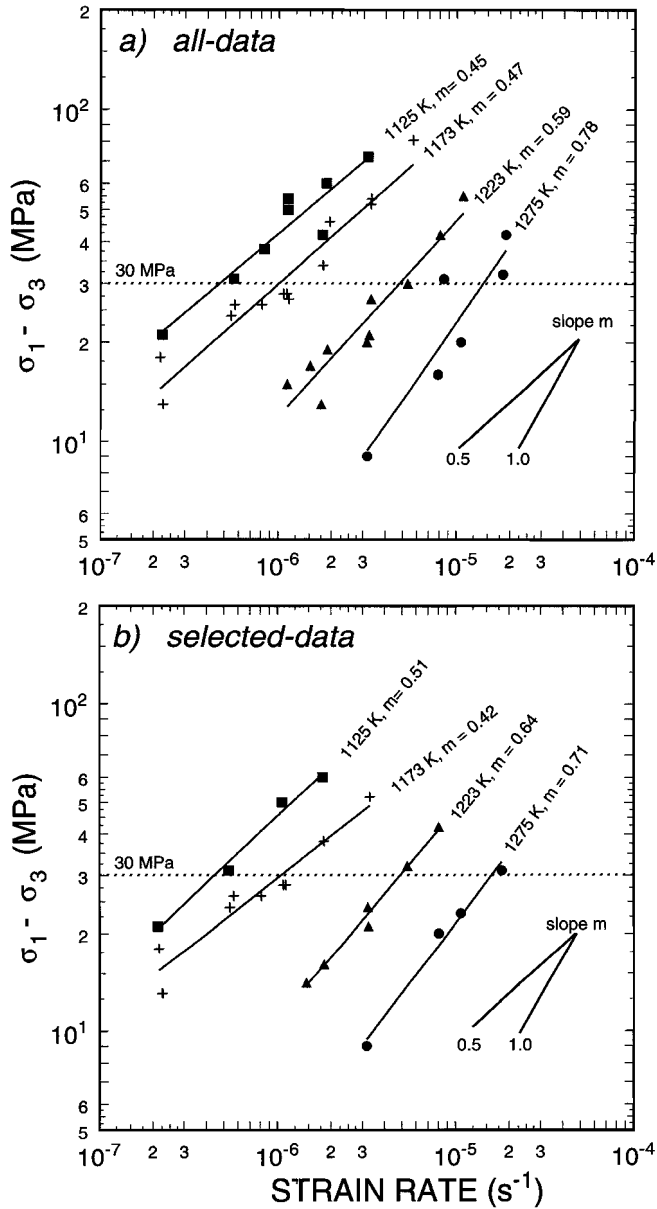


Figure 4.8a,b. Plots of differential stress versus strain rate (log₁₀ axes) for the data sets identified as 'all data' and 'selected data' respectively. Solid lines represent individually fitted isotherms at 1125, 1173, 1223 and 1275 K. Slopes give the strain rate sensitivity ($m = 1/n$). Reference slopes of $m = 0.5$ and $m = 1.0$ are indicated. The dotted line indicates the 30 MPa section used to determine the apparent activation energy (see Figure 4.10).

| Temperature (K) | m (n) all data | m (n) selected data |
|-----------------|----------------|---------------------|
| 1125 | 0.45 (2.2) | 0.51 (2.0) |
| 1173 | 0.47 (2.1) | 0.42 (2.4) |
| 1223 | 0.59 (1.7) | 0.64 (1.6) |
| 1275 | 0.78 (1.3) | 0.71 (1.4) |

Table 4.7. Strain rate sensitivities (m) and stress exponents (n - values in brackets) from the two data sets determined for individual isotherms. Note the trend of increasing m values with increasing temperature.

| Data set | n | ln A | Q _c (kJ mol ⁻¹) |
|---------------|---------------------|--------------|----------------------------------------|
| all data | n = 2.14 ± 0.18 | 10.22 ± 1.85 | 302 ± 21 |
| | constrained : n = 1 | 7.46 ± 2.02 | 237 ± 20 |
| Selected data | 2.19 ± 0.20 | 13.66 ± 1.90 | 338 ± 21 |
| | constrained: n = 1 | 11.47 ± 2.54 | 278 ± 25 |

Table 4.8. Results of Marquardt-Levenberg non-linear regression of the two data sets to a Dorn-type power law creep equation. Two fits are given for each data set: firstly, a fit using the three parameters n, lnA and Q_c, and secondly a fit where n has been constrained to unity.

On all curves, the sub-horizontal dotted lines indicate either extrapolation to 5% strain from assumed steady state flow, or interpolation between steps at constant displacement rate.

From inspection of Figures 4.3 to 4.7, the stepping data clearly show that flow stress ($\sigma_t - \sigma_3$) increases with increasing strain rate and decreasing temperature. In order to represent the dependence of flow stress on strain rate and temperature contained in the stepping data, the data have been grouped into two different sets. The need for this lies in the fact that the present multi-stepping temperature and displacement rate tests, though providing the maximum amount of data from each test, have the drawback that the attainment of steady state flow is not clearly demonstrated in all steps. Moreover, at stresses > 50 to 60 MPa, deformation of the end-wall of the gold capsules may have influenced the stress strain behaviour. Taking these points into account, an 'all data' set has been compiled consisting of data taken from all steps. A list of steps used in this 'all data' set is given in Table 4.5. The stress and strain rate values appearing in this table correspond to the step mid points. Several steps have been rejected from this table in further data analysis since near steady state clearly cannot be assumed (i.e. the steps at the highest strain rates in tests fo24 and fo22, and the final step in test fo23). These have been marked with an asterisk on the stress versus strain curves and in Table 4.5. A second, more limited 'selected data' set, incorporating the steps where near steady state is most clearly demonstrated, or where flow stresses can be interpolated between steps at constant displacement rate, has also been constructed (see Table 4.6). The corresponding stress and strain rate data are quoted for 5% strain using the dotted tie-lines and lines of extrapolation inserted into Figures 4.3 to 4.6.

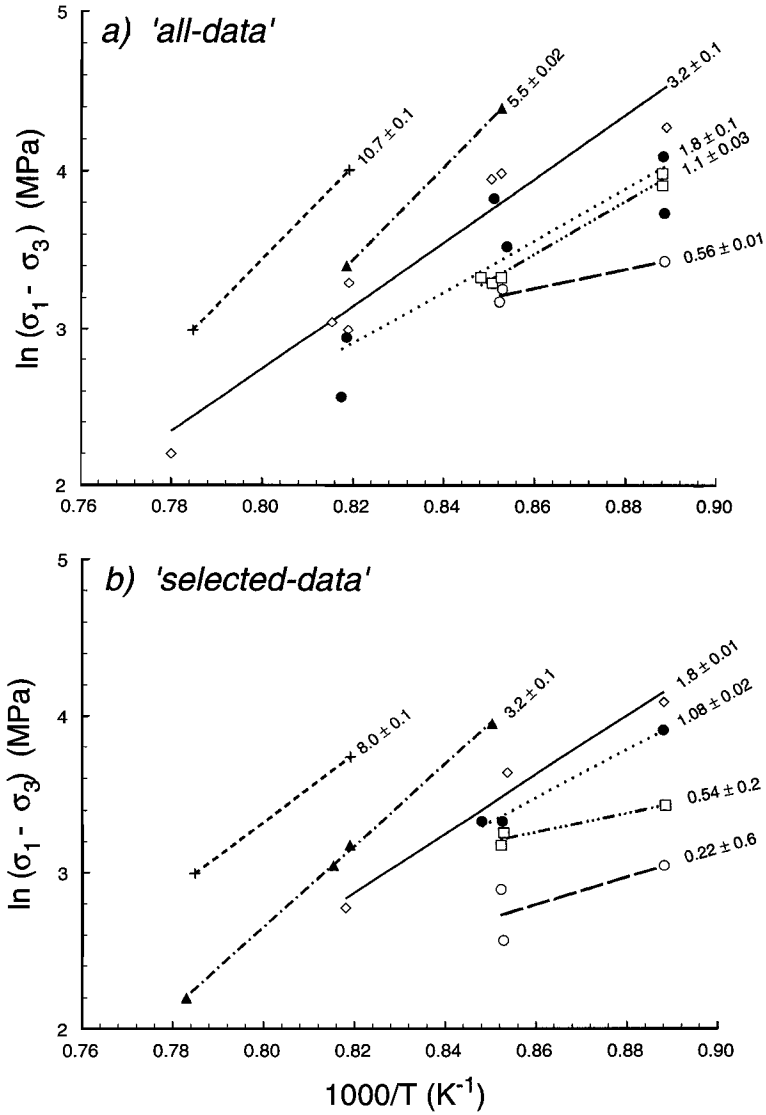


Figure 4.9a,b. Plots of the natural logarithm of the differential stress versus $1000/T$ for the 'all data' and 'selected data' sets. The lines represent individual fits for data in the strain rate ranges indicated ($\times 10^{-6} \text{ s}^{-1}$).

The above two data sets have been processed in parallel to determine the stress and temperature dependence of creep behaviour. The results are graphed in Figures 4.8 (stress versus strain rate) and 4.9 (log stress versus reciprocal temperature) and have been analyzed using the Dorn-type steady state flow relation written in the form

$$\dot{\epsilon} = A\sigma^n e^{\left(\frac{-Q_c}{RT}\right)} \quad 4.2$$

to obtain a purely empirical description of the results. Referring to Figure 4.8, both data sets show a systematic increase of flow stress ($\sigma_1 - \sigma_3$) with increasing strain rate, with the Dorn-type power law fits to individual isotherms yielding stress exponents (n) in the range 1.8 ± 0.5 i.e. strain rate sensitivities ($m = 1/n$) in the range 0.6 ± 0.2 (see also Table 4.7). Note that the results for the two data sets are more or less indistinguishable and that both sets show a systematic increase in m (decrease in n) with increasing temperature ($n \sim 2.1$ at $T = 1125$ K; $n \sim 1.35$ at $T = 1275$ K). Furthermore, both data sets show a systematic decrease of flow stress with increasing temperature at constant strain rate, as shown in Figure 4.9. Dorn-type (Arrhenius) fits to describe the temperature dependence of creep rate, for the two data sets at a constant stress of 30 MPa, yield apparent activation energies (Q_c) of around 280 - 290 kJ mol⁻¹ (see Figures 4.10 a,b). These figures were constructed from the intersection of the best fit isotherms plotted in Figures 4.8 a and b with the 30 MPa abscissa.

In addition to the above treatment, non-linear regression of the two data sets has been carried out to find the best multidimensional fits to the Dorn-type flow relation. This has been done using a rearranged form of the Equation 4.2, written

$$\ln \sigma = \left(\ln \dot{\epsilon} - \ln A + \frac{Q_c}{R} \cdot \frac{1}{T} \right) / n \quad 4.3$$

Flow stress (differential stress) was taken as the dependent variable, and fitting was achieved using the Marquardt-Levenberg non-linear least squares fitting algorithm (Marquardt, 1963). Equation 4.3 was thus fitted to both data sets, firstly without constraints on the parameters n , $\ln A$ and Q_c , to obtain the true best fit to the data. Secondly, for purposes of later comparison with theoretical models for diffusion creep in which $n = 1$, Equation 4.3 was fitted to the data assuming a Newtonian (linear) stress dependence, i.e. constraining n to be equal to unity and fitting $\ln A$ and Q_c only. The results of the non-linear regression are presented in Table 4.8. Note once again that the two data sets show relatively little difference in parameter values producing $n \sim 2$ and $Q_c \sim 320 \pm 40$ kJ mol⁻¹ for the unconstrained fits and 260 ± 48 kJ mol⁻¹ for the constrained fits ($n = 1$).

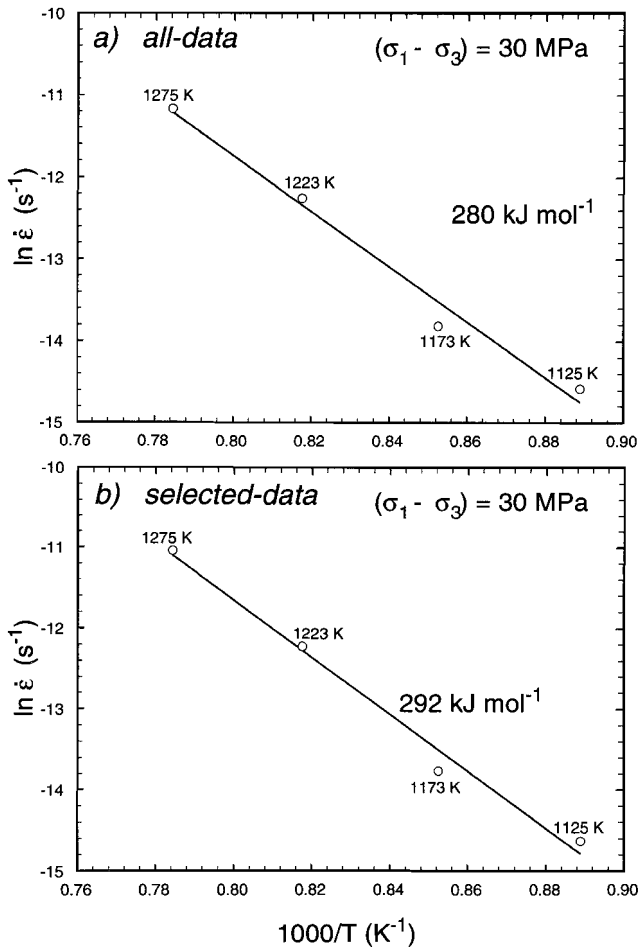


Figure 4.10 a,b. Arrhenius plots of the natural logarithm of strain rate versus $1000/T$ for the 'all data' and 'selected data' sets respectively. Slope of the best fit line equals $-Q_c/R$.

4.4. Microstructural analysis

4.4.1. Techniques

The microstructure of the starting ceramic (after sintering and before HIPing) has been studied, along with that of the dry control and all five wet-deformed samples, using a Philips XL30 FEG (field emission gun) scanning electron microscope (SEM) operated in orientation contrast mode. Both qualitative and quantitative work were carried out in this mode operating the XL30 FEG at an acceleration voltage of 15 to 20 kV, a tilt angle of 70° , with automatic tilt correction and dynamic focus. In addi-

tion, a single wet deformed sample (fo21) has been examined by means of transmission electron microscopy (TEM) performed using a Philips CM200 FEG TEM. The same sample has also been investigated using electron backscatter diffraction (EBSD), in the Philips XL 30 FEG SEM to determine the crystallographic orientation distribution.

Samples were prepared for the SEM analysis by Syton™ polishing (colloidal silica) for between 12 and 24 hours; this preserves the crystalline structure of the surface layer. In orientation contrast mode, unetched, uncoated samples thus prepared can be studied, the contrast between the grains being largely dependent on their crystallographic orientation. This technique has the advantage that features such as grain boundaries and pores do not undergo the damage which is inherent in the use of etchants. TEM samples were prepared using conventional ion-beam thinning.

Quantitative image analysis was carried out on the orientation contrast images produced for all relevant materials (starting material, dry control and wet deformed samples) using three images of each sample studied. These were obtained from randomly selected areas viewed in the σ_1/σ_3 plane at a magnification giving an image width of $\sim 25 \mu\text{m}$. The images were saved using the microscope's computer system as 8-bit, 256 greyscale bit mapped graphics using the Tagged Image File Format (TIFF) with 712×484 pixels. Distortion introduced into the images on saving as TIFF files - related to the non-square nature of the microscope pixels - was overcome by resizing all images to the dimensions 645×484 pixels. The resized images were subsequently enhanced (using Adobe Photoshop Pro software) to make the grain boundaries as clear as possible. The images were then printed (23.94×18 cm) using a high-resolution laser printer and a check was made to ensure that no distortion of the image had taken place. The grain boundaries were then carefully traced onto an acetate sheet using a fine marker pen. Care was taken to fully shade any intergranular pores, so that they did not appear as grains, and to use continuous lines. The finished tracing was scanned using a conventional flat-bed scanner, set up to produce an 832×1144 pixel, bi-level image. After again checking that no distortion had taken place these images were converted to 8-bit, 256 greyscale images and analyzed using the UTHSCSA Image Tool software running under Windows 95™ (from the University of Texas Health Science Center, San Antonio, and available by anonymous FTP from maxrad6.uthscsa.edu). Using Image Tool, a spatial calibration was undertaken to set the software to measure in appropriate units (e.g. 750 pixels $\approx 25 \mu\text{m}$). The program was then used to identify and analyse the grains, returning the following data: grain area, perimeter length, equivalent circular diameter (ECD), roundness, elongation, major axis length and orientation, minor axis length and orientation, and the coordinates of the grain centres.

4.4.2. General microstructural description

Examination of the *starting material* using the above SEM methods showed it to be microstructurally homogeneous (see Figure. 4.11a). The grains show a foam texture and have a narrow grain size distribution with an average grain size (d) of ~ 1 to $2 \mu\text{m}$ (see Figure 4.11b). Grain boundaries are generally straight or gently curved and equilibrium triple junctions of 120° are common. Both intra-granular and intergranular pores are present. Intergranular pores account for $\sim 7\%$ porosity. These pores are generally of low coordination, i.e. located between 2 to 5 neighbouring grains, and around one half to a tenth of the grain diameter in size (see Figure 4.11c). The intergranular pores are round-

ed and disconnected in two dimensional (2-D) cross-section and where they intersect grain boundaries they are characterized by apparent dihedral angles $> 60^\circ$. This geometry is consistent with the observation, made in Chapter 2, that the permeability of the starting material cuts off at approximately 8% porosity. Intragranular pores account for $\sim 1\%$ porosity and are generally less than one seventh of the grain diameter. No glassy intergranular films/blebs or other grain boundary phases have been observed at the scale of observation employed.

The single *dry control sample* studied (fo17) is microstructurally very similar to the starting material. This is not surprising since no HIPing or permanent deformation was achieved (see Figures 4.12a, b and c). Inspection shows that the average grain size of the dry control material is still around 1 to 2 μm and that the grain size distribution is narrow. Lamellae are occasionally visible within the enstatite grains which are of similar size to the forsterite grains. These lamellae are most probably clinoenstatite within orthoenstatite and may have resulted from either microplasticity (shearing induced - Riecker and Rooney, 1967; Raleigh et al., 1971; Coe and Kirby, 1975) or quenching (cooling induced - Sclar et al., 1964; Boyd and England, 1965; Grover, 1972).

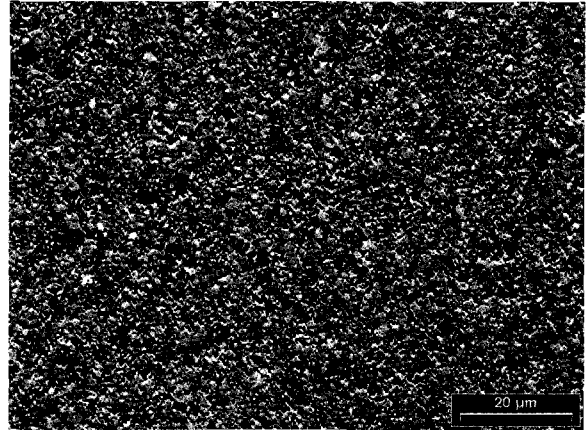
The *wet-deformed samples* remained cylindrical after HIPing and deformation, and appear to be homogeneously deformed macroscopically. They are also microstructurally homogeneous and again show a narrow grain size distribution with an average value of 1 to 2 μm (see Figures 4.13 and 4.14). Despite the $\sim 10\%$ deformation of the samples the grains still exhibit a foam texture, with little or no evidence of grain flattening or prominent grain boundary alignment. Both straight and gently curved grain boundaries occur ($\sim 50\%$ of each), and more prominent curvature has been observed at enstatite-forsterite interphase boundaries, which are generally convex towards forsterite. The porosity is clearly lower than in the starting material, being reduced to $\sim 2\%$ due to the loss and redistribution of intergranular pores, though both intragranular and intergranular pores are still present. In 2-D, the grains have between three and eight sides, with the majority having between five and seven. Serrated grain boundaries and subgrains are not observed. The grain boundaries are free from second-phase particles or intergranular films at the scale of SEM observation. Enstatite grains are of similar size to the forsterite grains and commonly exhibit lamellae. The intragranular pores, inherited from the starting material, commonly appear circular in cross-section and are small in comparison with the grains. The number and distribution of these intragranular pores appears to be relatively unaltered with respect to the starting material. Intergranular pores occur along grain boundaries, and at triple and four-grain junctions. In contrast to the starting material these intergranular pores are often connected to form crack-like arrays separating columns of 2-4 grains, and often oriented sub-parallel to the compression direction, suggesting cavitation and cavity coalescence (see Figures 4.13c and 4.14c) of the type associated with grain boundary sliding (Blanchard and Chan, 1993; Ree, 1994).

In addition to the above SEM observations, sample fo21 was studied using transmission electron microscopy (TEM; see Figure 4.15) in collaboration with Dr. Herman van Roermund. In accordance with the SEM observations for the wet samples, the TEM observations on this sample show a foam texture with straight or gently curved grain boundaries. The majority of grains ($> 80\%$) appear to be dislocation free and subgrains were not observed. Intergranular pores exhibit apparent dihedral angles $< 60^\circ$ where they intersect with grain boundaries. Intragranular pores often show negative crystal forms (see Figure 4.15c) and appear to be free from attached dislocations. Many of the grain

Figure 4.11a,b,c.

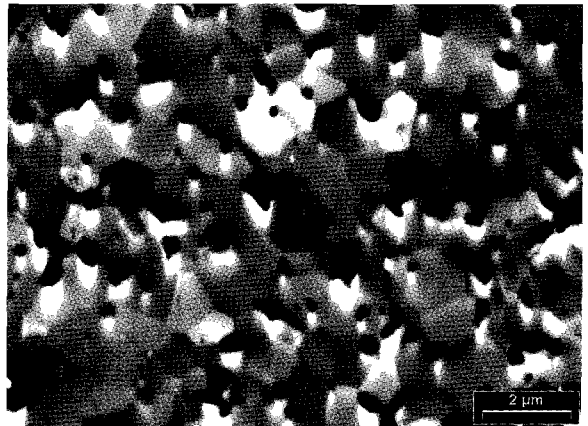
SEM orientation contrast photomicrographs of starting material 30.31.32 sintered at 1673 K for 60 minutes, scales as shown.

a) Low magnification image showing the homogeneity of the material.



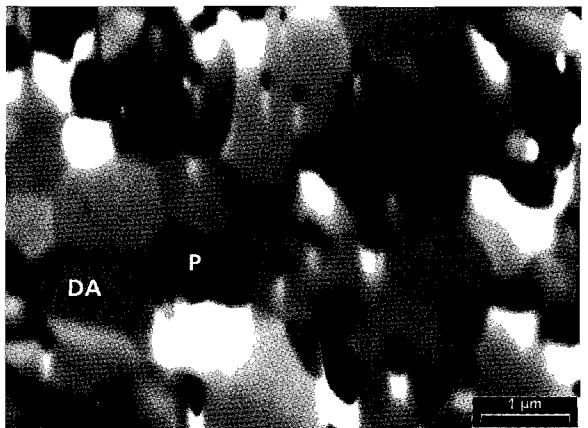
a

b) Intermediate magnification. Numerous rounded intergranular pores commonly with 2 to 5 neighbouring grains are visible. Note the small circular intragranular pores included in the grains during synthesis. Straight and gently curved grain boundaries and 120° triple junctions are common.



b

c) High magnification detail of pores (P) showing their rounded outline and high apparent dihedral angles (DA).

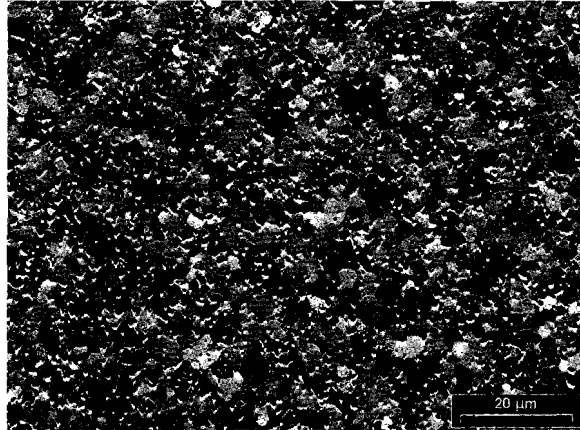


c

Figure 4.12a,b,c.

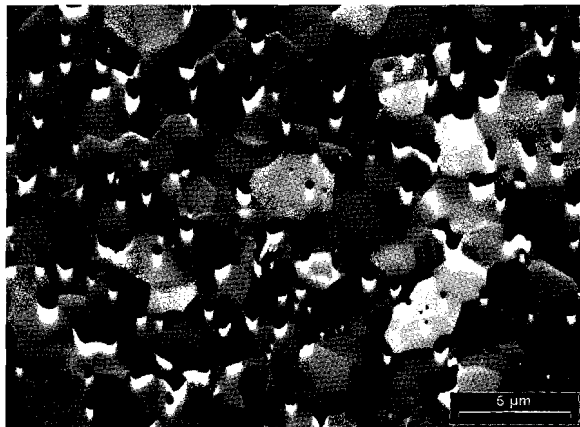
SEM Orientation contrast photomicrographs of dry control sample fo17, viewed in the σ_1/σ_3 plane with σ_1 horizontal. Scales as indicated.

a) Low magnification image showing the homogeneity of the material.

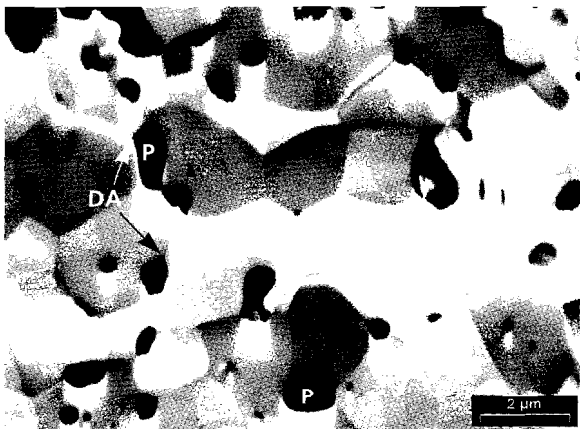


a

b) and c) Intermediate and high magnifications views. Notice the similarity to the starting microstructure (Figure 4.11). Numerous rounded intergranular pores (P) commonly with 2 to 5 neighbouring grains with high apparent dihedral angles (DA) are visible along with smaller, circular, intragranular pores. Straight and gently curved grain boundaries and 120° triple junctions are common.



b

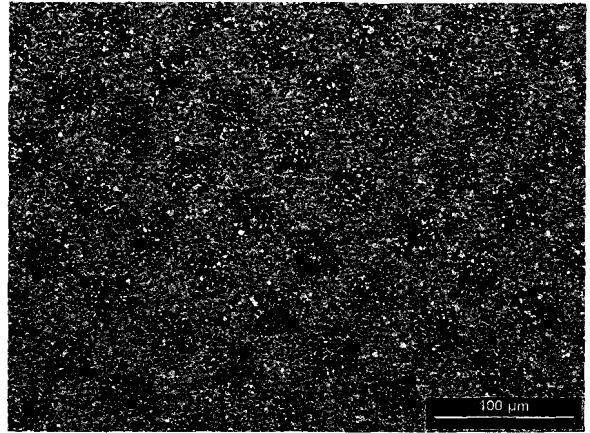


c

Figure 4.13a,b,c.

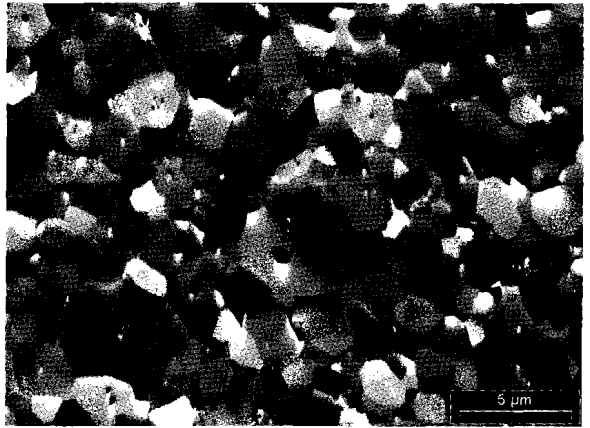
SEM orientation contrast photomicrographs of wet deformed sample fo21 viewed in the σ_1/σ_3 plane with σ_1 horizontal. Scales as indicated.

a) Low magnification image showing the homogeneity of the material.



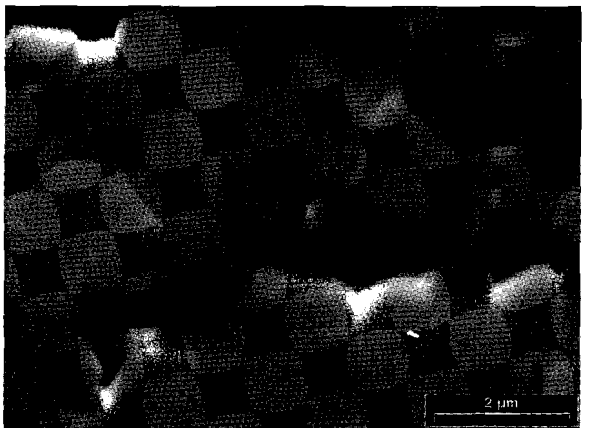
a

b) Intermediate magnification: Note the reduced porosity compared to the starting material. Several intergranular pores extend along entire grain boundaries.



b

c) High magnification: detail of pores and grain boundaries. Intergranular pores extending along several grain boundaries a feature consistent with cavity coalescence during grain boundary sliding.

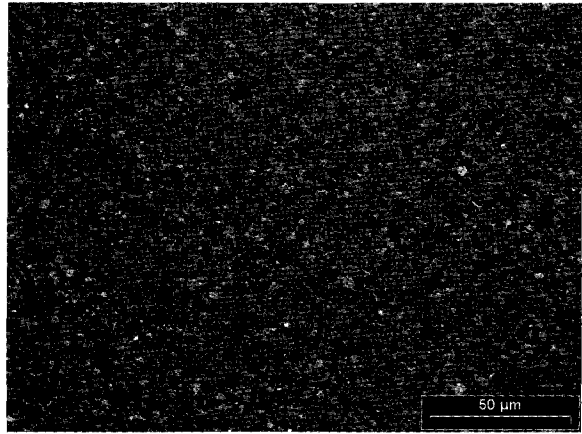


c

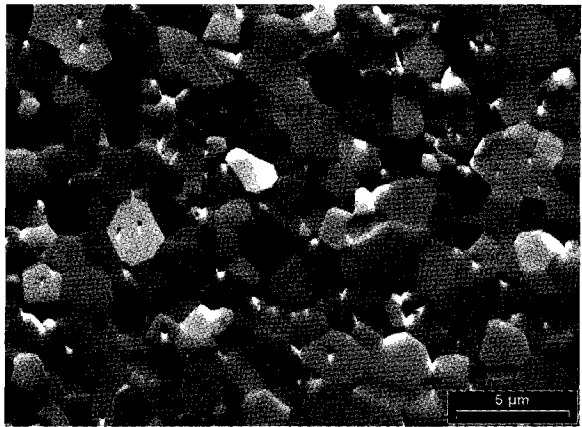
Figure 4.14a,b,c.

SEM orientation contrast photomicrographs of wet deformed sample fo25 viewed in the σ_1/σ_3 plane, with σ_1 horizontal. Scales as indicated.

a) Low magnification view showing the homogeneity of the material.



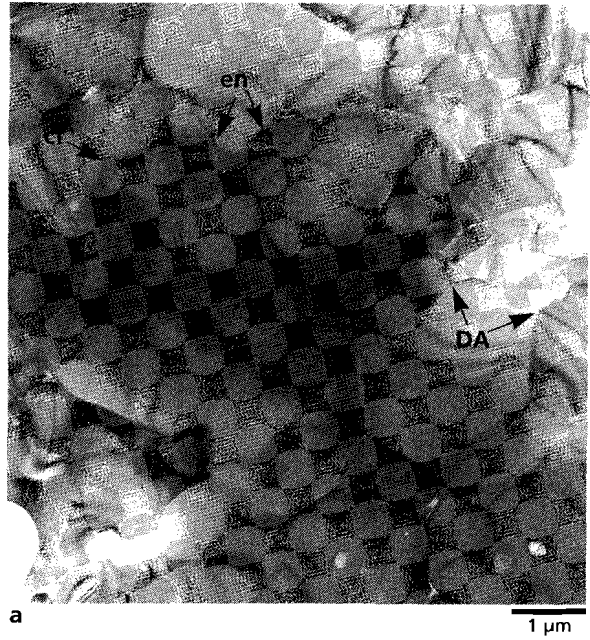
b) Intermediate magnification: lamellae are visible in the enstatite grains (en) and both straight and gently curved grain boundaries are common. Note the reduced porosity compared to the starting material. Several intergranular pores extend along entire grain boundaries.



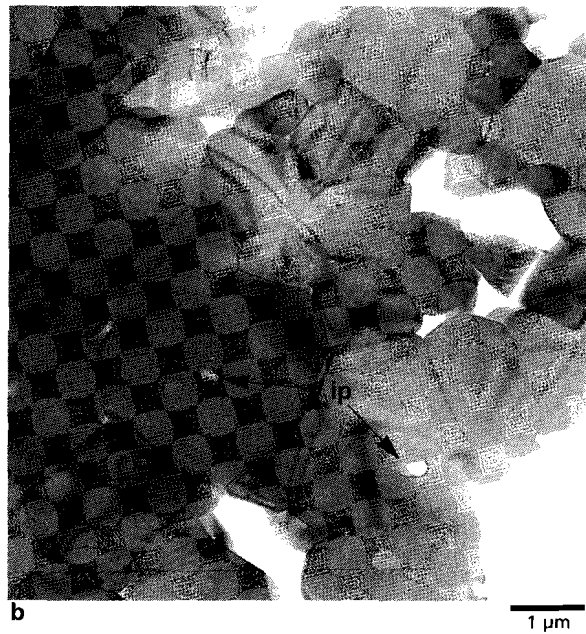
c) High magnification: detail of pores and grain boundaries. Enstatite grain (centre) shows lamellae. Note that the pores adjacent to the enstatite grain extend along one or more grain boundaries.



Figure 4.15a,b.
TEM images of wet deformed sample fo21.



a) Note the enstatite lamellae (en), the apparent dihedral angles $< 60^\circ$ (DA) and the contrast at grain boundaries (cf).



b) Note the dislocation free nature of the grains and the lack of dislocations associated with intragranular pores (ip).

Figure 4.15c,d.

TEM images of wet deformed sample fo21.

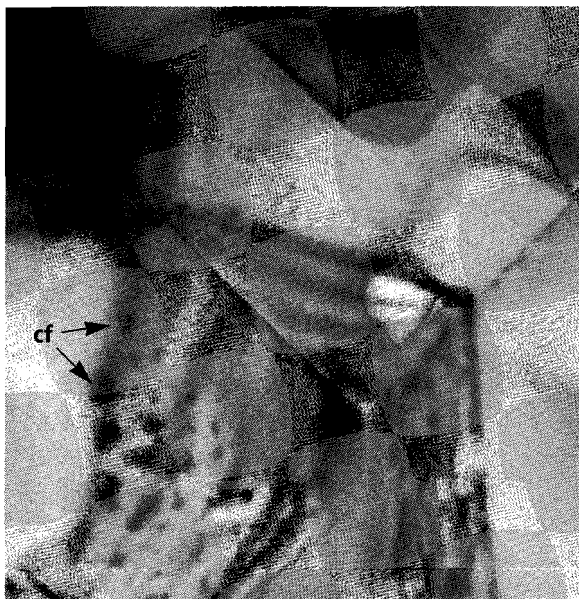
c) Intragranular pores showing negative crystal forms and absence of associated dislocations.



c

500 nm

d) Close-up of grain boundaries inclined to the beam; contrast features resembling inclusions are visible on the grain boundary (cf).



d

200 nm

boundaries, but not all, show trains of elliptical (2-D) or ellipsoidal (3-D) regions of contrast (concentric fringes) each up to 100 nm in length, reminiscent of inclusion arrays. The absence of these features in the drier samples (see Chapter 6) suggests that these grain boundary features may be related to trapped fluid inclusions. No melt features or amorphous films could be resolved along grain boundaries and therefore, if present, must represent only a small volume fraction of the material.

4.4.3. Quantitative microstructural data

Image processing of SEM images as described above has been used to measure grain size and to determine the grain size distributions of the starting material, the dry control sample and the 5 wet deformed samples. The results are summarized in Table 4.9 in terms of mean grain area, mean equivalent circular diameter (ECD), mean \log_{10} area, standard deviation in \log_{10} area, ECD of mean \log_{10} diameter and calculated mean intercept length (L_3). The ECD of a grain is simply the diameter of a circle with an area equal to the measured projected grain area. The measured grain areas from all the samples are more or less log-normally distributed as illustrated for sample fo22 in Figure 4.16. The mean of this distribution and its standard deviation are thus appropriate statistics for description of the distribution of projected grain areas (see Table 4.9). To compare the grain size distributions for the starting material (stm 30.31.32), dry control sample and the five wet experiments, the cumulative distribution function of ECD has been plotted for all materials examined (see Figure 4.17). In this figure the data from the five wet deformed samples and the starting material overlie each other and have the same form, thus illustrating that the grain size distributions of these samples are very similar. The dry sample, from a different batch of material, shows a similar distribution but shifted to larger grain sizes.

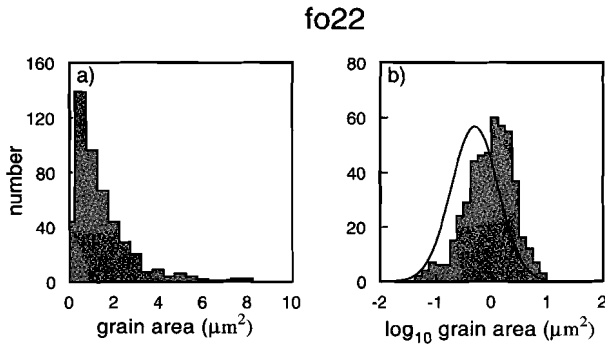
Several approaches can be taken to determine a single valued expression of grain size from the data given in Table 4.9. For example, grain size can be defined simply as the mean ECD, or ECD obtained from the mean of the \log_{10} area distribution (cf. Russ, 1986). It is also possible to calculate a value for comparison with grain sizes obtained using the conventional mean linear intercept method (Underwood, 1970). A theoretical value for the mean linear intercept length, L_3 , can be calculated from the mean projected area, assuming the structure is made up of single size tetrakaidecahedra (truncated octahedra) using the relation

$$L_3 = 1.69 \cdot \sqrt{\frac{\bar{A}'}{6.696}} \quad 4.4$$

where L_3 is the mean linear intercept length (m) and \bar{A}' is the mean projected area (m^2); see Underwood (1970). Tetrakaidecahedra are the space-filling polyhedra which best approximate the average ideal shape for a polycrystalline structure resulting from normal grain growth (Mendelson, 1969). This theoretical value of L_3 can then be multiplied by the factor 1.56 commonly used to obtain grain size from mean linear intercept length. From Table 4.9, it is clear that the mean ECD is very close to the value obtained from this calculation ($L_3 \times 1.56$). For this reason, the mean ECD has been chosen as a single value expression of grain size measurement. The mean ECD of all wet deformed samples falls in the range $1.2 \pm 0.07 \mu m$. The value of $1.14 \mu m$ determined for the starting material falls within this range and is evidence to the fact that only very minor grain growth has taken place.

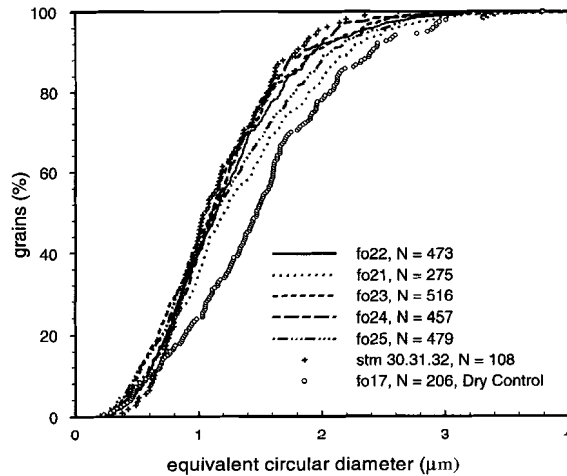
| Sample no. | N | mean area (μm ²) | mean ECD (μm) | mean log ₁₀ area (μm ²) | SD log ₁₀ area (μm ²) | ECD of mean log ₁₀ area (μm) | L ₃ (μm) | L ₃ × 1.56 (μm) |
|-------------------|-----|------------------------------|---------------|------------------------------------------------|----------------------------------------------|-----------------------------------------|---------------------|----------------------------|
| Fo17 | 206 | 2.14 | 1.50 | +0.1417 | 0.461 | 1.33 | 0.955 | 1.49 |
| Starting Material | 108 | 1.18 | 1.14 | -0.0491 | 0.336 | 1.07 | 0.780 | 1.25 |
| Fo21 | 275 | 1.70 | 1.32 | +0.0258 | 0.466 | 1.16 | 0.851 | 1.33 |
| Fo22 | 473 | 1.41 | 1.22 | -0.0301 | 0.422 | 1.08 | 0.775 | 1.21 |
| Fo23 | 516 | 1.34 | 1.17 | -0.0750 | 0.442 | 1.03 | 0.756 | 1.18 |
| Fo24 | 457 | 1.28 | 1.17 | -0.0467 | 0.390 | 1.07 | 0.739 | 1.15 |
| Fo25 | 479 | 1.50 | 1.24 | -0.0369 | 0.474 | 1.08 | 0.800 | 1.25 |

Table 4.9. Results of the grain size analysis (ECD = equivalent circular diameter). The grain area distributions are log-normal and therefore the mean log area and its standard deviation statistics serve to describe the observed distributions. To allow comparison of results with data obtained from the more commonly used linear intercept method a theoretical value of the linear intercept (L₃) has been calculated from the mean projected area using the relations from Underwood (1970) and assuming the grains to be single size truncated octahedra (see Equation 4.4). These theoretical values for L₃ can then be converted into a grain size by multiplying by the factor 1.56. Note that the resulting values are approximately equal to the values for the mean ECD.



← **Figure 4.16a,b.** Typical results of grain size analysis (from sample fo22). a) Histogram of measured grain area (μm²). Note the skew to smaller grain areas. b) Histogram of log₁₀ grain area (μm²) illustrating the approximately log-normal nature of grain area. The solid curve represents a normal distribution based on the mean log₁₀ grain area of -0.0301 and a standard deviation of 0.422 (see Table 4.9 for grain size statistics).

Figure 4.17. Cumulative grain size distribution plots. Grain size expressed as equivalent circular diameter (μm). The data for the five wet deformed samples more or less overlie one another, and fall close to the distribution for the starting material (stm 30.31.32), indicating that only minor grain growth has occurred during deformation. Note approximately 60% of grains fall within a 0.75 - 1.7 (μm) interval.



The dry control sample, which came from a different gel batch and was not processed along with the other samples, has a mean ECD of $1.50\ \mu\text{m}$. An attempt was made to quantitatively describe the grain fabric in terms of grain roundness and using standard fry plots. However, errors associated with the microscope tilt correction were found to be too great to allow this analysis. In addition, an attempt was made to determine if there was a preferred orientation of intergranular pores, but, this was com-

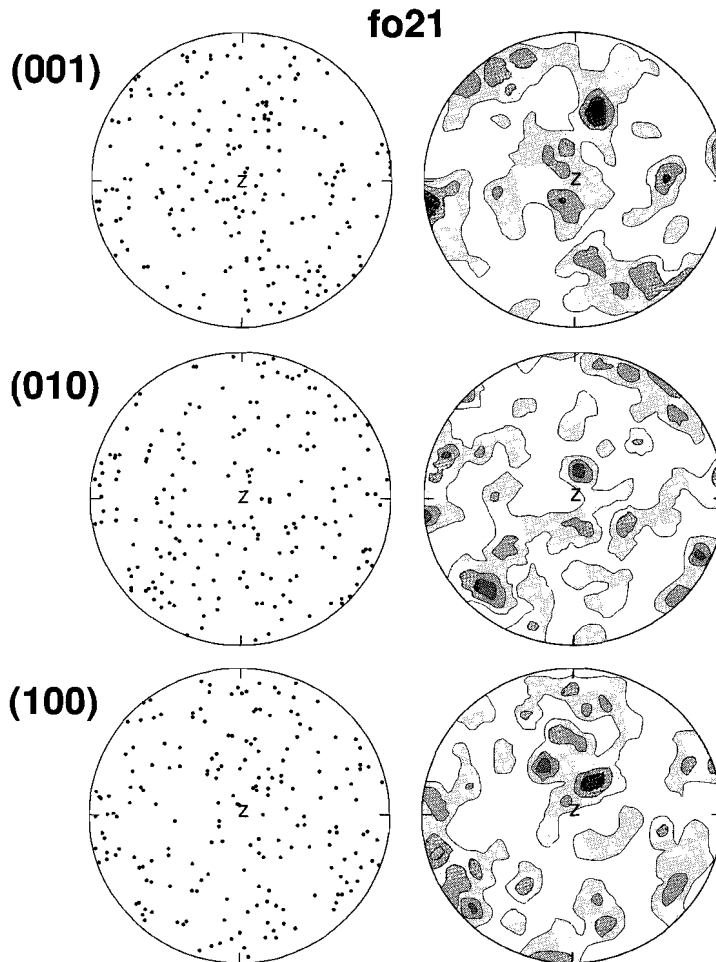


Figure 4.18. Upper hemisphere equal area pole figures and contours for (001), (010) and (100) planes for 200 grains from wet-deformed sample fo21, analysed using electron backscatter diffraction (EBSD). The patterns appear to be random, indicating that no crystallographic preferred orientation (CPO) has developed. Compression direction parallel to z. Total strain $\approx 11,5\%$. Contours 1234x uniform.

plicated by the presence of near-circular intragranular porosity and a more in depth analysis is required.

4.4.4. Electron backscatter diffraction

Electron backscatter diffraction (EBSD) was carried out on wet deformed sample fo21 using the XL30 FEG SEM. This technique provides crystallographic orientation information on a grain to grain basis (see Randle, 1992). Two hundred grains were analysed from five randomly chosen areas, with ~ 40 adjacent grains being measured within each area. Care was taken to keep the orientation of the sample compression direction constant with respect to the microscope reference axis. The electron backscatter patterns (EBSP's) were indexed using software running on the microscope's computer system. The results have been plotted as upper hemisphere, equal area pole figures for the (100), (010) and (001) planes in Figure 4.18. From these projections, it seems that little or no crystallographic preferred orientation (CPO) was developed within wet deformed sample fo21.

4.5. Discussion

4.5.1. Interpretation of mechanical data

Under the conditions imposed in the present experiments, a marked water weakening effect has been observed in the fine-grained forsterite plus 2.5 vol% enstatite ceramic materials used. This effect is apparent in both the HIPing results and from the deformation tests. Densification during HIPing only occurred in wet samples, proving a water enhanced deformation process. In the deformation tests, the dry control sample (fo17) showed purely elastic deformation at 950 °C with a confining pressure (P_c) ~ 600 MPa and strain rates of 1×10^{-6} and $1 \times 10^{-7} \text{ s}^{-1}$ up to stresses of 300 MPa. Wet material (~ 0.5 wt% H₂O), on the other hand, exhibited near steady state flow in constant displacement rate tests with P_c ~ 600 MPa at temperatures in the range 850 - 1000 °C, at strain rates in the range 2×10^{-7} to $5 \times 10^{-5} \text{ s}^{-1}$ with flow stresses in the range of only 9 to 81 MPa. The wet samples are thus at least a factor 16 times weaker at constant strain rate than the ultimate flow strength of the dry material at 950 °C, and a chemical weakening effect is implied.

Polyphase effects on mechanical behaviour are assumed to be relatively unimportant in this system given the low second phase (enstatite) content of only 2.5 volume %. However, the presence of enstatite will have important chemical effects under both dry and wet conditions, with the activity of silica in the system being buffered by the reaction:



Focusing on near steady state flow in the wet samples, the observed stress and temperature dependence of creep has been fitted to a Dorn type power law allowing comparison with microphysical models and previous data. The best fit analysis of data for individual isotherms results in stress exponents (n) ranging from 1.3 to 2.2 which show a systematic decrease with increasing temperature, and the multidimensional best fit for 'all data' yielded $n = 2.14 \pm 0.18$. Comparison of the experimentally

| Mechanism | Stress exponent (n) | Grain size exponent (n) | Diffusion coefficient | Accommodating mechanism | Microstructures |
|--------------------------------------------------------------------------------------------------------------------------------------------------------------------------------------------------------------------------------------------------------------------------------------------------------------------------------------------------------------------------------|--------------------------------------|-------------------------------------------------------------|---------------------------------------------------------------------------------------------------------------------------------------------------|----------------------------------------------------------------------------------------------------------------------------------------------------------------------------------------------------------------------------------------------|-------------------------------------------------------------------------------------------------------------------------------------------------------------------------------------------|
| <p>Dislocation creep</p> <p>Recovery controlled - no distinction made here. (Weertman, 1968, 1978; Frost and Ashby, 1982)</p> <p>Harper-Dorn creep (Harper and Dorn, 1957; Mohamed and Ginter, 1982)</p> | <p>3 to 6.5</p> <p>1</p> | <p>grain size insensitive</p> <p>grain size insensitive</p> | <p>D_v or D_{core}</p> | <p>For 5 independent slip systems no accommodating mechanism is necessary</p> | <p>General microstructural features of dislocation creep:</p> <p>Grain flattening, CPO developed, high dislocation densities, subgrain development, dynamic recrystallisation.</p> |
| <p>Grain boundary sliding (GBS) dominated creep (superplasticity)</p> <p>Plasticity accommodated ($d < \lambda$) (Mukerjee, 1971,1975; Gifkins, 1976, Langdon, 1995)</p> <p>Ashby-Verral type creep (Ashby and Verral, 1973)</p> <p>- diffusion control</p> <p>- interface control (Langdon, 1995)</p> <p>Grain boundary film control (Langdon, 1995)</p> | <p>~2</p> <p>1</p> <p>2</p> <p>1</p> | <p>~2</p> <p>2 or 3</p> <p>2 or 3</p> <p>3</p> | <p>D_{gb}</p> <p>D_v or D_{gb}</p> <p>interface reaction kinetics control</p> <p>D_{film}</p> | <p>Limited intragranular dislocation movement. Grain boundary and mantle dislocations are important.</p> <p>Vacancy diffusion</p> <p>Diffusion</p> <p>Diffusion in a grain boundary amorphous / liquid film or penetrated grain boundary</p> | <p>General microstructural features of superplasticity:</p> <p>fine grain size, equant grains, no CPO, grain boundary cavitation.</p> |
| <p>Diffusion creep:</p> <p>Coble creep (grain boundary diffusion creep; Coble, 1963)</p> <p>Nabarro-Herring creep (lattice diffusion creep; Nabarro, 1948; Herring, 1950, 1951)</p> <p>Solution-precipitation creep (Rutter, 1983; Raj, 1982; Spiers and Schutjens, 1990)</p> | <p>1</p> <p>1</p> <p>1</p> | <p>3</p> <p>2</p> <p>3</p> | <p>D_{gb}</p> <p>D_v</p> <p>D_{liq}</p> | <p>Grain boundary sliding</p> <p>Grain boundary sliding</p> <p>Grain boundary sliding</p> | <p>Grain flattening, no CPO.</p> <p>Grain flattening, no CPO.</p> <p>Grain indentations, truncations and overgrowths.</p> |

Table 4.10. Predicted stress and grain size dependencies from theoretical creep models. D_{gb} is grain boundary diffusivity, D_{core} is dislocation core diffusivity and D_v is volume or lattice diffusivity.

determined stress dependence (n-value) with that expected from models for creep (Poirier, 1985; Ranalli, 1987; see Table 4.10) indicates that the measured stress exponent (n) is *inconsistent* with both pure dislocation creep and pure diffusion creep. The values are however in the range expected for

grain boundary sliding (GBS) dominated mechanisms (superplasticity, see the recent review by Langdon, 1995). The fact that the stress exponent decreases with increasing temperature for the entire set of experiments may indicate that there is a change in relative importance of the diffusion or dislocation mechanism which may be accommodating GBS. Alternatively, the observed behaviour could be transitional between diffusion and dislocation creep with relatively minor amounts of GBS. This might explain the work hardening observed at the higher stresses (if not caused by gold deformation). Unfortunately the grain size dependence of creep, which is a very useful criterion for the identification of the dominant mechanism, has not been determined.

| Author | Species | D_0 ($m^2 s^{-1}$) or $D_0 \delta$ ($m^3 s^{-1}$) | Q ($kJ mol^{-1}$) | T range | Diffusion (K) | Direction Path | conditions |
|--------------------------|---------|---------------------------------------------------------|-----------------------|-------------|----------------|----------------------------|-------------------------------------------------------------|
| Andersson et al., 1989 | Mg | 1.38×10^{-4} | 377 ± 77 | 1373 - 1723 | lattice | [001] | dry |
| Chakraborty et al., 1994 | Mg | 9.6×10^{-4} | 400 ± 60 | 1273 - 1573 | lattice | [001] | dry $fO_2 = 10^{-12}$ |
| Farver et al., 1994 | Mg | 2.1×10^{-10} ($m^3 s^{-1}$) | 343 ± 27 | 1273 - 1573 | grain boundary | not applicable | (wet) $fO_2 = 10^{-13}$ H ₂ + CO ₂ |
| | Mg | 7.7×10^{-10} ($m^3 s^{-1}$) | 376 ± 47 | 1273 - 1573 | grain boundary | | (dry) $fO_2 = 10^{-13}$ CO + CO ₂ |
| Ando et al., 1981 | O | 2.85×10^{-6} | 416 | 1745 - 2007 | lattice | [100] | dry |
| Jaoul et al., 1980 | O | | 320 ± 40 | 1423 - 1873 | lattice | all | dry, independent of fO_2 |
| Reddy et al., 1980 | O | 3.5×10^{-7} | 372 ± 13 | 1548 - 1898 | lattice | [010] | dry |
| Oshi and Ando, 1984 | O | 2.85×10^{-6} | 416 | 1745 - 2007 | lattice | ? | dry |
| Andersson et al., 1989 | O | 6.86×10^{-10} | 302 ± 20 | 1523 - 1723 | lattice | independent of orientation | dry |
| Joaul et al., 1981 | Si | 1.5×10^{-10} | 377 ± 42 | 1573 - 1973 | lattice | all | dry |
| Andersson et al., 1989 | Si | 7.58×10^{-9} | 418 ± 38 | 1523 - 1793 | lattice | independent of orientation | dry MgSiO ₃ buffered |
| | Si | 2.67×10^{-12} | 320 ± 40 | 1523 - 1793 | lattice | as above | dry MgO buffered |

Table 4.11. Representative data for lattice and grain boundary diffusion for pure forsterite from studies in which the activation energy for diffusion has been determined.

The apparent activation energy (Q_c) for creep in the wet samples determined from the unconstrained non-linear best fit analysis ($n \sim 2.1$) has an average value of $\sim 320 \pm 40$ kJ mol⁻¹. A value of ~ 285 kJ mol⁻¹ was obtained from analyzing individual isotherm fits (see Figure 4.10 a,b). These values have been compared with the results from diffusion studies on forsterite (Jaoul et al., 1980, 1981; Reddy et al., 1980; Ando et al., 1981; Oshi and Ando, 1984; Andersson et al., 1989; Chakraborty et al., 1994; Farver et al., 1994; see Table 4.11). From these studies it is clear that silicon is the slowest diffusing species in the forsterite lattice, followed by oxygen and magnesium ($D_{Si} \ll D_O \ll D_{Mg}$). However there is a large degree of overlap between the activation energies for dry lattice-diffusion

of magnesium, oxygen and silicon in forsterite (see Table 4.11) and little data for either dry or wet grain boundary diffusion. From Table 4.11 it can be seen that the range of measured activation energies for dry lattice diffusion (all species), albeit generally measured at temperatures higher than those used in the current experiments, is $360 \pm 58 \text{ kJ mol}^{-1}$ with an average of 371 kJ mol^{-1} . Assuming that grain boundary diffusion is characterized by an activation energy approximately two thirds of the lattice diffusion value (as in metals; following Karato et al., 1986 and Tsenn and Carter, 1987), the range of values expected for dry grain boundary diffusion is $239 \pm 38 \text{ kJ mol}^{-1}$. Moreover, values of $376 \pm 47 \text{ kJ mol}^{-1}$ and $343 \pm 27 \text{ kJ mol}^{-1}$ have been determined by Farver et al. (1994) for dry and wet (in the presence a $\text{H}_2 + \text{CO}_2$ gas mixture) grain boundary diffusion respectively. Thus, the unconstrained apparent activation energy for creep obtained in the present experiments falls within the range of experimentally determined values for both dry lattice diffusion of silicon, oxygen, and magnesium and for wet and dry magnesium grain boundary diffusion in forsterite. The activation energy of $\sim 257 \pm 43 \text{ kJ mol}^{-1}$ for creep, obtained in the current study when constraining the stress exponent to unity, is on the low side compared with the dry lattice diffusion data listed in Table 4.11, or with the inferred values for dry grain boundary diffusion, and may therefore imply the role of fluid enhanced grain boundary diffusion (cf. Yund, 1997). Estimates for the activation energy for wet lattice diffusion (Q_v) and wet grain boundary diffusion (Q_{gb}) can be made from wet dislocation creep data by assuming that the activation energy for wet dislocation creep (Q_d) is equal to that for wet lattice diffusion and that the activation energy for grain boundary diffusion is again two thirds this value (i.e. $Q_d = Q_v$ and $Q_{gb} = (2/3)Q_v$). Tsenn and Carter (1987) carried out just such an analysis and obtained $Q_{gb} = 328.6 \text{ kJ mol}^{-1}$ for wet polycrystalline olivine. Repeating this procedure using the average value for Q_d for wet materials of 462 kJ mol^{-1} from Table 4.1, a value for Q_{gb} of 308 kJ mol^{-1} is obtained. These estimated values for the activation energy for wet grain boundary diffusion are close to the apparent activation energy for creep determined from the present experiments using the unconstrained fit ($320 \pm 40 \text{ kJ mol}^{-1}$) but are significantly higher than that obtained by constraining the stress exponent to unity ($n = 1$). Thus, while the temperature dependence of flow seen in the present wet experiments is consistent in broad terms with expected values for dry lattice diffusion and with the very limited data available for both wet and dry grain boundary diffusion, it is not possible to discriminate from activation energies what kind of diffusive process may have controlled wet deformation. On the other hand, since the dry control sample showed no deformation, dry lattice or grain boundary diffusion can be ruled out as rate controlling processes in the wet tests, leaving wet lattice or grain boundary diffusion as possible candidates.

In summary of the above, it is clearly not possible to draw unambiguous inferences regarding the dominant deformation mechanism, from the present wet experiments using the mechanical data alone. However, the observed stress and temperature dependence are consistent with a) transitional behaviour between water enhanced dislocation and diffusion creep, and b) GBS dominated (superplastic) deformation accommodated by water enhanced diffusion or dislocation activity. Pure dislocation or pure diffusion creep can be ruled out as the dominant deformation mechanism

4.5.2. Interpretation of microstructural observations

The fact that the single *dry* control sample tested in the current study showed little microstructural change compared with the starting material is consistent with its macroscopic elastic behaviour.

Recapping on the microstructure, the *wet* tested samples show a polygonal grain structure with little or no grain shape fabric or crystallographic preferred orientation (CPO). They have undergone little or no grain growth (grain boundary migration) or recrystallisation. Subgrains have not been observed and the dislocation densities are low, with most grains (> 80%) being dislocation free. Noteworthy is the fact that no association of dislocations with the intragranular pores was observed; such pores might be expected to impede dislocations gliding through the grain interiors, pinning them into an immobile configuration (cf. Karato et al., 1986; their figure 12d). Cavities (pores) are present, showing that the intergranular porosity has not only been reduced but redistributed. Equant, polygonal grains with little or no CPO are *inconsistent* with dislocation creep dominated deformation, at least for strains > 10 - 20%. The observed lack of dislocations, even at intragranular pores, also seems inconsistent with dislocation creep as an important deformation mechanism. However, on the basis of the piezometric relation established for olivine by Van der Wal (1993, page 117), it is apparent that the sample grain size ($d \sim 1.2 \mu\text{m}$) is well below the minimum expected average steady state subgrain size (l) of $\sim 6 \mu\text{m}$ appropriate for the maximum flow stress (81 MPa) observed. With $d < l$, dislocations are generally assumed to be free to move through the grains and along grain boundaries (Langdon, 1995) and will not accumulate within the grains. In view of this, and the relatively low strains ($\sim 10\%$) achieved in the present *wet* experiments, neither the low dislocation densities nor the equant grain structure and lack of CPO completely rule out dislocation creep as an important mechanism.

On the other hand, fine grain size, equant grains and lack of a strong CPO are all *consistent* with GBS or diffusion dominated deformation mechanisms. Moreover, the equality $d \leq l$ has been cited as a criterion for the onset of dislocation accommodated GBS (superplasticity) in metals (Langdon, 1995). In addition, the cavitation-like features observed in the *wet* tested samples are also *consistent* with GBS (cf. Walker et al., 1990), resembling the cavities formed during superplastic and diffusional flow in unconfined metals and ceramics (e.g. Chokshi and Langdon, 1987; Blanchard and Chan, 1993). Furthermore, the growth of cavities during superplasticity has been shown to be promoted as the ratio of the mean effective stress to the differential stress is decreased (Pilling and Ridley, 1988; Chokshi and Mukherjee, 1993). Therefore, cavitation in the materials studied here is *consistent* with the inferred high fluid pressures in the current *wet* experiments (~ 600 MPa), implied by the final porosities of the samples and the mass of water added, and the corresponding low effective pressures (see Section 6.5.1). *All* of the microstructural features observed in the *wet* samples are thus *consistent* with plasticity- or diffusion-accommodated GBS dominated deformation mechanisms (see Table 4.10).

On the basis of these arguments, it is clear that the microstructures observed in the *wet*-tested samples support the inference drawn from the mechanical data that deformation was dominated by GBS (accommodated by either dislocation motion or diffusion) or by transitional behaviour

between dislocation and diffusion creep with minor sliding. However, it is still not possible to discriminate further between these possible mechanisms with certainty, although the striking absence of dislocation microstructures (especially at intragranular pores) may favour GBS mechanisms.

4.5.3. Comparison with previous experiments

Several previous studies have shown that the flow behaviour of fine-grained olivine at low stresses is characterized by stress exponents in the range $n = 1.5 \pm 0.5$ (see Table 4.2) and water weakening effects comparable with those reported here have been observed in the GSS regime (Karato et al., 1986). As indicated in the introduction, previously determined values for the activation energies for both wet and dry creep in fine grained olivine have, with one exception (Rutter and Brodie, 1988), been determined at high temperatures > 1200 °C (Cooper and Kohlstedt, 1984a; Chopra, 1986; Hirth and Kohlstedt, 1995a) and this must be borne in mind when making comparisons with the present results. In general, the values determined for dry fine-grained olivine have been found to be close to the values for activation energies for dry lattice diffusion in olivine (Cooper and Kohlstedt, 1984a - 380 kJ mol⁻¹; Hirth and Kohlstedt, 1995a - 315 kJ mol⁻¹; see Tables 4.2 and 4.10), whereas those for wet fine-grained olivine are significantly lower, at $\sim 240 \pm 50$ kJ mol⁻¹ (Chopra, 1986; Rutter and Brodie, 1988). Furthermore, the apparent activation energies for creep in both dry and wet fine-grained olivine materials are in general lower than the apparent activation energies determined for wet GSI dislocation creep in coarser materials which have a mean value of ~ 462 kJ mol⁻¹ (see Table 4.1). Moving now to the role of grain size, grain size exponents for creep in fine-grained olivine tested under both wet and dry conditions have been found to be close to -3 (Cooper and Kohlstedt, 1984a; Karato et al., 1986; Karato, 1989b; Wolfenstine and Kohlstedt, 1994; Hirth and Kohlstedt, 1995a) which is a value consistent with grain boundary diffusion control (Coble, 1963; Ashby and Verral, 1977; see Table 4.11). Microstructural observations from previous studies have often found equant grains (e.g. Chopra, 1986; Karato et al., 1986) with little or no CPO (Karato et al., 1986) and several studies have inferred the importance of GBS accommodated primarily by diffusion (Karato et al., 1986; Rutter and Brodie, 1988). Strong variations in dislocation densities between individual grains within single samples have also been observed in a number of studies and interpreted as indicating some role of dislocation motion in accommodating GBS (Karato et al., 1986; cf. calcite, Schmid et al., 1977).

Clearly the findings from the current study are broadly consistent with previous work on fine-grained olivine. Taking into account the grain size dependence of deformation reported by other workers, the implication is that the most likely mechanism in the present wet experiments is GBS predominantly, with (water enhanced) grain boundary diffusion and/or dislocation accommodation (see Table 4.10). Note, however, that the flow behaviour observed in previous experiments and here is also broadly consistent with a gradual transition between water-enhanced dislocation and diffusion creep regimes with only minor sliding.

Another alternative, Harper-Dorn (H-D) creep, has been proposed by Wang as a mechanism leading to low n -value (strictly Newtonian) rheology in polycrystalline materials including olivine (Wang and Langdon, 1994; Wang, 1994). H-D creep is believed to be a dislocation climb controlled process and is *independent* of grain size (Harper and Dorn, 1957; Mohamed and Ginter, 1982). Wang's

reanalysis of the low n data of Karato et al. (1986) claims a possible role of H-D creep (Wang, 1994). However, his analysis reveals a strong grain size dependence for $d < 15 \mu\text{m}$ and $d < 30 \mu\text{m}$ for wet and dry samples, respectively. Accordingly, H-D creep is not believed to be an important mechanism at the fine grain sizes used in the current study.

To conclude, comparison of the current findings for wet fine-grained forsterite with data from previous studies points to the role of GBS with grain boundary diffusion and/or dislocation controlled accommodation, but this still needs to be directly demonstrated for the material under investigation.

4.5.4. *The role of water*

Water may facilitate deformation in a number of ways, both chemical and physical. However, in line with the conclusions drawn above, it seems likely that the key role of water in the current experiments will be to affect GBS and the processes accommodating GBS. In principle, water may enable the accommodation of GBS by enhancing the kinetics of either dislocation creep or diffusion mechanisms via the introduction of water related point defects, leading to a change from intrinsic to extrinsic lattice diffusion. Alternatively, water may enhance grain boundary diffusivity by affecting the grain boundary defect structure, by enabling solution-precipitation mechanisms such as pressure solution, or by causing the formation of thin grain boundary melt-films due to wet melting. No direct evidence of melting has yet been observed in the samples studied and the system is well away from the equilibrium wet solidus (see Section 6.4.1). On the other hand, the TEM observations of contrast features suggesting the presence of tiny inclusions within the grain boundaries of the wet tested samples may indicate that the grain boundaries have been penetrated by fluid or melt, or that there has been precipitation in the grain boundaries on cooling. Overall, it thus seems likely that the samples deformed by GBS with grain boundary diffusion as the accommodating mechanism, this being enhanced by one of the above grain boundary processes. The presence of a high pressure pore fluid may also have physical effects on the system such as the reduction of effective stress, though these effects are likely to be minor due to the low volume fraction and presumably disconnected nature of the fluid phase. However, they may be important immediately adjacent to cavities. The details of the role of water in these materials is obviously of key importance and will be addressed more specifically in Chapter 6.

4.5.5. *Empirical flow relation and its implications*

It has been argued above that the mechanism of deformation most consistent with the results obtained for the wet-tested samples is one of GBS accommodated by diffusion and/or dislocation motion. Since uncertainty remains, however, no attempt has been made to fit a microphysically based model for a specific GBS - dominated mechanism (see Table 4.10) to describe the measured flow behaviour. Rather, the choice is made here to adopt the empirical description obtained (in Section 4.3) by fitting the Dorn equation to the data set identified as 'all data'. Making use of the corresponding parameter values listed in Table 4.8, the flow equation which results is written

$$\dot{\epsilon} = \exp(10 \cdot 22) \cdot \exp\left(\frac{-302000}{RT}\right) \cdot \sigma^{2.14} \quad 4.6$$

where $\dot{\epsilon}$ is in s^{-1} , and σ is in MPa. Since this equation is characterized by an n -value of ~ 2 it is consistent with a variety of models for GBS dominated flow (see Table 4.10), but is purely empirical in status. As seen from Table 4.8, an almost identical relation is obtained by fitting the Dorn equation to the 'selected data' set, so that separate treatment is not needed.

The flow behaviour described by equation 4.6 is now compared, at a temperature of 1173 K (900 °C), with a) the actual experimental data from which it is derived, b) the best fit to the 'all data' set obtained by constraining $n = 1$ (see Table 4.8), and c) extrapolations of the GSS flow laws for wet fine-grained olivine obtained by Karato et al. (1986) and Rutter and Brodie (1988); see Figure 4.19. From this Figure, it is evident that the chosen equation (Equation 4.6) forms a good fit to the present experimental data whereas the constrained fit ($n = 1$) is poor. In addition, it is apparent that the flow laws of Karato et al. (1986) and Rutter and Brodie (1988), which also take $n = 1$, predict flow stresses which are 1 to 2 orders of magnitude lower than those observed in the current experiments.

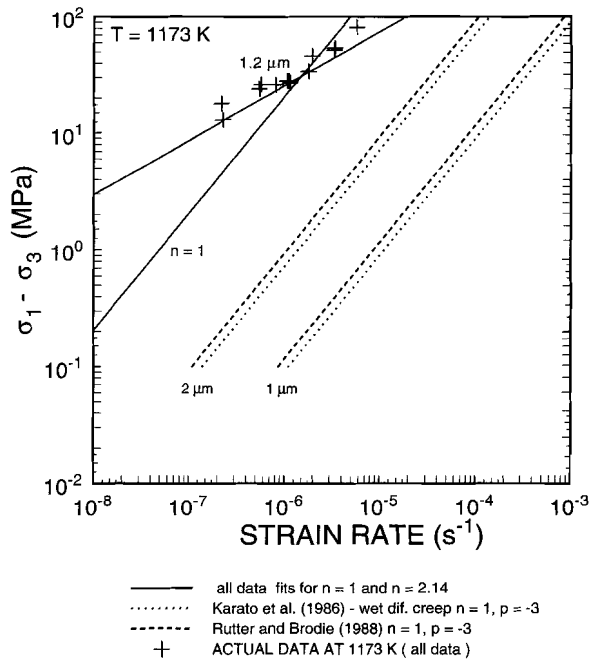


Figure 4.19. Comparison of observed flow behaviour at 1173 K with flow relations for wet polycrystalline olivine from this study, Karato et al. (1986) and Rutter and Brodie (1988). Crosses - show experimental data from this study (all data). Solid lines - flow equation 4.6 and data from this study constrained to $n = 1$. Dotted lines - predicted flow behaviour from Karato et al. (1986) at grain sizes of 1 and 2 μm . Stippled lines - predicted flow behaviour from Rutter and Brodie (1988) at grain sizes of 1 and 2 μm .

These previous flow equations were obtained for Fe-bearing systems and, therefore, may better represent the behaviour of natural olivine. On the other hand, in constructing Figure 4.19 they have been extrapolated far, in both grain size and temperature, from the conditions under which they were determined.

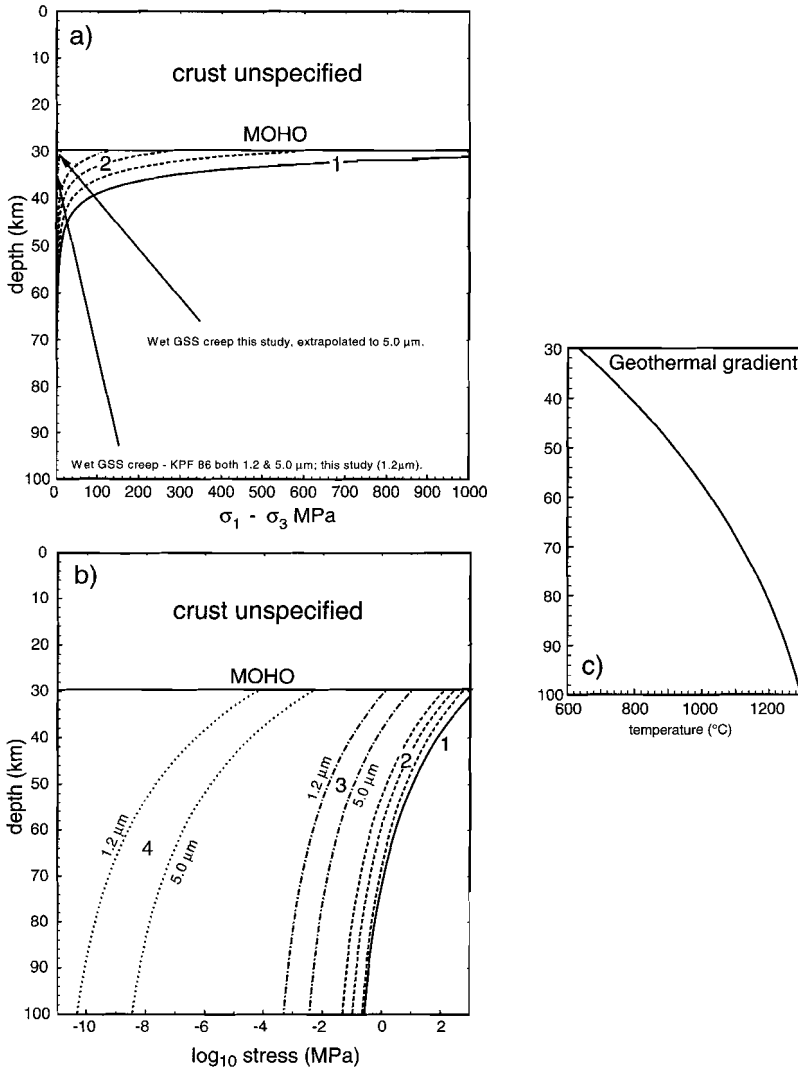


Figure 4.20 a,b,c. Strength profiles and geothermal gradient for the upper mantle in a tectonic setting corresponding to extension/rifting of the continental lithosphere. a) linear axes: 1 (solid-line), dry dislocation creep at a strain rate of $1.83 \times 10^{-15} \text{ s}^{-1}$; 2 (dashed-lines) wet dislocation creep at strain rates of (from left to right) 1.83×10^{-15} , 1.83×10^{-14} and $1.83 \times 10^{-13} \text{ s}^{-1}$; the arrows indicate the low strength of GSS mechanisms indicated at a strain rate of $1.83 \times 10^{-13} \text{ s}^{-1}$. b) Log flow stress versus depth plot. 1 and 2 as in (a); 3 (dot-dash lines), wet flow relation from this study plotted for the grain sizes indicated and at a strain rate of $1.83 \times 10^{-13} \text{ s}^{-1}$; 4 (dotted-lines) wet diffusion creep extrapolated using data from Karato et al., 1986 to the grain sizes indicated, taking a strain rate of $1.83 \times 10^{-13} \text{ s}^{-1}$. The dislocation creep data also come from Karato et al. (1986). c) Geothermal gradient as used by Vissers et al. (1995).

The empirical flow equation (Equation 4.6) for wet, fine-grained olivine presented above can now be extrapolated to geological strain rates in an attempt to describe the rheology of hydrous, fine-grained peridotite mylonites zones of the type recognized by Vissers et al. (1995) as possibly playing a major role in reducing the strength of the lithospheric upper mantle during continental rifting. The application of the current flow equation to the appropriate conditions involves relatively little extrapolation in terms of grain size and temperature when compared to the application by Vissers et al. (1995) of the data of Karato et al. (1986). Extrapolation in strain rate is considered justified by the fact that Vissers et al. (1995) inferred, from microstructural evidence, the importance of a GSS diffusion accommodated GBS mechanism for the Erro-Tobbio mylonites. Figure 4.20, which shows strength profiles for the lithospheric upper mantle, has been constructed using a geotherm appropriate for the initial stages of uniform extension of the continental lithosphere (Vissers et al., 1995). Three strain rates have been chosen, namely $1.83 \times 10^{-15} \text{ s}^{-1}$ (appropriate for homogeneous extension), $1.83 \times 10^{-14} \text{ s}^{-1}$ (appropriate for deformation in a 5 km tectonite shear zone following Vissers et al., 1995) and $1.83 \times 10^{-13} \text{ s}^{-1}$ (appropriate for deformation in a 500 m wide hydrated mylonite shear zone following Vissers et al., 1995). Strength profiles have been drawn using flow equations from Karato et al. (1986) for dry dislocation creep at a strain rate of $1.83 \times 10^{-15} \text{ s}^{-1}$ (curve 1 in Figure 4.20 a,b), wet dislocation creep at strain rates of 1.83×10^{-15} , 1.83×10^{-14} and $1.83 \times 10^{-13} \text{ s}^{-1}$ (curves labelled 2 in Figure 4.20 a,b), and for wet diffusion creep extrapolated to grain sizes of 1.2 μm (comparable with the current experiments) and 5.0 μm (mid-range for the grain sizes observed in fine-grained domains within the Erro-Tobbio mylonites; curves labelled 4 in Figure 4.20b). Additional profiles have been drawn using the current wet data (Eqn 4.6) for strain rates of $1.83 \times 10^{-13} \text{ s}^{-1}$, both unextrapolated in grain size (i.e. for $\sim 1.2 \mu\text{m}$ material) and extrapolated to 5.0 μm (curves labelled 3 in Figure 4.20b). The extrapolation of equation 4.6 in grain size was carried out assuming a d^{-3} grain size dependence as this is the strongest grain size dependence expected for a GSS mechanism, and thus leads to an upper bound estimate. From the strength profiles, it is clear that the GSS mechanisms are substantially weaker than both dry and wet dislocation creep over the range of strain rates plotted. The strength profiles based on the results of the current study fall between those for wet dislocation and wet diffusion creep based on Karato et al. (1986) with a maximum flow stress of $\sim 10 \text{ MPa}$ at the MOHO (for 5 μm grain size). Nonetheless, the experimental results of this study imply a dramatic weakening of the lithospheric upper mantle (top 20 km) during extension, if deformation becomes localized into fine-grained mylonites, rather than occurring by wet or dry dislocation creep in either a wide tectonite shear zone or more homogeneously deforming mantle. This is most apparent from the linear plot (Figure 4.20 a), in which the integrated strength of the lithospheric upper mantle is represented by the area under the curves. Bearing in mind the chemically simple (Fe-free) nature of the system investigated and uncertainties regarding the water content of (or activity in) natural materials, it is arguable whether the present results can be directly applied to natural compositions. However, it seems reasonable to suppose that the weakening observed is also to be expected in wet natural fine-grained Fe-bearing olivine under similar conditions. The results described here therefore provide additional evidence for the role of wet GSS creep in olivine at temperatures appropriate for the top of the upper mantle, under conditions where no (appreciable) melting occurs. These findings support the conclusion of Vissers et al. (1995) that localization of deformation into wet fine-

grained mylonites shear zones implies a dramatic weakening of the upper lithospheric mantle. Extrapolation to other mantle conditions is probably not useful since this would require large extrapolations in temperature, grain size, strain rate and mineral chemistry, and since the roles of water and enstatite content are unknown.

4.6. Conclusions

The deformation behaviour of HIPed synthetic dunite (forsterite plus 2.5 vol. % enstatite ceramics) with a grain size of 1.2 μm has been investigated with and without added water (~ 0.5 wt%) in combined displacement rate and temperature stepping/cycling tests, using a gas medium deformation apparatus operated at a confining pressure of ~ 600 MPa. The results demonstrate that, whereas dry material behaves purely elastically at 950 °C and strain rates of 1×10^{-6} and $1 \times 10^{-7} \text{ s}^{-1}$, wet samples deform by near steady state flow at temperatures between 850–1000 °C, strain rates between 5×10^{-5} and $2 \times 10^{-7} \text{ s}^{-1}$ and flow stresses between 9 and 81 MPa. Strains up to 12% have been achieved in the wet samples.

The stress and temperature dependence of flow rate observed in the wet samples has been fitted to a Dorn type power law. This analysis results in stress exponents (n) ranging from 1.3 to 2.2 for individual isotherm fits, and a value of $\sim 2.1 \pm 0.18$ for full multidimensional regression analysis. The value of apparent activation energy for creep has been determined as ~ 285 and $320 \pm 40 \text{ kJ mol}^{-1}$ from the isothermal and full regression fits respectively. The wet deformed samples show equant, polygonal grains and no crystallographic preferred orientation. The grains have undergone little or no grain growth or recrystallization. Sub-grains were not observed and dislocation densities appear to be zero in most grains. Cavities are observed along grain boundaries and may be continuous for several grains. Pores, isolated on grain boundaries, show apparent dihedral angles $< 60^\circ$ and the grain boundaries appear to have been wetted during deformation. Comparison of the mechanical data and microstructural observations with both microphysical models for creep and previous work on fine-grained olivine leads to the conclusion that the wet samples have probably deformed by a grain size sensitive (GSS) grain boundary sliding (GBS) dominated mechanism, though the exact nature of the mechanism accommodating GBS remains unclear, and the possibility of transitional behaviour between dislocation creep and diffusion creep cannot be eliminated. The flow behaviour observed in the wet samples is, in general, consistent with the findings of Karato et al. (1986) for fine-grained iron-bearing olivine although the materials in the present study are somewhat stronger.

Extrapolation of the flow equation determined for the wet material to natural strain rates of the order expected in hydrated, peridotite mylonites confirm the prediction of Vissers et al. (1995) that localized deformation in upper mantle shear zones, under conditions corresponding to lithospheric extension/rifting, will lead to a highly significant weakening of the upper 10 to 20 km of the lithospheric upper mantle when compared to localized flow by wet dislocation creep.

The effect of varying enstatite content on the deformation behaviour of fine-grained synthetic peridotite

5.1. Introduction

It has been conventionally assumed that upper mantle rheology will be controlled by the flow behaviour of the dominant phase, olivine, and that the rheology of the upper/middle crust will be controlled by the flow behaviour of quartz. Accordingly, most experimental studies addressing the steady state flow behaviour of upper mantle and crustal materials have focused, for simplicity, on systems composed more or less entirely of olivine or quartz (e.g. Chopra and Paterson, 1981, 1984; Chopra 1986; and Karato et al., 1986 for olivine; Jaoul et al., 1984; Kronenberg and Tullis, 1984; Koch et al., 1989; Paterson and Luan, 1990 for quartz). However, natural rocks are generally polyphase, often with significant fractions of secondary phases. It is important, therefore, to understand the possible effects of secondary phases on rheology before simply applying (near) single-phase flow data to natural systems (Fliervoet, 1995).

The possible effects of the additional phases on bulk rheology have been considered by various authors (see reviews by Evans and Dresen, 1991 and Bons, 1993). These effects are complex and so far poorly understood. In general terms, the strength of a two-phase material is related to factors such as the relative strengths of the two phases, the operative deformation mechanisms and the size, shape and dispersion of the grains. A key point, however, is that the addition of a second phase can lead to both physical and chemical interactions with the matrix phase, which may influence the behaviour of the matrix and/or additive phase.

In the absence of major chemical or physical interaction effects, the deformation behaviour of a two-phase material is broadly speaking some weighed average of the properties of the individual phases (see Tullis et al., 1991). However, when physical interactions occur, more complex behaviour results. For example, dispersed rigid inclusions (precipitates) may lead to hardening of materials if they form obstacles to dislocation glide (e.g. Humphreys, 1985). On the other hand, small volume fractions (~ 5 vol. %) of rigid particles have been observed to weaken superplastically deforming metals by promoting grain refinement (e.g. Humphreys and Kalu, 1990; Yoon and Chen, 1990). Important chemical interaction effects associated with the addition of a second phase and affecting bulk rheology include a) changes in point defect chemistry which may influence diffusion rates and dislocation mobility in both phases, b) interphase boundary diffusion (Martin and Perrillon, 1979), and c) coupled effects related to the presence of interphase boundaries, involving stress induced interface reac-

tions, interphase boundary migration and interphase boundary diffusion (Chen, 1982, 1985; Wheeler, 1992). The latter lead to rate control by the fastest rather than the slowest diffusing species and can therefore produce weakening relative to regular grain boundary diffusion creep in the pure phases.

As already indicated, most previous experimental work on the rheology of the upper mantle has focused on nearly single-phase olivine starting materials under the assumption that this predominant constituent will dominate upper mantle flow behaviour. However, natural upper mantle materials (peridotites) consist of olivine with significant amounts of one or more additional phases, e.g. orthopyroxene, clinopyroxene, plagioclase, spinel and garnet. Possible polyphase effects cannot therefore be neglected. Although many of the natural dunites used in previous experimental studies contain several percent of secondary phases (e.g. Chopra and Paterson, 1981, 1984), only very few studies, using synthetic aggregates, have specifically attempted to systematically study the role of second phase content on olivine rheology (Hitchings et al., 1989; Gleason et al., 1994; Daines and Kohlstedt, 1996). In essence these have shown that, for dry olivine–orthopyroxene materials deforming in the dislocation creep field, the two-phase materials are weaker than the end-members (Hitchings et al., 1989; Daines and Kohlstedt, 1996). For example, at a constant strain rate of $1 \times 10^{-5} \text{ s}^{-1}$ Hitchings et al. (1989) determined flow stresses of ~ 200 and ~ 100 MPa for olivine and olivine plus 30% orthopyroxene respectively (at 1500 K and 300 MPa confining pressure). The role of a second phase in buffering the point defect chemistry of olivine is well known. For example, Ricoult and Kohlstedt (1985) reported that Fe-bearing olivine single crystals buffered with orthopyroxene deform ten times faster than magnesio-wüstite buffered samples at constant stress. Also focusing on dislocation creep, Gleason et al. (1994) investigated the effect of changing the second phase from 3% MgO to 3% enstatite in forsterite materials and showed that the MgO-bearing samples were a factor of 2 times stronger at constant strain rate than the enstatite-buffered samples and interpreted the results in terms of the role of composition dependent melting temperature (T_m) and thus homologous temperature. However, these effects are similar to those attributed by several studies to oxide activity buffering of point defect chemistry (see Smyth and Stocker, 1975; Stocker and Smyth, 1978; Hobbs, 1983), which may be the ultimate cause of the effects observed by Gleason et al. (1994). In contrast, for low stress (< 100 MPa) deformation in the diffusion creep field ($n \sim 1.2$) at temperatures between 1150 and 1255 °C, strain rates between 1×10^{-7} and $1 \times 10^{-3} \text{ s}^{-1}$ at 300 MPa gas confining pressure, Daines and Kohlstedt (1996) report no effect of orthopyroxene content on flow strength of dry, olivine–orthopyroxene aggregates across a large range of enstatite contents (5, 50, 95% enstatite).

Aside from these experimental findings on the effect of orthopyroxene content on olivine/dunite rheology, Wheeler (1992) has developed a theory for Coble creep in polyphase systems (cf. Chen, 1982). This predicts a weakening in the forsterite/enstatite system with respect to flow of the end members by Coble creep (grain boundary diffusion control). In Wheeler's model, since forsterite and enstatite have MgO and SiO₂ components in common, deformation can be accommodated by the interphase boundary diffusion of either component away from stressed interphase boundaries, combined with interphase boundary migration perpendicular to the grain boundary. In other words, it is possible to produce strain at a stressed forsterite–enstatite boundary either by diffusion of silica combined with the production of forsterite or by the diffusion of MgO combined with the production of enstatite. This implies that the deformation rate and microstructure will be controlled by the fastest

diffusing species, if the kinetics of the interface reactions are rapid, thus producing weakening. Furthermore, the degree of weakening predicted for the two-phase (fo + en) materials compared with single-phase material will be related to the ratio of the diffusivities of SiO₂ and MgO. Unfortunately, data for the interphase boundary diffusivities of the individual species are not available and therefore estimates of the absolute weakening expected cannot be made. However, for these effects to be important a high proportion of interphase boundaries are required, implying high second phase contents.

On the basis of the experimental data reviewed above, it appears that the addition of enstatite to forsterite produces a weakening effect in the dislocation creep field (Hitchings et al., 1989; Daines and Kohlstedt, 1996) with little effect in the diffusion creep (low n) field (Daines and Kohlstedt, 1996). However, the available data are extremely limited and the observed behaviour is poorly understood and only partly consistent with theoretical expectations. In the interests of applying laboratory data to the upper mantle, the question of the effect of enstatite content on the flow behaviour of olivine needs further investigation. An issue of particular interest is the effect of enstatite content on the flow of fine-grained, forsterite-enstatite aggregates under wet conditions. The behaviour of this material is relevant to hydrated peridotite mylonite zones which may play an important role in controlling lithospheric strength as discussed by Vissers et al. (1995; see Chapter 4).

The present Chapter describes an attempt to systematically study the role of second phase (enstatite) content on the flow behaviour of wet fine-grained forsterite-plus-enstatite materials for enstatite contents in the range 1 to 20 vol%. It represents an extension of the work on wet forsterite plus ~ 2.5 vol% enstatite materials reported in Chapter 4, and is relevant to understanding the effects of second phases on rheology in general, as well as on peridotite and peridotite mylonite flow behaviour in particular.

5.2. Experiments

The experiments reported here consist of a series of 12 tests on synthetic forsterite-plus-enstatite ceramic materials, presented along with results from run fo21 previously reported in Chapter 4. The experiments were performed with ~ 0.5 wt% water added to the samples. The initially porous samples (~ 8 %) were first hot isostatically pressed (HIPed; at ~ 600 MPa and 1223 K for 24 hours) and then directly deformed in a gas apparatus, using displacement rate and temperature stepping methods, at strain rates in the order of 10⁻⁷ to 10⁻⁵ s⁻¹, temperatures between 1123 and 1279 K and a confining pressure of ~ 600 MPa. The enstatite content of the samples was varied from 0 to 20 vol%, a range chosen to avoid significant mechanical contact between enstatite grains (Scher and Zallen, 1970; Bouvard and Lange, 1991; Isichenko, 1992).

5.2.1. Sample preparation

The nominally pure forsterite and forsterite-plus-enstatite ceramic samples used in the total of 13 experiments described here consisted of right cylinders (10 mm diameter by 25 mm in length) cored from sintered billets with varying enstatite contents. The billets were produced in 6 batches (Table

5.1; i.e. starting materials - stm 15, 19, 26, 30.31.32, 35.36.37 and 38.39.40) using the sol-gel based fabrication method described in Chapter 2. The starting ceramic samples were characterized by enstatite contents 0, 1, 2.5, 15 and 20 volume percent, mean grain sizes ranging from 1 to 2 μm and post-sintering (i.e. pre-HIPing) porosities ranging between 7.1 and 9.2 % (see Table 5.1). Porosities were determined using the Archimedes method (see Chapter 2) and by comparison of the theoretical density with the densities calculated from the sample dimensions and the dry weight (values in brackets in Table 5.1). The enstatite content data are based on the bulk reagent proportions (after appropriate yield corrections) used during synthesis alone, and have been checked using powder X-ray diffraction (XRD) analysis of the starting materials as sintered (see appendix) and, in the case of samples fo19, fo21, fo31 and fo34, also by point-count estimates from chemical analyses obtained using energy dispersive X-ray analyses on the Philips CM 200 transmission electron microscope.

| Expt. No. | Gel Batch | Vol % en | Sintering temperature (K) and duration (mins) | Initial porosity (%) | wt% water |
|-----------|-------------|----------|-----------------------------------------------|----------------------|-----------|
| fo10 | stm15 | 1 | 1723:120 | 8.2 (8.6) | 0.46 |
| fo11 | stm15 | 1 | 1723:120 | 8.0 (8.2) | 0.36 |
| fo12 | stm15 | 1 | 1723:120 | 8.8 (9.7) | 0.52 |
| fo13 | stm15 | 1 | 1723:120 | 8.8 (8.8) | 0.53 |
| fo16 | stm19 | 0 | 1755:420 | 7.1 (7.6) | 0.59 |
| fo18 | stm26 | 2 | 1723:84 | 8.2 (8.5) | 0.44 |
| fo19 | stm26 | 2 | 1723:84 | 8.1 (8.3) | 0.44 |
| fo20 | stm26 | 2 | 1723:66 | 9.2 (9.7) | 0.51 |
| fo21 | stm30.31.32 | 2.5 | 1673:60 | 8.4 (8.6) | 0.46 |
| fo31 | stm35.36.37 | 15 | 1673:42 | 8.1 (8.4) | 0.46 |
| fo33 | stm35.36.37 | 15 | 1673:36 | 8.6 (8.8) | 0.41 |
| fo34 | stm38.39.40 | 20 | 1673:96 | 8.4 (9.1) | 0.45 |
| fo35 | stm38.39.40 | 20 | 1673:96 | 8.5 (8.8) | 0.43 |

Table 5.1. Initial composition, sintering conditions, porosity and water contents.

Before HIPing and mechanical testing, the machined samples were cleaned using distilled water and dried in an oven at 200 °C for 24 hours. Drying for longer produced no further weight loss and it was assumed that this treatment was sufficient to dry the samples to water contents below the resolution of the balance used (~ 0.002 wt%). Subsequently, water was introduced into each sample by immersion in distilled water under vacuum for ~ 10 minutes. The vacuum was then vented to air and the sample left in the water for up to one hour to allow infiltration. It was then carefully dried at ~ 95 °C until the desired final weight, corresponding nominally to ~ 0.5 wt% water (see Table 5.1), was achieved. Finally each sample was encapsulated in a gold jacketing tube (0.2 mm wall thickness) sealed at each end with a welded-in end-closure cup made from gold foil (0.25 mm thick). Loss of water was avoided during welding by placing the sample in an ice-cooled block (see Chapter 3).

5.2.2. Deformation apparatus

The encapsulated samples were hot isostatically pressed and subsequently deformed in axisymmetric compression mode using the constant volume, gas-medium deformation apparatus described in Chapter 3. This apparatus consists of a horizontally mounted 1 GPa pressure vessel with an internal furnace module. During deformation experiments, axial force is applied to the sample by using an Instron 1362 testing machine to advance the pressure compensation yoke and dynamically sealed deformation piston assembly. The force on the sample is measured using an internal force gauge (100 kN full scale with a ~ 20 N resolution). Piston displacement is measured externally using the Instron ram displacement transducer and gas pressure is measured using a strain gauge type pressure transducer. The internal, three-zone Kanthal-AF wire furnace is controlled using a proportional-integral-differential (PID) controller in combination with an S-type primary control thermocouple located adjacent to the windings of the near load cell furnace zone. Sample temperature is monitored using 3 S-type sample thermocouples placed adjacent to the capsule (see Figure 3.8b). Calibration runs have shown that temperature gradients within the sample are of the order of 1 to 2 °C, and that the sample temperature can be assumed to equal that measured by the centre thermocouple (see Chapter 3).

5.2.3. Hot isostatic pressing stage

In setting up individual experiments, the jacketed sample was first inserted into the apparatus and the vessel was flushed and pressurized with argon gas to ~ 600 MPa at room temperature. After allowing several hours to check for leaks, the external water cooling system was turned on. The sample was then brought to a temperature of 1223 K, maintaining the pressure at ~ 600 MPa.

Once both pressure and temperature stabilized (after ~ 15 minutes), the deformation piston was advanced until a signal was obtained from the internal force gauge, corresponding to the application of a small force (~ 200 N) to the sample. The initial touch position was noted and the sample was then left to hot isostatically press (HIP) for ~ 24 hours. After HIPing, a new touch point was found and the measured displacement was used to calculate the amount of compaction undergone by the sample and its new (post-HIPing) porosity, assuming isotropic strain. The small touch-point load was then removed from the sample and the base load cell output signal, corresponding to zero load at the confining pressure ~ 600 MPa used throughout all tests, was determined. Note that one sample (fo11) was removed after HIPing in order to test the accuracy of the approach used to calculate the post-HIPing sample dimensions and porosity, based on the measured Instron displacement and the assumption of isotropic strain. The results indicated that the post-HIPing sample dimensions, and therefore post-HIPing porosity, could be calculated from the measured Instron displacements with relative errors of ± 0.5 % and 10 % respectively.

5.2.4. Deformation testing procedure

To initiate the deformation stage of each experiment, the Instron testing machine was run in position-control mode to advance the deformation piston so as to shorten the sample at a constant displacement rate. Experiments were performed using both displacement rate and temperature stepping methods at strain rates between 2×10^{-7} and $3 \times 10^{-5} \text{ s}^{-1}$, and temperatures between 1123 and 1279 K (850 - 1006 °C). Displacement rate (and hence strain rate) stepping was achieved by programming the Instron ramp function generator in a stepwise manner, allowing 1-2 % strain per step. In the earlier runs (test/sample numbers fo18, fo19 and fo20), temperature stepping was carried out by changing the set point on the temperature controller during continuous deformation. However, this method was found to be unsatisfactory due to the introduction of pressure and force transients, producing spikes on the resulting stress versus strain curves. Subsequent temperature stepping tests (fo21, fo25, fo33 and fo34) were therefore carried out by halting deformation and completely unloading the sample prior to changing the temperature. When the new temperature was found to be stable and the pressure had been readjusted to 600 MPa, the test was resumed with a new touch point and new base load cell output.

After ~ 10 % strain was achieved, the tests were terminated as follows (see also Chapter 3). First, the deformation piston was halted and the sample completely unloaded. The final (unloaded) load cell output signal was then checked while still at test pressure and temperature, and the furnace was switched off. The sample reached room temperature within ~ 10 minutes, with a confining pressure of ~ 400 MPa remaining at this temperature. The gas was then released slowly from the vessel. The seals were subsequently allowed to relax for ~12 hours before the vessel was opened and the deformed sample removed. The encapsulated samples were then reweighed to check that no water had been lost. Lastly, the capsules were opened and the final dimensions of the samples measured.

5.2.5. Data acquisition and processing

The conditioned output signals from the internal force gauge, gas pressure transducer, Instron position transducer, external Instron force gauge and the three sample and one primary control thermocouples (S-type) were logged using two IBM-compatible personal computers. In calculating the axial stress and sample strain as a function of time, the internal force gauge readings were corrected for pressure effects on the load cell output and the measured displacement data were corrected for apparatus stiffness (see Chapter 3 for details). Sample temperature within a given HIPing, strain rate or temperature step was calculated as the average (settled) value for the step as measured by the central sample thermocouple. From the estimated post-HIPing porosities and the measured final porosities, it is clear that a post-HIPing densification of several percent took place during deformation. This compaction was neglected when calculating the stress on the sample, i.e. constant volume was assumed. Consider now the contribution to measured strain of the thin gold sheets (capsule end-walls) separating the sample from the piston anvils. Taken together, the gold capsule end-walls have an initial thickness of $2 \times 0.25 \text{ mm}$. During the test these become deformed. However, flow of the gold is strongly restricted by the piston anvils and trial experiments, performed using rigid ceramic test pieces, have shown that significant deformation of the gold typically requires axial stresses in excess of 50 to 60 MPa under the conditions of the experiments reported here. Moreover, measure-

ment of the final gold thickness after individual tests reaching stresses up to 100 MPa has shown that gold deformation then contributes a maximum of 0.1 mm to the measured displacement, which is equivalent to 0.4 % strain. Since the stresses achieved in steps where near steady state was achieved mostly fall below or close to 60 MPa (see Table 5.3), no attempt has been made to correct for this gold deformation in calculating the stress strain curves for wet samples. Strain rate or temperature steps reaching higher stresses may be affected, thus showing strains up to 0.4 % greater than actually achieved in the sample. On the other hand, in cases where steady state flow is approached, gold deformation of this order will not significantly affect interpretation of the data in terms of near steady state flow and corresponding strain rate. Note that several of the high stress steps shown in the stress strain curves clearly remain far from steady state and these have been treated accordingly (see Table 5.3). In conclusion, taking into account all errors, the internal force measurements are accurate to ~ 1 % of the measured value and displacements to within ~ 2 μm .

5.3. Results

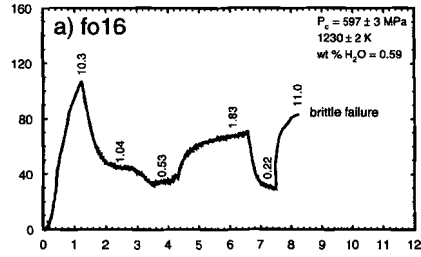
5.3.1. Mechanical results

The post-HIPing porosities obtained from the touch point data for each test (Table 5.2) show that all samples densified during the initial 24 hour HIPing stage at 1223 K and 600 MPa. However, the estimated densification was variable, ranging from between 2.4 % for sample fo16 and 5.8 % densification for sample fo21. Note that the values are more consistent within each batch of material; no

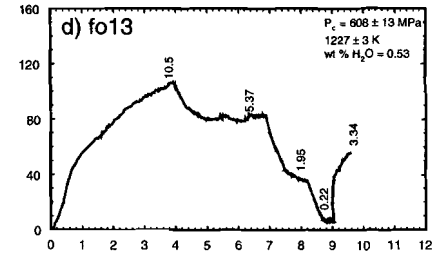
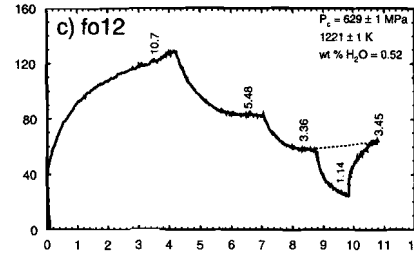
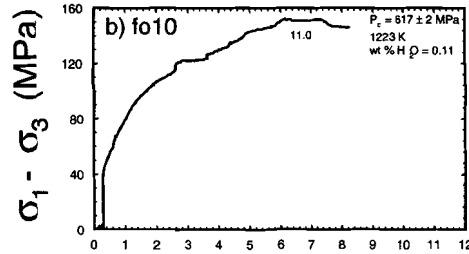
| Experiment Number | Gel Batch | en content (vol. %) | Estimated post-HIPing porosity (%) | Densification during HIPing (%) |
|-------------------|--------------|---------------------|------------------------------------|---------------------------------|
| fo10 | stm 15 | 1 | 2.9 | 5.3 |
| fo11 | stm 15 | 1 | 2.3 | 5.7 |
| fo12 | stm 15 | 1 | 3.4 | 5.4 |
| fo13 | stm 15 | 1 | 4.6 | 4.2 |
| fo16 | stm 19 | 0 | 4.7 | 2.4 |
| fo18 | stm 26 | 2 | 5.1 | 3.1 |
| fo19 | stm 26 | 2 | 4.5 | 3.6 |
| fo20 | stm 26 | 2 | 5.9 | 3.3 |
| fo21 | stm 30.31.32 | 2.5 | 2.6 | 5.8 |
| fo31 | stm 35.36.37 | 15 | 4.0 | 4.1 |
| fo33 | stm 35.36.37 | 15 | 4.5 | 4.1 |
| fo34 | stm 38.39.40 | 20 | 4.3 | 4.1 |
| fo35 | stm 38.39.40 | 20 | 4.8 | 3.7 |

Table 5.2. Estimated post-HIPing porosities and densification on HIPing.

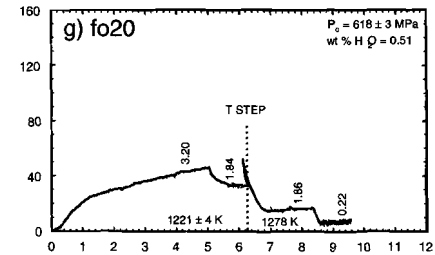
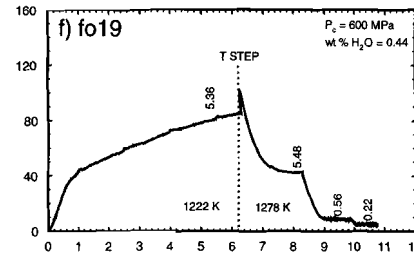
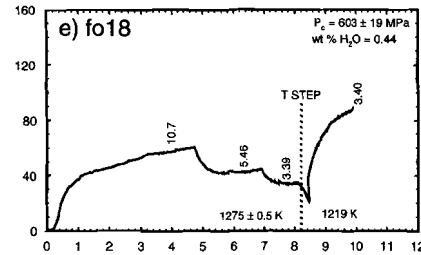
a) material batch - stm 19, pure fo, sample fo16



b,c,d) material batch - stm 15, 1% en, samples fo10, 12 and 13



e,f,g) material batch - stm 26, 2% en, samples fo18, 19 and 20



STRAIN (%)

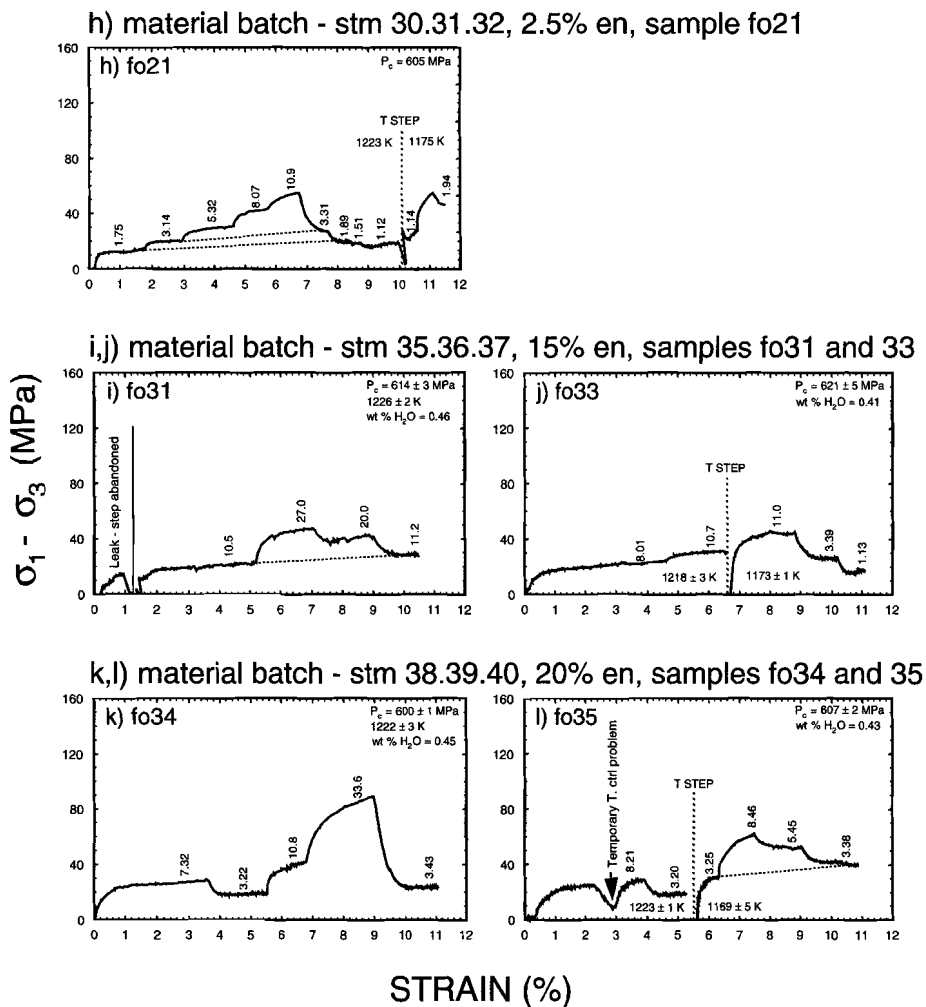


Figure 5.1. Stress versus strain curves for the 12 deformation runs with varying enstatite contents. N.B. Run fo11 was HIPed only and is therefore not shown. For each run the confining pressures, temperatures and water contents were as indicated. Strain rates are indicated for each step ($\times 10^{-6} \text{ s}^{-1}$). Position of temperature steps is indicated by a vertical dotted line. The data are tabulated in Table 5.3.

| Expt. No. | Gel batch No. | vol. % en | T (K) | Confining Pressure (MPa) | Disp. Rate (mm s ⁻¹) | $\sigma_1 - \sigma_3$ (MPa) | Strain rate (s ⁻¹) | Total strain (%) | |
|---------------------------|-----------------|-----------|--------|--------------------------|----------------------------------|-----------------------------|--------------------------------|------------------|--|
| fo10 | stm 15 | 1 | 1223 | 619 to 615 | 2.50×10^{-4} | 149 | 1.10×10^{-5} | 8.2 | |
| fo12 | | | 1222 | 631 to 630 | 2.50×10^{-4} | no steady state | 1.07×10^{-5} | 10.8 | |
| | | | 1222 | 630 to 629 | 1.25×10^{-4} | 83 | 5.48×10^{-6} | | |
| | | | 1222 | 629 to 629 | 7.50×10^{-5} | 57 | 3.36×10^{-6} | | |
| | | | 1220 | 629 to 629 | 2.50×10^{-5} | 25 | 1.14×10^{-6} | | |
| | | | 1220 | 628 to 628 | 7.50×10^{-5} | 62 | 3.45×10^{-6} | | |
| fo13 | stm 15 | 1 | 1224 | 622 to 613 | 2.40×10^{-4} | no steady state | 1.05×10^{-5} | 9.5 | |
| | | | 1226 | 613 to 609 | 1.25×10^{-4} | 81 | 5.37×10^{-6} | | |
| | | | 1225 | 609 to 604 | 4.45×10^{-5} | 46 | 1.95×10^{-6} | | |
| | | | 1229 | 604 to 596 | 5.01×10^{-6} | 6 | 2.21×10^{-7} | | |
| | | | 1228 | 596 to 595 | 7.45×10^{-5} | 58 | 3.34×10^{-6} | | |
| fo16 | stm 19 | 0 | 1225 | 600 to 600 | 2.50×10^{-4} | no steady state | 1.03×10^{-5} | 8.3 | |
| | | | 1228 | 600 to 599 | 2.50×10^{-5} | 44 | 1.04×10^{-6} | | |
| | | | 1233 | 599 to 598 | 1.25×10^{-5} | 34 | 5.27×10^{-7} | | |
| | | | 1231 | 598 to 596 | 4.24×10^{-5} | 67 | 1.83×10^{-6} | | |
| | | | 1229 | 596 to 594 | 5.01×10^{-6} | 30 | 2.19×10^{-7} | | |
| | | | 1228 | 594 to 594 | 2.50×10^{-4} | brittle failure | 1.10×10^{-5} | | |
| fo18 | stm 26 | 2.5 | 1275 | 623 to 613 | 2.40×10^{-4} | 61 | 1.07×10^{-5} | 9.8 | |
| | | | 1275 | 613 to 606 | 1.25×10^{-4} | 44 | 5.46×10^{-6} | | |
| | | | 1274 | 606 to 596 | 7.50×10^{-5} | 35 | 3.39×10^{-6} | | |
| | | | T step | | | | | | |
| | | | 1219 | 596 to 584 | 7.50×10^{-5} | no steady state | 3.40×10^{-6} | | |
| fo19 | stm 26 | 2.5 | 1222 | 601 to 600 | 1.25×10^{-4} | no steady state | 5.36×10^{-6} | 10.8 | |
| | | | T step | | | | | | |
| | | | 1278 | 608 to 608 | 1.25×10^{-4} | 43 | 5.48×10^{-6} | | |
| | | | 1278 | 608 to 607 | 1.25×10^{-5} | 9 | 5.57×10^{-7} | | |
| | | | 1279 | 607 to 606 | 5.01×10^{-6} | 5 | 2.25×10^{-7} | | |
| fo20 | stm 26 | 2.5 | 1224 | 617 to 615 | 7.50×10^{-5} | 46 | 3.20×10^{-6} | 9.6 | |
| | | | 1216 | 615 to 615 | 4.24×10^{-5} | 33 | 1.84×10^{-6} | | |
| | | | T step | | | | | | |
| | | | 1277 | 624 to 623 | 4.24×10^{-5} | 16 | 1.86×10^{-6} | | |
| | | | 1277 | 623 to 621 | 5.01×10^{-6} | 7 | 2.24×10^{-7} | | |
| fo21 see Chap. 4 | stm 30.31.33 | 2.5 | 1223 | 608 to 607 | 4.24×10^{-5} | 13 | 1.75×10^{-6} | 11.5 | |
| | | | 1221 | 607 to 606 | 7.50×10^{-5} | 20 | 3.14×10^{-6} | | |
| | | | 1221 | 606 to 605 | 1.25×10^{-4} | 30 | 5.32×10^{-6} | | |
| | | | 1221 | 605 to 605 | 1.87×10^{-4} | 42 | 8.07×10^{-6} | | |
| | | | 1221 | 605 to 605 | 2.50×10^{-4} | 55 | 1.09×10^{-5} | | |
| | | | 1221 | 605 to 605 | 7.50×10^{-5} | 27 | 3.31×10^{-6} | | |
| | | | 1221 | 604 to 604 | 4.24×10^{-5} | 19 | 1.89×10^{-6} | | |
| | | | 1221 | 603 to 603 | 3.37×10^{-5} | 17 | 1.51×10^{-6} | | |
| | | | 1223 | 603 to 602 | 2.50×10^{-5} | 15 | 1.12×10^{-6} | | |
| | | | T step | | | | | | |
| | | | 1175 | 602 to 602 | 2.50×10^{-5} | 27 | 1.14×10^{-6} | | |
| | | | 1175 | 602 to 602 | 4.24×10^{-5} | 46 | 1.94×10^{-6} | | |

| Expt. No. | Gel batch No. | vol. % en | T (K) | Confining Pressure (MPa) | Disp. Rate (mm s ⁻¹) | $\sigma_1 - \sigma_3$ (MPa) | Strain rate (s ⁻¹) | Total strain (%) |
|-----------|-----------------|-------------------------|----------------|--------------------------|----------------------------------|----------------------------------------|--------------------------------|------------------|
| fo31 | stm 35.36.37 | 15 | 1226 | 617 to 616 | 1.87 x 10 ⁻⁴ | step abandoned 20 47 40 28 | 7.60 x 10 ⁻⁶ | 10.5 |
| | | | 1223 | 616 to 612 | 2.50 x 10 ⁻⁴ | | 1.05 x 10 ⁻⁵ | |
| | | | 1228 | 612 to 611 | 6.25 x 10 ⁻⁴ | | 2.70 x 10 ⁻⁵ | |
| | | | 1226 | 611 to 611 | 4.54 x 10 ⁻⁴ | | 2.00 x 10 ⁻⁵ | |
| | | | 1225 | 611 to 611 | 2.50 x 10 ⁻⁴ | | 1.12 x 10 ⁻⁵ | |
| fo33 | stm 35.36.37 | 15 | 1220 | 626 to 621 | 1.92 x 10 ⁻⁴ | 22 | 8.01 x 10 ⁻⁶ | 11.2 |
| | | | 1216 | 621 to 620 | 2.50 x 10 ⁻⁴ | 31 | 1.07 x 10 ⁻⁵ | |
| | | | T step 1171 | 625 to 622 | 2.50 x 10 ⁻⁴ | 44 | 1.10 x 10 ⁻⁵ | |
| | | | 1173 | 622 to 620 | 7.58 x 10 ⁻⁵ | 27 | 3.39 x 10 ⁻⁶ | |
| | | | 1174 | 620 to 616 | 2.50 x 10 ⁻⁵ | 16 | 1.13 x 10 ⁻⁶ | |
| fo34 | stm 38.39.40 | 20 | 1221 | 601 to 599 | 1.87 x 10 ⁻⁴ | 28 | 7.82 x 10 ⁻⁶ | 11.2 |
| | | | 1222 | 599 to 599 | 7.58 x 10 ⁻⁵ | 18 | 3.22 x 10 ⁻⁶ | |
| | | | 1219 | 599 to 599 | 2.50 x 10 ⁻⁴ | 41 | 1.08 x 10 ⁻⁵ | |
| | | | 1218 | 599 to 599 | 7.58 x 10 ⁻⁴ | 87 | 3.36 x 10 ⁻⁵ | |
| | | | 1225 | 600 to 599 | 7.58 x 10 ⁻⁵ | 24 | 3.43 x 10 ⁻⁶ | |
| fo35 | stm 38.39.40 | 20 | 1222 | 605 to 605 | 1.92 x 10 ⁻⁴ | 27 | 8.21 x 10 ⁻⁶ | 10.8 |
| | | | 1224 | 605 to 605 | 7.50 x 10 ⁻⁴ | 18 | 3.20 x 10 ⁻⁶ | |
| | | | T step 1171 | 610 to 607 | 7.50 x 10 ⁻⁵ | 30 | 3.25 x 10 ⁻⁶ | |
| | | | 1169 | 607 to 607 | 1.92 x 10 ⁻⁴ | 63 | 8.46 x 10 ⁻⁶ | |
| | | | 1164 | 607 to 605 | 1.23 x 10 ⁻⁴ | 53 | 5.45 x 10 ⁻⁶ | |
| 1164 | 605 to 605 | 7.50 x 10 ⁻⁵ | 41 | 3.38 x 10 ⁻⁶ | | | | |

Table 5.3. Mechanical data from the deformation stage. N.B. temperature steps indicated.

clear systematic relationship between densification and enstatite content was apparent, however.

The deformation test results for all runs are summarized in Tables 5.3 and 5.4. Differential stress versus strain curves are presented in Figure 5.1 a to l. From the stress versus strain curves, it is apparent that ductile flow occurred in all experiments and that near steady state flow was approached in most steps, with flow stresses falling in the range 10 to 60 MPa. Flow at higher stresses was characterized by significant work hardening. In Figures 5.2 and 5.3, the differential flow stress ($\sigma_1 - \sigma_3$) values, obtained from strain rate steps exhibiting near steady state behaviour, have been plotted against the corresponding strain rate (measured at the step mid-point) using logarithmic scales in order to describe the mechanical data using the empirical Dorn type power law relation:

$$\dot{\epsilon} = A \sigma^n e^{\left(\frac{-Q_c}{RT}\right)} \quad 5.1$$

Here, $\dot{\epsilon}$ is the axial strain rate (s⁻¹), σ is differential stress ($\sigma_1 - \sigma_3$, MPa), A is a pre-exponential constant (MPa⁻ⁿ s⁻¹), Q_c is the apparent activation energy for creep (J mol⁻¹), R is the gas constant (8.314 J mol⁻¹ K⁻¹), T is absolute temperature (K) and n is the stress exponent or stress sensitivity. In general terms, it is apparent from Figure 5.2 that the data for individual batches of material show increas-

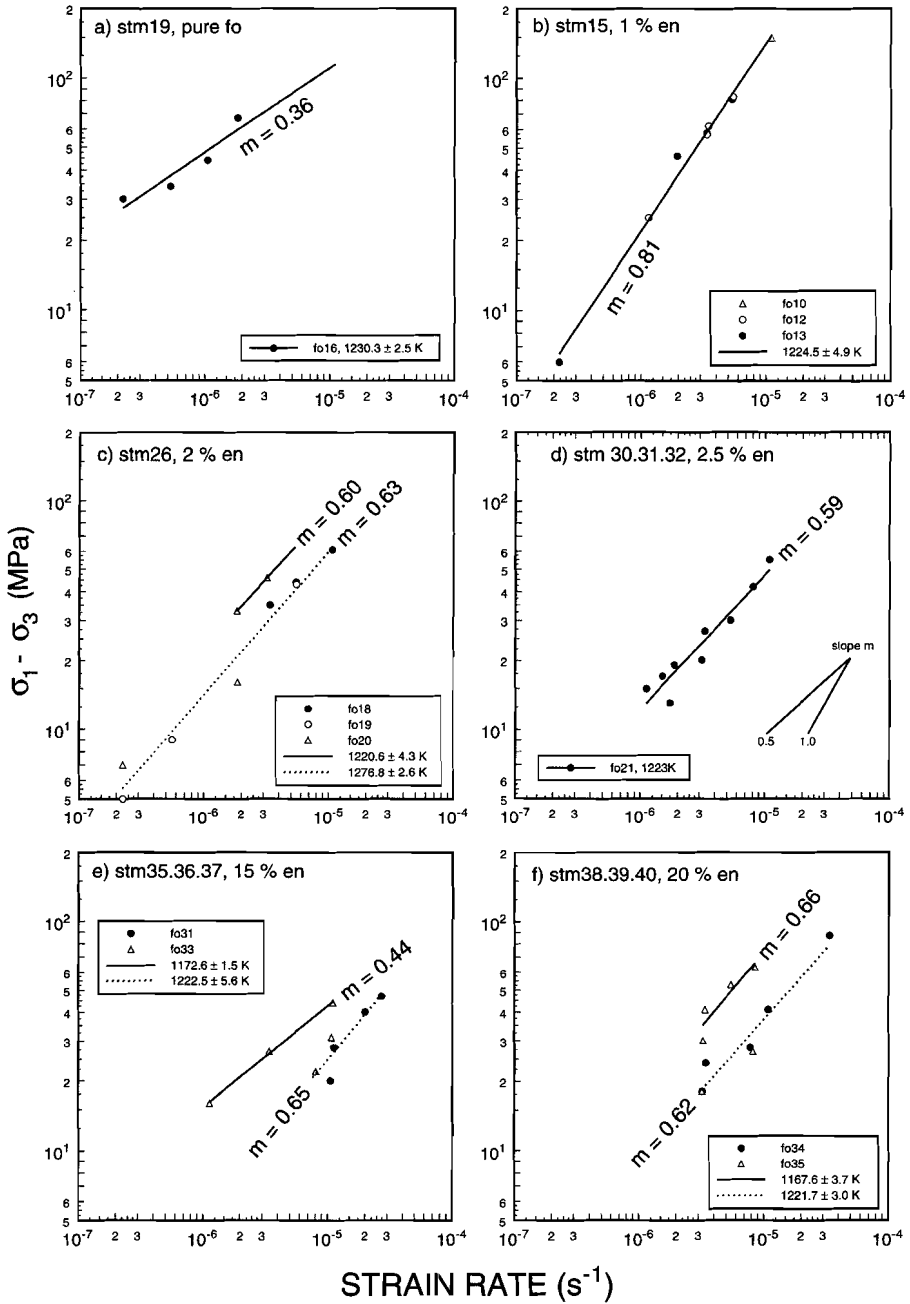


Figure 5.2 a to f. Differential stress versus strain rate (log-log axes) for the six materials investigated. Strain rate sensitivities (m) for each isotherm determined from least squares fitting are as indicated.

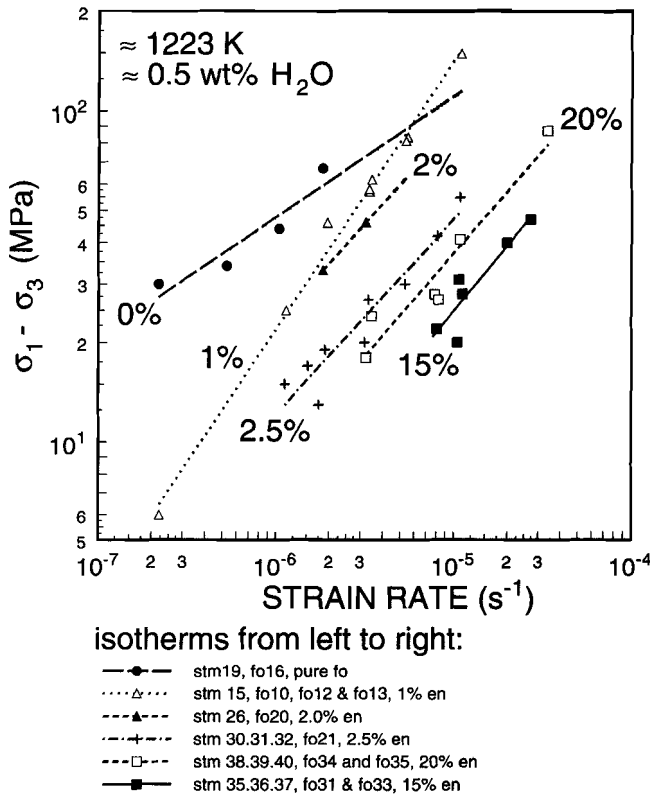


Figure 5.3. Comparative plot of differential stress versus strain rate (log - log scales) for the six starting materials at constant temperature of $T \sim 1223$ K. Note the marked difference in strength between the materials.

ing differential flow stress with increasing strain rate and decreasing differential flow stress with increasing temperature. Values of the strain rate sensitivity ($m = 1/n$) have been determined from power-law best fits of the Dorn relation to the various isothermal data sets for individual gel batches as shown in Figure 5.2. The temperature stepping data obtained for the materials with 2, 15 and 20 % enstatite content (runs fo18, fo19, fo20, fo33 and fo35) have been used to estimate the apparent activation energy for creep assuming a Dorn type Arrhenius temperature dependence using the logarithmic form of Equation 5.1. This is illustrated in Figure 5.4 which has been constructed using the best fit equations for the isotherms in Figure 5.2 (c, e and f) at constant stresses of 10, 30 and 50 MPa. However, due to the fact that only two temperatures were investigated for each material, the resulting values for the apparent activation energies are poorly constrained and fall in the range 305 ± 142 kJ mol⁻¹ (see Table 5.4). Focusing now on the effect of enstatite content on the flow behaviour, it is clear from Figures 5.2 and 5.3 that at the temperatures investigated (principally ~ 1223 K, Figure 5.3) materials with enstatite contents > 1 % show similar strain rate sensitivities, with values mostly of $m \approx 0.6$ ($n \approx 1.7$). At the lower enstatite contents, the picture is less consistent, the nomi-

nally pure material (sample fo16) showing a lower strain rate sensitivity ($m = 0.36$, $n = 2.8$), whereas the material with $\sim 1\%$ enstatite (fo10, fo12 and fo13) shows a strain rate sensitivity of $m = 0.81$ ($n = 1.23$). In addition to the effect of enstatite content on strain rate sensitivity, inspection of Figures 5.2 and 5.3 shows a significant decrease in flow stress with increasing enstatite content in the range 0 to 2.5%. This decrease (a factor of 3 to 10) is illustrated further in Figure 5.5 which plots the dependence of flow stress on enstatite content at a series of selected strain rates.

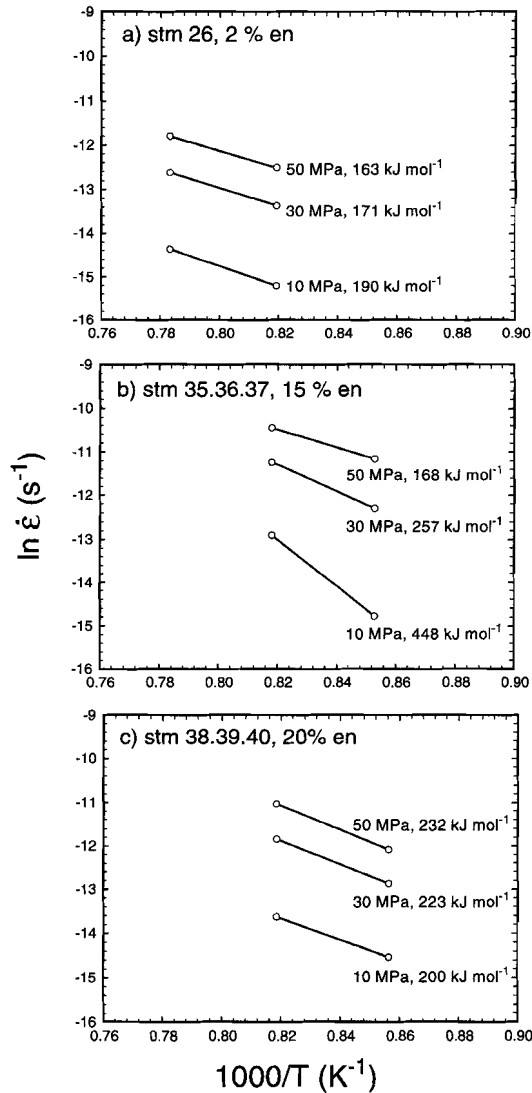


Figure 5.4. The apparent activation energies for creep determined from the isotherms shown in figure 5.2 at stresses of 10, 30 and 50 MPa and assuming an Arrhenius temperature dependence.

| Experiment numbers | Starting material | Vol% enstatite | Strain rate sensitivity (m) and stress exponent (n in brackets) | Q_c (kJ mol ⁻¹) |
|--------------------|-------------------|----------------|-----------------------------------------------------------------|-------------------------------------------------|
| fo15, fo16 | stm19 | 0 | 0.36 (2.8) at 1230 K | ---- |
| fo10, fo12, fo13 | stm15 | 1 | 0.81 (1.2) at 1224 K | ---- |
| fo18, fo19, fo20 | stm26 | 2 | 0.60 (1.7) at 1220 K 0.63 (1.6) at 1277 K | 190 at 10 MPa 171 at 30 MPa 163 at 50 MPa |
| fo21 | stm30.31.32 | 2.5 | 0.59 (1.7) at 1223 K | ---- |
| fo31, fo33 | stm35.36.37 | 15 | 0.44 (2.3) at 1172 K 0.65 (1.5) at 1222 K | 448 at 10 MPa 257 at 30 MPa 168 at 50 MPa |
| fo34, fo35 | stm38.39.40 | 20 | 0.66 (1.5) at 1168 K 0.62 (1.6) at 1222 K | 257 at 30 MPa 223 at 30 MPa 232 at 50 MPa |

Table 5.4. Strain rate sensitivities, stress exponents (in brackets) and apparent activation energies. The activation energies are poorly constrained and fall in the range 305 ± 142 kJ mol⁻¹.

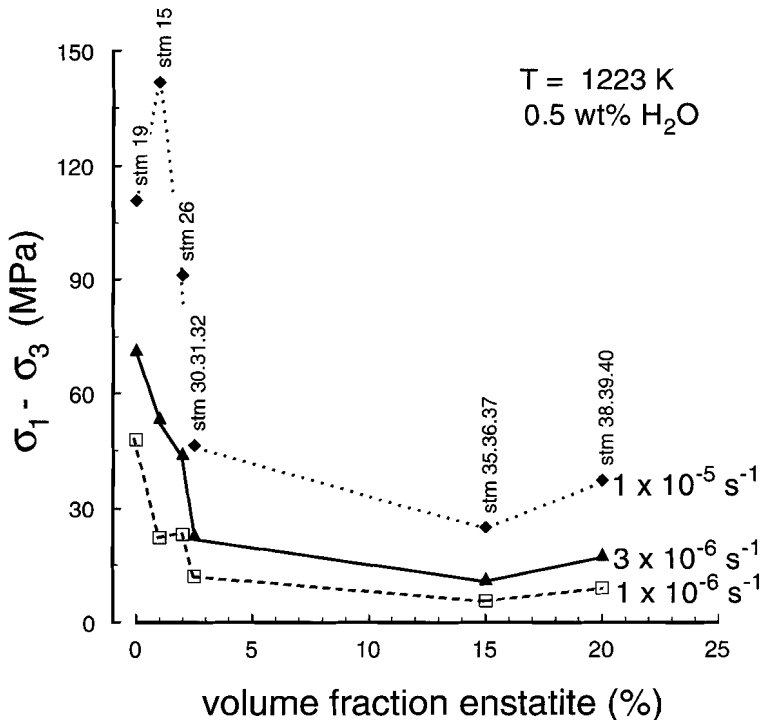


Figure 5.5. Plot of differential stress versus volume fraction enstatite, at strain rates indicated. Data carried from figure 5.3. Note that the flow stress at constant rate falls sharply in the 0 to 2.5 % enstatite range, with relatively little change at higher enstatite content.

5.3.2. SEM observations

General observations

On macroscopic inspection after deformation, samples were found to be still cylindrical in form and appeared to be homogeneously deformed (see Figure 5.6). All were sawn in half parallel to the compression direction (σ_1) for microstructural analysis. The σ_1/σ_3 surface of the resulting half cylinders (one half from each sample) were then polished and finished using Syton™ polish (colloidal silica). The samples were then examined (uncoated and unetched) using a Philips XL30 field emission gun (FEG) scanning electron microscope (SEM) operated in orientation contrast mode, using a tilt angle of 70°, 20 kV accelerating voltage, automatic tilt correction and dynamic focus.

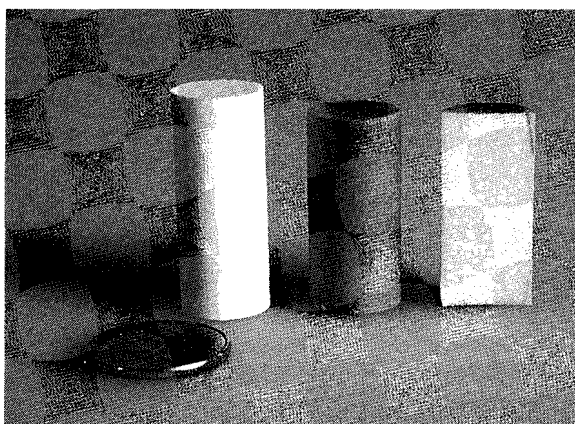


Figure 5.6.

Photograph of an undeformed sample and deformed samples fo13 and fo12 (half cylinder).

The starting materials were found to be similar to those described previously in Chapter 4, being homogeneously fine-grained (~ 1 to $2 \mu\text{m}$) with a foam texture with porosities $\sim 8\%$ and dihedral angles $> 60^\circ$. The HIPed only sample (fo11, 0.36 wt % water, 1 % en) exhibited a homogeneous foam texture with a grain size $\sim 2 \mu\text{m}$ (see Figure 5.7 a). The polygonal grains have straight or gently curved grain boundaries. Intergranular pores observed at 3 to 5 grain junctions account for $\sim 1.5\%$ porosity. Notably, these do not extend along entire grain boundaries or link to form crack-like cavities of the type described previously in Chapter 4 for wet deformed material. Where the pores intersect grain boundaries they are characterized by dihedral angles $< 60^\circ$. Small intragranular pores, introduced during material synthesis, appear circular in outline and make up $\sim 0.7\%$ porosity.

Moving now to the deformed samples, these were found to be microscopically homogeneous internally, exhibiting a foam texture, with little or no evidence of grain flattening or grain boundary alignment (see Figures 5.7 b,c,d). The grain size was very uniform for each batch of material. However, clear differences in grain size (d - expressed as equivalent circular diameters, ECD) were observed between the different starting compositions ranging from $2.2 \mu\text{m}$ in material stm 26 with ~ 2 vol% enstatite to $\sim 1.0 \mu\text{m}$ in material stm 35.36.37 with ~ 15 vol. % enstatite. Enstatite grains, which can be recognized by the presence of lamellae, are of similar grain size to the forsterite grains but exhibit a more tabular form. Both straight and gently curved grain boundaries occur. In two dimensions, the grains show between three and eight sides but generally have five to seven. Serrated

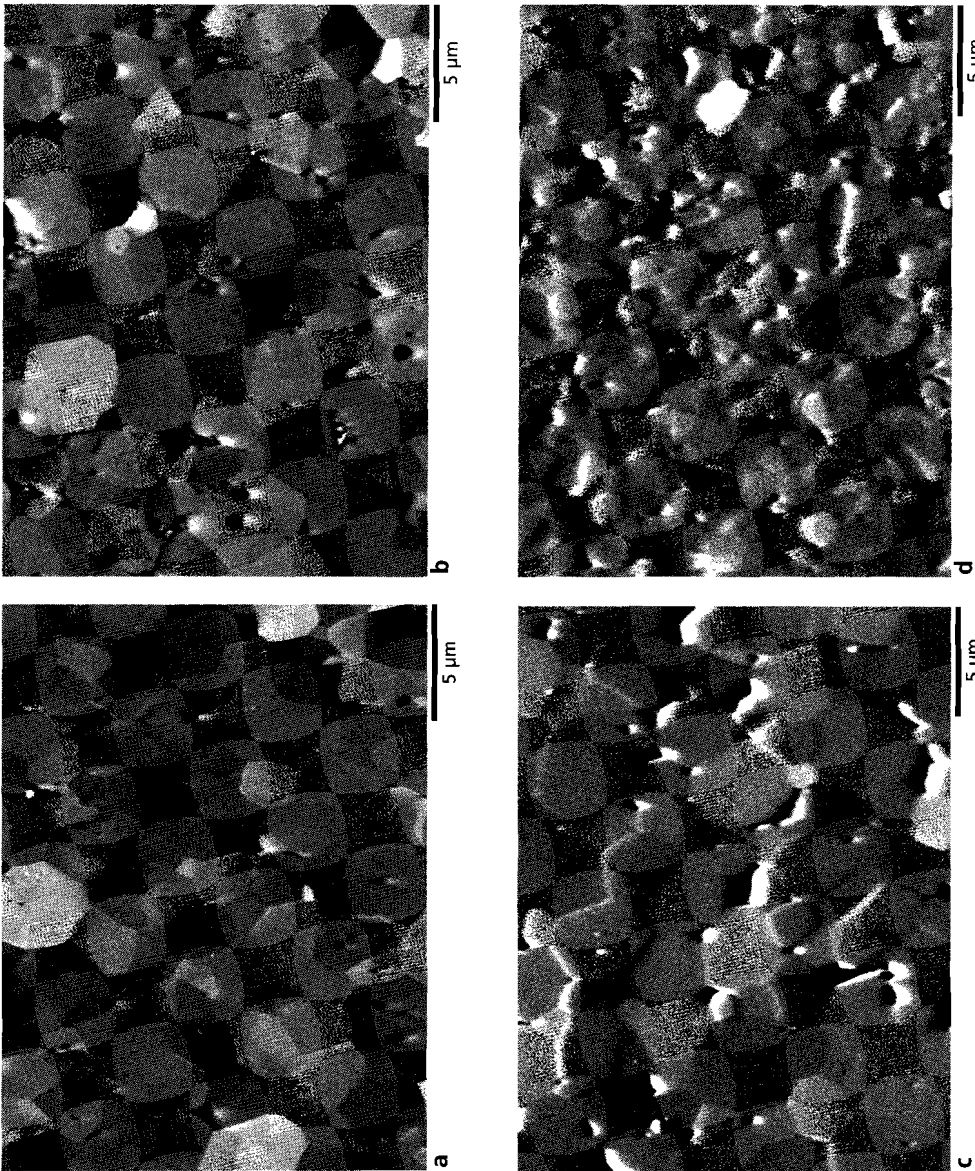


Figure 5.7 a, b, c and d. SEM orientation contrast micrographs. **a**) HIPed only control sample fo11 (stm 15) with ~ 1 vol.% en. Note that although intergranular pores remain they do not extend along entire grain boundaries (compare with fo12 in (b)). **b**) Wet deformed sample fo12 (stm 15) with ~ 1 vol.% en. Note that the intergranular pores are more open than in fo11 and extend along grain boundaries. The small particles in the pores are remnants of the Syton polish. **c**) Wet deformed sample fo16 (stm 19), nominally pure forsterite. Note that several intergranular pores extend along grain boundaries. **d**) Wet deformed sample fo34 (stm 38.39.40) with ~ 20 vol.% en. Note the tabular nature of enstatite grains. Note also the variation of grain size between the samples shown in (b), (c) and (d). For the deformed samples (b,c and d) the compression direction is parallel to the long axis of the micrograph.

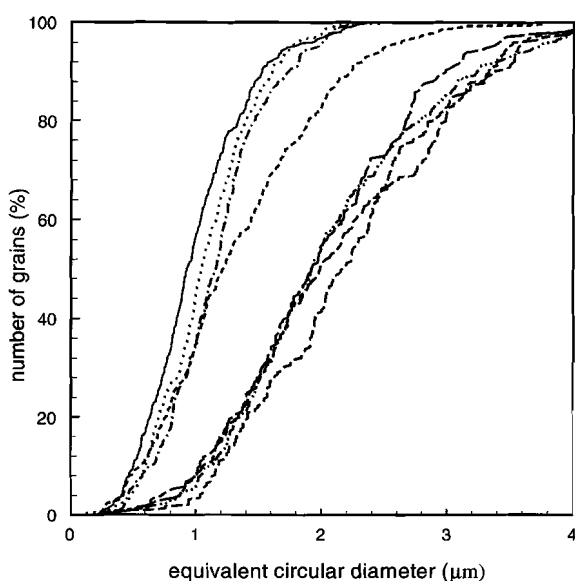
boundaries and subgrains are not observed. The grain boundaries are free from second-phase particles or amorphous films at the scale of SEM observation. Both intragranular and intergranular pores are present. The intragranular pores (contributing 0.5 to 1 % porosity), inherited from the starting material, commonly appear circular in cross-section and are small in comparison with the grains ($< d/10$). Intergranular pores (contributing 2 to 3 % porosity) occur along two-grain boundaries, and at triple and four-or-more grain junctions. Dihedral angles of $< 60^\circ$ are developed where grain boundaries intersect these intergranular pores (cf. Watson et al., 1990). The pores at 4-or-more grain junctions are larger ($\sim d/2$ to $d/4$) than the pores at triple junctions ($\sim d/10$) and within grain boundaries ($< d/10$) and are often angular with faceted grain surfaces. These larger intergranular pores frequently separate 'columns' of two to four grains and are reminiscent of the cavities developed in unconfined superplastically deformed metals and ceramics (Yusada et al., 1989; Chokshi and Langdon, 1987, 1991; Ridley and Wang, 1994, 1995). Note that such cavities were absent from the HIPed only sample fo11 (cf. Figures 5.7a and 5.7b).

Quantitative grain size analysis

As stated above, the grain size of the deformed samples was very uniform within a given batch of material. However, clear differences in grain size between batches of material were observed. Grain size analysis was therefore carried out on representative samples from each batch, in order to quantify the grain size distributions and to allow comparison between batches of material with different enstatite content. To this end, computer image analysis was undertaken using the UTHSCSA Image Tool program (developed at the University of Texas Health Science Centre at San Antonio, Texas and available by FTP from maxrd6.uthscsa.edu). This was used to analyze digitized grain boundary tracings produced by tracing orientation contrast SEM images using image widths of $\sim 25 \mu\text{m}$ (see Chapter 4 for details). No distinction was made between forsterite and enstatite grains as these were similar in size.

| Sample No. | Gel Batch | Vol. % en. | N | mean area (μm^2) | mean ECD (μm) | mean log ₁₀ area (μm^2) | standard deviation log ₁₀ area (μm^2) | ECD of mean log ₁₀ area | L ₃ (μm) | L ₃ × 1.56 (μm) |
|------------|--------------|------------|-----|-------------------------------|----------------------------|-------------------------------------------------|---------------------------------------------------------------|------------------------------------|----------------------------------|-----------------------------------------|
| fo12 | stm15 | 1 | 218 | 3.58 | 1.99 | +0.4220 | 0.371 | 1.83 | 1.23 | 1.93 |
| fo16 | stm19 | 0 | 255 | 4.14 | 2.12 | +0.4625 | 0.4102 | 1.92 | 1.33 | 2.07 |
| fo18 | stm26 | 2 | 277 | 4.33 | 2.20 | +0.5137 | 0.3636 | 2.04 | 1.36 | 2.12 |
| fo20 | stm26 | 2 | 374 | 3.94 | 2.07 | +0.4508 | 0.3767 | 1.90 | 1.30 | 2.02 |
| fo21 | stm 30.31.32 | 2.5 | 275 | 1.70 | 1.32 | +0.0258 | 0.4660 | 1.16 | 0.85 | 1.33 |
| fo31 | stm35.36.37 | 15 | 461 | 0.90 | 0.99 | -0.1917 | 0.3778 | 0.90 | 0.62 | 0.97 |
| fo33 | stm35.36.37 | 15 | 246 | 1.03 | 1.08 | -0.1042 | 0.3507 | 1.00 | 0.66 | 1.03 |
| fo34 | stm38.39.40 | 20 | 193 | 1.18 | 1.16 | -0.0363 | 0.3515 | 1.08 | 0.71 | 1.11 |

Table 5.5. Grain size statistics for representative deformed samples corresponding to each batch of starting material.



Grain size frequency curves from left to right:

- stm 35.36.37, 15% en, fo31, N = 461
- stm 35.36.37, 15% en, fo33, N = 246
- stm 38.39.40, 20% en, fo34, N = 193
- stm 30.31.32, 2.5 % en, fo21, N = 275
- stm 15, 1% en, fo12, N = 218
- stm 26, 2% en, fo20, N = 374
- stm 19, pure fo, fo16, N = 255
- stm 26, 2% en, fo18, N = 277

Figure 5.8 a. Cumulative grain size distributions from representative deformed samples corresponding to the 6 starting material batches used.

The resulting grain size distributions are shown in Figure 5.8a expressed in terms of the cumulative frequency of grain equivalent circular diameters (ECD). The ECD is simply the diameter of circle having an area equal to the measured grain area (see Chapter 4). The measured grain areas show a more or less log-normal distribution and so the grain size distributions can be described by the mean \log_{10} area and its standard deviation for each batch of material investigated. A theoretical mean intercept length (L_3) and equivalent grain size ($L_3 \times 1.56$) has been calculated assuming that the structure is made up of single size tetrakaidecahedra (Underwood, 1970; see Section 4.4.3 for details). This was done to allow comparison with previous studies in which grain size has been obtained using the intercept method. The complete set of grain size statistics obtained is given in Table 5.5 and the mean equivalent circular grain diameter is plotted against enstatite content in Figure 5.8b. From these data it is evident that the grain size determined is not simply correlated with enstatite content. Rather there is a sharp drop in ECD grain size from $\sim 2.0 \mu\text{m}$ at enstatite contents of $< 2 \%$ to $\sim 1.3 \mu\text{m}$ at 2.5 % enstatite with little further decrease in ECD at higher enstatite fractions.

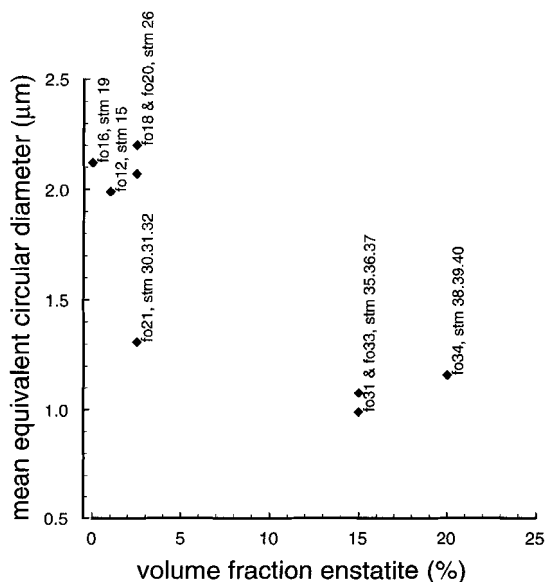


Figure 5.8 b. Mean ECD grain size versus the volume fraction enstatite.

5.3.3. TEM observations

Ion beam thinned foils of samples fo12 (stm15), fo19 (stm26), fo21 (stm30.31.32), fo31 (stm35.36.37) and fo34 (stm38.39.40) were examined using a Philips CM200 transmission electron microscope in collaboration with Dr. Herman van Roermund (see Figure 5.9 a,b,c,d). In accordance with the SEM observations, the samples were seen to have a foam texture, with straight or gently curved grain boundaries. Dislocation densities are low (the vast majority of grains appear to be dislocation free), and subgrains were not observed. One feature particularly worth noting is that occasional isolated grains in sample fo34 were observed to have high dislocation densities (see Figure 5.9 d). The intra-granular pores, seen also using the SEM, often exhibit negative crystal forms and grains adjacent to the larger intergranular pores are faceted. Small intergranular pores along grain boundaries and at triple junctions generally show apparent dihedral angles $< 60^\circ$. The grain boundaries commonly show diffraction contrast features in 2-D reminiscent of a string of beads. When the grain boundary surface was viewed these features were seen to consist of discrete, disconnected subspherical zones of contrast with a diameter of 4 to 20 nm, suggesting the presence of grain boundary inclusions. Again confirming SEM observation, the enstatite grains (most clearly seen in sample fo31 and fo34) commonly contain numerous lamellae and are of similar size to the olivine grains, though they are often more tabular in form. No additional phases were observed in the TEM. No glass films or blebs were observed at the scale of observation, although no attempt was made to carry out high resolution TEM of grain boundaries.

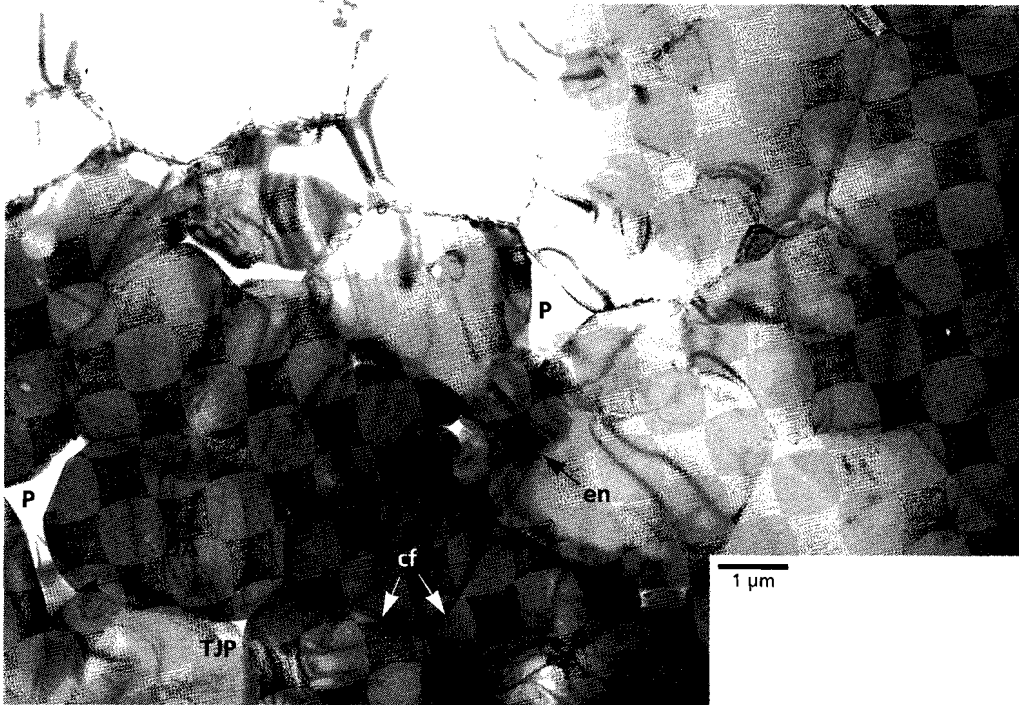


Figure 5.9 a. TEM composite micrograph of wet deformed sample fo19 (stm 26) with 2 vol.% enstatite and a grain size of ~ 2.0 μm (orientation w.r.t. compression direction unknown). Note that the majority of grains are dislocation free, and that the apparent dihedral angles are generally less than 60° .

key to figures 5.9 a,b.

The following abbreviations are used: P- intergranular pore, ip- intragranular pore, DA - dihedral angle, en - enstatite grain with lamellae, cf - grain boundary contrast features, and TJP - triple junction pore.

Figure 5.9 b. TEM composite micrograph of wet deformed sample fo21 (stm 30.31.32) with 2.5 vol.% enstatite and a grain size of ~ 1.3 μm (orientation w.r.t. compression direction unknown). Note that the majority of the grains are dislocation free, and that the intragranular pores (ip) are not associated with dislocations.

Figure 5.9 b



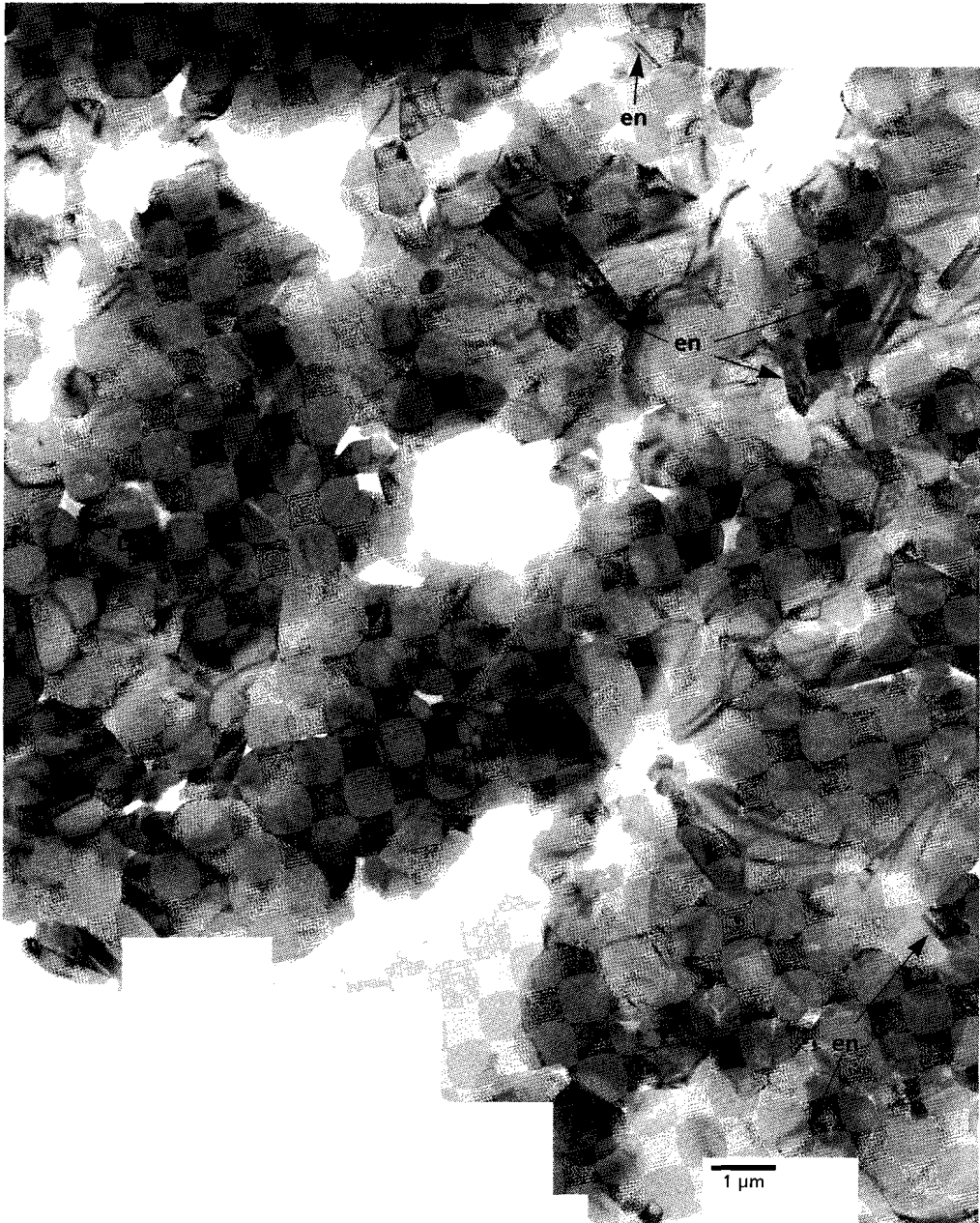


Figure 5.9 c. TEM composite micrograph of wet deformed sample fo31 (stm 35.36.37) with 15 vol.% enstatite and a grain size of $\sim 1.0 \mu\text{m}$ (orientation w.r.t. compression direction unknown). Note that the majority of grains are dislocation free.

key to figures 5.9 c,d. DA - dihedral angle, en - enstatite grain with lamellae.

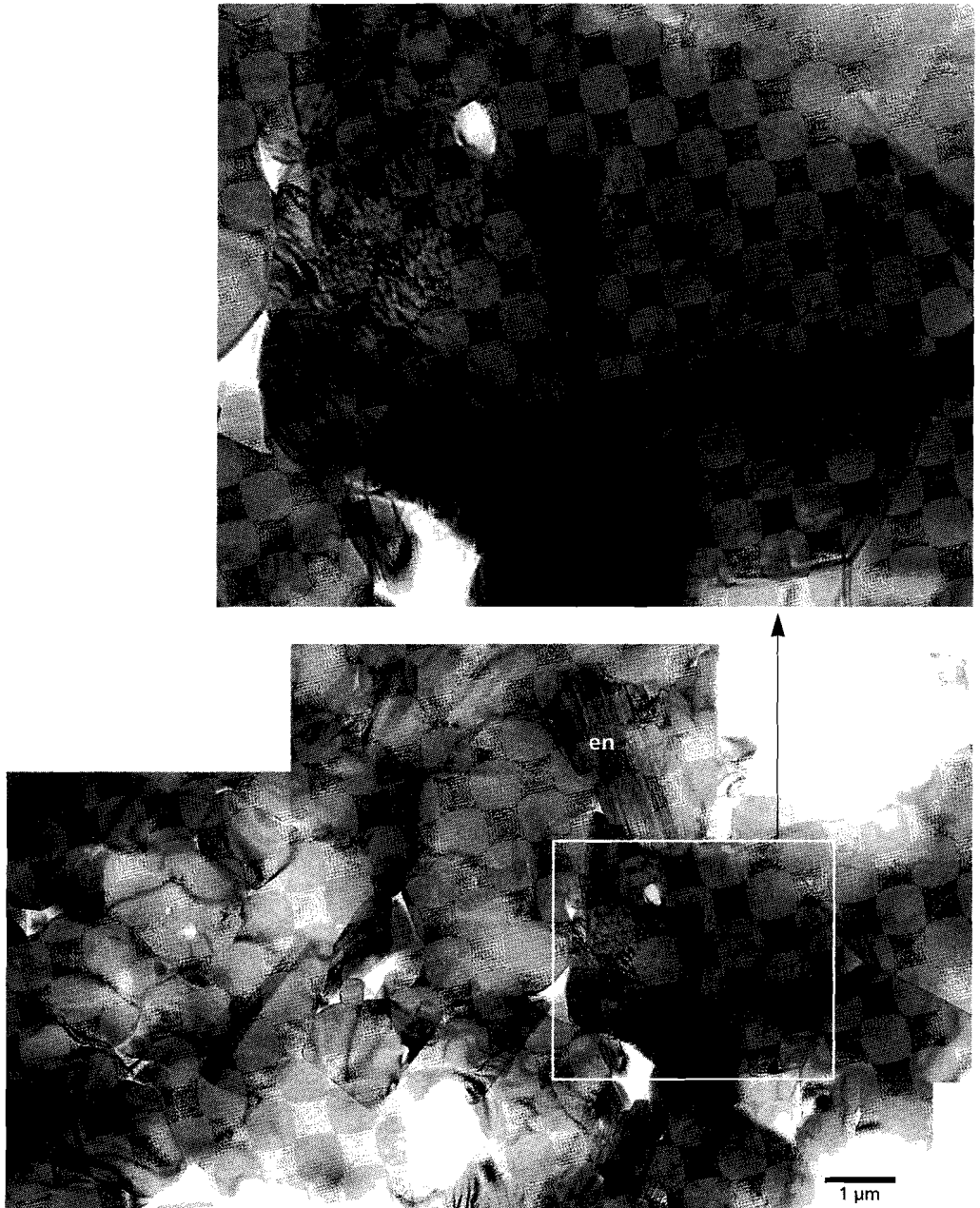


Figure 5.9 d. TEM composite micrograph of wet deformed sample fo34 (stm 38.39.40) with 20 vol.% enstatite and a grain size of $\sim 1.1 \mu\text{m}$ (orientation w.r.t. compression direction unknown). Note that isolated grains such as those in the enlarged window show high dislocation densities.

5.3.4. Crystallographic orientation data

Electron backscatter diffraction (EBSD) analysis was carried out using the XL30 FEG SEM on the HIPed-only control sample fo11 and on deformed sample fo12 (10.8 % strain), both from material batch stm15. This technique provides crystallographic orientation information on a grain to grain basis (see Randle, 1992). In HIPed only sample fo11, 175 grains were analyzed from four randomly chosen areas; in deformed sample fo12, 200 grains were analyzed from five randomly chosen areas. Care was taken to keep the orientation of the sample compression direction constant with respect to the microscope reference axis during analysis. The electron backscatter patterns (EBSPs) were indexed using software running on the microscope's computer system on a 'real time' basis. The crystallographic orientations obtained are plotted as upper hemisphere, equal area pole figures for the (100), (010) and (001) planes. From these projections (shown in Figures 5.10 a,b), it is clear that little or no crystallographic preferred orientation (CPO) was developed within either the HIPed-only control sample fo11 or the deformed sample fo12. Although, there is some evidence for a weak (010) maximum parallel to the long axis of the HIPed only sample.

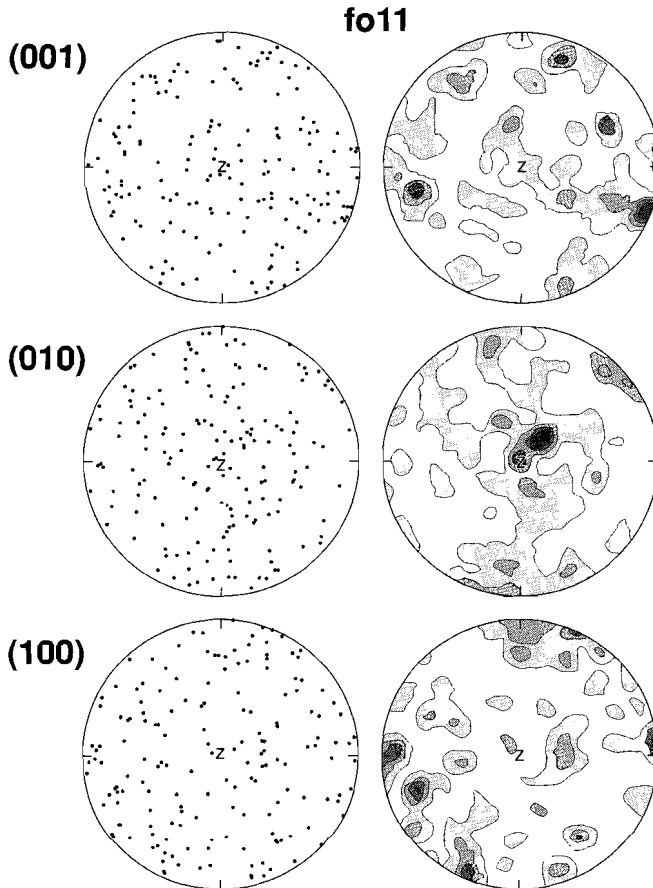


Figure 5.10a. Upper hemisphere equal area pole figures and contours for (001), (010) and (100) planes for 175 grains from HIPed only sample fo11, analysed using electron backscatter diffraction (EBSD). A weak (010) maximum is observed parallel to the long axis of the sample Z. Contours 1234x uniform.

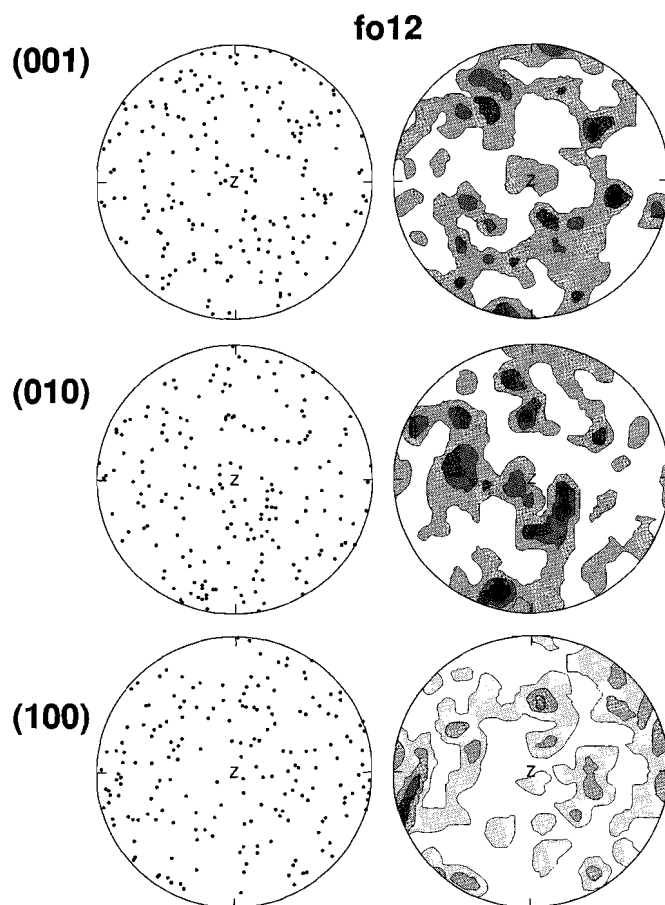


Figure 5.10b. Upper hemisphere equal area pole figures and contours for (001), (010) and (100) planes for 200 grains from wet-deformed sample fo12, analysed using electron backscatter diffraction (EBSD). The patterns appear to be more or less random, indicating that little or no crystallographic preferred orientation (CPO) has developed. Compression direction parallel to Z. Total strain 10.8%. Contours 1234x uniform.

5.4. Discussion

This study aims to investigate the effect of enstatite content on the deformation behaviour of fine-grained forsterite–enstatite materials with similar water contents and to this end a number of starting materials with varying enstatite contents have been fabricated, HIPed and subsequently deformed. However, the microstructural observations reported have shown that it was not possible to vary enstatite content independently of grain size (although materials from the same batch were very homogeneous in grain size). Rather, the addition of increasing amounts of enstatite seems to have controlled grain growth such that samples with higher enstatite content are finer grained ($\sim 2 \mu\text{m}$ at 0 – 2 % enstatite versus $\leq 1.32 \mu\text{m}$ at 2.5 to 20 % enstatite). The role of a second phase in control-

ling grain size is well known in material science where the effect is exploited to produce fine-grained materials (see Olgaard and Evans, 1986). Since it has been shown in Chapter 4 that little grain growth occurs in forsterite-enstatite materials containing 2.5 % enstatite during HIPing and deformation under the present conditions (compare also runs fo11 and fo12; Figure 5.7 a,b), grain size control exerted by the presence of enstatite in the current samples must have occurred mainly during the sintering stage of material preparation. In interpreting the experimental data, this question needs to be taken into careful account, particularly with respect to the fact that observed differences in mechanical behaviour between different batches of material may be potentially attributed to the effects of either enstatite content or grain size.

5.4.1. HIPing behaviour

The limited data presented for the HIPing stage of the present experiments have shown that, while densification occurred in all samples, there seems to be no clear systematic relationship between the degree of densification and enstatite content. However, the amount of densification which can occur during HIPing of samples with low porosity will be very strongly dependent on added water content, i.e. on the pore fluid pressure which develops during HIPing (see Section 6.4.1). Since the initial porosity of the present samples was $\sim 8\%$ only, and since the added water contents varied in the range 0.36 (fo11) to 0.59 wt %, significantly different fluid pressures would be developed in different samples, influencing the densification accordingly. For this reason, a possible effect of enstatite content on densification may have been obscured and cannot be ruled out.

5.4.2. Flow behaviour and likely mechanisms

Consider now the behaviour observed in the deformation stage of the experiments. In broad terms, the near steady state flow behaviour seen at relatively low stresses (mostly < 60 MPa) was similar for all enstatite compositions investigated, in the sense that consistently high strain rate sensitivities (i.e. low n values) were obtained for individual isotherms ($m \approx 0.6$, $n \approx 1.7$) independently of the apparent effect of composition on flow stress level (refer to Figures 5.3 and 5.5). Similar activation energies were also obtained insofar as investigated (only 3 compositions using a 50 K temperature interval), with the values determined falling in the range $\sim 305 \pm 142$ kJ mol⁻¹. Only the materials with nominal enstatite contents of 0 % and 1 % departed somewhat from this picture, since these showed m -values of respectively 0.36 ($n = 2.7$) and 0.81 ($n = 1.2$). This variability at low enstatite content could conceivably be related to uncertainties in composition stemming from the fact that enstatite contents quoted are $\pm 1\%$. Thus the samples with $\leq 1\%$ estimated enstatite content (particularly the nominally pure forsterite sample - fo16) may have contained small quantities ($< 0.5\%$) of MgO undetectable using the X-ray powder diffraction technique used (see appendix).

Viewed overall, however, the observed steady state flow behaviour was not only similar from material to material, but also showed similar strain rate sensitivity and activation energy values to those reported in Chapter 4 for samples containing 2.5 % enstatite and tested under identical conditions. Moreover, the microstructures reported for the present samples, namely the fine-grained polygonal texture and the absence of dislocation substructures in the majority of grains, are also closely consistent with those reported in Chapter 4 for material with 2.5 % enstatite. In Chapter 4, the

reported in values of 0.45 to 0.78 ($1.3 \leq n \leq 2.2$), the activation energy of $320 \pm 40 \text{ kJ mol}^{-1}$ and microstructural observation led to the conclusion that deformation occurred by grain boundary sliding (GBS) with accommodation by water-enhanced diffusion or dislocation motion in grain mantles (i.e. a superplastic flow mechanism), or possibly involved behaviour transitional between water enhanced dislocation and diffusion creep. This conclusion was based on a comparison of results with a) theoretical models for dislocation creep ($n = 3$ to 6.5), GBS dominated flow (GSS, $n = 1$ to 2) and diffusion creep (GSS, $n = 1$), and b) previous data on GSS creep in wet fine-grained forsterite (Karato et al., 1986). Following the same reasoning, it is inferred that broadly the same mechanism(s) must have operated in the present near steady state runs on the various material compositions studied. In other words, steady state flow in the present experiments also involved either GBS, with water enhanced diffusion of dislocation accommodation, or mixed dislocation and diffusional mechanisms. The action of GBS in the current experiments is further supported by a) the fact that the cavity-like intergranular pores, of the type observed in the wet deformed samples, are absent from the HIPed only sample, and b) the observation of high dislocation densities in isolated grains in sample fo34, which is reminiscent of the microstructure associated with locked cooperative grain boundary sliding (Friedel creep), in which the grains blocking sliding deform plastically in response to the locally high stresses (see Figure 5.9d; see Gifkins, 1982).

Before considering why samples with different enstatite content showed different flow stresses in the (near) steady state regime, it is important to consider briefly the work hardening behaviour seen in samples which were stepped to the higher strain rates investigated, and thus supported higher stresses ($> 60 \text{ MPa}$). In some cases, the observed hardening can be accounted for in terms of deformation ('squeeze flow') of the gold foil end-caps separating the sample from the deformation pistons/anvils; this is known to start at stresses > 50 to 60 MPa , as mentioned in the description of the experimental method (Section 5.2.5). However, deformation of the gold end caps has been shown to be capable of producing only $\sim 0.4 \%$ strain at the stresses reached in the present tests (see Chapter 4). Since strongly work hardening flow exceeding strains of 4% has been observed in a few high strain rate (high stress) tests/steps (e.g. fo10 and fo12), it seems likely that some kind of work hardening flow mechanism must have operated in the corresponding samples, perhaps indicating an increased component of plastic flow at high stress. The minor hardening seen in some stepping runs within the near steady state regime (stresses mostly $< 60 \text{ MPa}$) could equally reflect involvement of dislocation processes, though there is no microstructural evidence for this. Alternatively, if deformation is dominated by GBS or diffusion mechanisms ($\dot{\epsilon} \propto d^{-p}$, $p = 2-3$), this hardening could be caused by minor grain growth occurring during deformation (see Chapter 4 and Karato et al., 1986).

5.4.3. *The relative roles of enstatite content and grain size*

The present data for the samples achieving near steady state flow have clearly demonstrated that increasing enstatite content is associated with decreasing flow strength. Notably, the flow strength of the materials is not a simple, continuous function of the enstatite content, but shows a sharp drop in the composition range 0 to 2.5 % (see Figure 5.5). As already pointed out, however, the enstatite contents of the starting materials could not be varied independently of grain size, and both these variables must therefore be considered in attempts to explain the observed differences in flow strength

between samples of different composition. This is particularly important in view of the fact that both GBS dominated and diffusional flow mechanisms, which are always GSS, have been put forward as contributing to the observed deformation behaviour. In order to determine the relative importance of enstatite content versus grain size in controlling the observed flow behaviour let us now consider the correlation of the observed flow rates with both these variables independently.

Correlation with enstatite content

Beginning with the correlation between enstatite content and flow stress expressed directly in Figure 5.5, it is apparent that little or no change in flow stress (at constant strain rate) occurs beyond the initial sharp drop at enstatite contents in the range 0 - 2.5 %, at least up to contents of 20 %. If the weakening effect of increased enstatite were related to the presence of interphase boundaries (i.e. to rapid interphase diffusion or to coupled interphase diffusion/migration effects of the type invoked by Wheeler, 1992), a smooth decrease in strength would be expected with increasing enstatite content (i.e. increasing interphase boundary frequency). Since this is not the case, interphase diffusion/migration effects seem an unlikely explanation for the observed effect of enstatite content. In contrast, sharp changes in flow stress are to be expected when small quantities of a chemical buffer are added to a system in which deformation rate is affected by point defect chemistry. Since such buffering effects are known to occur in the forsterite-enstatite system (Smyth and Stocker, 1975; Stocker and Smyth, 1978; Hobbs, 1983), and since the uncertainty in the present enstatite contents is of the order of 1 %, chemical and point defect buffering by added enstatite (or the presence of minor MgO in the nominally pure sample) cannot yet be eliminated as a potential explanation for the observed weakening. A similar argument applies to the (related) possibility of weakening caused by a reduction of homologous temperature due to the addition of enstatite.

Correlation with grain size

Microphysical models for GBS dominated flow (with accommodation by diffusion or dislocation motion) and for diffusion creep predict constitutive equations of the form:

$$\dot{\epsilon} = A \cdot \frac{D(T)\Omega}{RT} \cdot \frac{\sigma^n}{d^p} \quad 5.2$$

where $\dot{\epsilon}$ is the axial strain rate (s^{-1}), $D(T)$ is a diffusion coefficient ($m^2 s^{-1}$), d is the grain size (m), σ is the differential flow stress (Pa), Ω is the molar volume ($J Pa^{-1} mol^{-1}$), R is the gas constant ($J mol^{-1} K^{-1}$), and T is the absolute temperature (K). In this equation, the stress sensitivity or stress exponent n , the grain size exponent p and the diffusion coefficient $D(T)$ take on specific values and/or significance, depending on the detailed process controlling GBS rate or the rate of diffusional flow. Values of n , p and $D(T)$ are given in Table 5.6 for the known mechanisms of GBS dominated and diffusional flow.

Taken together, Equation 5.2 and Table 5.6 illustrate the fact that models for known mechanisms of GBS dominated flow or for diffusional flow are characterized by n -values of 1 to 2 and p values from 2 to 3. In order to determine if there is any such correlation between the observed flow behaviour of the different material batches and their grain size, a plot of \log_{10} strain rate, calculated using

| Mechanism | Stress exponent (n) | Grain size exponent (n) | Diffusion coefficient | Accommodating mechanism |
|------------------------------------------------------------------------------------------------|---------------------|-------------------------|-------------------------------------|---------------------------------------------------------------------------------------------------|
| Grain boundary sliding (GBS) dominated creep (superplasticity) | | | | |
| Plasticity accommodated ($d < \lambda$) (Mukerjee, 1971, 1975; Gifkins, 1976, Langdon, 1995) | -2 | -2 | D_{gb} | Limited intragranular dislocation movement. Grain boundary and mantle dislocations are important. |
| Ashby-Verral type creep (Ashby and Verral, 1973) | | | | |
| - diffusion control | 1 | 2 or 3 | D_v or D_{gb} | Vacancy diffusion |
| - interface control (Langdon, 1995) | 2 | 2 or 3 | interface reaction kinetics control | Diffusion |
| Grain boundary film control (Langdon, 1995) | 1 | 3 | D_{film} | Diffusion in a grain boundary amorphous / liquid film or penetrated grain boundary |
| Diffusion creep: | | | | |
| Coble creep (grain boundary diffusion creep; Coble, 1963) | 1 | 3 | D_{gb} | Grain boundary sliding. |
| Nabarro-Herring creep (lattice diffusion creep; Nabarro, 1948; Herring, 1950, 1951) | 1 | 2 | D_v | Grain boundary sliding. |
| Solution-precipitation creep (Rutter, 1983; Raj, 1982; Spiers and Schutjens, 1990) | 1 | 3 | D_{liq} | Grain boundary sliding. |

Table 5.6. Predicted stress and grain size dependencies from theoretical creep models. D_{gb} is grain boundary diffusivity and D_v is volume or lattice diffusivity.

the equations for the best fit 1223 K isotherms (see Figure 5.3) at a differential stress of 40 MPa, versus \log_{10} mean ECD grain size has been plotted for the samples representing each batch of material investigated (see Figure 5.11). This Figure shows that there is a clear correlation between strain rate (at constant stress and temperature) with mean ECD grain size, with the exception perhaps of run fo16 which corresponds to the nominally pure forsterite sample. A best fit line to all data has a slope of 3.4, whereas a best fit ignoring the outlying point fo16 has a slope of 2.9. This analysis indicates that it is possible to explain the observed difference in steady state flow strength between the different material batches in terms of a grain size dependence of flow behaviour expressed as a grain size

exponent of $p = -3$. This result is consistent with previous studies on both wet and dry fine-grained olivine materials showing grain size sensitive (GSS) deformation, e.g. the studies by Karato et al. (1986) and Wolfenstine and Kohlstedt (1994). In addition, comparison with the mechanisms listed in Table 5.6 shows that the observed flow behaviour (n -value) and apparent grain size dependence are most consistent with a mechanism of GBS dominated flow accommodated by a grain boundary diffusion process (such as Coble creep or solution-precipitation transport) and/or a dislocation accommodation mechanism.

Alongside the above, further support for a correlation between strain rate and grain size raised to the power -3 is obtained by applying the empirical flow law developed in Chapter 4 (Equation 4.6; for material with 2.5 % enstatite and a grain size of $1.2 \mu\text{m}$, $n = 2.14$) to predict the flow stresses expected in the present experiments, assuming a d^{-3} dependence of strain rate. The predictions are plotted in Figure 5.11 as open diamonds, and clearly agree well with the present data (solid diamonds).

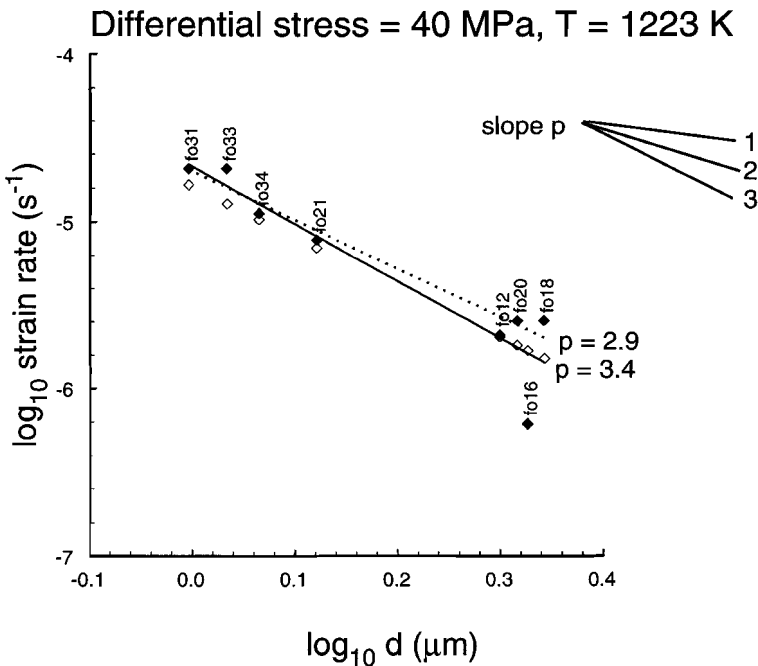


Figure 5.11. Log10 strain rate versus log10 ECD grain size. Solid diamonds represent experimental data points obtained from individual best fit isotherms (1223 K) for a fixed stress of 40 MPa (see Figure 5.3). Solid line - least squares best fit to solid diamond data points; dotted line - least squares fit to solid diamonds excluding run fo16 on nominally pure forsterite. Open diamonds are predicted strain rates using the unconstrained flow relation determined in Chapter 4 (Equation 4.6) modified assuming a grain size exponent (p) of -3 .

Inferences

On the basis of the above discussion, the following inferences are drawn:

- a) the most likely mechanism of steady state flow in the present experiments (as well as those presented in Chapter 4) is one of GBS with accommodation by grain boundary diffusion and/or dislocation activity; transitional behaviour between dislocation creep and diffusion creep cannot be eliminated but seems unlikely given the inferred grain size dependence ($p = -3$) and the lack of evidence for dislocation related microstructures,
- b) the observed effect of enstatite content is probably not a chemical interaction effect (i.e. interphase boundary, buffering or homologous temperature effect) but mainly due to an indirect physical effect related to grain size control by the added enstatite.

Point (b) is consistent with the results of Daines and Kohlstedt (1996) who found no significant difference in flow strength between samples with differing enstatite contents in dry, olivine-enstatite materials deforming with low n -values ($n = 1.2$). In the current study, there is nonetheless some, albeit weak, evidence for a small compositional effect between the forsterite-enstatite samples and the nominally pure forsterite sample (fo16), since the latter material appears to be significantly stronger than the two-phase materials of similar grain size (Figure 5.11). The absence of enstatite might have important chemical effects on the system (affecting silica activity), resulting in changes in defect chemistry and affecting the SiO_2 content of the supercritical aqueous fluid (due to the incongruent dissolution of enstatite; Morey and Hesselgesser, 1951; Nakamura and Kushiro, 1974; Schneider and Eggler, 1986). Alternatively, this might be explained by homologous temperature arguments similar to those proposed by Gleason et al. (1994) for MgO-buffered and enstatite-buffered forsterite, as the melting point of pure forsterite is substantially higher than the solidus in the two-phase forsterite plus enstatite system.

5.4.4. Implications

The present findings imply that enstatite content has little or no direct effect on the flow behaviour of wet forsterite-enstatite materials in the GSS creep field, at enstatite contents up to 20%, i.e. interphase diffusion/migration effects are minimal. Such effects are presumably not to be expected in natural olivine-orthopyroxene rocks, with comparable pyroxene content, deforming in the wet GSS regime. For example, it seems unlikely that the flow behaviour of wet fine-grained peridotite mylonites, such as those proposed by Vissers et al. (1995) to be important in controlling the strength of the lithospheric upper mantle, would be much influenced by orthopyroxene content via interphase boundary diffusion/migration or other chemical effects (though this cannot be completely eliminated for Fe-bearing systems). However, orthopyroxene content may influence grain size and hence the flow strength of natural olivine-orthopyroxene rocks deforming by wet GSS creep, in accordance with the grain size control effect of second phase content used in materials science to promote superplasticity.

5.5. Conclusions

The deformation behaviour of HIPed, wet synthetic peridotite (forsterite–enstatite ceramics plus ~ 0.5 wt % water) with enstatite contents of 0, 1, 2, 2.5, 15 and 20 % and grain sizes in the range 1 to 2 μm has been investigated in combined displacement rate and temperature stepping tests, using a gas medium deformation apparatus operated at 1123 to 1279 K and at confining pressure of ~ 600 MPa. The samples exhibited near steady state flow at stresses ≤ 60 MPa with a few runs showing work hardening at high stresses. Focusing on the near steady state behaviour, the results show that, at constant strain rate, increasing enstatite content is associated with sharp decrease (factor 3 to 10) in flow strength in the range 0 to 2.5 % enstatite. For individual compositions with ≥ 2 % enstatite content consistently high strain rate sensitivities ($m \approx 0.6$, $n \approx 1.7$) were obtained, whereas materials with nominal enstatite contents of 0 and 1 % were less consistent, having m -values of 0.36 ($n = 2.7$) and 0.81 ($n = 1.2$) respectively. The apparent activation energies for flow fall in the range 305 ± 142 kJ mol⁻¹. Microstructurally, the deformed samples showed equant, polygonal grains with no preferred crystallographic orientation. Subgrains were not observed and dislocation densities in the majority of grains appears to be zero. Cavities were observed along some grain boundaries, often extending for 2 - 3 grains, and showing no clear orientation relationship to the compression direct. Significantly, grain size analysis showed a clear negative correlation between grain size and enstatite content, indicating that enstatite content played a role in controlling the grain size of the materials due to the inhibition of grain growth during material preparation. Comparison of the mechanical data and microstructural observations with microphysical models for creep and with previous work (see Chapter 4) leads to the conclusion that the samples most probably deformed by a grain boundary sliding (GBS) dominated mechanism, accommodated by water enhanced diffusion and/or dislocation activity. A high correlation between measured flow strength and grain size was observed, consistent with a grain size exponent of -3, and thus also consistent with expectations for the inferred flow mechanism. Therefore, the effect of enstatite content on flow strength is envisaged as being an indirect physical effect caused by grain size control. The observed sharp drop in flow strength with increasing enstatite content in the range 0 to 2.5 % enstatite is inconsistent with expectations for interphase boundary diffusion/migration mechanisms of the type proposed by Wheeler (1992) and indicates that such effects were unimportant under the conditions investigated. Accordingly, such effects are not to be expected in natural olivine - orthopyroxene rocks, with pyroxene contents up to 20 %, deforming in the wet GSS regime. On the other hand orthopyroxene and other phases may influence GSS flow via grain size control.

Appendix : Estimation of enstatite content

The enstatite contents of the different material batches has been determined from the bulk compositions used during the synthesis backed up by evidence from powder X-ray diffraction analysis and scanning and transmission electron microscopy. In order to determine the sensitivity to second phase content of the XRD technique used, mechanical mixtures of forsterite with either MgO or enstatite were produced from commercially available forsterite powder (Cerac BV), synthetic enstatite produced hydrothermally at 800°C and 600 MPa from an oxide mixture using an internally heated pressure vessel, and pure MgO powder (UBE Industries, Japan). The resulting diffractograms are shown in Figures 5.A1 and 5.A2 and indicate that the standard powder X-ray diffraction procedure used will detect enstatite contents of ≥ 1 vol% (using peaks: $d = 2.870$ Å; hkl 610; $I = 100$; and $d = 3.17$ Å; hkl = 420; $I = 75$; JCPDS index card 19-768) and MgO of contents ≥ 0.5 vol % (using peak $d = 2.106$ Å; hkl = 200; see JCPDS index card 4-829). Note that the commercially available forsterite powder was found to contain (~ 1 %) MgO. It is important to search for the 2.106 Å MgO peak in the starting material as this phase will be present in materials with silica contents < 42.71 wt% silica and may therefore appear during attempts to produce compositions close to forsterite (42.71 wt% SiO₂ , 57.29 wt% MgO). MgO may also be present along with enstatite in materials which have not reacted fully during synthesis; MgO and enstatite are incompatible phases and will not coexist in fully reacted samples.

Powder XRD analysis of the starting materials demonstrate that no MgO or enstatite peaks were observed from the nominally pure forsterite composition stm19 and that no MgO peaks were observed in the more silica rich enstatite-bearing compositions (Figure 5.A3). Increasing enstatite peak heights were clearly observed from the starting materials in line with the reagent proportions. The enstatite contents quoted have been based on these proportions and are believed to accurate to within ~ 1 vol% enstatite.

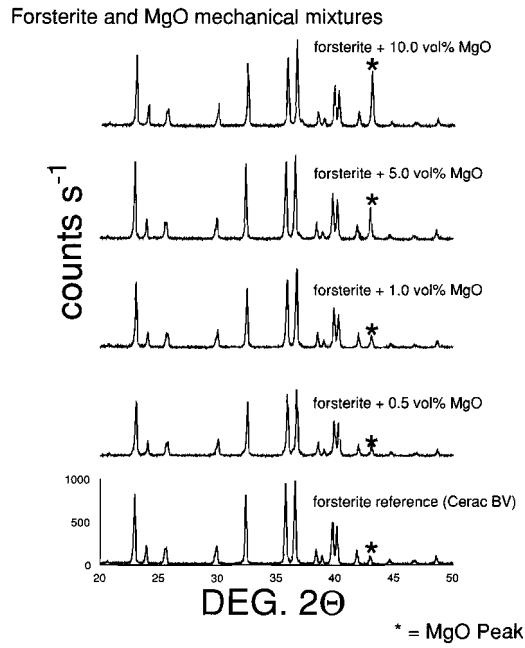


Figure 5.A1. Powder X-ray diffractograms of mechanical mixtures of forsterite plus MgO

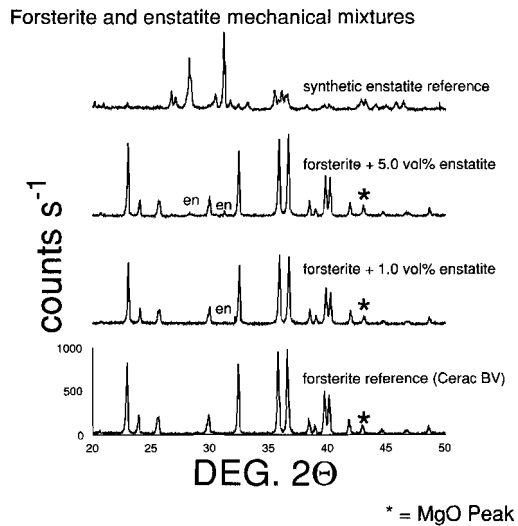


Figure 5.A2. Powder X-ray diffractograms for forsterite/enstatite mechanical mixtures.

Forsterite – enstatite starting materials

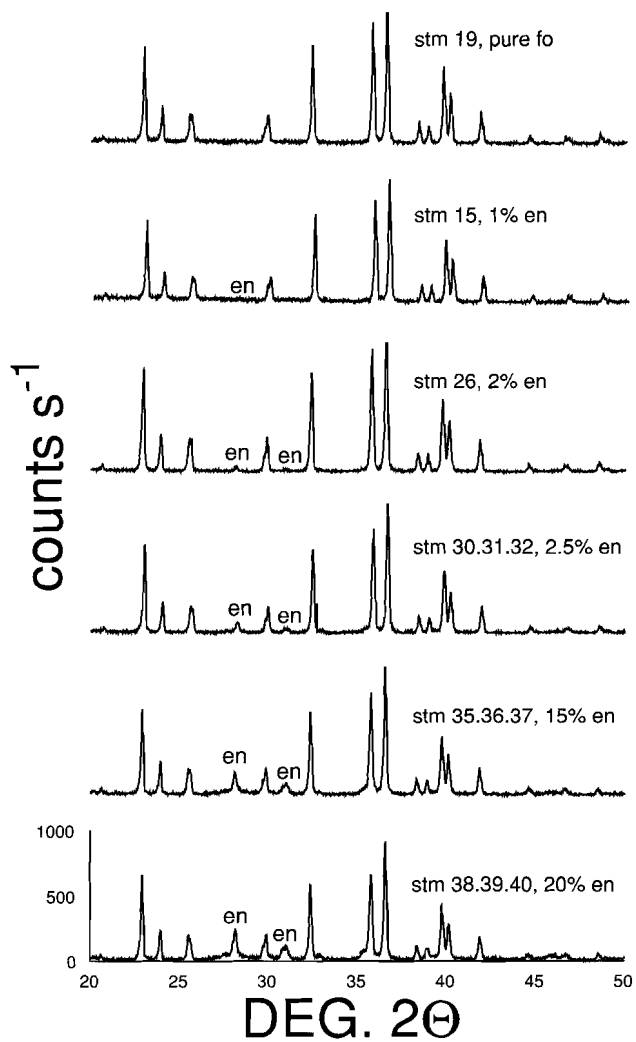


Figure 5.A3. Powder X-ray diffractograms for the 6 forsterite and forsterite/enstatite starting materials used in the current study.

The effect of varying water content on the deformation behaviour of fine-grained synthetic dunite

6.1. Introduction

Previous studies of the solid state flow behaviour of olivine single crystals (Poumellec and Jaoul, 1983; Mackwell et al., 1985) and polycrystals (Carter and Ave'Lallemant, 1970; Blacic, 1972; Post, 1977; Zeuch and Green, 1979; Chopra and Paterson, 1981, 1984; Karato et al., 1986; see also Chapter 4), at high temperatures (700 to 1450 °C) and pressures (mostly 0.3 to 3 GPa), have shown significant water weakening effects in both the dislocation and diffusion creep fields. These weakening effects have important implications for modelling mantle geodynamics. For example, Hirth and Kohlstedt (1996) have recently proposed that the strength profile of the oceanic upper mantle is controlled by the extraction of water from peridotite by melting at mid-oceanic ridges, with the residual harzburgitic material forming a strong lithosphere. Focusing on the continental lithosphere, Vissers et al. (1995) proposed that the strength profile of the lithospheric upper mantle during rifting may in some cases be controlled by water weakening effects occurring within fine-grained mylonitic shear zones transecting the top 10 to 20 km of the mantle (see also Chapter 4).

The role of water in weakening polycrystalline olivine can be highly complex. First, water may be active within the grains, producing changes in point defect chemistry and leading to intracrystalline weakening effects, i.e. increased dislocation glide or climb mobility as inferred from single crystal work (Hobbs, 1984; Poumellec and Jaoul, 1984; Mackwell et al. 1985). Second, water may be chemically active along grain boundaries and within pores, leading to enhanced grain boundary self diffusivity, facilitating solution-precipitation mechanisms, causing melting and/or enhancing grain boundary sliding (Chopra and Paterson, 1981, 1984; Karato et al., 1986; This study Chapters 4, 5). Third, water may have direct physical effects such as reducing the effective stress and mechanically decoupling grain boundaries, thus also facilitating grain boundary sliding (Chopra and Paterson, 1981). These possible roles of water may work in parallel to produce the weakening observed. However, little is known about their relative importance and their sensitivity to varying water content. This poses considerable problems for extrapolation of laboratory flow equations for wet rocks to natural conditions, e.g. for modelling upper mantle strength profiles such as those considered by Vissers et al. (1995).

This Chapter reports results from a series of six experiments in which an attempt has been made to systematically investigate the effect of bulk water content on the flow behaviour of fine-grained

synthetic dunite in the grain size sensitive (GSS) creep regime at a temperature of ~ 1223 K and a confining pressure of ~ 600 MPa. As far as the author is aware, it is the first study to directly address the effect of total bulk water content on the rheology of polycrystalline, olivine-dominated material. The samples used consisted of well-characterized forsterite (Mg_2SiO_4) - enstatite (2.5 vol% , MgSiO_3) ceramics with a grain size of ~ 1.5 μm and porosities of a few percent. Results from experiments carried out on very similar forsterite-enstatite sample material, at a constant water content of ~ 0.5 wt % and on dry control material, have already indicated that water has a marked weakening effect on deformation behaviour (see Chapters 4 and 5). In those experiments, dry control material behaved elastically up to differential stresses of 300 MPa, at 1223 K (950 °C) and at strain rates as low as $1 \times 10^{-7} \text{ s}^{-1}$. However, wet samples showed (near) steady state flow at stresses of only 5 to 60 MPa under comparable conditions. The stress and temperature dependence of creep in the wet samples was determined from stepping tests performed at strain rates in the range 5×10^{-5} to $2 \times 10^{-7} \text{ s}^{-1}$ and temperatures in the range 1123 to 1273 K. These yielded power law behaviour with stress exponents falling in the range 1.3 to 2.2, apparent activation energies of $\sim 320 \pm 40 \text{ kJ mol}^{-1}$ (see Chapter 4) and an inferred grain size exponent (p) close to -3. Combining the mechanical data with microstructural observations led to the inference that grain size sensitive (GSS) grain boundary sliding (GBS), accommodated by grain boundary diffusion and possibly some dislocation activity, was probably the main deformation mechanism in the wet samples.

The present Chapter addresses the question of the role of water in the GSS regime in the hope that the behaviour of the simple system considered will shed light on more complex natural (Fe-bearing) systems. The following added water contents have been investigated: 0.48, 0.28, 0.11, 0.05, 0.02 (wt%), as well as nominally dry material. The samples were sealed within undrained gold capsules, so that the pore fluid pressure, and consequently the water fugacity, developed during the experiments was dependent on the amount of water added, the pore volume (which is in turn dependent on the amount of compaction occurring during the experiment), and the distribution of water within the sample. This simple attempt to vary bulk water content from test to test differs from previous experiments on fine-grained synthetic olivine aggregates and natural polycrystals (Chopra and Paterson, 1981, 1984; Karato et al., 1986), in that previous experiments have generally been regarded as either wet or dry, with no control on or systematic variation of the amount of water involved, and with the implicit assumption that water pressures were equal to the applied confining pressures throughout deformation.

6.2. Experiments

6.2.1. Sample preparation

The samples used in the six experiments described here consisted of right cylinders (10 mm in diameter by 25 mm in length) cored, using a water-lubricated diamond coring tool, from sintered billets of forsterite plus 2 - 2.5 vol% enstatite ceramic with a grain size of 1 - 2 μm , synthesized using the sol-gel processing based fabrication method described in Chapter 2. One dry control sample (fo17 - see also Chapter 4) was produced from a different gel batch than the other samples investigated. The

dry control sample material was prepared by sintering at 1450 °C for 120 minutes, reaching a porosity of 6.8 % (see Table 6.1). The samples used for the five runs with controlled water contents were all made from a single batch of material. The corresponding cold isostatically pressed compacts (billets) were all sintered at 1450 °C. However, due to problems obtaining the desired post-sintering porosity of ~ 8.0 %, two firing times were used. Two of the cold-pressed billets (fo29 and fo30) were fired together for 66 minutes producing porosities of 7.0 and 7.1 % respectively; the remaining three (fo26, fo27 and fo28) were fired together for 60 minutes reaching porosities of 8.7, 8.9 and 8.8 % respectively (see Table 6.1 for the synthesis conditions). The (post-sintering) porosities of the final, cored samples were determined by the Archimedes method (see Chapter 2) and by comparison of the theoretical density with the densities calculated from the sample dimensions and the dry weight (values in brackets in Table 6.1). Note that the porosities determined from the sample dimensions are systematically higher than those obtained by the Archimedes method. The error in porosities determined by the Archimedes method is ± 0.6 %.

After coring and density measurement, the machined ceramic samples were cleaned using distilled

| Experiment/ sample No. | Gel Batch | Sintering temperature (K) and duration (mins) | Initial sample length (mm) | Initial sample diameter (mm) | Dry sample weight (g) | Initial sample porosity (%) | Volume % enstatite |
|---------------------------|--------------|--------------------------------------------------------|-------------------------------------|---------------------------------------|--------------------------------|--------------------------------------|--------------------------|
| fo17 | 26 | 1723:120 | 25.115 | 9.930 | 5.7950 | 6.80 (7.18) | 2.0 |
| fo26 | 27.28 | 1723:60 | 25.008 | 9.916 | 5.6404 | 8.69 (9.02) | 2.5 |
| fo27 | 27.28 | 1723:60 | 25.071 | 9.908 | 5.6370 | 8.88 (9.15) | 2.5 |
| fo28 | 27.28 | 1723:60 | 24.920 | 9.917 | 5.6090 | 8.80 (9.22) | 2.5 |
| fo29 | 27.28 | 1723:66 | 25.049 | 9.939 | 5.7847 | 7.06 (7.27) | 2.5 |
| fo30 | 27.28 | 1723:66 | 25.067 | 9.925 | 5.7621 | 7.10 (7.44) | 2.5 |

Table 6.1. Synthesis conditions, initial dimensions, weight and porosity, and composition of the machined cylindrical samples tested in the present experiments. Note that the initial sample porosities given refer to the post-sintering porosity, determined by the Archimedes method and from sample dimensions (values in brackets).

water and then dried in an oven at 200° C for 24 hours. Drying for longer than 24 hours produced no further weight loss and it was therefore assumed that this treatment was sufficient to dry the samples to water contents below the resolution of the balance used (~ 0.002 wt%). After drying, a controlled amount of water was introduced into the samples to be tested wet in the following manner: the sample was first submerged in a beaker of distilled water under a vacuum for ~ 10 minutes; the vacuum was then vented to air and the samples left in the water for up to one hour to allow water to penetrate into the pores; the sample was subsequently dried at ~ 95 °C until the desired final weight was achieved. This procedure was successful for all samples with the exception of fo30, which had a relatively low porosity and apparently much lower permeability than the other samples (presumably due to percolation threshold effects). As a result 9 of the 16 mg of water added to this sample for deformation testing had to be added as free water during the jacketing procedure described below. Water penetration into the other low porosity sample fo29 was successful for the desired value of 0.05 wt %. The water contents of the samples as tested are listed in Table 6.2.

| Experiment No. | Weight H ₂ O (g) | Weight % H ₂ O |
|----------------|-----------------------------|---------------------------|
| fo17 | dry | < 0.002 |
| fo26 | 0.0060 | 0.11 |
| fo27 | 0.0012 | 0.02 |
| fo28 | 0.0272 | 0.48 |
| fo29 | 0.0032 | 0.05 |
| fo30 | 0.0162 | 0.28 |

Table 6.2. The amounts of water added to the experiments. The low porosity of sample fo30 (7.1%) led to problems with the introduction of the 0.28 wt% water and extra water had to be added to the sample in the capsule. This was not a problem with the other low porosity sample (fo29 ~ 7.0 % porous), as only 0.05 wt% was introduced.

To conclude the sample preparation procedure, all five wet samples and the single dry sample were finally welded into gold capsules. Loss of water during welding was avoided by placing the sample in an ice-cooled block and by controlled semi-automated welding. The details of this procedure and capsule configuration are described in Chapters 3 and 4. All the encapsulated samples were weighed to provide a means of checking for water loss after the experimentation. The integrity of the welds was tested by first placing the encapsulated samples in a silicon oil bath at 120 °C to check for escaping vapour. A further check was carried out by placing the samples in a cold-seal pressure vessel and subjecting them to 50 MPa argon gas pressure at room temperature for ten minutes. After this treatment, the gas was rapidly released from the pressure vessel so that any leaking capsules would inflate due to trapped argon. None of the capsules was found to leak.

6.2.2. Deformation apparatus and testing procedure

After jacketing, the samples were first *hot isostatically pressed* (HIPed) and then *deformed* in axisymmetric compression mode at controlled imposed displacement rates, using the gas-medium deformation apparatus and experimental procedure described in detail in Chapters 3 and 4. In brief, the apparatus consists of a horizontally mounted, internally heated, 1 GPa pressure vessel. Axial force can be applied to the sample using an Instron 1362 testing machine to load a dynamically sealed *deformation piston* assembly. Constant volume of the pressure vessel is achieved by a compensation piston which is coupled to the deformation piston via an external yoke. Force on the sample is measured using an internal force gauge (100 kN full scale with a ~ 20 N resolution). Piston displacement is measured externally using the Instron ram displacement transducer and gas pressure is measured using a strain gauge type pressure transducer. High temperatures are achieved using a three-zone, Kanthal-AF wire furnace, controlled by a proportional-integral-differential (PID) controller using an S-type control thermocouple as input. The sample temperature is monitored by 3 S-type sample thermocouples located close to the capsule. Calibration runs have shown that the temperature gradients within the sample are of the order of 1 to 2 °C, and that the sample temperature can be assumed to equal that given by the centre thermocouple (see Figure 3.8b).

In setting up individual experimental runs, the jacketed sample was located within the apparatus, the vessel was flushed with argon and then pressurized at room temperature to ~ 600 MPa with argon gas. The samples were subsequently brought to 1223 K while maintaining the confining pressure at 600 ± 20 MPa. As soon as both pressure and temperature were found to be stable (i.e. after ~ 15 minutes heating), the deformation piston was advanced until a touch (200 N force) was indicated by the internal force gauge. The sample was then left to HIP for ~ 24 hours. After HIPing, a new touch

point was located and the measured displacement was used to calculate the compaction undergone by the sample, as well as its new porosity, assuming isotropic strain. Axial load was then removed from the sample.

Immediately after hot pressing, the pressure and temperature conditions of the apparatus were trimmed to the desired fixed values of 600 MPa and 1223 K. In order to deform each sample, the Instron testing machine was then operated in position-control to run the deformation piston into the sample at a constant displacement rate. Deformation experiments were performed using the displacement rate stepping method to achieve strain rate steps between 1×10^{-7} and $1 \times 10^{-6} \text{ s}^{-1}$. After a total of $\sim 10\%$ deformation, the sample was unloaded rapidly, while still at pressure and temperature. The furnace was then switched off, which results in cooling of the sample to room temperature within ~ 10 minutes, with a confining pressure of ~ 400 MPa remaining at this temperature. The gas was then released slowly from the vessel. After removal from the apparatus, the encapsulated samples were reweighed to check that no water was lost. Lastly, the capsules were opened and the final dimensions of the samples measured and their porosities determined using the Archimedes method.

6.2.3. Data acquisition and processing

The conditioned output signals from the apparatus' internal force gauge, gas pressure transducer, the Instron position transducer (LVDT-based), external Instron force gauge and the three sample and one primary control thermocouples were displayed and logged using two IBM-compatible personal computers (one handling temperature signals and one for all other channels, using 16 bit A/D conversion).

In processing the logged data to yield stress versus strain data, the internal force gauge readings were corrected for pressure effects, and the displacement data were corrected for apparatus stiffness (see Chapter 3 for details). Sample temperature was calculated as the average (settled) value for the strain rate step in question, as measured by the central thermocouple. From the estimated post-HIPing porosities and the directly measured final porosities given in Table 6.3, it is clear that a post-HIPing densification of ~ 1 to 2 vol% takes place during deformation. This compaction has been neglected when calculating the stress on the sample, i.e. constant volume is assumed. With regard to calculating sample strains, the contribution to measured strain of the thin gold sheets (capsule end-walls) separating the sample from the piston anvils must be considered. Taken together, the gold capsule end-walls have an initial thickness of 2×0.25 mm. During the test these become deformed. However, flow of the gold is strongly restricted by the piston anvils and trial experiments, performed using rigid ceramic test pieces, have shown that significant deformation of the gold typically requires axial stresses in excess of 50 to 60 MPa under the conditions of the experiments reported here. Moreover, measurement of the final gold thickness after individual tests reaching stresses up to 100 MPa has shown that gold deformation then contributes a maximum of 0.1 mm to the measured displacement, which is equivalent to 0.4 % strain. Since the stresses achieved in tests fo26, fo28 and fo30 reported here mostly fall below 50 to 60 MPa, no attempt has been made to correct for this gold deformation in calculating the stress strain curves for wet samples. Strain rate or temperature steps reaching higher stresses may be affected, thus showing strains up to 0.4 % greater than actually

achieved in the sample. On the other hand, in cases where steady state flow is approached, gold deformation of this order will not significantly affect interpretation of the data in terms of steady state flow and corresponding strain rate. In the case of experiments fo17, fo27 and fo29 in which stresses greater than 50 to 60 MPa are achieved, and in which steady state flow is not approached in the sample, errors in the stress strain curve due to gold deformation will be important and, in principle, need to be corrected for. However, the gold deformation behaviour has been found to be insufficiently reproducible at high stresses (>50 MPa) to allow usefully accurate correction. For this reason, the higher stress curves presented here have not been corrected for gold deformation and are interpreted accordingly. In conclusion, taking into account all errors, the internal force measurements are accurate to $\sim 1\%$ of the measured value and displacements to within $\sim 2 \mu\text{m}$.

6.3. Results

6.3.1. Hot isostatic pressing results and mechanical data

The results of the HIPing stage of the six experiments are given in Table 6.3 and in Figure 6.1, which shows the initial and post-HIPing porosities plotted against bulk water content. Note that the dry control sample (fo17) showed no measurable compaction during the HIPing stage. The slightly wet samples fo27 (0.02 wt% H_2O) and fo29 (0.05 wt% H_2O) showed minor porosity reduction (2.7 and 0.6 % respectively). However, the wetter samples, i.e. fo26 (0.11 wt% H_2O), fo30 (0.28 wt% H_2O) and fo28 (0.48 wt% H_2O), showed much more porosity reduction (5.8, 3.3 and 5.9 % respectively), reaching post-HIPing porosities of $\sim 3\%$. It is evident then that the amount of densification during HIPing initially increases with increasing water content but appears to be more or less constant for 3 to 0.1 wt % water (Figure 6.1).

Turning to the behaviour observed during deformation testing and recalling that the stress strain curves are uncorrected for gold end-wall deformation of the capsule (which generally becomes sig-

| Experiment no. (wt% H_2O) | HIPing duration at 1223 K and 600 MPa (hrs:mins) | Estimated post-HIPing porosity (%) | Final porosity (%) | Permanent strain (%) |
|--------------------------------------------|--------------------------------------------------|------------------------------------|--------------------|----------------------|
| fo17 (<0.002) | 23:00 | 6.8 | 6.8 | 0.0 |
| fo26 (0.11) | 25:00 | 2.9 | 0.3 | 10.1 |
| fo27 (0.02) | 23:50 | 6.1 | 5.8 | 1.5 |
| fo28 (0.48) | 24:00 | 2.9 | 2.0 | 12.0 |
| fo29 (0.05) | 25:15 | 6.4 | 6.6 | 0.8 |
| fo30 (0.28) | 24:00 | 3.8 | ---- | ~ 7.0 |

Table 6.3. HIPing duration, post-HIPing porosity, measured final porosity after deformation (Archimedes method) and permanent axial strain after deformation calculated from the final dimensions. The final porosity estimates have an error of $\pm 0.6\%$.

nificant at differential stresses > 50 to 60 MPa), it is noteworthy that measurement of the dry control sample fo17 after deformation showed no permanent strain whatsoever, despite the total treatment of 24-hours HIPing at 600 MPa and 1223 K followed by axial loading to a differential stress of

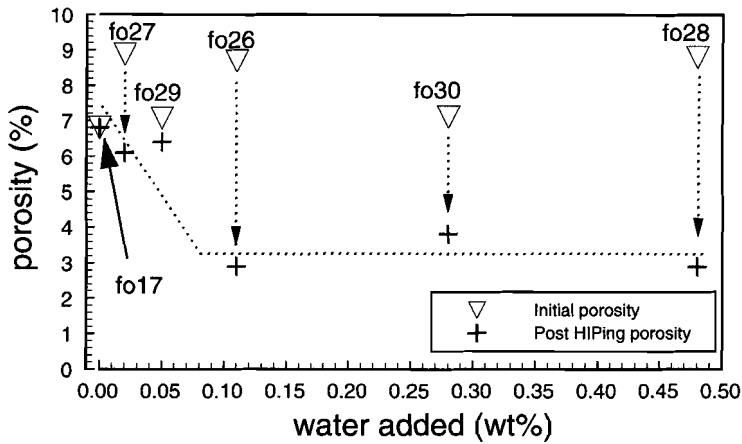


Figure 6.1. Plot of initial porosity and post-HIPing porosity versus the weight percent water added. The initial porosities of samples fo26, fo27 and fo28 are very similar. Note the lower initial porosities of samples fo29 and fo30. The dotted line indicates the trend shown by the final porosities. Dotted arrows highlight the porosity reduction of the individual samples during HIPing.

300 MPa at rates down to $1 \times 10^{-7} \text{ s}^{-1}$. The dry sample must therefore have behaved elastically in rough accordance with the inferred elastic loading curve inserted into Figure 6.2a.

The stress-strain curves obtained for the five water-added experiments are shown in Figures 6.2 b to f and the corresponding differential flow stress versus strain rate stepping results are tabulated in Table 6.4. While all showed some degree of water weakening relative to fo17, these water added samples fall into two groups. The stress strain curves for samples fo27 and fo29 with $< 0.1 \text{ wt}\% \text{ H}_2\text{O}$ showed strong hardening at strain rates of between 1×10^{-6} and $2 \times 10^{-7} \text{ s}^{-1}$, reaching differential stresses up to $\sim 230 \text{ MPa}$. Measurement of these samples after deformation showed that only small permanent strains were achieved (up to 1.5 %; gold deformation of $\sim 1.3 \%$). In contrast, samples fo28 and fo26 with $\geq 0.1 \text{ wt}\% \text{ H}_2\text{O}$ deformed by low stress, (near) steady state flow, reaching permanent strains measured after deformation of ~ 10.1 to 12.0% (gold deformation $< 0.3 \%$). Sample fo30 also showed low stress flow but failed brittly at $\sim 7 \%$ strain due to jacket failure. Differential stress versus strain rate data are plotted for samples fo28 and fo26 in Figure 6.3. Adopting a conventional power law description of the stress versus strain data, samples fo26 and fo28 showed strain rate sensitivities (m) of 0.65 and 0.60, i.e. stress exponents ($n = 1/m$) of 1.5 and 1.7 respectively. Note that sample fo26, with 0.11 wt% H_2O , was found to be a factor of ~ 2 stronger than sample fo28, with 0.48 wt% H_2O , at constant strain rate (see Figure 6.3). In view of the problems encountered in run fo30 (0.28 wt% H_2O), which showed ductile behaviour with intermittent jumps in flow stress (presumably cracking events, see 6.2e) before brittle failure at $\sim 7 \%$ strain due to jacket failure, data from this sample are omitted from Figure 6.3.

The final porosities of the deformed samples are shown in Table 6.3. Note that sample fo26 (0.11 wt% H_2O) showed a particularly high density (final porosity only $\sim 0.3 \%$); this measurement was backed up by naked eye inspection of the sample, which had a waxy appearance, unlike the more porous samples, which were whiter and less translucent.

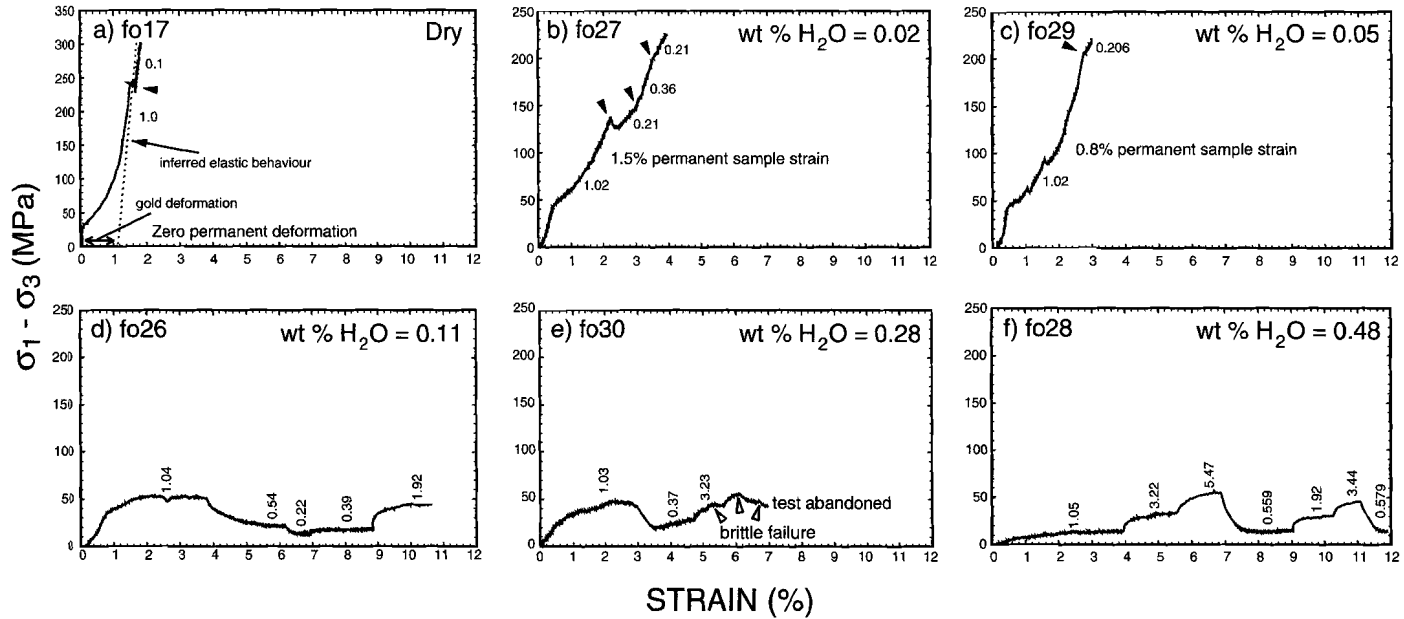


Figure 6.2 a to f. Stress versus strain curves obtained for the dry control sample (fo17) and the five water-added samples (all at ~ 1223 K). Note that no correction has been applied for deformation of the gold end-walls separating the sample from the loading pistons, which starts to become significant at differential stresses > 50 MPa. Strain rates are as indicated ($\times 10^{-6} \text{ s}^{-1}$). The permanent sample strains shown for samples fo17, fo27 and fo29 (a,b,c) are based on the final measured sample length. The position of the displacement rate steps in (a),(b) and (c) are indicated with a solid arrowhead. N.B. the stress axis in (a) is to 350 MPa, ref. 250 in (b) to (d).

| Experiment No. | Displacement rate (mm s ⁻¹) | Strain rate (s ⁻¹) | Differential stress (MPa) |
|----------------------------------|--------------------------------------------|-----------------------------------|------------------------------|
| fo26 (0.11 wt% H ₂ O) | 2.50 x 10 ⁻⁵ | 1.04 x 10 ⁻⁶ | 52 |
| | 1.25 x 10 ⁻⁵ | 5.41 x 10 ⁻⁷ | 22 |
| | 5.00 x 10 ⁻⁶ | 2.19 x 10 ⁻⁷ | 13 |
| | 8.76 x 10 ⁻⁶ | 3.88 x 10 ⁻⁷ | 18 |
| | 4.24 x 10 ⁻⁵ | 1.92 x 10 ⁻⁶ | 44 |
| fo27 (0.02 wt% H ₂ O) | 2.50 x 10 ⁻⁵ | 1.02 x 10 ⁻⁶ | no steady state |
| | 5.00 x 10 ⁻⁶ | 2.07 x 10 ⁻⁷ | no steady state |
| | 8.76 x 10 ⁻⁶ | 3.63 x 10 ⁻⁷ | no steady state |
| | 5.00 x 10 ⁻⁶ | 2.09 x 10 ⁻⁷ | no steady state |
| fo28 (0.48 wt% H ₂ O) | 2.50 x 10 ⁻⁵ | 1.05 x 10 ⁻⁶ | 13 |
| | 7.50 x 10 ⁻⁵ | 3.22 x 10 ⁻⁶ | 32 |
| | 1.25 x 10 ⁻⁴ | 5.47 x 10 ⁻⁶ | 55 |
| | 1.25 x 10 ⁻⁵ | 5.59 x 10 ⁻⁷ | 15 |
| | 4.24 x 10 ⁻⁵ | 1.92 x 10 ⁻⁶ | 30 |
| | 7.50 x 10 ⁻⁵ | 3.44 x 10 ⁻⁶ | 45 |
| | 1.25 x 10 ⁻⁵ | 5.78 x 10 ⁻⁷ | 15 |
| fo29 (0.05 wt% H ₂ O) | 2.50 x 10 ⁻⁵ | 1.02 x 10 ⁻⁶ | no steady state |
| | 5.00 x 10 ⁻⁶ | 2.06 x 10 ⁻⁷ | no steady state |
| fo30 (0.28 wt% H ₂ O) | 2.50 x 10 ⁻⁵ | 1.03 x 10 ⁻⁶ | 45 (hardening) |
| | 8.76 x 10 ⁻⁶ | 3.70 x 10 ⁻⁷ | 28 (hardening) |
| | 7.50 x 10 ⁻⁵ | 3.23 x 10 ⁻⁶ | brittle failure |

Table 6.4. Mechanical results. Strain rate steps and corresponding differential stresses (at near steady state) for the five water-added experiments.

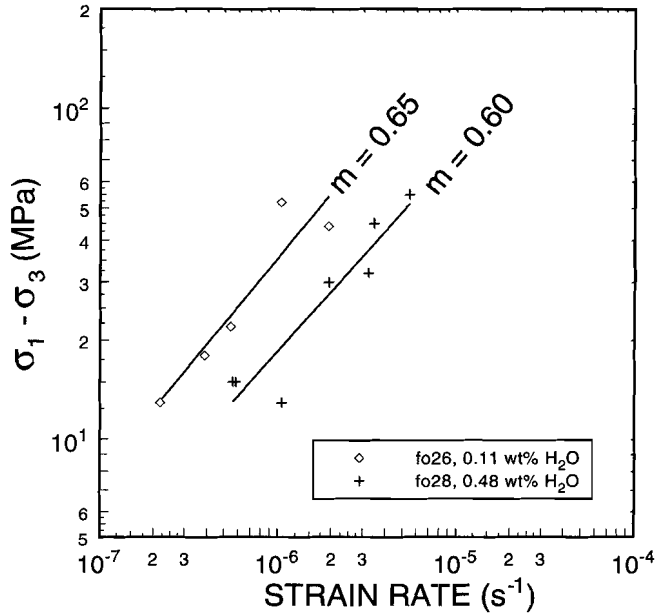


Figure 6.3. Plot of differential stress versus strain (log scaling) for the wetter runs fo26 and fo28 which showed (near) steady state flow at low stresses. The strain rate sensitivities have been determined using a power law fit to the complete data set obtained for each run and the values are as indicated.

6.3.2. Grain size analysis and microstructural observations

Microstructural analysis of *as sintered* starting material (batch stm 27.28) and of wet and dry deformed samples was carried out using scanning electron microscopy (SEM), performed with a Philips XL30 field emission gun (FEG) microscope, and transmission electron microscopy (TEM), performed with the Philips CM200. Grain size analysis was carried out on the *as sintered* starting material (porosity ~ 9 %) and the deformed samples using computer image analysis of scanned grain boundary tracings obtained from orientation contrast SEM images of unetched, uncoated samples (see Chapter 4 for details of these techniques). No distinction was made between forsterite and enstatite grains as these were similar in size. Average sample grain size (d) values quoted here are expressed as the mean equivalent circular diameter (ECD) as these values correspond well with the theoretical mean linear intercept grain sizes calculated, and therefore allow comparison with previous studies (see Table 6.5). The theoretical mean linear intercept grain sizes were determined by calculating a theoretical mean intercept length value (L_3) and the corresponding grain diameter ($L_3 \times 1.56$) from the measured projected grain areas for each sample, assuming the grains to be single size tetrakaidecahedra shaped grains (Underwood 1970; see Equation 4.4, Section 4.4.3). The ECD grain size distributions have been plotted in Figure 6.4 for all samples tested plus starting material stm 27.28. They are approximately log-normal in form, resembling those described for similar material in Chapters 4 and 5. Table 6.5 lists the grain size statistics obtained. Clearly, grain growth during HIPing and deformation has been minor. The detailed microstructure of the various samples will now be discussed.

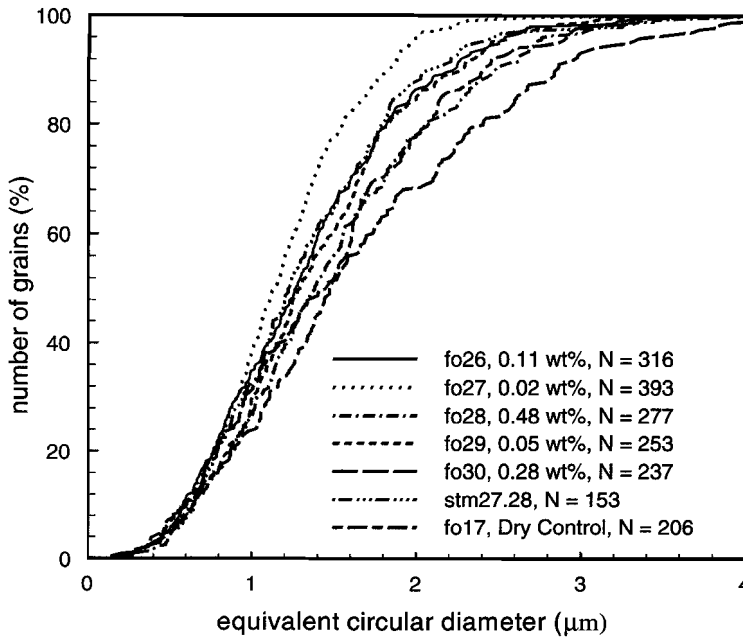


Figure 6.4. ECD grain size frequency plot for the starting material, dry control and five samples with added water. The grain size distributions are all approximately log-normal and only minor grain growth has occurred.

| Sample No. | N | Mean area (μm^2) | Mean ECD (μm) | Mean \log_{10} area (μm^2) | Standard deviation \log_{10} area (μm^2) | ECD of mean \log_{10} area | L_3 (μm) | $L_3 \times 1.56$ (μm) |
|---------------------------------------|-----|-------------------------------|----------------------------|-------------------------------------------|---------------------------------------------------------|------------------------------|-------------------------|-------------------------------------|
| stm 27.28 as sintered | 153 | 1.56 | 1.29 | +0.0205 | 0.435 | 1.15 | 0.816 | 1.27 |
| fo17 (dry) | 206 | 2.14 | 1.50 | +0.1417 | 0.461 | 1.33 | 0.955 | 1.49 |
| fo26 (0.11 wt% H_2O) | 316 | 1.69 | 1.34 | +0.0368 | 0.445 | 1.17 | 0.849 | 1.32 |
| fo27 (0.02 wt% H_2O) | 393 | 1.24 | 1.17 | -0.0377 | 0.368 | 1.08 | 0.727 | 1.13 |
| fo28 (0.48 wt% H_2O) | 277 | 2.12 | 1.49 | +0.1360 | 0.444 | 1.32 | 0.951 | 1.61 |
| fo29 (0.05 wt% H_2O) | 253 | 1.74 | 1.36 | +0.0649 | 0.444 | 1.21 | 0.861 | 1.34 |
| fo30 (0.28 wt% H_2O) | 237 | 2.61 | 1.60 | +0.1611 | 0.521 | 1.36 | 0.974 | 1.52 |

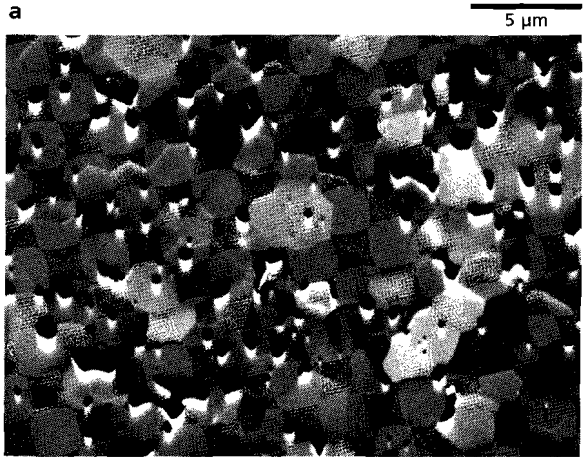
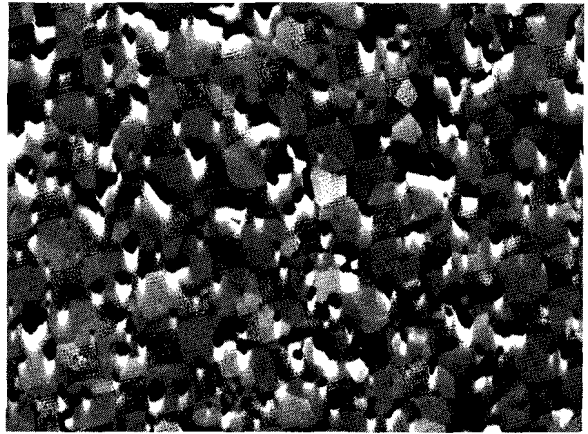
Table 6.5. Grain size analysis statistics. ECD is the equivalent circular diameter, L_3 is the calculated mean linear intercept length, and $L_3 \times 1.56$ denotes the theoretical mean linear intercept grain size.

Examination of the as sintered *starting material* using the above mentioned SEM methods showed it to be microstructurally homogeneous throughout (Figure 6.5a). The grains have a foam texture and have a narrow grain size distribution with an average ECD grain size (d) of $\sim 1.29 \mu\text{m}$ (Table 6.5). Grain boundaries are generally straight and equilibrium triple junctions of 120° are common. Both intragranular and intergranular pores are present totaling $\sim 9\%$ porosity. The bulk of the porosity ($\sim 8\%$) is made up of intergranular pores. These are generally along grain boundaries and at triple

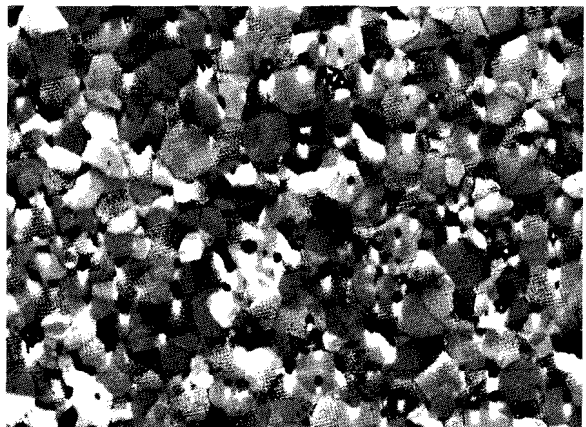
Figure 6.5 a to c.

SEM orientation contrast micrographs: a) Starting material stm 27.28; b) Dry deformed control sample fo17 (stm 26); c) Wet deformed sample fo27, 0.02 wt% H₂O. Note the similarity between the starting material (a), the dry sample fo17 (b) and fo27 (c). Note the change in pore distribution and geometry between sample fo27 (c) and samples fo26 and fo28 (d,e) with > 0.1 wt% H₂O. Note in addition, that the density of sample fo26 with 0.11 wt% H₂O (e) is higher than sample fo28 with 0.48 wt% H₂O (d). Note that the wet deformed samples all come from batch stm 27.28. For the deformed samples (c to f) the compression direction is horizontal.

a) Starting material stm 27.28.



b) Dry deformed control sample fo17 (stm 26).

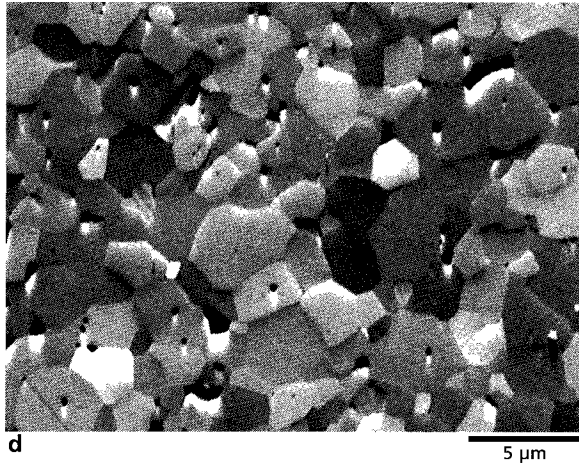


c) Wet deformed sample fo27, 0.02 wt% H₂O.

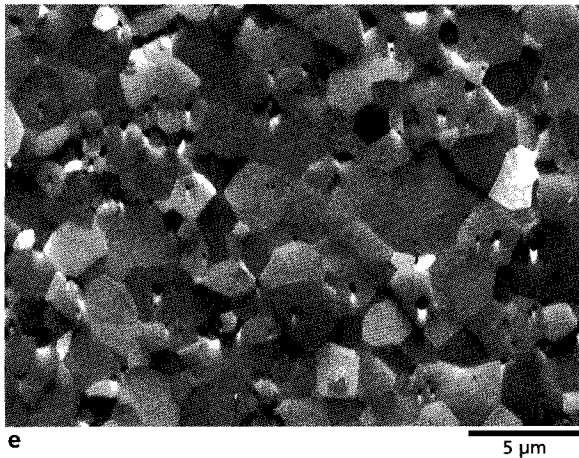
Figure 6.5 d to f.

SEM orientation contrast micrographs: d) Wet deformed sample fo28, 0.48 wt% H₂O; e) Wet deformed sample fo26, 0.11 wt% H₂O; f) Wet deformed sample fo30, 0.28 wt% H₂O.

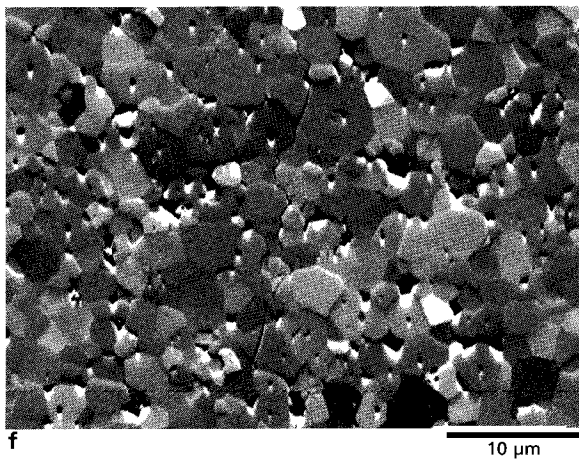
d) Wet deformed sample fo28, 0.48 wt% H₂O.



e) Wet deformed sample fo26, 0.11 wt% H₂O.



f) Wet deformed sample fo30, 0.28 wt% H₂O, shows intergranular and transgranular fracturing associated with capsule failure.



and 4 - 6 grain junctions, and are smaller than the grains themselves ($d/2$ to $d/10$). They are characterized by apparent dihedral angles $> 60^\circ$ and are rounded and disconnected in 2-D cross-section. This geometry is consistent with the observation that the permeability of the starting material cuts off at approximately 7.5 % porosity as the percolation threshold is approached. No melts or grain boundary phases have been observed at the scale of observation employed.

The single *dry control sample* studied (fo17) is microstructurally highly similar to the starting material (compare Figures 6.5a and b). This is not surprising since no measurable HIPing or permanent deformation was achieved. Lamellae visible in the enstatite grains are most probably of clinoenstatite within orthoenstatite and may have resulted from either microplasticity during loading (shearing induced - Riecker and Rooney, 1966; Coe and Kirby, 1975) or quenching (cooling induced - Sclar et al., 1964; Boyd and England, 1965; Grover, 1972). The mean ECD grain size of the dry control material is 1.50 μm .

Microstructurally, the *wet-tested samples* fall into two groups depending on water content (Figures 6.5 c to f). Those with > 0.1 wt% water (i.e. samples fo28 - 0.48 wt% H_2O , fo30 - 0.28 wt% H_2O , and fo26 - 0.11 wt% H_2O), have a dense appearance (Figures 6.5 d - f) with relatively few intergranular pores remaining, whereas samples fo29 (0.05 wt% H_2O) and fo27 (0.02 wt% H_2O) show a highly porous microstructure more similar to the undeformed starting material and the dry control sample. In addition, while all samples have an ECD grain size of 1.2 to 1.6 μm (Table 6.5), the wetter samples, particularly fo28 (1.49 μm) and fo30 (1.60 μm), are somewhat coarser than the drier samples, which may indicate that the fluid has facilitated minor grain growth. Focusing on the *relatively dry samples* (< 0.1 wt% H_2O), these show a foam texture with numerous intergranular pores which have apparent dihedral angles generally $> 60^\circ$ (see Figure 6.5c). The enstatite grains are of a similar grain size to the forsterite grains, and exhibit thin lamellae. The grain boundaries are often gently curved and show unusually high contrast. The microstructure of the *wetter samples* fo28 and fo26 are shown in Figures 6.5c and 6.5d respectively. While these samples are dense in comparison with the starting material and the drier samples (fo27 and fo29), sample fo26 (0.11 wt% H_2O) is more dense than sample fo28 (0.48 wt% H_2O), with a noticeable reduction in the number of intergranular pores. In other respects, however, these two samples are very similar. They have foam textures with very gently curved or straight grain boundaries. The apparent dihedral angles subtending the relatively few intragranular pores are reduced in comparison with the drier samples, being $\leq 60^\circ$. The enstatite grains show well developed lamellae. Figure 6.5f shows sample fo30 and, taking into account the strain reached in this sample, its microstructure is similar to the other wetter samples (fo28, fo26). However, clear evidence is also visible for brittle fracture associated with jacket failure.

In addition to the SEM observations on the wet-tested samples reported above, wet-tested samples fo27 (0.02 wt% H_2O), fo29 (0.05 wt% H_2O) and fo28 (0.48 wt% H_2O) have been examined using transmission electron microscopy (TEM; Figures 6.6 a to h) in collaboration with Dr. Herman van Roermund. In all of these samples, the vast majority of the grains ($> 80\%$) were observed to be dislocation and subgrain free. No identifiable melts were observed in any of the samples and if melts are indeed present they must represent a very low volume fraction of the sample. Clear differences exist between the TEM microstructure of the two drier, water-added samples, fo27 and fo29 (0.02 and 0.05 wt % H_2O), and the wetter sample, fo28 (0.48 wt %). First, the drier samples show higher

Figure 6.6 a to b.
TEM micrographs.

fo27 0.02 wt% water. Note the high porosity (P), large angular pores with apparent dihedral angles (DA) generally $> 60^\circ$, and the inclusion free grain boundaries (gb).

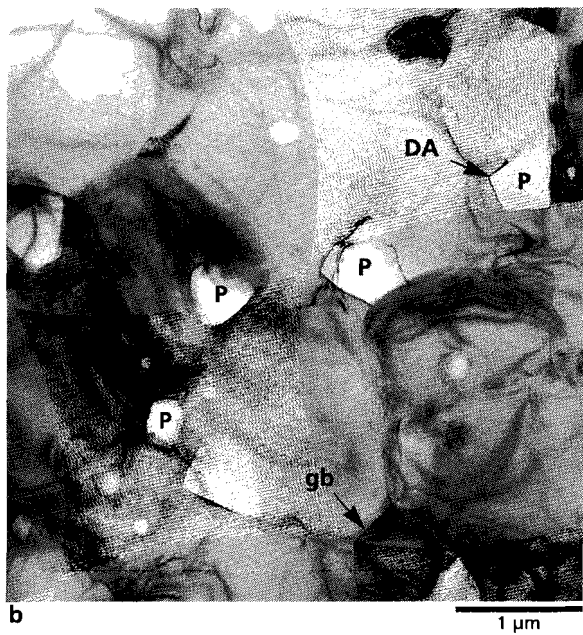


Figure 6.6 c and d.

fo29 0.05 wt% water. Note the high porosity (P), large angular pores with apparent dihedral angles (DA) generally $> 60^\circ$, and the inclusion free grain boundaries (gb).

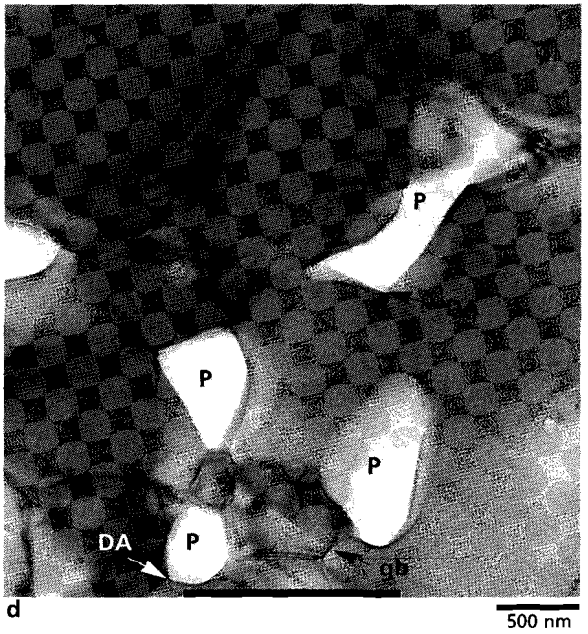
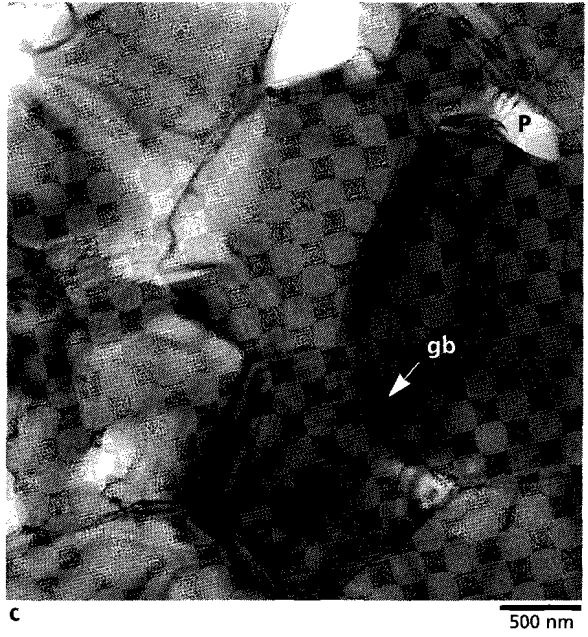


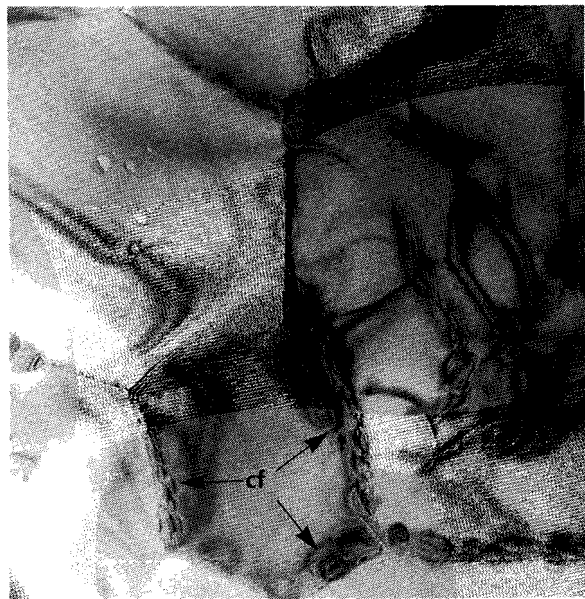
Figure 6.6 e and f.

fo28 with 0.48 wt% water. Note the much reduced porosity (P) compared with the drier samples, numerous triple junction pores (TJP); the apparent dihedral angles (DA) are generally $< 60^\circ$. The grain boundaries show concentric fringes (cf) of contrast presumably related to grain boundary inclusions.



e

1 µm



f

500 nm

Figure 6.6 g and h.

fo28 with 0.48 wt% water. Note grain boundary contrast features (cf) and triple junctions (TJ).



porosity and apparent dihedral angles $> 60^\circ$ (Figures 6.6 a - d) as observed also with the SEM. Second, the grain boundaries of the drier samples are free from inclusions and generally show parallel arrays of contrast fringes (Figures 6.6 a - d). In the wetter sample fo28, the porosity is low, the apparent dihedral angles are often $< 60^\circ$ (Figure 6.6 e) and many, though not all, of the grain boundaries show trains of elliptical (2-D) or ellipsoidal (3-D) regions of contrast (concentric fringes) each up to 100 nm in length. These are reminiscent of inclusion arrays but do not appear to be centred on either voids or particles at the scale of TEM observation used (6.6 e - f). These features have been observed to move in the TEM beam (pers. comm. Herman van Roermund). Note their absence in the drier samples and the fact that no trace of similar features was seen in the SEM images of the wetter material.

6.4. Discussion

The present experiments represent an attempt to systematically investigate the role of bulk water content on the flow behaviour of fine grained olivine materials. A clear relationship between the bulk (added) water content and the degree of hot isostatic pressing (HIPing) and water weakening during deformation has been found, with water enhanced HIPing and weakening becoming 'turned on' with the addition of ~ 0.1 wt% water with relatively little change at higher water contents. However, only six tests have been carried out and the data are not without their problems. Firstly, samples fo29 and fo30, although being compositionally identical to the other water-added samples, had initial porosities ~ 1.5 % lower than the other samples. The lower porosities, and therefore lower permeabilities of these two samples, led to some difficulties with water infiltration. This was particularly the case for sample fo30, where 9 mg of the 16 mg of water added had to be introduced separately into the capsule. These two samples showed somewhat higher than expected post-HIPing porosities (see Figure 6.1) when compared with the other samples, and this is believed to result from poor distribution of fluid in these samples. The behaviour of fo29, and perhaps even the brittle failure of sample fo30, during deformation may also have been related to problems of fluid distribution and or uneven fluid pressure. Fortunately, the remaining wet samples (fo26, fo27 and fo28) all had very similar starting porosities, and the corresponding experiments spanned the entire range of water contents explored. Accordingly, if the problems with water distribution in samples fo29 and fo30 are borne in mind, a picture of the role of bulk water content can still be drawn. Secondly, the dry control sample (fo17) is from a different batch of material than the other five samples investigated, though with very similar composition (~ 2 vol% en). However, additional tests (fo18, fo19 and fo20; see Chapter 5) have shown that material from the same batch as fo17 undergoes a similar water weakening to that observed here, and that the sample used is a valid dry control.

In the following, the partitioning, pressure and fugacity of water within the forsterite-enstatite system studied will be discussed before moving on to discuss the observed effects of water on HIPing and deformation, and its possible role in enhancing deformation. Lastly, the implications of the findings will be briefly discussed.

6.4.1. Partitioning of water and estimation of fluid pressures and water fugacities

In the wet forsterite-enstatite system investigated here, water and water related species (OH⁻, H⁺) will be partitioned between the various phases present in the system, i.e. dissolved in the solid phases, dissolved in any melts or melt films, present as a free fluid in pores and in any grain boundary fluid films, and/or dissolved in the grain boundaries.

The effect of water on the melting relations of forsterite and enstatite have been investigated by Kushiro and coworkers (Kushiro and Yoder, 1969). The presence of water substantially lowers the melting point of pure forsterite and the solidus temperature of the forsterite plus enstatite system, and causes the melting point/solidus temperatures of these systems to move to lower temperatures with increasing pressure (which is opposite to the behaviour seen in the dry systems). In the pure forsterite system at 600 MPa, the wet solidus is at ~ 1600 °C (Kushiro and Yoder, 1969) compared with dry melting at the same pressure at ~ 1910 °C (Davis and England, 1964). The addition of water also has important effects on the high pressure melting of enstatite, causing a change from (dry) congruent to incongruent melting (Kushiro et al., 1968). At 600 MPa the solidus in the wet forsterite plus enstatite system is at ~ 1410 °C (Kushiro and Yoder, 1969). Thus it is clear that under the conditions employed in the current study the system used should be melt-free and no melts have been observed. Therefore, any melts that are present would have to be melt films or blebs of unresolved dimensions and minor volumetric importance. Taking this observation into account, any role of melts in controlling the partitioning of water in the system is inferred to be negligible.

Focusing now on the forsterite phase, due to the lack of data on the solubility of water-related species in pure Mg-forsterite, water solubility data from iron-bearing olivine must be used to obtain a rough estimate of the water partitioned into the forsterite phase. For Fe-bearing olivine, the work

| Experiment No. | Weight % H ₂ O | Estimated Initial P _f (MPa) and f _{H₂O} (MPa) in brackets | Estimated P _f after HIPing (MPa) and f _{H₂O} (MPa) in brackets | Estimated P _f range for the end of deformation (MPa) |
|----------------|---------------------------|------------------------------------------------------------------------------------------|-----------------------------------------------------------------------------------------------|-----------------------------------------------------------------|
| fo17 | < 0.002 | ---- | ---- | ---- |
| fo26 | 0.11 | 20 (19) | 61 (59) | 497 to >1000 |
| fo27 | 0.02 | 4 (4) | 6 (6) | 6 to 6.5 |
| fo28 | 0.48 | 86 (81) | 348 (333) | 613 to > 1000 |
| fo29 | 0.05 | 13 (13) | 14 (14) | 13 to 15 |
| fo30 | 0.28 | 64 (61) | 209 (191) | ---- |

Table 6.6. Pore fluid pressures and water fugacities before HIPing (initial P_f and f_{H₂O}), after HIPing, and the estimated pore fluid pressures for the end of deformation. Values calculated assuming all the water existed as a pure H₂O fluid phase evenly distributed throughout the available porosity using steam tables (Haar et al., 1984).

of Bai and Kohlstedt (1993) implies that the incorporation of water is facilitated by the presence of Fe³⁺ which dictates the overall defect population and which acts as an electron acceptor enabling incorporation of protons into M-site vacancies. The absence of an electron acceptor-cation in pure Mg-forsterite is therefore expected to mean that the solubility of water related species will be lower than in Fe-bearing olivine. Solubility data for the Fe-bearing system are thus believed to give an

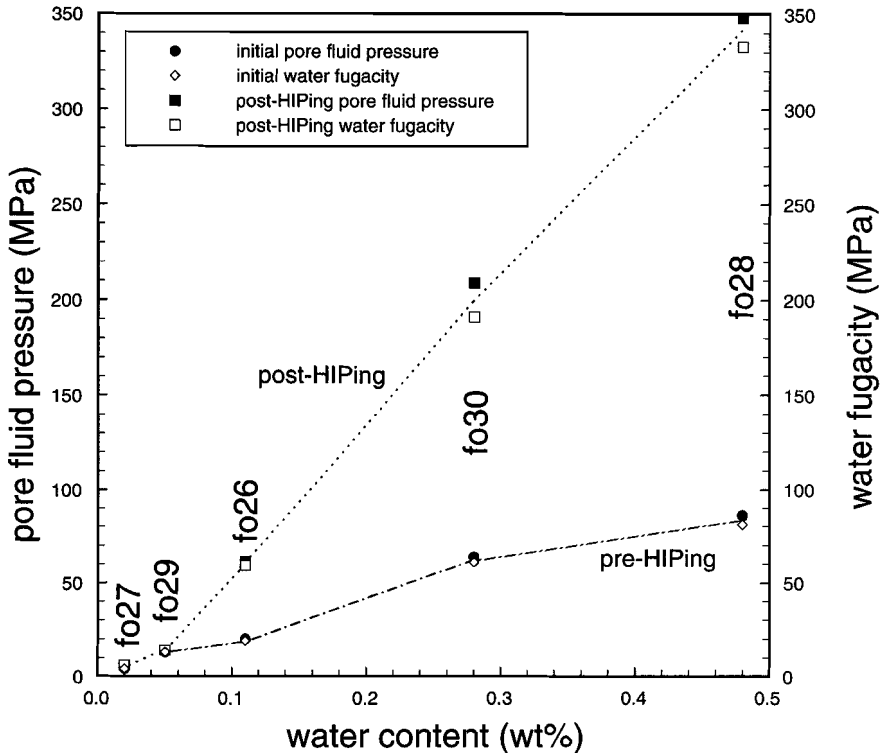


Figure 6.7. Plot of initial (pre-HIPing) pore fluid pressures/water fugacities and post-HIPing pore fluid pressures/water fugacities versus water content. For the experiments fo27 and fo29 the four data points for each experiment plot on top of one another. In experiments fo26, fo30 and fo28 the pore fluid pressure and water fugacity increase during HIPing due to densification. The P_f and f_{H_2O} values were calculated using the initial and post-HIPing pore volumes, the masses of water added, and the data of Haar et al. (1984), assuming all water remained in the fluid phase.

upperbound estimate of water solubility in pure forsterite. In iron-bearing olivine, the solubility of water has been found to increase with increasing fluid pressure (Bai and Kohlstedt, 1993). At a fluid pressure of 600 MPa, the solubility of water in iron-bearing olivine is $\sim 316 \text{ H} / 10^6 \text{ Si}$, which equals $\sim 0.002 \text{ wt\%}$ water. Accordingly, this value has been taken as an upper limit for solubility of water in forsterite for the current experiments. From this, it can be seen that there is more than sufficient water in all the water-added experiments (minimum added water = 0.02 wt %) to saturate the forsterite over the entire range of possible fluid pressures ($\leq 600 \text{ MPa}$). This fact, along with the observed absence of detectable melt, implies that almost all of the fluid in the experiments with added water (0.02 to 0.48 wt%) must have existed as an aqueous fluid within the pores and perhaps along grain boundaries. The solubility of water in enstatite has been neglected when considering the partitioning of water, as only a small volume fraction ($\sim 2.5 \text{ vol\%}$) of this phase is present.

On the basis of the above, if the assumption is made that *all* the water present in the samples exist-

ed as a pure H₂O fluid phase evenly distributed throughout the available porosity, the evolution of the pore fluid pressure and water fugacity during the experiments (HIPing and deformation stages) can be modelled using data from Steam Tables (Haar et al., 1984), graphically calculating fugacities using the method described by Nordstrom and Munoz (1985, p. 131). Fluid pressures and water fugacities based on these assumptions have been calculated for each experimental run to obtain instantaneous pore fluid pressure values corresponding to the start of HIPing (from initial porosity data), the end of HIPing (from post-HIPing porosity data), and the end of deformation (from final porosity data). These values are shown in Table 6.6. The measured porosities have an error of ± 0.6 %, which does not greatly affect the fluid pressures calculated at the higher porosities. Therefore, a single fluid pressure has been calculated for the initial porosity and the post-HIPing porosity (Table 6.6 and Figure 6.7). This error in porosity does, however, introduce a large error in the calculated fluid pressure as the porosities become small, as is the case for samples fo26 (0.11 wt% H₂O) and fo28 (0.48 wt% H₂O) which have high water content. Therefore, for the deformed samples, a range of fluid pressures have been calculated, taking into account the 0.6 % error (Table 6.6). In addition to this modelling exercise, fluid pressure has been calculated as a continuous function of porosity for each experiment. This has been carried out using the equations of state for water taken from Kerrick and Jacobs (1981) and the results are shown in Figure 6.8. From this figure it is clear that, for samples fo28 and fo26, the fluid pressure will equal the confining pressure at

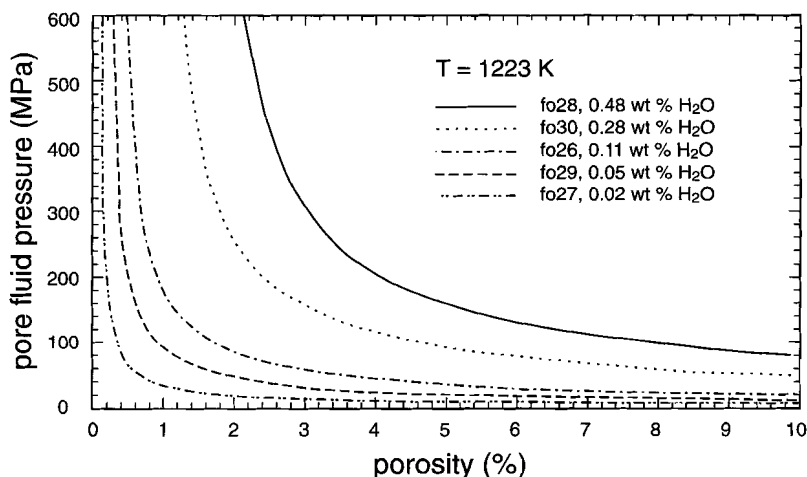


Figure 6.8. Calculated fluid pressure as a function of porosity at 1223 K for water contents corresponding to the five water-added experiments. Calculated using the EOS for water from Kerrick and Jacobs (1981).

porosities of ~ 2.1 and ~ 0.5 % respectively. These calculated porosities are close to the measured final porosities from these experiments of 2.0 and 0.3 % respectively (Table 6.3). On this basis, and with reference to Table 6.6 and Figure 6.7, it appears likely that in experiments fo26 and fo28 porosity reduction took place, firstly during HIPing and then during subsequent deformation,

until the fluid pressure reached a value close to the confining pressure of 600 MPa. This explains the high final density of sample fo26, which had 0.11 wt% water, compared with the lower final density of sample fo28, with 0.48 wt% water. In contrast, samples fo27 and fo29, with 0.02 and 0.05 wt% water respectively, did not densify, either during HIPing or deformation, to the point where the pore fluid pressure approached the confining pressure. Clearly then, increasing the water content from 0.05 to 0.11 % drastically enhances densification during deformation, as well as enhancing ductile flow.

An instructive alternative to viewing the fluid as existing in the total porosity (larger isolated pores plus films) is to consider the thickness of films that would have to be present if *all* the fluid, in the two samples which have compacted leading to pore fluid pressures close to the confining pressure (i.e. sample fo26 and fo28), were present in continuous films of uniform thickness. It can easily be shown, for thin films around cubic grains, that the film thickness (t) is related to the volume fraction of fluid and the grain size (d) by the following approximation: $t \approx (\text{vol. fraction fluid} \cdot d)/3$. From the mass of water added, the equation of state of water (Kerrick and Jacobs, 1981), and assuming a confining pressure of 600 MPa, it is possible to estimate the thickness of films which would have to be present if all the fluid were found in such films. For sample fo28, the films would thus have to be ~ 10 nm thick. If all the fluid present in sample fo26 existed as thin films these would be ~ 1.3 nm thick. These values are a maximum since in reality many intergranular pores are present. It is interesting to note that if water had indeed penetrated the grain boundaries in films of this order of thickness, any traces remaining after quenching, such as fluid inclusions, would not be directly observable at the TEM resolution used.

6.4.2. Observed deformation behaviour and the role of water in the experiments

Noting that the dry sample investigated in the present study behaved purely elastically during HIPing and deformation, an attempt is now made to infer the deformation mechanism which led to ductile flow in the wet samples, and to gain insight into the detailed nature of the associated water weakening effect.

Samples with ≥ 0.1 wt % water

Samples fo26, fo28 and fo30 with ≥ 0.1 wt % water and initial pre-HIPing water fugacities of 19, 81 and 61 MPa, respectively, showed a marked densification during HIPing. Subsequently, samples fo26 and fo28 showed (near) steady state flow at low stresses, as did fo30 until capsule failure problems set in.

Focusing now on fo26 and fo28, the deformation behaviour (m and n values) and microstructure of these samples are closely consistent with the results obtained in Chapters 4 and 5 for similar material with ~ 0.5 wt% water content. The previous results showed low stress exponents ($n = 1.3$ to 2.2 , $m = 0.8$ to 0.4), low activation energies of $\sim 320 \pm 40$ kJ mol⁻¹, an inferred grain size dependence of strain rate of $\sim d^{-3}$, low dislocation densities, little or no crystallographic preferred orientation, evidence for cavitation and an insensitivity to enstatite content (up to 20 % en). On the basis of comparison with microphysical models and other workers' data, a grain boundary sliding (GBS) mechanism accommodated by water enhanced grain boundary diffusion and/or dislocation activity has been proposed to explain these observations (see Chapters 4 and 5). Direct comparison of the exper-

imentally determined flow behaviour of the present sample fo28 (0.48 wt% H₂O, d = 1.49 μm) with the behaviour predicted by the empirical, grain size sensitive flow relation for fine grained forsterite plus enstatite material (0.5 wt % water, 2.5 % enstatite) presented in Chapter 4, assuming a grain size exponent of -3, shows good agreement (see Figure 6.9). It is accordingly inferred that the present samples with ≥ 0.1 wt % water also deformed by a water enhanced mechanism involving GBS with grain boundary diffusional and/or dislocation accommodation. The question remains, however, as to the exact role of water in this process.

To address this question further, let us consider the possible effects which water might have at grain boundaries, leading to enhanced grain boundary diffusivities and hence enabling grain boundary sliding creep. In general, water may enhance grain boundary diffusivity by a) leading to the formation of grain boundary melt films (Wang and Raj, 1984; Clarke 1987, 1989; Hwang and Chen, 1990; Wakai et al, 1994), b) dissolving in grain boundaries to form water related grain boundary defects or structural changes (Nowotny, 1991) which enhance solid state grain boundary diffusion, c) penetrating grain boundaries in the form of fluid inclusions which act as short circuit (solution transfer) diffusion paths in series with solid state grain boundary diffusion (cf. Cooper and Kohlstedt, 1984b; Den Brok, 1992), or d) facilitating pressure solution with grain boundary diffusion occurring in a thin aqueous grain boundary film or island channel structure. Note that any of the grain boundary structure modifications implied by the above processes a), b), and d) could become further modified after deformation (on quenching) to produce features such as grain boundary nano-inclusions observed using TEM. Since no identifiable melt has been observed in the present TEM work, and since the experimental conditions fall > 400 °C below the wet solidus, it seems unlikely that melt film diffusion was responsible for the low stress, water enhanced flow seen in samples fo26 and fo28. On the other hand, though unlikely, this possibility cannot be completely eliminated since the grain boundary contrast features seen in the TEM may have been centred around unseen nanoscale glass inclusions. Pressure solution (point d) above) also seems unlikely, as the apparent activation energies determined in earlier experiments (Chapter 4 ; 320 ± 40 kJ mol⁻¹) are far higher than expected for solution transfer processes (Rutter, 1983; Nakashima, 1995). Turning to point b), if the grain boundary contrast features observed in the TEM are in some way related to the presence of minute fluid inclusions, the spatial density of the inferred fluid inclusions on grain boundaries (fo28) would be low (<< 50 % area fraction; see Figures 6.6 e-f). Accordingly, short circuit diffusion through fluid inclusions, in series with dry solid state grain boundary diffusion, also seems an unlikely explanation for the water weakened flow behaviour seen in samples with ≥ 0.1 wt% water. The most probable explanation for the promotion of grain boundary sliding creep by water in the wetter samples, relative to the dry material, thus seems to lie in the notion b) above that solid state grain boundary diffusivity is enhanced by the incorporation of water-related grain boundary defects or associated grain boundary structural changes (cf. Karato et al., 1986). In this case, the observed grain boundary contrast features might be centred on either water related defect clusters or on exsolved water nano-inclusions.

The observation that fo26, with 0.11 wt% water, shows flow stresses which are roughly twice those exhibited by fo28, with 0.48 wt % water, may reflect differences in water fugacity (and hence grain boundary defect concentration) developed during deformation (see Table 6.6). On the other hand, it was argued in Section 6.4.1 that compaction took place during deformation until pore fluid

pressures close to the confining pressure were achieved. Accordingly, the water fugacities in the two experiments would have reached similar values at some point during deformation, even though the samples contained different volume fractions of fluid. The observed difference in flow strength between fo26 and fo28 may therefore be somehow related to these differences in fluid volume fraction.

Recently, Yund (1997) has shown that water contents ≥ 0.1 wt% increase the diffusivity of forsterite grain boundaries by ~ 28 times at 1000 °C and 700 MPa confining pressure compared with vacuum dried samples at the same conditions. This result again points to the possible role of water enhanced grain boundary diffusivities in enhancing creep rates. However, the diffusivity measured by Yund (1997; $\delta D_{gb} = 2.7 \times 10^{-22} \text{ m}^3 \text{ s}^{-1}$) combined with a conventional Coble creep equation, or a grain boundary diffusion accommodated GBS equation, predicts strain rates 2-3 orders of magnitude faster than observed. This may indicate that the mechanism of grain boundary diffusion in the present experiments was different from that in Yund's, or perhaps that GBS was accommodated more by dislocation activity.

Samples with < 0.1 wt% water

Samples fo27 (0.02 wt% H₂O) and fo29 (0.05 wt% H₂O) showed reduced HIPing compared to the wetter samples with ≥ 0.1 wt% water. Moreover, during the deformation stage, samples fo27 and fo29 remained far from steady state and only small permanent strains and minor densification were achieved. An important difference in the microstructure of these samples, compared with the denser, wetter fo28 is that the grain boundaries appeared free from the TEM contrast features seen in the grain boundaries of the wetter sample. This indicates that water did not have the effect on the grain boundaries, in these drier samples, that it had in the wetter samples. Furthermore, the average water fugacities during deformation were much lower in the drier than the wetter samples (Table 6.6). It is therefore inferred that water fugacity was too low to enable the incorporation of the water related grain boundary defects and associated weakening that occurred in the wetter samples to operate effectively. However, it is striking that the difference in water fugacity at the onset of HIPing between samples with > 0.1 wt % water (fo26 and fo28) and those with 0.02 and 0.05 wt % (fo27, fo29) was fairly modest (a factor ranging from only 2 to 20 - see initial $f_{\text{H}_2\text{O}}$ values, Table 6.6), but nonetheless sufficient to allow much more effective densification in the wetter samples, followed by a much greater weakening effect during axial deformation. This highlights the point that the behaviour of the samples in the present experiments is exceedingly sensitive to changes in water content in the range 0.02 to 0.11 wt % and even 0.05 to 0.11 wt %. Interestingly, Yund (1997), combining the observations of Farver et al. (1994) on the effect of hydrous gas mixtures on ²⁶Mg grain boundary diffusion and of Farver and Yund (1995) on the effect of water pressure on the diffusivity of ⁴¹K in K-feldspar aggregates with his observations of the effect of water on enstatite and forsterite grain boundary diffusivities, suggests that the first 0.1 wt% water has the greatest effect on enhancing grain boundary diffusion and that higher water contents or fugacities have only a minor effect. Clearly, the observed effects of water on deformation described in this Chapter are broadly consistent with Yund's observation.

6.4.3. *Some comparisons with previous work*

Previous studies into the role of water on the deformation behaviour of polycrystalline olivine in both the dislocation (Chopra and Paterson, 1981, 1984; Karato et al., 1986) and diffusion (Karato et al., 1986) creep regimes have been carried out either 'wet' or 'dry'. Well known flow equations are represented in Figure 6.9 where they are extrapolated to the conditions of the present experiments. The previously investigated wet materials have generally had bulk water contents > 0.1 wt%. The Aheim and Anita Bay dunites studied by Chopra and Paterson (1981, 1984) had initial water contents of 0.18 and 0.55 wt% respectively. These authors do, however, report the loss of water from one sample during deformation, with no increase in flow strength, and they speculate either that the flow strength of dunite was independent of water content or that the water was lost early in the test. Furthermore, these authors go on to suggest that a systematic study into the effect of bulk water content on the deformation behaviour of dunite should be made before extrapolation of the wet data to geologically relevant conditions.

Moving on to the experiments carried out by Karato et al. (1986), these workers deformed wet and dry synthetic olivine aggregates in both the dislocation and diffusion creep regimes. Although a controlled amount (300 mg) of water was added to the samples before wet hot isostatic pressing, the quantity of water remaining during subsequent deformation was determined by the densification of the aggregates during HIPing and the concurrent expulsion of water from the sample. From the final densities (which imply porosities in the range 2.3 ± 1.7 % for the wet samples) and the micrographs presented by Karato et al. (1986, their Fig. 3a and b, page 8154), it seems likely that > 0.1 wt% water remained in the samples during deformation. However, much of this fluid appears to have been included within the grains during grain growth on HIPing resulting in halos of fluid inclusions. Therefore, both the bulk water content and its distribution are somewhat unclear in these experiments. Comparison of the current results for the wetter samples plus those from Chapters 4 and 5 with the extrapolated wet diffusion creep law of Karato et al. (1986) indicate that the current materials are considerably stronger (two orders at 1223 K, 10^{-6} s^{-1}) than those of Karato et al. (1986); see Figure 6.9. The reason for this is not known but may be related to reduced diffusivity in the current material compared to the iron-bearing systems previously studied, in which the defect chemistry would have been strongly influenced by the imposed oxygen fugacity via its influence on the redox state of iron. The present data for water contents > 0.1 wt % imply that the discrepancy is too large to be accounted for by possibly higher water contents in the samples of Karato et al. (1986). Notably, the present data agree more closely with the dry diffusion creep law of Karato et al. (1986) than with the wet (Figure 6.9). No explanation can be given for this at present.

6.4.4. *Extrapolation and implications*

The change in flow behaviour observed in the current experiments at water contents in the range 0.02 to 0.11 wt % and above has important implications for the extrapolation of experimentally determined wet diffusion creep data to natural conditions. At water contents > 0.1 wt%, deformation by a water enhanced mechanism of grain boundary sliding with grain boundary diffusion and/or dislocation accommodation has been inferred, and although an effect of bulk water content has been observed in the range 0.1 to 0.5 wt %, this effect is of limited extent. Direct use of the empirical flow

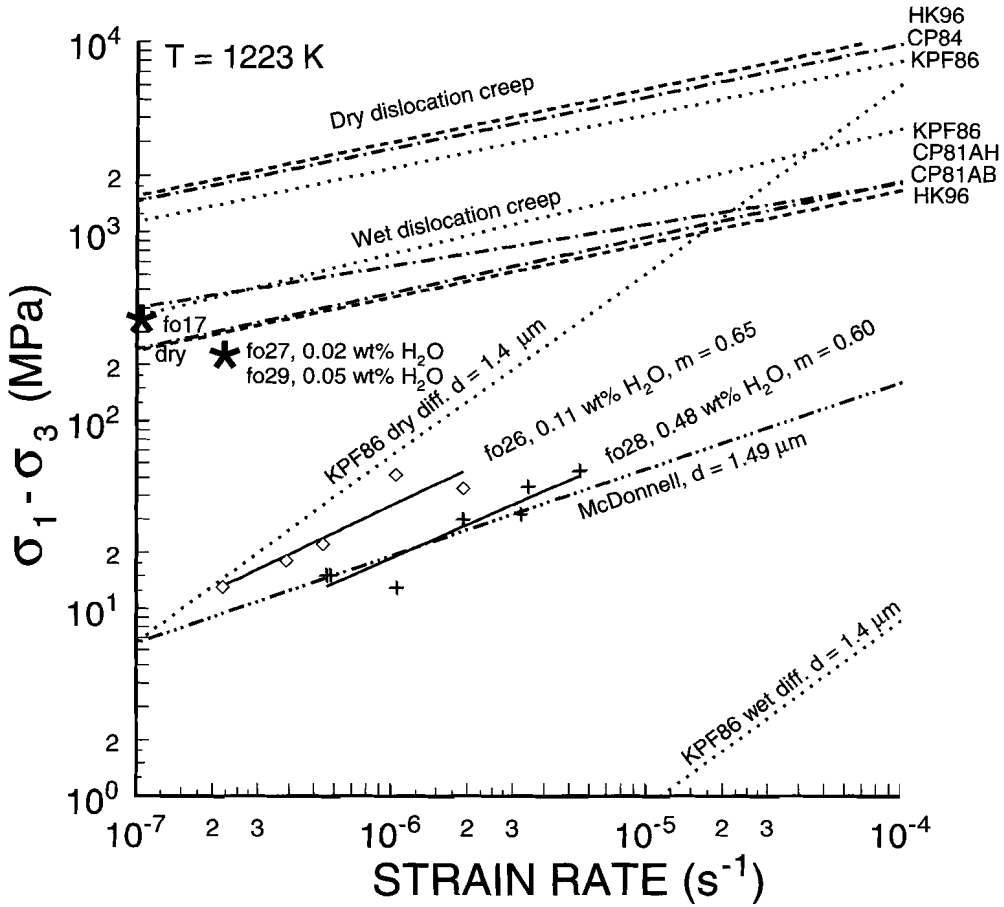


Figure 6.9. Plot of differential stress versus strain rate (log scaling) giving the positions of the current results in respect to previous studies on wet versus dry creep. Experiment fo30 has been rejected due to the problems with capsule failure. The two strain rate stepping tests which exhibited steady state creep fo28 (crosses) and fo26 (open diamonds) are plotted with individual data points for each strain rate step. These have been fitted to a power law and the strain rate sensitivities are as indicated. Experiments fo27, fo29 and fo17 are plotted as asterisks which indicate the maximum stress achieved and the strain rates at these stresses. The dotted lines indicate extrapolation based on data from Karato, Paterson and FitzGerald (1986 = KPF86) for wet/dry dislocation and diffusion creep (grain size (d) as indicated). Further extrapolation for wet/dry dislocation creep come from Chopra and Paterson (1981, 1984 = CP81 and CP84 respectively, AB = Anita Bay, AH = Aheim) and Hirth and Kohlstedt (1996 = HK96). The predicted flow behaviour using the empirical flow equation from Chapter 4 (Equation 4.6); modified to take account of the grain size dependence assuming a grain size exponent of -3, and extrapolated to a grain size (d) of 1.49 μm , is shown for direct comparison with run fo28 ($Q = 302 \text{ kJ mol}^{-1}$; $n = 2.14$; $p = -3$; $A = 47427.8$; $T = 1223.15$).

law derived in Chapter 4 for this mechanism is therefore reasonably justified for water contents > 0.1 %. At water contents ≤ 0.1 wt%, however, extreme sensitivity to water content has been observed, and there is no basis therefore for extrapolation of wet data from the experiments with > 0.1 wt% water to lower water contents.

Considering the relatively high water contents used in previous studies, and the conclusions of Yund (1997) regarding the effects of water on grain boundary diffusivity, there also seems to be good general reason for caution when extrapolating available wet data to water contents < 0.1 wt%. This is particularly relevant to the application of wet diffusion creep data to upper mantle materials where the water contents are ~ 0.1 wt% (Ringwood, 1975), since this appears to be close to a 'critical' water content for flow behaviour, at least in experiments. Further work is clearly needed to investigate the mechanisms occurring at low water contents.

Taking into account the above difficulties, an attempt will now be made to consider the implications of the present findings for the strength of upper mantle mylonitic shear zones as considered by Vissers et al. (1995). On the basis of a field and microstructural study of peridotite mylonites in the Voltri massif, Vissers et al. (1995) have proposed that localization of deformation in the lithospheric upper mantle, with the formation of hydrated peridotite mylonites deforming by grain size sensitive mechanisms, will lead to dramatic weakening of the lithosphere during extension/rifting as compared to models assuming more distributed deformation by dislocation creep. The conclusions of Vissers et al. (1995) were based on the application of the wet diffusion data of Karato et al. (1986). New data on wet fine-grained forsterite plus enstatite material (~ 0.5 wt% water, 2.5 vol% enstatite) presented in Chapter 4, although predicting higher strengths than those of Karato et al. (1986), do not significantly alter the conclusions of Vissers et al. (1986); see Chapter 4. However, the results presented in the present Chapter indicate that the bulk water content may well have an important effect on the rheology of such shear zones and that a free fluid phase (> 0.1 wt %) may be necessary to induce weakening via water enhanced grain boundary diffusion. Vissers et al. (1995) infer that there has been an influx of water rich fluid into the Voltri mylonite zones, on the basis of the occurrence of syn-tectonic amphiboles as fibrous growths on fractured and pull-apart pyroxenes and in ultra-fine anastomosing bands. Vissers and coworkers also infer that fluid pressures were high enough to allow microfracturing of porphyroclasts. It seems likely then that a free fluid phase was present within the Voltri mylonites at periods during their activity. The presence of a free fluid in such situations is also supported by several studies pointing to the possible role of localized shear zones as paths of enhanced fluid permeability (Rutter and Brodie, 1985; Kronenberg et al., 1990; Peach, 1991 - page 212). In light of the above, it seems likely that there was sufficient fluid within the Voltri mylonite zones, at least at some period, to produce the dramatic weakening expected for wet conditions. However, the long term strength of such zones may in fact be determined by the supply of fluid as ongoing hydration reactions will consume the fluid phase and may thus inhibit water enhanced grain size sensitive flow.

6.5. Conclusions

An attempt has been made to systematically investigate the role of bulk water content on the flow strength of fine-grained ($\sim 1.4 \mu\text{m}$) forsterite plus enstatite materials (2.5 vol% enstatite) at a temperature of $\sim 1223 \text{ K}$, using a gas-confining pressure of $\sim 600 \text{ MPa}$. Water contents of 0.48, 0.28, 0.11, 0.05, 0.02 (wt%) and nominally dry were investigated. The dry sample behaved elastically up to a differential stress of 300 MPa at imposed strain rates of $1 \times 10^{-7} \text{ s}^{-1}$. Samples with water contents $> 0.1 \text{ wt } \%$ showed near steady state, low stress flow with stress exponents (n) of around 1.6 ($m = 0.6$). From SEM and TEM analysis, these wetter samples showed equant grains and apparent dihedral angles $< 60^\circ$ at intergranular pores. The majority of the grains were found to be dislocation free and subgrains were absent. No evidence was found for melting. The final porosities (2.1 and 0.3 %) are consistent with compaction until pore fluid pressures became close to the confining pressure. Comparison of the mechanical and microstructural observations made on the wetter samples with previous findings for similar material (Chapters 4 and 5) has led to the inference that a water enhanced process involving grain boundary sliding accommodated by grain boundary diffusion and/or dislocation motion is the most likely deformation mechanism. On the basis of tentative activation energy, water fugacity and microstructural arguments, the water weakening is believed to result from enhanced grain boundary diffusivity related to the formation of water related grain boundary defects and/or associated grain boundary structural changes. At water contents $< 0.1 \text{ wt } \%$ only very minor weakening was observed, presumably because the lower water fugacity produced less enhancement of grain boundary diffusion. In view of the observed extreme sensitivity to water contents in the range 0.02 to 0.11 wt %, caution is advised when applying wet diffusion creep data, obtained at water contents $> 0.1 \text{ wt } \%$, to lower water contents. For significant water weakening in experiments, water contents $> 0.1 \text{ wt } \%$ appear to be required. If this threshold behaviour occurs in nature it may have important implications, for example for the flow of hydrated mylonite zones in the upper mantle, where weakening may be related to the supply of fluid to the shear zone. The results presented here are limited and point to the need for further study of water weakening in both the dislocation and diffusion creep regimes at low water contents.

General conclusions and suggestions for further work

This thesis has investigated the synthesis and deformation behaviour of fine-grained forsterite and forsterite-enstatite materials in the system MgO-SiO_2 , focusing on the influence of added water and enstatite content on (near) steady state flow behaviour under conditions expected to favour grain size sensitive (GSS) deformation mechanisms. The method of material synthesis developed was based on sol-gel processing. The deformation experiments were carried out using a gas medium apparatus operated at 600 MPa and at temperatures in the range 850 to 1000 °C (1123 to 1273 K). The purpose of this final chapter is to summarize and draw together general conclusions based on the findings of the preceding chapters, and to consider some of the implications for flow in wet peridotitic systems in the upper mantle. In addition, unanswered questions are identified and suggestions made for further research.

7.1 Sol-gel synthesis of fine-grained forsterite-enstatite materials

The investigation described in Chapter 2 has led to a method for the production of fine-grained (1-2 μm), magnesium end-member forsterite-enstatite (0 - 50 vol% en) ceramic materials with densities of up to 98% of the theoretical density (TD). These materials can be reproducibly manufactured with independently variable porosity (down to 2%) and enstatite content. They have high purity and a stable, uniform microstructure, and thus form ideal synthetic reference material for rock deformation and other rock physics experiments. Though departing from the composition of natural Fe-bearing olivine-enstatite materials, the chemically simple magnesium end-member system chosen substantially simplifies synthesis and experimentation compared with Fe-bearing systems. Production involves a multi-step process, based on a sol-gel stage with subsequent powder processing and firing. The sol-gel stage involves the formation of a structurally and chemically diphasic gel, produced from a colloidal sol consisting of 50 nm MgO particles suspended in ethanol, plus amorphous silica produced from tetraethyl orthosilicate (silicon alkoxide) solution.

The present process was developed after exhaustive trials of a number of previous methods described in the literature (Kazakos et al., 1990; Shiono et al., 1991). While these previous methods all resulted in ceramic materials containing forsterite-plus-enstatite or forsterite-plus-MgO, the compositional and microstructural control and degree of reproducibility offered by these methods was found inadequate for production of the desired fine-grained reference materials. The principal new features of the present process are a) the use of 50 nm MgO powder, b) the use of a $\text{HN}_3\text{OH}(\text{aq})$ catalyst, c) allowance for the effects of the adsorbed water content of the colloidal MgO powder on bulk composition, and d) the use of ethylene glycol binder during cold isostatic pressing.

7.2. Deformation behaviour of wet, fine-grained forsterite-enstatite materials

As indicated above, the deformation experiments reported in this thesis were aimed at gaining an understanding of the deformation behaviour occurring in wet fine-grained (1–2 μm) peridotite materials under conditions where grain size sensitive (GSS) flow mechanisms are expected to dominate. The study was principally motivated by recent structural geological findings suggesting that such mechanisms, operating in hydrated mylonitic shear zones transecting the upper 10 to 20 km of the mantle, may be important in controlling the strength of the lithosphere during rifting (Vissers et al., 1995). More general motivations included the desire to obtain a fundamental understanding of water weakening effects in olivine-rich rocks and to test hypotheses, recently raised in the literature (Chen, 1982; Wheeler, 1992), regarding the role of interphase boundary diffusion/migration in two-phase materials. These hypotheses imply that the addition of enstatite to a forsterite polycrystal may lead to significant weakening, in the GSS flow field, caused by coupled interphase boundary migration (local phase transformation) and interphase boundary diffusion.

7.2.1. *Water weakening and flow behaviour*

In Chapter 4, deformation experiments on forsterite-enstatite materials containing 2.5 vol% enstatite and 0.5 wt% water were reported. These mainly showed (near) steady state flow at stresses in the range 5 to 60 MPa, under the temperature (850 to 1000 °C) and strain rate (10^{-7} to 10^{-5} s $^{-1}$) conditions imposed, whereas dry material was purely elastic up to differential stresses of ~ 300 MPa. A major water weakening effect was thus demonstrated. The wet flow behaviour was described using a Dorn formulation and was characterized by stress sensitivities or n -values of 1.3 to 2.2 (i.e. strain rate sensitivities of between 0.78 and 0.45) and an apparent activation energy falling in the range 320 ± 40 kJ mol $^{-1}$. The microstructure of the wet deformed samples was characterized by polygonal, dislocation free grains with no significant crystallographic preferred orientation, and by evidence for cavitation, and showed little or no grain growth during the experiments. This overall behaviour is consistent with models for fluid-enhanced, grain boundary sliding dominated mechanisms accommodated by diffusion and/or dislocation activity. The observed behaviour is also broadly similar to that reported by Karato et al. (1986) for wet, fine-grained, Fe-bearing olivine deformed at 1300 °C, suggesting a similar deformation mechanism. From data on the grain size sensitivity of flow behaviour, Karato et al. (1986) tentatively proposed a mechanism of grain boundary sliding (GBS) accommodated by grain boundary diffusion.

7.2.2 *Effect of enstatite and water content*

In addition to the above tests on samples consisting of forsterite plus 2.5 vol% enstatite, experiments have been performed (Chapter 5) under the same conditions, and using the same water content (~ 0.5 wt%) to investigate the effect of varying enstatite content (0 – 20 vol%). Similar stress sensitivities ($n = 1$ to 2), activation energies and microstructures were obtained for all enstatite-bearing samples (3 vol% enstatite) as were observed for material with 2.5 vol% enstatite (Chapter 4). This suggests that the same deformation mechanism operated at all enstatite contents. However, flow stresses were found to decrease rapidly with increasing enstatite content in the range 0 – 2.5 vol%, though with

little effect thereafter. At the same time, sample grain size (d) was found to decrease slightly with increasing enstatite content, suggesting a possible causal relationship between flow stress and grain size. Analysis of the correlation between flow stress and grain size showed a relationship consistent with a d^{-3} dependence of strain rate at constant stress. Models for grain boundary sliding dominated creep accommodated by grain boundary diffusion, lattice diffusion or dislocation processes predict grain size sensitivities of -3, -2 and -2 respectively (Ashby and Verrall, 1973, 1977; Gifkins, 1976; Langdon, 1995). Taking into account the support for a GBS dominated mechanism afforded by the stress sensitivities and microstructures reported in Chapters 4 and 5, it is inferred that the effect of enstatite content on flow stress operates through its role in controlling grain size, and that the most likely deformation mechanism in the present experiments is one of GBS accommodated mainly by grain boundary diffusion. Accordingly, chemical effects of enstatite content, such as interphase boundary diffusion/migration processes (Wheeler, 1992) are believed to be unimportant in controlling grain size sensitive creep in wet forsterite-enstatite systems for enstatite contents in the range 1 to 20 %. From the point of view of chemical buffering, however, it seems likely that the presence of enstatite, as opposed to its absence (0% enstatite), or the presence of MgO, will influence deformation behaviour via its role in fixing point defect chemistry. This is supported by the somewhat anomalously high stress sensitivity ($n = 2.7$) observed for material with nominally zero enstatite content.

Further experiments (Chapter 6) on forsterite plus 2.5 vol% enstatite aimed at investigating the role of water content, have shown similar flow behaviour to that obtained in Chapters 4 and 5 (0.5 wt% water), down to water contents of 0.1 wt%. Flow stresses at 0.1 wt% water are a factor of ~ 2 higher than at 0.5 wt%. At water contents in the range 0.11 to 0.02 wt%, however, samples work hardened and showed only small permanent strains, demonstrating that the weakening effect is drastically reduced in this range. No evidence has been found for the presence of melt phases or films within the deformed samples, and the apparent activation energies for flow are too high for solution transfer processes (usually characterized by values $< 100 \text{ kJ mol}^{-1}$; Nakashima, 1995). Accordingly, the mechanism of water weakening leading to GBS dominated flow, in the present forsterite-enstatite materials, is believed to involve an increase in grain boundary diffusivity caused by the formation of water related grain boundary defects and associated grain boundary structural changes.

7.2.3 Final flow equation including the effect of grain size and water content

An attempt is now made to develop an empirical flow equation for the inferred grain boundary sliding dominated mechanism in wet fine-grained forsterite-enstatite materials, explicitly taking into account the effect of grain size and of water content in the range 0.1 to 0.5 wt%. The starting point is the empirical flow equation presented in Chapter 4 (Equation 4.6) for materials with 0.5 wt% water, 2.5 vol% enstatite and a grain size of 1.2 μm . This is written

$$\dot{\epsilon} = A \cdot \exp\left(\frac{-Q_c}{RT}\right) \cdot \sigma^n \quad 7.1$$

where $\dot{\epsilon}$ is the strain rate (s^{-1}), σ is the differential stress (MPa), R is the gas constant ($\text{J mol}^{-1} \text{K}^{-1}$), T is the absolute temperature (K), n is the stress sensitivity ($n = 2.14$), Q_c is the apparent activation energy ($Q_c = 302000 \text{ J mol}^{-1}$), and A is the pre-exponential constant ($A = \exp(10.22) \text{ MPa}^{-n} \text{ s}^{-1}$).

Note that while the strain rate sensitivity (n) and apparent activation energy value in this equation are broadly consistent with expectations based on theoretical models for the inferred mechanism ($n = 1$ to 2 , $Q_c =$ activation energy for grain boundary diffusion; Farver et al., 1994; Langdon, 1995), the equation remains empirical in status. Now, having concluded that there is a d^{-3} dependence of strain rate on grain size, from the experiments with varying enstatite content reported in Chapter 5, Equation 7.1 can be modified to account for grain size by dividing the right hand side by d^3 and by replacing $A = \exp(10.22)$ by

$$A' = A \cdot (1.2)^3 \quad 7.2$$

This follows from the fact that $1.2 \mu\text{m}$ was the grain size of the material for which Equation 7.1 was obtained. Since enstatite content was inferred to have no effect in the range 1 to 20 vol%, it does not need to be taken into account in the final equation for this range of enstatite contents.

Turning to the effect of water content, it was shown in Chapter 6 that the inferred water-enhanced deformation mechanism required water contents ≥ 0.1 wt% to be effective at laboratory rates. Analysis of the data presented in Chapter 6 (Figures 6.3 and 6.9), taking into account minor differences in grain size from sample to sample (fo26 to fo28), shows that the deformation rate decreases by a factor of 3.8, at constant stress, concomitant with a decrease in water content from ~ 0.5 (0.48) to ~ 0.1 (0.11) wt%. This effect of water content, in the range 0.5 to 0.1 wt% (at a pressure of 600 MPa), can crudely be accounted for by assuming a linear dependence of $\ln A'$ on water content (X wt%) given by

$$\begin{aligned} \ln A' &= (9.107 + 3.22 \cdot X) \\ &= \ln[A \cdot (1.2)^3] \text{ when } X = 0.5 \text{ wt \% (cf. Eqn. 7.2)}. \end{aligned} \quad 7.3$$

At water contents less than 0.1 wt% the sensitivity of flow behaviour to water content in the system studied is extreme and cannot be quantified at present. However, for water contents in the range 0.1 to 0.5 wt% (at a pressure of 600 MPa), the final equation for grain size sensitive flow in wet forsterite-enstatite materials with enstatite contents of 1 to 20% can now be written

$$\dot{\epsilon} = \frac{A' \cdot \sigma^{2.14} \cdot e^{(-302000/RT)}}{d^3} \quad 7.4$$

where for clarity, $\dot{\epsilon}$ is the strain rate (s^{-1}), σ is the differential stress (MPa), R is the gas constant ($\text{J mol}^{-1} \text{K}^{-1}$), T is the absolute temperature (K), d is the grain size in (μm) and A' is given from equation 7.3 as $A' = \exp(9.10 + 3.22 \cdot X)$ ($\text{MPa}^{-2.14} \text{s}^{-1} \mu\text{m}^{-3}$).

7.2.4 Implications for grain size sensitive flow of wet peridotites in the upper mantle.

On the basis of a field and microstructural study of peridotite mylonites in the Voltri massif, Vissers et al. (1995) proposed that localization of deformation in the lithospheric upper mantle, with the formation of hydrated peridotite mylonites deforming by grain size sensitive mechanisms, will lead to dramatic weakening of the lithosphere during extension/rifting as compared to models assuming more distributed deformation by dislocation creep. The conclusions of Vissers et al. (1995) were based on the application of the wet diffusion data of Karato et al. (1986).

In Chapter 4, the exercise conducted by Vissers et al. (1995) was repeated using a preliminary version of Equation 7.4 (i.e. Eqn 7.1). This application of the flow equation requires only minor extrapolation in grain size and temperature, and extrapolation in strain rate can be justified on the grounds that similar mechanisms were inferred for both the experimental and mylonitic materials. Strength profiles constructed for the lithospheric upper mantle, using the geotherm proposed by Vissers et al. (1995) as appropriate for the initial stages of extension of the continental lithosphere, and using strain rates in the range 10^{-15} to 10^{-13} s^{-1} appropriate for homogeneous extension and localized deformation, illustrate the weakening effect of localization of deformation into wet mylonites on the entire lithosphere. From the strength profiles produced (Chapter 4, Figure 4.20), it is clear that GSS flow mechanisms are substantially weaker than both dry and wet dislocation creep over the range of strain rates plotted. The strength profiles based on the results of the current study fall between those for wet dislocation and wet diffusion creep based on Karato et al. (1986). Nonetheless, the experimental results of this study imply a dramatic weakening of the lithospheric upper mantle (top 20 km) during extension, if deformation becomes localized into wet, fine-grained mylonites, rather than occurring by wet or dry dislocation creep in either a wide tectonite shear zone or more homogeneously deforming mantle. Bearing in mind the chemically simple (Fe-free) nature of the system investigated and uncertainties regarding the water content of (or activity in) natural material, it is arguable whether the present results can be directly applied to natural compositions. However, it seems reasonable to suppose that the weakening observed is also to be expected in wet natural fine-grained Fe-bearing olivine under similar conditions. The results described in Chapter 4 therefore provide additional evidence for the role of GSS creep in wet olivine at temperatures appropriate for the top of the upper mantle, under conditions where melting does not occur, and back up the conclusion of Vissers et al. (1995).

Since enstatite content does not have much effect on flow behaviour it does not affect the above result (see Chapter 5), though the secondary phases found in the natural mylonitic shear zones studied by Vissers et al. (1995) are undoubtedly important in keeping the grain size fine and promoting GSS flow. However, the results presented in Chapter 6 indicate that the bulk water content may well have an important effect on the rheology of such shear zones and that a free fluid phase (> 0.1 wt%) may be necessary to induce weakening. Vissers et al. (1995) infer that there has been an influx of water rich fluid into the Voltri mylonite zones, on the basis of the occurrence of syntectonic amphiboles as fibrous growths on fractured and pull-apart pyroxenes and in ultra-fine anastomosing bands. Vissers and coworkers also infer that fluid pressures were high enough to allow microfracturing of porphyroclasts. It seems likely then that a free fluid phase was present within the Voltri mylonites at periods during their activity. The presence of a free fluid in such situations is also supported by sev-

eral studies pointing to the possible role of localized shear zones as paths of enhanced fluid permeability (Rutter and Brodie, 1985; Kronenberg, 1990; Peach, 1991 - page 212). In light of the above, it seems likely that there was sufficient fluid within the Voltri mylonite zones, at least at some period, to produce the dramatic weakening expected for wet conditions. However, the long-term strength of such zones may in fact be determined by the supply of fluid, as ongoing hydration reactions will consume the fluid phase and may thus inhibit fluid enhanced GSS flow.

With regard to applying the present results to other regions of the upper mantle the following points should be made:

- (a) It is not possible to extrapolate Equation 7.4 unless water contents lie in the range 0.1 to 0.5 wt%. Therefore the application of wet GSS creep data to upper mantle materials with water contents of < 0.1 wt% (or fugacities different from the present experiments) is not possible. Non-mylonitic, wet upper mantle rocks commonly have a water content of ~ 0.1 wt% (Ringwood, 1975). Since this appears to be close to a 'critical' water content for flow behaviour, at least in experiments, extrapolation of flow equations determined for wetter material (such as Eqn 7.4) should be done with caution.
- (b) The results presented in Chapter 5 imply that enstatite content has little or no direct effect on the flow behaviour of wet forsterite-enstatite materials in the GSS creep field, at enstatite contents up to 20 %, i.e. interphase diffusion/migration effects are minimal. Accordingly, such effects are presumably not to be expected in natural olivine-orthopyroxene rocks, with comparable pyroxene content, deforming in the wet GSS regime.

7.3. Suggestions for further work

While the present study has addressed a substantial number of questions posed in the introduction, it will be apparent that many remain unanswered or only partly answered, and that some new questions have been raised. In the following, suggestions for further work are proposed.

- 1) In the present study, a method has been developed which allows the production of forsterite and forsterite-enstatite materials with well-controlled composition, microstructure and porosity (down to 2 %). However, it has not been possible to vary grain size independently of porosity and enstatite content to produce a range of well-spaced grain sizes. Further research is needed to achieve this. Material with a grain size below the 1 to 2 μm currently possible can probably be made by briefly firing the present greenbody at ~ 1000 °C to complete the reaction of the forsterite-enstatite precursor. Subsequent hot isostatic pressing of the ultra-fine grained product should enable grain sizes as low as 100 to 200 nm to be achieved. Coarser material (> 2 μm) could perhaps be made by using coarser grained MgO powders (> 50 nm) during the sol-gel step, so that the diphasic nature of the gel will have a coarser 'wavelength' from the outset. Note that 500 nm and 1 μm MgO powders are commercially available.

- 2) The present forsterite-enstatite material, while forming a well-controlled reference material for the system MgO-SiO₂, is not directly comparable with natural Fe-bearing compositions. To produce similar reference material with these compositions, future research on material synthesis should focus on including iron in the system. This could presumably be achieved by adding an Fe-bearing component in stoichiometric proportions during the sol-gel step, but would require control of oxygen fugacity during all high temperature stages of the synthesis.
- 3) Steady state flow has been approached in many of the strain rate and temperature stepping runs carried out in the present deformation experiments on wet forsterite-enstatite material. However, it would be desirable in future to conduct a number of constant strain rate, large strain (~ 15 %) control experiments designed to confirm steady state behaviour under the conditions investigated. These experiments should be followed by full microstructural characterization to verify the present microstructural observations.
- 4) The deformation mechanism inferred to operate in the present wet experiments, on the basis of mechanical behaviour and microstructural observations, is one of grain boundary sliding accommodated by diffusion or possibly dislocation activity. However, no direct evidence has been obtained for grain boundary sliding. Further work is required to verify this mechanism unambiguously. This could be done by performing split cylinder experiments (Spiers, 1979) in an attempt to directly assess the contribution of grain boundary sliding from measured grain boundary offsets. Furthermore, careful microstructural analysis is required to quantify both grain boundary and cavity orientations in high strain samples. In addition, the grain size dependence of flow behaviour needs to be directly determined by conducting experiments on samples with fixed enstatite content but with varying grain sizes, produced as described under point 1).
- 5) The effect of enstatite content on the deformation behaviour of wet forsterite-enstatite materials has been explored only over a limited range (up to 20 vol%). The flow behaviour in this range has been inferred to be uninfluenced by second phase weakening effects such as interphase diffusion phenomena. However, the range of enstatite contents investigated should be extended across the full range (0 to 100 %) to determine if effects such as interphase boundary diffusion/migration processes become important at high second phase content.
- 6) Water content has been shown here to have a marked effect on the flow strength of the forsterite-enstatite materials studied. In particular, water contents < 0.1 wt% have been observed to have a critical effect on deformation behaviour. However, steady state flow could not be achieved for these water contents, since water weakening was not effective enough at the strain rates employed. In view of the high sensitivity to water content in the range 0 to 0.1 wt%, and since this range is possibly the most relevant for upper mantle materials, further experiments are clearly needed at water contents < 0.1 wt% and/or at controlled water pressure/fugacity. These will need to access lower strain rates than the present experiments (< 10⁻⁷ s⁻¹).

- 7) A confining pressure of 600 MPa was chosen for the present deformation experiments, since orthoenstatite and forsterite are known to be stable phases at this pressure for the temperature investigated. In future, the influence of confining pressure on flow behaviour could also be investigated. The pressure sensitivity of flow (activation volume) might give further insight into the mechanisms of flow and water weakening.
- 8) The current study has focused on the flow behaviour of a chemically simple reference system (MgO-SiO₂). This system is however somewhat removed from natural compositions and therefore begs the question as to the validity of extrapolation to natural materials. Future research aimed at using Fe-bearing systems under carefully controlled chemical environments is therefore desirable (see point 2 above).
- 9) The polymorphic phase relations of enstatite need to be investigated, both in the starting materials and the deformed samples, in order to evaluate the role of pressure, temperature, deformation and quenching on the stability of the proto-, clino- and ortho-enstatite polymorphs.

References

- Anders, E. and Ebihara, M., 1982. Solar-system abundance of the elements. *Geochim. Cosmochim. Acta*, 46: 2363-2380.
- Andersson, K., G., B., Scherrer, S. and Weber, S., 1989. Self-diffusion in Mg_2SiO_4 (forsterite) at high temperature - A model case study for SIMS analyses on ceramic surfaces. *Fresenius Z. Anal. Chem.*, 333: 385-385.
- Ando, K., Kurokawa, H., Oishi, Y. and Takei, H., 1981. Self-diffusion coefficient of oxygen in single-crystal forsterite. *Comm. Am. Ceram. Soc.*, February: C-30.
- Ashby, M.F. and Verral, R.A., 1977. Micromechanisms of flow and fracture, their relevance to the rheology of the upper mantle. *Phil. Trans. R. Soc. Lond.*, A288: 59-95.
- Ashby, M.F. and Verrall, R.A., 1973. Diffusion accommodated flow and superplasticity. *Acta Metall.*, 21: 149-163.
- Bai, Q. and Kohlstedt, D.L., 1992a. High-temperature creep of olivine single crystals: 3. Mechanical results for unbuffered samples and creep mechanisms. *Philosophical Magazine A.*, 66(6): 1149-1181.
- Bai, Q. and Kohlstedt, D.L., 1993. Effects of chemical environment on the stability and incorporation mechanism for hydrogen in olivine. *Phys. Chem. Minerals*, 19: 460-471.
- Bai, Q., Maxwell, S.J. and Kohlstedt, D.L., 1991. High temperature creep of olivine single crystals: 1. Mechanical results for buffered samples. *J. Geoph. Res.*, 96: 2441-2463.
- Bai, Q.B. and Kohlstedt, D.L., 1992b. High-temperature creep of olivine single crystals: 2. Dislocation structures. *Tectonophysics*, 206: 1-29.
- Bassi, G., 1995. Relative importance of strain-rate and rheology for the mode of continental extension. *Geoph. J. Int.*, 122: 195-210.
- Bassi, G. and Bonnin, J., 1988. Rheological modeling and deformation instability of lithosphere under extension II. Depth-dependent rheology. *Geoph. J.*, 94: 559-565.
- Beeman, 1989. Deformation of olivine-glass aggregates at high temperatures and confining pressures. PhD Thesis. Cornell University, Ithaca, NY. 118pp.
- Beeman, M.L. and Kohlstedt, D.L., 1993. Deformation of fine-grained aggregates of olivine plus melt at high temperatures and pressures. *J. Geoph. Res.*, 98(B4): 6443-6452.
- Blacic, J.D., 1972. Effect of water on the experimental deformation of olivine. In: H.C. Heard, I.Y. Borg, N.L. Carter and C.B. Raleigh (Eds), *Flow and fracture of rocks*. Geoph. Monograph A.G.U., Washington, pp. 109-115.
- Blanchard, C.R. and Chan, K.S., 1993. Evidence of grain-boundary-sliding-induced cavitation in ceramics under compression. *J. Am. Ceram. Soc.*, 76(7): 1651-1660.
- Bons, P.D., 1993. Experimental Deformation of Polyphase Rock Analogues. Publ. PhD. Thesis. Geologica Ultraiectina No.110. Utrecht University. 207 pp.
- Borch, R.S. and Green II, H.W., 1989. Deformation of peridotite at high pressure in a new molten salt cell: comparison of traditional and homologous temperature treatments. *Phys. Earth Planet. Inter.*, 55: 269-276.
- Boullier, A.M. and Gueguen, Y., 1975. SP-mylonites: Origin of some mylonites by superplastic flow. *Contrib. Mineral. Petrol.*, 50: 93-104.
- Bouvard, D. and Lange, F.F., 1991. Relation between percolation and particle coordination in binary powder mixtures. *Acta Metall. Mater.*, 39(12): 3083-3090.
- Boyd, F.R. and Engl, J.C., 1965. The rhombic enstatite-clinoenstatite inversion. *Carnegie Inst. Wash. Am. Rept. Dir. Geophys. Lab.*, 1964-65: 117-120.
- Brace, W.F. and Kohlstedt, D.L., 1980. Limits on lithospheric stress imposed by laboratory experiments. *J. Geoph. Res.*, 85(B11): 6248-6252.
- Brambilla, G., Gerontopoulos, P. and Neri, D., 1970. The SNAM process for the preparation of ceramic nuclear fuel microspheres: Laboratory Studies. *Energia Nucleare*, 17: 217-224.
- Braun, J. and Beaumont, C., 1989. A physical explanation of the relation between flank uplifts and the break-up unconformity at rifted continental margins. *Geology*, 17: 760-764.
- Brindley, G.W. and Hayami, R., 1965. Kinetics and mechanism of formation of forsterite (Mg_2SiO_4) by solid state reaction of MgO and SiO_2 . *Philos. Mag.*, 12: 505-514.
- Burke, J.E., 1996. Lucalox (TM) Alumina: The ceramic that revolutionized outdoor lighting. *MRS Bulletin*, 21(6): 61-68.
- Burlitch, J.M., Beeman, M.L., Riley, B.B. and Kohlstedt, D.L., 1991. Low temperature synthesis of olivine and forsterite facilitated by hydrogen peroxide. *Chem. Mater.*, 3: 692-698.
- Carter, N.L., 1975. High-temperature flow of rocks. *Rev. Geoph. Space Phys.*, 13(3): 344-381.
- Carter, N.L. and Avé Lallemant, H.G., 1970. High temperature flow of dunite and peridotite. *Geol. Soc. Am. Bull.*, 81: 2181-2202.
- Chakraborty, S., Farver, J.R., Yund, R.A. and Rubie, D.C., 1994. Mg tracer diffusion in synthetic forsterite and San Carlos olivine as a function of P, T and fO₂. *Phys. Chem. Minerals*, 21: 489-500.
- Chen, I.-W., 1982. Diffusional creep of two-phase materials. *Acta Metall.*, 30: 1655-1664.
- Chen, I.-W., 1985. Superplastic flow of two-phase alloys. In: B. Baudelet and M. Suéry (Eds), *Superplasticity*. CNRS, Paris, pp. 5.1-5.20.
- Chokshi, A.H., 1991. Cavitation behaviour during superplastic flow. In: S. Hori, M. Tokizane and N. Furushiro (Eds), *Superplasticity in Advanced Materials*. The Japan Society for Research on

References

- Superplasticity, Osaka, pp. 171-180.
- Chokshi, A.H. and Langdon, T.G., 1987. A model for diffusion cavity growth in superplasticity. *Acta Metall.*, 35: 1089-1101.
- Chokshi, A.H. and Mukherjee, A.K., 1993. The influence of hydrostatic pressure on grain boundary sliding in superplasticity: implications for cavitation. *Mat. Sci. Eng.*, 171(1-2): 47-54.
- Chopra, P.N., 1986. The plasticity of some fine-grained aggregates of olivine at high pressure and temperature. In: B.E. Hobbs and H.C. Heard (Eds), *Mineral and rock deformation: Laboratory studies*. Geoph. Monogr. Am. Geoph. Union, pp. 25-33.
- Chopra, P.N. and Paterson, M.S., 1981. The experimental deformation of dunite. *Tectonophysics*, 78: 453-473.
- Chopra, P.N. and Paterson, M.S., 1984. The role of water in the deformation of dunite. *J. Geoph. Res.*, 89(B9): 7861-7876.
- Clarke, D.R., 1987. On equilibrium thickness of intergranular glass phases in ceramic materials. *J. Am. Ceram. Soc.*, 70: 15-22.
- Clarke, D.R., 1989. High-temperature microstructure of a hot-pressed silicon nitride. *J. Am. Ceram. Soc.*, 72: 1604-1609.
- Cloetingh, S., Wees van, J.D., Beek van der, P.A. and Spadini, G., 1995. Role of pre-rift rheology in kinematics of extensional basin formation: constraints from thermomechanical models of Mediterranean and intracratonic basins. *Marine and Petroleum Geology*, 12(8): 793-807.
- Coble, R.L., 1963. A model for boundary-diffusion controlled creep in polycrystalline materials. *J. Appl. Phys.*, 34: 1679-1682.
- Coe, R.S. and Kirby, S.H., 1975. The orthoenstatite to clinoenstatite transformation by shearing and reversion by annealing: mechanisms and potential applications. *Contrib. Mineral. Petrol.*, 52: 29-55.
- Cooper, R.F. and Kohlstedt, D.L., 1984a. Sintering of olivine and olivine-basalt aggregates. *Phys. Chem. Minerals*, 11: 5-16.
- Cooper, R.F. and Kohlstedt, D.L., 1984b. Solution-precipitation enhanced diffusional creep of partially molten olivine-basalt aggregates during hot-pressing. *Tectonophysics*, 107: 207-233.
- Cooper, R.F. and Kohlstedt, D.L., 1986. Rheology and structure of olivine-basalt partial melts. *J. Geoph. Res.*, 91(B9): 9315-9323.
- Daines, M.J. and Kohlstedt, D.L., 1996. Rheology of Olivine-Pyroxene Aggregates. *EOS*, 77(46): F711.
- Darot, M. and Gueguen, Y., 1981. High-temperature creep of forsterite single crystals. *J. Geoph. Res.*, 86(B7): 6219-6234.
- Davies, B.T.C. and England, J.C., 1964. The melting of forsterite up to 50 kilobars. *J. Geoph. Res.*, 69: 1113-1116.
- De Mott, G.J., 1987. Preparation of fayalite by solution-precipitation methods. M.S. Thesis. Cornell University, N.Y. University.
- Den Brok, S.W.J., 1992. An experimental investigation into the effect of water on the flow of quartzite. Publ. Ph.D. Thesis. *Geologica Ultraeactina* No. 95. Utrecht University. 178 pp.
- Dislich, H. and Hinz, P., 1982. History and principles of the sol-gel process and some new multicomponent oxide coatings. *J. non-Cryst. Sol.*, 48: 11-16.
- Drury, M.R., Hoogerduijn Strating, E.H. and Vissers, R.L.M., 1990. Shear zone structures and microstructures in mantle peridotites from the Voltri Massif, Ligurian Alps, N.W. Italy. *Geol. Mijnbouw*, 69: 3-17.
- Drury, M.R., Vissers, R.L.M., Van der Wal, D. and Hoogerduijn Strating, E.H., 1991. Shear localization in upper mantle peridotites. *Pure Appl. Geoph.*, 137: 439-460.
- Dunbar, J.A. and Sawyer, D.S., 1989. How pre-existing weaknesses control the style of continental breakup. *J. Geoph. Res.*, 94: 7278-7292.
- Durham, W.B., Froideveaux, C. and Jaoul, O., 1979. Transient and steady state creep of pure forsterite at low stress. *Phys. Earth Planet. Int.*, 19: 263-274.
- Durham, W.B. and Goetze, C., 1977a. A comparison of the creep properties of pure forsterite and iron-bearing olivine. *Tectonophysics*, 40: T15-T18.
- Durham, W.B. and Goetze, C., 1977b. Plastic flow of oriented single crystals of olivine. *J. Geoph. Res.*, 82(B6): 5737-5753.
- Durham, W.B., Goetze, C. and Blake, B., 1977. Plastic flow of oriented single crystals of olivine: 2. Observations and interpretations of the dislocation structures. *J. Geoph. Res.*, 82: 5755-5770.
- Echeverria, L.M., 1992. Enstatite ceramics: a multicomponent system via sol-gel. *J. non-Cryst. Sol.*, 147&148: 559-564.
- Edgar, A.D., 1973. *Experimental Petrology - Basic Principles and Techniques*. Clarendon Press, Oxford, 217 pp.
- Evans, B. and Dresen, G., 1991. Deformation of earth materials: Six easy pieces. *Rev. of Geoph.*, supplement: 823-843.
- Evans, B. and Goetze, C., 1979. The temperature variation of hardness of olivine and its implication for polycrystalline yield stress. *J. Geoph. Res.*, 84(B10): 5505-5524.
- Farver, J.R. and Yund, R.A., 1995. Grain boundary diffusion of oxygen, potassium and calcium in natural hot-pressed feldspar aggregates. *Contr. Min. Petr.*, 118: 340-355.
- Farver, J.R., Yund, R.A. and Rubie, D.C., 1994. Magnesium grain boundary diffusion in forsterite aggregates at 1000°- 1300°C and 0.1 MPa to 10 GPa. *J. Geoph. Res.*, 99(B10): 19809-19819.
- Finnerty, T.A., Waychunas, G.A. and Thomas, W.M., 1978. The preparation of starting mixes for mineral syntheses by a freeze-dry technique. *Am. Min.*, 63: 415-418.
- Flack, C.A., Klemperer, S.L., McGeary, S.E., Snyder, D.B. and Warner, M.R., 1990. Reflections from mantle fault zones around the Britain Isles. *Geology*, 18: 528-532.
- Fletcher, J.M. and Hardy, C.J., 1968. Application of sol-

- gel processes to industrial oxides. *Chem. Ind.*, Jan: 48-51.
- Fliervoet, T.F., 1995. Deformation mechanisms in fine grained quartz-feldspatic mylonites: An electron microscopy study. Publ. PhD. Thesis. *Geologica Ultraiectina* No. 131. Utrecht University. 167 pp.
- Frost, H.J. and Ashby, M.F., 1982. Deformation-mechanism maps - The plasticity and creep of metals and ceramics. Pergamon press, Oxford.
- Garrett, M.H., Chan, V.H., Jessen, H.P., Whitmore, M.H., Sacra, A., Singel, D.J. and Simkin, D.J., 1991. Comparison of chromium-doped forsterite and akermanite laser host crystals. *Opt. Soc. Am. Proc. Adv. Solid-State Lasers*, 10: 76-80.
- Gifkins, R.C., 1976. Grain-boundary sliding and its accommodation during creep and superplasticity. *Metallurgical Transactions*, 7A: 1225-1232.
- Gifkins, R.C., 1982. Mechanisms of superplasticity. In: N.E. Baton and C.H. Hamilton (Eds), *Superplastic forming of structural alloys*. *Metall. Soc. AIME*, pp. 3-26.
- Gleason, G., Green, H.W.I. and Zhou, Y., 1994. The rheology of periclase- and enstatite-buffered forsterite polycrystals. *EOS*, 75(44): 586.
- Goetze, C., 1978. The mechanisms of creep in olivine. *Phil. Trans. R. Soc. Lond.*, A 288: 99-119.
- Goetze, C. and Evans, B., 1979. Stress and temperature in the bending lithosphere as constrained by experimental rock mechanics. *Geoph. J. R. Astr. Soc.*, 59: 463-478.
- Goleby, B.R., Shaw, R.D., Wright, C.K., B.L.N. and Lambeck, K., 1988. Geophysical evidence for "thick-skinned" crustal deformation in central Australia. *Nature*, 337: 325-337.
- Gonczy, S.T., Lawson, R.J. and Rosen, B.I., 1986. Preparation of ceramics. United States Patent No. 4608215.
- Gordon, R.B., 1965. Diffusion creep in the Earth's upper mantle. *J. Geoph. Res.*, 70: 2413-2418.
- Govers, R. and Wortel, N.J.R., 1993. Initiation of asymmetric extension in continental lithosphere. *Tectonophysics*, 223: 75-96.
- Grossman, L., 1972. Condensation in the primitive solar nebula. *Geochim. Cosmochim. Acta*, 36: 597-619.
- Grover, J.E., 1972. The stability of low-clinoenstatite in the system $Mg_2Si_2O_6 - CaMgSi_2O_6$. *Trans. A.G.U.*, 53: 539.
- Haar, L., Gallagher, R. and Kell, G.S., 1984. NBS/NRC Steam Tables. Hemisphere Publ. Co., Washington.
- Hamilton, D.L. and Henderson, C.M.B., 1968. The preparation of silicate compositions by a gelling method. *Min. Mag.*, 36: 832-838.
- Harper, J. and Dorn, J.E., 1957. Viscous creep of aluminium near its melting temperature. *Acta met.*, 5: 654-665.
- Hench, L.L. and West, J.K., 1990. The Sol-Gel Process. *Chem. Rev.*, 90: 33-72.
- Herring, C., 1950. Diffusional viscosity of a polycrystalline solid. *J. Appl. Phys.*, 21: 437-445.
- Herring, C., 1951. Surface tension as a motivation for sintering. In: W.E. Kingston (Ed), *The physics of powder metallurgy*. McGraw-Hill, New York.
- Hillert, M., 1965. On the theory of normal and abnormal grain growth. *Acta Metall.*, 13: 227-238.
- Hirth, G. and Kohlstedt, D.L., 1995a. Experimental constraints on the dynamics of the partially molten upper mantle: 2. Deformation in the dislocation creep regime. *J. Geoph. Res.*, 100: 15441-15449.
- Hirth, G. and Kohlstedt, D.L., 1995b. Experimental constraints on the dynamics of the partially molten upper mantle: Deformation in the diffusion creep regime. *J. Geoph. Res.*, 100(B2): 1981-2001.
- Hirth, G. and Kohlstedt, D.L., 1996. Water in the oceanic upper mantle: implications for rheology, melt extraction and the evolution of the lithosphere. *Earth Plan. Sci. Lett.*, 144: 93-108.
- Hitchings, R.S., Paterson, M.S. and Bitmead, J., 1989. Effects of iron and magnetite additions in olivine-pyroxene rheology. *Phys. Earth Planet. Inter.*, 55: 277-291.
- Hobbs, B.E., 1983. Constraints on the mechanism of deformation of olivine imposed by defect chemistry. *Tectonophysics*, 92: 35-69.
- Hobbs, B.E., 1984. Point defect chemistry of minerals under a hydrothermal environment. *J. Geoph. Res.*, 89(B6): 4026-4038.
- Hogan, M., Martin, E., Ober, C.K., Hubbard, C.R., Porter, W.D. and Cavin, O.B., 1992. Poly(methacrylate) precursors to forsterite. *J. Am. Ceram. Soc.*, 75(7): 1831-1838.
- Holloway, J.R. and Wood, B.J., 1988. *Simulating the Earth - Experimental Geochemistry*. Unwin Hyman, Boston.
- Hoogerduijn Strating, E.H., 1991. The evolution of the Piemonte-Ligurian ocean. A structural study of ophiolite complexes in Liguria (NW Italy). Publ. PhD. Thesis. *Geologica Ultraiectina* No. 74. Utrecht University. 128+ xviii pp.
- Hoogerduijn Strating, E.H., Rampone, E., Piccardo, G.B., Drury, M.R. and Vissers, R.L.M., 1993. Subsolidus emplacement of mantle peridotites during incipient oceanic rifting and opening of the mesozoic Tethys (Voltri Massif, N.W. Italy). *J. Petr.*, 34: 901-927.
- Huang, C.H., Kuo, D.H., Kim, Y.J. and Kriven, W.M., 1994. Phase stability of chemically derived enstatite ($MgSiO_3$) powders. *J. Am. Ceram. Soc.*, 77(10): 2625-2631.
- Humphreys, F.G., 1985. Dislocation-particle interactions, Dislocations and properties of real materials. *Metals Soc. R. Soc.*, pp. 175-204.
- Humphreys, F.J. and Kalu, P.N., 1990. The plasticity of particle-containing polycrystals. *Acta Metall.*, 38: 917-930.
- Hwang, C.M.J. and Chen, I.W., 1990. Effect of a liquid phase on superplasticity of 2-mol%- Y_2O_3 -stabilized tetragonal zirconia polycrystals. *J. Am. Ceram. Soc.*, 73: 1626-1632.

References

- Isichenko, M.B., 1992. Percolation, statistical topography, and transport in random media. *Rev. Mod. Phys.*, 64: 961-1043.
- Jaoul, O., Froidevaux, C., Durham, W.B. and Michaut, M., 1980. Oxygen self-diffusion in forsterite: Implications for the high-temperature creep mechanism. *Earth Planet. Sci. Lett.*, 47: 391-397.
- Jaoul, O., Poumellac, M., Froidevaux, C. and Havette, A., 1981. Silicon diffusion in forsterite: A new constraint for understanding mantle deformation. In: F.D. Stacey, M.S. Paterson and A. Nicolas (Eds), *Anelasticity in the Earth*. Geodyn. Ser. Am. Geophys. Union, pp. 95-100.
- Jaoul, O., Tullis, J. and Kronenberg, A., 1984. The effect of varying water contents on the creep behavior of Heavytree quartzite. *J. Geoph. Res.*, 89(B6): 4298-4312.
- Johnson, D.W.J., 1985. Sol-gel processing of ceramics and glass. *Am. Ceram. Soc. Bull.*, 64(12): 1597-1602.
- Johnson, D.W.j.e.a., 1983. Preparation of high-silica glasses from colloidal gels: II, sintering. *J. Am. Ceram. Soc.*, 66(10): 688-693.
- Karato, S.-I., 1989a. Defects and Plastic deformation in olivine. In: S.-I. Karato and M. Toruimi (Eds), *Rheology of solids and of the Earth*. Oxford University Press.
- Karato, S.-I., 1989b. Grain growth kinetics in olivine aggregates. *Tectonophysics*, 168: 255-273.
- Karato, S.-I. and Ogawa, M., 1982. High-pressure recovery of olivine: implications for creep mechanisms and creep activation volume. *Phys. Earth Planet. Inter.*, 28: 102-117.
- Karato, S.-I., Paterson, M.S. and FitzGerald, J.D., 1986. Rheology of synthetic olivine aggregates: influence of grain size and water. *J. Geoph. Res.*, 91(B8): 8151-8176.
- Karato, S.-I. and Wu, P., 1993. Rheology of the upper mantle: A synthesis. *Science*, 260: 771-778.
- Kazakos, A., Komarneni, S. and Roy, R., 1990. Preparation and densification of forsterite (Mg_2SiO_4) by nanocomposite sol-gel processing. *Materials Letters*, 9(10): 405-409.
- Keefer, K.D., 1984. The effect of hydrolysis conditions on the structure and growth of silicate polymers. *Mat. Res. Soc. Sym. Proc.*, 32: 15-24.
- Keen, C.E., McLean, B.C. and Kay, W.A., 1991. A deep seismic reflection profile across Nova Scotia continental margin offshore eastern Canada. *Can. J. Earth Sci.*, 28: 1112-1120.
- Kerrick, D.M. and Jacobs, G.K., 1981. A modified Redlich-Kwong equation for H_2O , CO_2 , and H_2O-CO_2 mixtures at elevated pressures and temperatures. *Am. J. Sci.*, 281: 735-767.
- Kirby, S.H. and Raleigh, C.B., 1973. Mechanisms of high-temperature, solid-state flow in minerals and ceramics and their bearing on the creep behaviour of the mantle. *Tectonophysics*, 19: 165-194.
- Koch, P.S., Cristie, J.M., Ord, A. and George, R.P.j., 1989. The effect of water on the rheology of experimentally deformed quartzite. *J. Geoph. Res.*, 94: 13975-13996.
- Kohlstedt, D.L. and Goetze, C., 1974. Low-stress high-temperature creep in olivine single crystals. *J. Geoph. Res.*, 79(14): 2045-2051.
- Kohlstedt, D.L. and Hornack, P., 1981. Effect of oxygen pressure on the creep of olivine. In: M.S. Paterson and A. Nicolas (Eds), *Anelasticity in the Earth*. Geodyn. Ser. Am. Geoph. Union, pp. 101-107.
- Kohlstedt, D.L. and Ricoult, D.L., 1984. High-temperature creep of silicate olivines. In: R.E. Tressler and R.C. Bradt (Eds), *Deformation of Ceramic Materials II*. Plenum, New York, pp. 251-280.
- Komarneni, S., Suwa, Y. and Roy, R., 1987. Enhancing densification of 93% Al_2O_3 - 7% MgO tri-phasic xerogels with crystalline $\alpha-Al_2O_3$ and $MgAl_2O_4$ seeds. *J. Mater. Sci. Lett.*, 6(5): 525-527.
- Kronenberg, A.K., Segall, P. and Wolf, G.H., 1990. Hydrolytic weakening and penetrative deformation within a natural shear zone. *Geoph. Monograph*, 56: 21-36.
- Kronenberg, A.K. and Tullis, J., 1984. Flow strengths of quartz aggregates: grain size and pressure effects due to hydrolytic weakening. *J. Geoph. Res.*, 89(B6): 4281-4297.
- Kushiro, I. and Yoder, H.S., 1969. Melting of forsterite and enstatite at high pressures under hydrous conditions. *Carnegie Inst. Washington, Yearbook*, 67: 153-158.
- Kushiro, I., Yoder, H.S.j. and Nishikawa, M., 1968. Effect of water on the melting of enstatite. *Geol. Soc. Am. Bull.*, 79: 1685-1692.
- Langdon, T.G., 1995. Mechanisms of Superplastic Flow. In: N. Ridley (Ed), *Superplasticity: 60 years after Pearson*. Institute of Materials, London, pp. 9-24.
- Lister, G.A., Etheridge, M.A. and Symonds, P.A., 1991. Detachment models for the formation of passive continental margins. *Tectonics*, 10: 1038-1064.
- Lister, G.S., Etheridge, M.A. and Symonds, P.A., 1986. Detachment faulting and the evolution of passive continental margins. *Geology*, 14: 246-250.
- Liu, C., Komarneni, S. and Roy, R., 1995. Crystallization and seeding effect in $BaAl_2Si_2O_8$ gels. *J. Am. Ceram. Soc.*, 78(9): 2521-2526.
- Luth, W.C. and Ingamells, C.O., 1965. Gel preparation of starting materials for hydrothermal experimentation. *Am. Miner.*, 50: 255-258.
- Lynch, H.D. and Morgan, P., 1987. The tensile strength of the lithosphere and the localization of extension. In: M.P. Coward, J.F. Dewey and P.C. Hancock (Eds), *Continental extension tectonics*. *Geol. Soc.*, pp. 53-65.
- Mackenzie, J.D., 1982. Glasses from melts and glasses from gels, a comparison. *J. non-Cryst. Sol.*, 48: 1-10.
- Mackwell, S.J., Kohlstedt, D.L. and Paterson, M.S., 1985. The role of water in the deformation of olivine single crystals. *J. Geoph. Res.*, 90: 11319-11333.
- Marples, J.A.C., Nelson, R.L., Potter, P.E. and Robert, L.E.J., 1981. Chemistry in the development of nuclear power. In: R. Thomson (Ed), *Energy and Chemistry*. R. Soc. Chem., London, pp. 131-163.

- Marquardt, D.W., 1963. An algorithm for least squares estimation of nonlinear parameters. *J. Soc. Ind. Appl. Math.*, 2: 431-441.
- Martin, G. and Perraillon, B., 1979. Measurements of grain boundary diffusion. In: R.W. Balluffi (Ed), *Grain boundary structure and kinetics*. A.S.M., Milwaukee, pp. 239-295.
- Mazdiyasi, K.S., 1982. Powder synthesis from metal-organic precursors. *Ceram. Int.*, 8(2): 42-56.
- McKenzie, D.P., 1978. Some remarks on the development of sedimentary basins. *Earth Planet. Sci. Lett.*, 40: 25-31.
- Meier, L. and Eisbacher, G.H., 1991. Crustal kinematics and deep structure of the northern Rhine Graben, Germany. *Tectonics*, 10: 621-630.
- Mendelson, M.I., 1969. Average grain size in polycrystalline ceramics. *J. Am. Ceram. Soc.*, 52(8): 443-446.
- Mohamed, F.A. and Ginther, T.T., 1982. On the nature and origin of Harper-Dorn creep. *Acta Metall.*, 30: 1869-1881.
- Morey, G.W. and Hesselgesser, J.M., 1951. The solubility of some minerals in superheated steam at high pressures. *Econ. Geol.*, 46: 821-835.
- Morrell, R., 1985. *Handbook of properties of technical and engineering ceramics, part 1: An introduction for the engineer and designer*. Nat. Phys. Lab. - HMSO, London.
- Mukherjee, A.K., 1971. The Rate Controlling Mechanism in Superplasticity. *Mat. Sci. Eng.*, 8: 83-89.
- Mukherjee, A.K., 1975. High temperature creep. In: R.J. Arsenault (Ed), *Plastic deformation of materials*. Academic, Orlando, pp. 163-224.
- Nabarro, F.R.N., 1948. Deformation of crystals by the motion of single ions. In: G. Nooky (Ed), *Report of a Conference on Strength of Solids (Bristol)*. Phys. Soc., London, pp. 75-90.
- Nakashima, S., 1995. Diffusivity of ions in pore water as a quantitative basis for rock deformation rate estimates. *Tectonophysics*, 245: 185-203.
- Nakamura, Y. and Kushiro, I., 1974. Composition of the gas phase $Mg_2SiO_4-SiO_2-H_2O$. *Yearbook Carnegie Inst. Washington*, 73: 255-258.
- Nelson, R.C., Ramsay, J.D.F., Woodhead, J.C., Cairns, J.A. and Crossley, J.A.A., 1981. The coating of metals with ceramic oxides via colloidal intermediates. *Thin Solid Films*, 81: 329-337.
- Nogami, M. and Moriya, Y., 1982. Glass formation of $SiO_2-B_2O_3$ system by the gel process from metal alkoxides. *J. non-Cryst. Sol.*, 48: 359-366.
- Nordstrom, D.K. and Munoz, J.L., 1985. *Geochemical thermodynamics*. Benjamin Cummings Publ. Co. Inc., Menlow Park, 477 pp.
- Nowotny, J., 1991. Interface defect chemistry of oxide ceramic materials: unresolved problems. *Solid State Ionics*, 49: 119-128.
- Olgaard, D.L. and Evans, B., 1986. Effect of second-phase particles on grain growth in calcite. *Comm. Am. Ceram. Soc.*, 69(11): C272-C277.
- Omatete, O.O., Janney, M.A. and Strehlow, R.A., 1991. Gelcasting - A new ceramic forming process. *Am. Ceram. Soc. Bull.*, 70(10): 1641-1649.
- Oshi, Y. and Ando, K., 1984. Oxygen self diffusion coefficient in single-crystal forsterite. In: I. Sunagawa (Ed), *Materials Science of the Earths' Interior*, pp. 271-280.
- Park, D.G., Burlitch, J.M., Geray, R.F., Dieckmann, R., Barber, D. B. and Pollock, C.R., 1993. Sol-gel synthesis of chromium-doped forsterite. *Chem. Mater.*, 5: 518-524.
- Park, D.G., Duchamp, J.C., Duncan, T.M. and Burlitch, J.M., 1994a. Preparation of forsterite by pyrolysis of a Xerogel: The effect of water. *Chem. Mater.*, 6: 1990-1995.
- Park, D.G., Martin, H.E., Ober, C.K., Burlitch, J.M., Cavin, O.B., Porter, W.D. and Hubard, C.R., 1994b. Crystallization of precursors to forsterite and chromium-doped forsterite. *J. Am. Ceram. Soc.*, 77(1): 33-40.
- Paterson, M.S., 1962. O-ring piston seals for high pressure. *J. Sci. Instr.*, 39: 173-175.
- Paterson, M.S. and Luan, F.C., 1990. Quartzite rheology under geological conditions. In: R.J. Knipe and E.H. Rutter (Eds), *Deformation Mechanisms, Rheology and Tectonics*. Geol. Soc. Sp. Publ., London, pp. 299-307.
- Peach, C.J., 1991. Influence of deformation on the fluid transport properties of salt rocks. *Publ. PhD. Thesis. Geologica Ultraiectina No. 77. Utrecht University*. 238 pp.
- Petricevic, V., Gayen, S.K., Alfano, R.R., Yamagishi, K., Anzai, H. and Yamaguchi, Y., 1988. Laser action of Chromium-doped forsterite. *Appl. Phys. Lett.*, 52(13): 1040-1042.
- Phakey, P., Dollinger, G. and Christie, J., 1972. Transmission electron microscopy of experimentally deformed olivine crystals. In: H.C. Heard, I.Y. Borg, N.L. Carter and C.B. Raleigh (Eds), *Flow and fracture of rocks*. Geoph. Monogr. A.G.U., pp. 117-138.
- Pilling, J. and Ridley, N., 1988. Cavitation in superplastic alloys and the effect of hydrostatic pressure. *Res. Mech.*, 23: 31-63.
- Poirier, J.P., 1985. *Creep of crystals*. Cambridge University Press, Cambridge, 260 pp.
- Post, R.L.J., 1977. High-temperature creep of Mt. Burnet dunite. *Tectonophysics*, 42: 75-110.
- Poumellec, B. and Jaoul, O., 1984. Influence of pO₂ and pH₂O on the high temperature plasticity of olivine. In: R.E. Tressler and R.C. Bradt (Eds), *Deformation of Ceramic Materials II*. Plenum, New York., pp. 281-305.
- Puyane, R. and Gonzalez-Oliver, C.J.R., 1983. Thin film deposition using sol-gel technology. *Thin Film Technology*, 401: 307-311.
- Puyane, R., Harmer, A.C. and Gonzalez-Oliver, C.J.R., 1982. Optical fibre fabrication by sol-gel method, *European Conf. on Optical Comm.*, pp. C-24.
- Rabinovich, E.M.e.a., 1984. Sol-gel preparation of transparent silica glass. *J. non-Cryst. Sol.*, 63: 155-161.
- Rabinowich, E.M.e.a., 1983. Preparation of high-silica

References

- glasses from colloidal gels: I. Preparation for sintering and properties of sintered glass. *J. Am. Ceram. Soc.*, 66(10): 683-688.
- Raj, R., 1982. Creep in polycrystalline aggregates by matter transport through a liquid phase. *J. Geoph. Res.*, 87: 4731-4739.
- Raleigh, C.B., 1968. Mechanisms of plastic deformation of olivine. *J. Geoph. Res.*, 73: 5391-5406.
- Raleigh, C.B. and Kirby, S.H., 1970. Creep in the upper mantle. *Mineral. Soc. Am. Spec. Pap.*, 3: 113-121.
- Raleigh, C.B., Kirby, S.H., Carter, N.L. and Avé Lallemant, H.G., 1971. Slip and the clinoenstatite transformation as completing rate processes in enstatite. *J. Geoph. Res.*, 76(17): 4011-4022.
- Ramsay, J.D.F., 1988. Characterisation of colloids and gels. *Mat. Res. Soc. Symp. Proc.*, 121: 293-304.
- Ranalli, G., 1987. Rheology of the Earth; deformation and flow processes in geophysics and geodynamics. Allen and Unwin, London, 413 pp.
- Randle, V., 1992. Microtexture Determination and its Applications. Institute of Materials, London, 171 pp.
- Reddy, K.P.R., Oh, S.M., Major, L.D. and Cooper, A.R., 1980. Oxygen diffusion in forsterite. *J. Geoph. Res.*, 85(B1): 322-326.
- Ree, J.H., 1994. Grain boundary sliding and development of grain boundary openings in experimentally deformed octachloropropane. *J. Struct. Geol.*, 16(3): 403-418.
- Relandeau, C., 1981. High temperature creep of forsterite polycrystalline aggregates. *Geoph. Res. Lett.*, 9(7): 733-736.
- Reston, T.J., 1990. Mantle shear zones and the upper mantle during extension of continental lithosphere. *Geology*, 18: 272-275.
- Reston, T.J., 1993. Evidence for extensional shear zones in the mantle, offshore Britain, and their implications for extension of the continental lithosphere. *Tectonics*, 12: 492-506.
- Ricoult, D.L. and Kohlstedt, D.L., 1985. Experimental evidence for the effect of chemical environment upon the creep rate of olivine. In: R.N. Schock (Ed), Point defects in minerals. *Geoph. Monogr. AGU*, Washington, pp. 171-184.
- Ridley, N. and Wang, Z.C., 1994. Cavitation in superplastic metals. *Mat. Sci. Forum*, 170-172: 177-186.
- Ridley, N. and Wang, Z.C., 1995. Cavitation in superplastic materials. In: N. Ridley (Ed), Superplasticity: 60 Years after Pearson. Institute of Materials, Manchester, pp. 63-74.
- Riecker, R.E. and Rooney, T.P., 1967. Deformation and polymorphism of enstatite under shear stress. *Geol. Soc. Am. Bull.*, 78: 1045-1054.
- Ringwood, A.E., 1969. Composition and evolution of the upper mantle. In: P.J. Hart (Ed), The Earth's crust and upper mantle. *Geoph. Monogr. AGU.*, pp. 1-17.
- Ringwood, A.E., 1975. Composition and petrology of the Earth's Mantle. McGraw-Hill, New York, 618 pp.
- Ringwood, A.E., 1989. Significance of the terrestrial Mg/Si ratio. *Earth Planet. Sci. Lett.*, 95: 1-7.
- Ross, J.V., Avé Lallemant, H.G. and Carter, N.L., 1979. Activation volume for creep in the upper mantle. *Science*, 203: 261-263.
- Roy, D.M. and Roy, R., 1954. An experimental study of the formation and properties of synthetic serpentines and related layer silicate minerals. *Am. Mineralogist*, 39: 957-975.
- Roy, R., 1956. Aids in hydrothermal experimentation: II. *J. Am. Ceram. Soc.*, 39: 145-146.
- Roy, R., Suwa, Y. and Komarneni, S., 1986. Nucleation and epitaxial growth in diphasic (crystalline + amorphous) gels. In: L.L. Hench and D.R. Ulrich (Eds), Science of ceramic chemical processing. John Wiley and Sons Inc.
- Russ, J.C., 1986. Practical stereology. Plenum Press, New York, 185 pp.
- Rutter, E.H., 1983. Pressure solution in nature, theory and experiment. *J. Geol. Soc. London*, 140: 725-740.
- Rutter, E.H. and Brodie, K.H., 1985. The permeation of water into hydrating zones. In: A.B. Thompson and D.C. Rubie (Eds), Advances in physical geochemistry. Springer Verlag, Berlin.
- Rutter, E.H. and Brodie, K.H., 1988. Experimental 'syn-tectonic' dehydration of serpentinite under conditions of controlled pore water pressure. *J. Geoph. Res.*, 93(B5): 4907-4932.
- Sawyer, D.S., 1985. Brittle failure in the upper mantle during extension of continental lithosphere. *J. Geoph. Res.*, 90: 3021-3025.
- Scher, H. and Zallen, R., 1970. Critical density in percolation processes. *J. Chem. Phys.*, 53: 3759.
- Schmid, S.M., Boland, J.N. and Paterson, M.S., 1977. Superplastic flow in fine-grained limestone. *Tectonophysics*, 43: 257-291.
- Schmid, S.M., Patterson, M.S. and Boland, J.N., 1980. High temperature flow and dynamic recrystallization in Carrara marble. *Tectonophysics*, 65: 245-280.
- Schneider, M.E. and Eggler, D.H., 1986. Fluids in equilibrium with peridotite minerals: implications for mantle metasomatism. *Geochem. Cosmochim. Acta*, 50: 711-724.
- Schwenn, M.B. and Goetze, C., 1978. Creep of olivine during hot-pressing. *Tectonophysics*, 48: 41-60.
- Sclar, C.B., Carrison, L.C. and Schwartz, C.M., 1964. High pressure stability field of clinoenstatite and the orthoenstatite-clinoenstatite transition. *Trans. AGU.*, 45(1): 121.
- Scot, K.T. and Woodhead, J.C., 1982. Gel processed powders for plasma spraying. *Thin Solid Films*, 95: 219-225.
- Segal, D., 1989. Chemical synthesis of advanced ceramic materials (ed.1991). Chemistry of solid-state materials (vol.1). Cambridge University Press, Cambridge, 182 pp.
- Shiono, T., Nishida, T., Okamoto, Y., Sugishima, Y. and Nishikawa, T., 1991. Preparation and characterization of forsterite powder derived from silicon

- alkoxide and magnesium oxide. *Ceramic Trans.* (Ceram. Powder Sci. IV), 22: 6pp.
- Smyth, D.M. and Stocker, R.L., 1975. Point defects and non-stoichiometry in forsterite. *Phys. Earth Planet. Int.*, 10: 183-192.
- Spiers, C.J. and Schutjens, P.M.T.M., 1990. Densification of crystalline aggregates by fluid-phase diffusional creep. In: D.J. Barber and P.D. Meredith (Eds), *Deformation processes in minerals, ceramics and rocks*. Unwin Hyman, London, pp. 334-353.
- Spiers, C.J., 1979. Fabric development in calcite polycrystals deformed at 400 °C. *Bulletin de Mineralogie*, 102, 282-289.
- Stocker, R.L. and Ashby, M.F., 1973. On the rheology of the upper mantle. *Rev. Geoph. Space Physics*, 11(2): 391-426.
- Stocker, R.L. and Smyth, D.M., 1978. Effect of enstatite activity and oxygen partial pressure on the point-defect chemistry of olivine. *Phys. Earth Planet. Int.*, 16: 145-153.
- Sudo, S., Nakahara, M. and Inagaki, N., 1983. A novel high-rate fabrication process for optical fiber reforms., 4th Int. Conf. Integrated Optics and Optical Fibre Comm. Tech. Dig., pp. 14-15.
- Suwa, Y., Komarneni, S. and Roy, R., 1986a. Solid-state epitaxy demonstrated by thermal reactions of structurally diphasic xerogels: the system Al_2O_3 . *J. Mat. Sci. Lett.*, 5: 21-24.
- Suwa, Y., Roy, R. and Komarneni, S., 1986b. Lowering the sintering temperature and enhanced densification by epitaxy in structurally diphasic Al_2O_3 and Al_2O_3 -MgO xerogels. *Mater. Sci. Eng.*, 83: 151-159.
- Tsenn, M.C. and Carter, N.L., 1987. Upper limits of power law creep of rocks. *Tectonophysics*, 136: 1-26.
- Tullis, T.E., Horowitz, F.G. and Tullis, J., 1991. Flow laws of polyphase aggregates from end-member flow laws. *J. Geoph. Res.*, 96(B5): 8081-8096.
- Tullis, T.E. and Tullis, J., 1986. Experimental rock deformation techniques. In: B.E. Hobbs and H.C. Heard (Eds), *Geophysical Monographs*. AGU, Washington D.C., pp. 297-324.
- Twiss, R.J., 1976. Structural superplasticity and linear viscosity in the earth's mantle. *Earth Planet. Sci. Lett.*, 33: 86 - 100.
- Underwood, E.E., 1970. *Quantitative Stereology*. Addison-Wesley Publ. Comp., Reading, Massachusetts, 274 pp.
- Van der Wal, D., 1993. Deformation processes in mantle peridotites, with emphasis on the Rhonda peridotite of SW Spain. Publ. PhD. Thesis. *Geologica Ultraiectina* No. 102. Utrecht University, 180 pp.
- Vissers, R.L.M., Drury, M.R., Hoogerduijn Strating, E.H., Spiers, C.J. and Van der Wal, D., 1995. Mantle shear zones and their effect on lithosphere strength during continental breakup. *Tectonophysics*, 249: 155-171.
- Wakai, F., Sakaguchi, S., Murayama, N., Kodama, Y. and Kondo, N., 1994. Effect of impurities on deformation of Y_2O_3 -stabilized ZrO_2 polycrystals. *Trans. Mater. Res. Soc. Jpn.*, 16b: 947-52.
- Walker, A.N., Rutter, E.H. and Brodie, K.H., 1990. Experimental study of grain-size sensitive flow of synthetic, hot-pressed calcite rocks. In: R.J. Knipe and E.H. Rutter (Eds), *Deformation Mechanisms, Rheology and Tectonics*. Geol. Soc. Sp. Publ., London, pp. 259-284.
- Wang, J.G. and Raj, R., 1984. Mechanism of superplastic flow in a fine-grained ceramic containing some liquid phase. *J. Am. Ceram. Soc.*, 67: 399-409.
- Wang, J.N., 1994. Harper-Dorn creep in polycrystalline ferrite, beryllia, alumina, calcite and olivine. *Scripta Metallurgica et Materialia*, 30: 859-862.
- Wang, J.N. and Langdon, T.G., 1994. An evaluation of the rate controlling flow process in Harper-Dorn creep. *Acta Metall. Mater.*, 42(7): 2487-2492.
- Watson, B.E., Brennan, J.M. and Baker, D.R., 1990. Distribution of fluids in the continental mantle. In: M.A. Menzies (Ed), *Continental mantle*. Clarendon press, Oxford, pp. 111-125.
- Weertman, J., 1968. Dislocation climb theory of steady state creep. *Trans. A.S.M.*, 61: 681-694.
- Weertman, J., 1978. Creep laws for the mantle of the Earth. *Phil. Trans. R. Soc. London*, A288: 9-26.
- Wernicke, B., 1985. Uniform sense normal simple shear of the continental lithosphere. *Can. J. Earth Sci.*, 22: 108-125.
- Wheeler, J., 1992. Importance of pressure solution and Coble creep in the deformation of polymineralic rocks. *J. Geoph. Res.*, 97(B4): 4579-4586.
- Wolfenstine, J. and Kohlstedt, D.L., 1994. High-temperature creep and kinetic decomposition of Ni_2SiO_4 . *Phys. Chem. Minerals*, 21: 234-243.
- Wood, D.L.e.a., 1983. Preparation of high-silica glasses from colloidal gels: III, infrared spectrophotometric studies. *J. Am. Ceram. Soc.*, 66(10): 693-699.
- Woodhead, J.L. and Segal, D.L., 1984. Sol-gel processing. *Chemistry in Britain*, 20: 310-313.
- Yeager, K.E. and Burlitch, J.M., 1991. Magnesium methoxide derived catalysis of transesterification, hydrolysis, and condensation of $Si(OMe)_4$ in the sol-gel synthesis of magnesium silicates. *Chem. Mater.*, 3(3): 387-389.
- Yeager, K.E., J.M., B. and Loehr, T.M., 1993. Intermediates in the sol-gel synthesis of forsterite. *Chem. Mater.*, 5: 525-534.
- Yoldas, B.E., 1988. Molecular and microstructural effects of condensation reactions in alkoxide-based alumina systems. In: J.D. Mackenzie and D.R. Ulrich (Eds), *Ultrastructure processing of advanced ceramics*. John Wiley and Sons, New York.
- Yoon, C.K. and Chen, I.-W., 1990. Superplastic flow of two-phase ceramics containing rigid inclusions - zirconia/mullite composites. *J. Am. Ceram. Soc.*, 73: 1555-1565.
- Young, A.C., Lin, J.C., Yeh, T.S. and Cherng, C.L., 1993. Characteristics of tape casting slurries containing forsterite, PVB and organic solvent. *Mat. Chem. Phys.*, 34: 147-153.
- Young, C., 1969. Dislocations in the deformation of

References

- olivine. *Am. J. Sci.*, 267: 841-852.
- Yund, R.A., 1997. Rates of grain boundary diffusion through enstatite and forsterite reaction rims. *Contr. Min. Petr.*, 126: 224-236.
- Yusuda, E., Bao, Q. and Tanabe, Y., 1989. Superplasticity in ceramic materials. *Rep. Res. Lab. Eng. Mater., Tokyo Inst. Tech.*, 14: 49-59.
- Zeuch, D.H. and Green II, H.W., 1979. Experimental deformation of an anhydrous synthetic dunite. *Bull. Min.*, 102: 185-187.
- Zeuch, D.H. and Green II, H.W., 1984a. Experimental deformation of a synthetic dunite at high temperature and pressure: I. Mechanical behaviour, optical microstructure and deformation mechanism. *Tectonophysics*, 110: 233-262.
- Zeuch, D.H. and Green II, H.W., 1984b. Experimental deformation of a synthetic dunite at high temperature and pressure: II. Transmission electron microscopy. *Tectonophysics*, 110: 263-296.

Samenvatting

In de literatuur is voorgesteld dat fijnkorrelige gehydrateerde peridotiet mylonieten een belangrijke rol spelen bij het bepalen van de sterkte van de continentale lithosfeer tijdens riftingases. Het deformatiegedrag van natte fijnkorrelige forsteriet en forsteriet-enstatiet materialen in aanwezigheid van water, en de achterliggende deformatiemechanismen, zijn daarom onderwerp van grote belangstelling binnen de structurele geologie en tectonofysica. Bovendien is de deformatie van polykristallijn forsterietrijk materiaal van fundamenteel belang voor het begrijpen van het gedrag van bovenmantel materialen in het algemeen. In deze dissertatie wordt verslag gedaan van experimenteel materiaalkundig georiënteerd onderzoek gericht op het verschaffen van een beter begrip van het deformatiegedrag van natte fijnkorrelige olivijn en olivijn-enstatiet materialen onder condities die gunstig zijn voor korrelgrootte gevoelige deformatieprocessen.

In hoofdstuk 1 worden de problemen geïntroduceerd die in deze dissertatie worden behandeld, en worden de doelen gepresenteerd.

In hoofdstuk 2 wordt een praktische en betrouwbare methode voor de vervaardiging van forsteriet en forsteriet-enstatiet materialen in het systeem MgO-SiO₂. De methode is gebaseerd op de “sol-gel” techniek. De geproduceerde materialen hebben een zeepbeltextuur en zijn homogeen fijnkorrelig (1-2 μm). Het enstatietgehalte kan nauwkeurig worden gecontroleerd en dichtheden tot 98% van de theoretische dichtheid kunnen worden bereikt. De ontwikkelde methode is gebruikt om cilindrische monsters te vervaardigen met een lengte van 25 mm en een doorsnede van 10 mm, geschikt voor natte deformatietesten.

In hoofdstuk 3 wordt het gasdruk deformatieapparaat beschreven dat gebruikt is voor de huidige experimenten. Dit apparaat is dusdanig geconfigureerd dat het differentiële spanning, axiale vervorming en vervormingssnelheden kan meten, bij alzijdige drukken tot aan 700 MPa, monstertemperaturen tot ~ 1100 °C, en constante verplaatsingssnelheden.

In hoofdstuk 4 is het deformatiegedrag van synthetische duniet (forsteriet met 2,5 vol% enstatiet referentiemateriaal) met een korrelgrootte van 1 - 2 μm onderzocht, met en zonder toegevoegd water (~ 0,5 gew%) in gecombineerde verplaatsings-snelheid en stapsgewijze/cyclische testen uitgevoerd bij een alzijdige druk van ~ 600 MPa. De resultaten laten zien dat, terwijl het droge materiaal zich volledig elastisch gedraagt bij 950 °C en relatieve vervormingssnelheden van 1×10^{-6} en $1 \times 10^{-7} \text{ s}^{-1}$, natte monsters meestal deformereren door middel van “steady state” kruip bij temperaturen van 850 tot 1000 °C (1123 tot 1273 K) en vervormingssnelheden tussen 5×10^{-5} en $2 \times 10^{-7} \text{ s}^{-1}$. De natte monsters vloeiden bij differentiële spanningen tussen 5 en 60 MPa, waarbij vervormingen tot 12% zijn bereikt. De spannings- en temperatuursafhankelijkheid van de vloeisnelheid in de natte monsters zijn getoetst aan een Dorn type exponentiele vergelijking, hetgeen resulteert in spanningsexponenten (n) variërend van 1,3 tot 2,2 voor de afzonderlijke isotherme testen. Volledige nonlineaire regressie analyse van de complete set van “steady state” kruip data leverde een $n = 2,14 \pm 0,18$ op. De waarde van de schijnbare aktiveringsenergie (Q_c) voor kruip is bepaald op ~ 285 en $320 \pm 40 \text{ kJ mol}^{-1}$ met behulp van respectievelijk de isothermale en volledige regressie toetsen. De nat gedeformeerde monsters werden gekenmerkt door polygonale korrels, geen kristallografische voorkeursoriëntatie, weinig

of geen korrelgroei of rekristallisatie, geen “subgrains”, lage dislocatiedichtheden, en laten geen bewijs voor korrelgrenscavities zien. Aan de hand van vergelijking van de mechanische data en microstructurele observaties met zowel microfysische modellen voor kruip als eerder onderzoek aan fijnkorrelige olivijn, kan worden geconcludeerd dat de natte monsters waarschijnlijk deformeerden door middel van een korrelgrootte afhankelijk (GSS), door korrelgrensschuif (GBS) gedomineerd mechanisme, alhoewel de aard van het GBS accommodatiemechanisme onduidelijk blijft en de mogelijkheid van overgangsgedrag tussen dislocatie- en diffusiekruip niet kan worden uitgesloten. Extrapolatie van de vloeivergelijking voor het natte materiaal naar natuurlijke vervormingssnelheden verwacht voor gehydrateerde peridotiet mylonieten, bevestigt de voorspelling van Vissers et al. (1995) dat gelocaliseerde deformatie in bovenmantel mylonietzones, onder condities die corresponderen met lithosferische extensie/“rifting”, zal leiden tot een significante verzwakking van de bovenste 10 tot 20 km van de lithosferische bovenmantel.

In hoofdstuk 5 is het effect van variërende hoeveelheden enstatiet (tussen 0 en 20%) op het deformatiegedrag van het forsteriet-enstatiet referentiemateriaal met ~ 0,5 gew% toegevoegd water onderzocht. Experimenten zijn gedaan bij temperaturen van 850 tot 1006 °C (1123 tot 1279 K), vervormingssnelheden tussen 2×10^{-7} en $5 \times 10^{-5} \text{ s}^{-1}$ en een alzijdige druk van ~ 600 MPa. De monsters vertoonden (benaderden) “steady state” kruip bij spanningen ≤ 60 MPa. Een paar testen lieten ‘work hardening’ zien bij hoge spanningen. De bijna “steady state” resultaten laten zien dat, bij konstante vervormingssnelheid, een toename van de enstatietgehalte een scherpe afname (factor 3 tot 10) van vloeisterkte tot gevolg heeft tussen 0 en 2,5% enstatiet en een kleine verdere verandering bij hogere enstatietgehalte. Verder waren het waargenomen vloeigedrag (gemiddelde $n \approx 1,7$, $Q_c = 305 \pm 142 \text{ kJ mol}^{-1}$) en de microstructuren gelijk aan die gerapporteerd in hoofdstuk 4 voor materiaal met 2,5% enstatiet, wat wijst op optreden van dezelfde deformatiemechanismen. Verder moet worden opgemerkt dat korrelgrootteanalyse een negatieve correlatie tussen korrelgrootte (variërend slechts tussen 1 en 2 μm) en enstatietgehalte (0 tot 20 vol%) laat zien, wat wil zeggen dat de enstatietgehalte een rol speelde bij de beheersing van de korrelgrootte van het startmateriaal. Bij verder onderzoek is een sterke correlatie tussen gemeten vloeisterkte en korrelgrootte gevonden, overeenkomend met een korrelgrootteexponent van -3 in een conventionele GSS vloeivergelijking. Dit duidt op een door water geassisteerd deformatiemechanisme waarbij GBS is betrokken, waarschijnlijk geaccommodeerd door korrelgrensdiffusie en/of dislocatieactiviteit. Hierbij is het effect van enstatietgehalte op vloeisterkte een indirect fysisch effect, veroorzaakt door korrelgrootte beheersing. Mogelijke andere effecten van tweedefase-gehalte, zoals verzwakking veroorzaakt door diffusie/migratie processen op fasegrenzen, worden bijgevolg onbelangrijk geacht bij de onderzochte condities.

In hoofdstuk 6 is een poging beschreven om systematisch het effect van de bulk watergehalte op het vloeigedrag van fijnkorrelige forsteriet plus enstatiet materialen te onderzoeken bij dezelfde condities als beschreven in hoofdstukken 4 en 5. De experimenten werden daarom uitgevoerd op het forsteriet-enstatiet referentiemateriaal met 2,5 vol% enstatiet en een korrelgrootte van 1 tot 2 μm bij een temperatuur van 950 °C (1223 K) en een alzijdige druk van 600 MPa. Watergehaltes van 0,48, 0,28, 0,11, 0,05, 0,02 (gew%) en nominaal droog werden onderzocht. In overeenkomst met de eerdere resultaten gedroegen de droge monsters zich elastisch, terwijl monsters met een watergehalte $> 0,1$ gew% bij benadering “steady state” kruip lieten zien. De spanningsexponenten (n) van ongeveer 1,6

en de microstructuren zijn consistent met het eerder veronderstelde GBS gedomineerde mechanisme. Een verandering van watergehalte van 0,48 tot 0,11 gew% leidde tot een toename van vloeisterkte bij constante vervormingssnelheid van een faktor 2 tot 3. Bij een watergehalte < 0,1 gew% werd alleen een zeer kleine afname in vloeisterkte waargenomen. Dit wijst op een extreme gevoeligheid voor watergehalte in het bereik van 0,02 tot 0,11 gew%. Op grond van de experimenteel verkregen activeringsenergie, waterdruk en microstructurele argumenten, wordt de waargenomen afname in vloeisterkte door water in monsters met > 0,11 gew% toegeschreven aan een hogere korrelgrensdiffusiviteit veroorzaakt door de vorming van aan water gerelateerde korrelgrensdefecten en/of geassocieerde structurele korrelgrensveranderingen. Gezien de extreme gevoeligheid voor watergehalte in het bereik van 0,02 tot 0,11 gew%, wordt geadviseerd voorzichtig te zijn met het gebruiken van natte diffusiekruipdata, verkregen bij een watergehalte > 0,1 gew%, voor de bovenmantel, waar in het algemeen een lagere watergehalte wordt verwacht (~ 0,1 gew% - Ringwood, 1975).

In hoofdstuk 7 zijn de resultaten samengevoegd, worden algemene conclusies getrokken en suggesties gedaan voor verder onderzoek.

Acknowledgements

It is impossible to thank all those people who have helped, encouraged and guided me during both the research for and writing of this thesis.

Firstly, I would like to thank my supervisor, Professor C.J. Spiers. Chris has truly been an inspiration and it has been a privilege to work with an experimentalist with his wealth of knowledge and experience. His clear thinking and detailed criticism during the writing stage have been invaluable. I will always fondly remember the fact that we both managed to keep a sense of humour throughout.

I would also like to thank my co-supervisor, Dr. C.J. Peach. Colin has given me considerable help and advice in getting the experimental equipment and methods up and running, and always found time to help me out.

I would like to thank the entire HPT team - Dr. Hans de Bresser, Gert Kastelein, Eimert de Graaff, Peter van Krieken and Jaap Liezenberg, though special thanks are due to Gert (paranimf), who built and maintained the 10 kbar apparatus and helped me to carry out all the experiments reported in this thesis. His contribution to the ongoing development of the 10 kbar apparatus is immeasurable.

Dr. Herman van Roermund enthusiastically carried out all the TEM investigations reported in this thesis in double-quick time. His considerable experience with this technique has made a major contribution to this work. I am also indebted to Dr. Martyn Drury, for instructing me in the use of the XL30 FEG SEM, including the EBSP technique, and for always being willing to discuss details of olivine deformation. Thanks also to Dr. Coen ten Brink for his help, especially in the final stages of writing, particularly with the painstaking job of cross-checking references.

Several people were very kind to me when I arrived in Utrecht and I would particularly like to thank Ben Jansen and Ad van der Eerden, with whom I worked initially, and Prof. Bernard de Jong who always has an open door. Furthermore, several people have inspired my wish to stay in geology particularly Tony Carswell, Jack Soper and Prof. Dawson (Sheffield), and Giles Droop, Dave Hamilton and Dave Rubie (Manchester), Henk Kars (ROB in Amersfoort) and Reinoud Vissers and Prof. White (Utrecht).

I would like to thank all the staff in Utrecht who have assisted me during this research including: Magda Marthot-Martens, M. Reith (TGA), Thea Broer-de Jong (XRD), T. Zalm and T. Bouten (EPMA); the workshop staff Tony van der Gon Netscher and Hans Blik; the staff of the audio-visual department Izaak Santoe, Jaco Bergenhenegouwen, Fred Trappenburg, Brigitta Benders and Paul van Oudenallen for the thesis lay-out and the staff of the electron microscopy centre Pim van Maurik, Henk Pluijgers and Theo Krefit.

I would like to thank all my fellow students for making me so welcome when I first arrived in Utrecht, for their encouragement and for all the good laughs we have had. I particularly wish to thank my room-mate Siese de Meer (paranimf), Rian Visser, Ronald Bakker, Patrick Speck and Timon Fliervoet.

Dr. R. Terpstra, Dr. J. Gerritsen, Harry Gorter and Dr. P. Buining are thanked for their kindness and help during my very useful 2 month visit to the Centre for Technical Ceramics, Eindhoven. Harry Gorter located the key Shiono et al (1991) reference, and passed on a few tricks of the trade, many thanks Harry.

I have always been given support by my great friends back in the UK especially Rod, Andy, Treb, John Keane, Paul O'Hallaran and Nick Peel thanks lads, and here in NL Ruud, Daan, Rachel Collins, Bev, Simon, Paul and Jeroen.

Special thanks go to Sue McDonnell for her understanding, care, help and constant support over the many years that I have been involved in PhD research, and to my sister Janet, brother Ian and Sue's family for their constant support.

I gratefully acknowledge the Nederlandse Organisatie voor Wetenschappelijk Onderzoek (NWO) who provided the funding for the apparatus and the PhD studentship (project no. 751-353-026).

CURRICULUM VITAE

Robert Denis McDonnell B.Sc. (Hon.); FGS (London).

Date of birth: 30-10-1963

Place of Birth: Windlesham, Surrey, England, U.K.

High school education: 1977 - 1982: Salesian School, Highfield Rd, Chertsey, Surrey, UK.

Undergraduate studies: 1982 - 1985: University of Sheffield UK.

Graduated: 1985: BSc Honours Degree in Geology - class 2.1

Postgraduate and work experience:

1985 - 1988: University of Manchester.
NERC Research studentship in experimental petrology.
HPT Laboratory Department of Geology, Manchester, UK.

1988 - 1989: Production worker
Sealpak BV, Nijmegen, NL. Maintenance, adjustment
and operation of a rotation die-cutting machine.

1989 - 1990: Technician Digital Equipment Corp., Nijmegen, NL.
Testing and repair of Ethernet interfaces.

1990 - 1992: Geologist/Materials scientist
Rijksdienst voor het Oudheidkundig Bodemonderzoek
(ROB), Kerkstraat 1, Amersfoort, NL.

1992 - 1997: Universiteit Utrecht
NWO (OIO) PhD research studentship. HPT Laboratory.
Instituut voor Aardwetenschappen, Utrecht, NL.

September 1997 - present : Universiteit Utrecht
Researcher in petrophysics. HPT Laboratory.
Instituut voor Aardwetenschappen, Utrecht, NL.